Electron-quantum-optics experiments at the single particle level

Hermann Edlbauer

Communauté
UNIVERSITÉ Grenoble Alpes

THÈSE

Pour obtenir le grade de

DOCTEUR DE la Communauté UNIVERSITÉ GRENOBLE ALPES

Spécialité : **Nanophysique**

Arrêté ministériel : 7 Août 2019

Présentée par

Hermann EDLBAUER

Thèse dirigée par **Christopher BÄUERLE**

préparée au sein **de l'Institut Néel - CNRS**
et de **l'École doctorale de Physique**

Electron-Quantum-Optics Experiments at the Single Particle Level

Thèse soutenue publiquement le **9 Julliet 2019**,
devant le jury composé de :

Christopher J. B. Ford
Professeur, Université de Cambridge, Examinateur
Rodolfo Jalabert
Professeur, Université de Strasbourg, Rapporteur
Frédéric Pierre
Directeur de recherche, C2N-CNRS, Rapporteur
Benoit Boulanger
Professeur, Université Grenoble Alpes, Président
Christopher Bäuerle
Directeur de recherche, Institut Néel-CNRS, Directeur de thèse

Abstract

In the last 25 years there were significant advances on quantum-optics-like experiments with electrons. The progress is this young field of research brought up original techniques to trap, displace and manipulate electrons in solid-state devices and opened up new prospects to study fascinating quantum mechanical phenomena such as tunneling or entanglement with electrons. Due to the controllability that is demanded in implementations of quantum logic circuits, it is now a particularly appealing idea to perform electron quantum optics experiments with single flying electrons. In this thesis we address two related, but conceptually different, electron-quantum-optics experiments at the single-particle level[1].

First, we perform a Mach–Zehnder type electron interference experiment in the ballistic transport regime. Forming a large quantum dot in one of the interferometer branches, we study the phase shift in the wave function of a resonantly transmitted electron. In the course of our experimental investigations, we find signatures of a transmission behaviour which reflects the internal symmetries of the quantum dot eigenstates. Shedding light on the long-standing question about a universal transmission phase behaviour, our measurements set an important milestone to build a comprehensive understanding of resonant transmission of single flying electrons through quantum dots.

In a second experiment, we go beyond the ballistic transport regime and employ surface acoustic waves to transport a single electron between surface-gate defined quantum dots of a tunnel-coupled circuit of transport channels. In this course, we develop two essential building blocks to partition and couple single flying electrons in such a sound-driven circuit. By exceeding a single-shot transfer efficiency of 99 %, we show that a sound-driven quantum electronic circuit is feasible on a large scale. Our results pave the way for the implementation of quantum logic operations with flying electron qubits that are surfing on a sound wave.

[1] All of the experiments that were conducted in the course of this thesis were performed at cryogenic temperatures with Schottky-gate defined devices in AlGaAs/GaAs heterostructures.

L'abrégé

Au cours des 25 dernières années, il n'y a eu que quelques rapports sur des expériences de type optique quantique avec des électrons. Les progrès réalisés dans ce récent domaine de recherche ont permis de mettre au point des techniques originales pour piéger, déplacer et manipuler les électrons dans des dispositifs à l'état solide. Ces progrès ouvrent de nouvelles perspectives pour l'étude de phénomènes quantiques fascinants tels que l'effect tunnel ou l'intrication avec les électrons. En raison de la contrôlabilité exigée dans les implémentations possibles de circuits logiques quantiques, il est maintenant particulièrement intéressant de réaliser des expériences d'optique quantique électronique avec des électrons volants uniques. Dans cette thèse, nous abordons deux expériences liées, mais conceptuellement différentes, d'optique quantique électronique au niveau de la particule unique[2].

Tout d'abord, nous effectuons une expérience d'interférence d'électrons de type Mach-Zehnder dans le régime de transport balistique. En formant un grand point quantique dans l'une des branches de l'interféromètre, nous étudions le déphasage de la fonction d'onde d'un électron transmis de façon résonnante. Au cours de nos mesures, nous trouvons des signatures d'un comportement de transmission qui reflète les symétries internes des états propres des boîtes quantiques. Nos résultats mettent en lumière la question de longue date d'un comportement de phase de transmission universelle dans des boîtes quantiques en grand taille. Nous avons ainsi posé un jalon important vers une compréhension globale de la transmission par résonance d'électrons volants simples par des boîtes quantiques.

Dans une deuxième expérience, nous allons au-delà du régime de transport balistique. Nous utilisons des ondes acoustiques de surface pour transporter un seul électron entre les boîtes quantiques définies par la grille de surface dans un circuit couplé par l'effect tunnel. Nous développons deux blocs de base essentiels pour partitionner et coupler les électrons volants simples dans un tel circuit piloté par le son. En dépassant une efficacité de transfert simple de 99 %, nous montrons qu'un circuit électronique quantique piloté par le son est réalisable à grande échelle. Nos résultats ouvrent la voie à des opérations de logique quantique avec des qubits d'électrons volants qui surfent sur une onde acoustique.

[2]Toutes les expériences menées dans le cadre de cette thèse ont été réalisées à des températures cryogéniques avec des dispositifs définis par Schottky-gates dans des hétérostructures AlGaAs/GaAs.

Contents

List of abbreviations

2DEG	two-dimensional electron gas
AB	Aharonov–Bohm
AC	alternating current; oscillating bias
AlGaAs	aluminium gallium arsenide
a.u.	arbitrary unit
AWG	arbitrary waveform generator
CBP	Coulomb-blockade peak
DAC	digital-to-analog converter
DC	direct current; constant bias
DQD	double quantum dot
EM	electromagnetic
FPGA	field-programmable gate array
FWHM	full width at half maximum
GaAs	gallium arsenide
HBT	Hanbury-Brown–Twiss
HOM	Hong–Ou–Mandel
IDT	interdigital transducer
MZ	Mach–Zehnder
QD	quantum dot
QPC	quantum point contact
QR	quantum rail
RF	radio frequency; 20 kHz to 300 GHz
SAW	surface acoustic wave
SEM	scanning electron microscopy
SU-8	organic molecule (nanofabrication resist)
TCW	tunnel-coupled wire

List of constants

e	elementary charge, $e \approx 1.60 \cdot 10^{-19}$ As
h	Planck constant, $h \approx 4.14 \cdot 10^{-15}$ eVs
$\hbar$	Reduced Planck constant, $\hbar = h/(2\pi)$
m	effective electron mass in a GaAs crystal, $m \approx 0.067 \cdot m_0$
m_0	free electron rest mass, $m \approx 9.11 \cdot 10^{-31}$ kg
μ_B	Bohr magneton, $\mu_\mathrm{B} = e\dot{\hbar}/(2m) \approx 5.78 \cdot 10^{-5}$ eV/T

Introduction

Quantum mechanics has strongly enhanced our understanding of nature. Owing to the accurate quantum mechanical description of crystal structures, we gained a profound understanding of optical, mechanical, thermal and electrical properties of material compounds [Kit04; AM76]. The foundation of solid-state physics enabled the realisation of electronic semiconductor devices that triggered a technological revolution, which shapes life in our modern society [Bar56; Bra56; Sho56]. This progress came along with the success story of semiconductor industries that triggered the development of a vast set of new technologies enormously increasing the prospects of science. An important turning point in modern electronics was certainly marked by the discovery of the quantum Hall effect [KDP80; vKl85]. This ground-breaking finding allowed to establish a standard for the electrical resistance that is based on the conductance quantum e^2/h and motivated further experimental studies on quantisation effects in solid-state devices.

About thirty years ago, major advances on molecular beam epitaxy [Joy88], chemical vapour deposition [HLW91] and electron-beam lithography [MDD92] enabled the fabrication of nanoelectronic devices in high-electron-mobility transistors (HEMT). The GaAs/AlGaAs heterostructure became a particularly interesting platform to perform experiments with electrons in such nanostructures at cryogenic temperatures due to its exceptionally good lattice matching properties [Stö83; Smi96]. In these HEMT devices, electrons can be accumulated at the shallow GaAs/AlGaAs interface via positively polarised surface gates. Alternatively, it is possible to introduce a permanent two-dimensional electron gas (2DEG) at the GaAs/AlGaAs interface via the introduction of a Si-δ-doped layer near the surface [Stö79a; Stö79b; Bas79]. Polarising an electrode on the surface of such a semiconductor heterostructure with a negative voltage, one can locally deplete the electrons in the 2DEG.

From this technological progress, several nanoelectric devices emerged, which opened up the route for novel experimental demonstrations of quantum mechanical phenomena in a very controlled fashion. The implementation of surface-gate defined quantum point contacts (QPCs) allowed for instance the observation of quantised conductance plateaus that precisely reflect the number of transport modes in a one-dimensional potential constriction [vWe88; Wha88]. Employing this surface gate approach to form more complex potential landscapes such

as a quantum dot (QD), furthermore Coulomb blockade was demonstrated in a single-electron transistor [Kou91; vHo92]. Subsequent to this progress, QPCs and QDs were combined and it was shown that the occupancy of such a QD with single electrons can be traced by abrupt jumps in the current going through a close-by QPC [Ash92; Fie93]. These experimental achievements stimulated the development of more sophisticated surface-gate-defined quantum devices such as electron interferometers. With these electronic two-path structures, it was possible to observe Aharanov–Bohm (AB) oscillations showing that ballistic electron transport has a coherent component in a GaAs/AlGaAs heterostructure [Yac95]. This development showed up the potential of HEMT devices as powerful platform to study quantum effects of single electrons which have been so far difficult to investigate in experiment.

The title of the present thesis refers to quantum optics – a term that is typically associated to photons. It is a field of research investigating quantum mechanical phenomena of coherent light and its interactions with matter. The central tools of investigation exploit interference effects and photon absorption processes. Quantum optics emerged from the investigations of intensity correlations of light emitted from Sirius, the brightest star on the night sky. Robert Hanbury-Brown and Richard Q. Twiss employed this data to determine the angular size of that stellar object. The theoretical development of this modern field of research was triggered by the observation that indistinguishable photons which are emitted from a thermal boson source tend to bunch in the same quantum state. This physical phenomenon builds the basis of the Hanbury-Brown–Twiss (HBT) effect [HBT54] and the Hong–Ou–Mandel (HOM) effect [HOM87], which represent so far the most famous examples of quantum optics. Both of these effects root in the bosonic nature of light: The number of photons occupying a certain quantum state is not restricted. Consequently, indistinguishable photons tend to bunch into the same quantum state. To demonstrate these effects, typically a beam-splitter setup is used with photon detectors such as avalanche photodiodes that are placed at the two outputs of the device. As two indistinguishable photons enter simultaneously such a beam splitter at the same input (HBT effect) or at two different inputs (HOM effect), they tend to bunch in the same state and leave the device consequently at the same output. Analysing the counting statistics at these detectors one finds thus anti-correlation in subsequent two-photon detection events. Differently speaking, the bunching photons arrive respectively in pairs at one of the two-detectors.

The field of quantum optics is already quite advanced. Photonic experimental setups were for instance employed to demonstrate entanglement of quantum information that is encoded in the polarisation of light [O'B03], in cavity fields [Del08] or in the spin states of trapped atomic ions [BW08]. The demonstration of quantum logic operations on coherent rays of light stimulated moreover

the idea of a photonic quantum computer [Lan08]. An interesting application of quantum optics experiments is the implementation of quantum photonic chips to solve eigenvalue problems of chemical Hamiltonians [San18]. One central problem of quantum computation with photons is, however, that they hardly interact with other particles. It is thus difficult to store photons and to couple them efficiently. Besides these aspects it is further demanding to realise efficient single-photon sources that emit these particles in regular intervals of time. And also the detection of single photons is so far rather based stochastic absorption processes and post selection approaches [Had09]. These issues make photonic quantum logic gates so far working on relatively low efficiency.

In analogy to quantum optics, the rather young research field of electron quantum optics studies quantum mechanical phenomena of so-called flying electrons[3] and their interaction with matter and artificial atoms such as quantum dots. Different than a photon, an electron carries the elementary charge, $q_e = -e$, which allows the particle to propagate in an electric field due the Coulomb force. Owing to this electromagnetic interaction, one can trap and displace an electron in a very controlled fashion in solid-state devices what makes the conduction of quantum-optics-like experiments with electrons particularly favourable in an experimental framework such as a GaAs/AlGaAs heterostructure. The electron's charge makes interference phenomena of electrons further accessible via quantum phenomena like the AB effect. With their half-integer spin, electrons are fermions and obey the Pauli exclusion principle. This property restricts them to occupy the same quantum state. Imagining the aforementioned HBT or HOM experiment for electrons, we consequently expect anti-bunching of two indistinguishable electrons as a result of Pauli and Coulomb repulsion. Thus, two indistinguishable electrons that strongly interact in a beam splitter leave the device always at opposite, but never at the same output.

About twenty years ago, electronic HOM-interference has been already elegantly demonstrated in experiment [Liu98; Oli99]. Owing to the progress in nanofabrication techniques, it was possible to realise a beam-splitter setup via a narrow surface-gate that allowed to define a tunnel-barrier in the potential landscape of the 2DEG in a GaAs/AlGaAs heterostructure. As they simultaneously passed a continuous stream of electrons into the two channels of this tunnel-coupled wire (TCW), they observed a reduction of current noise power with respect to individual bias of the input terminals, what reflected HOM interference of flying electrons. This electron-quantum-optics experiment marked the starting point for novel interferometry experiments with flying electrons.

Employing the AB effect, pioneering experiments on electron two-path interferometry succeeded to observe interference fringes [Yac95] and to measure the

[3]The term "flying" does not indicate propagation in vacuum here, but the propagation of free electrons without scattering in the 2DEG of a semiconductor heterostructure.

transmission phase along a Coulomb blockade resonance [Sch97]. Subsequently, also Mach–Zehnder (MZ) type electron interferometer structures were developed using QPCs to form beam splitters for flying electrons that are propagating along quantum Hall channels [Ji03]. Inspired by these advances and the success of preceding TCW implementations [Liu98; Oli99], MZ-type two-path interferometers were also realised at low magnetic fields in the ballistic transport regime with tunnel-barriers acting as splitters of the coherent electron stream [Yam12]. These two-path interferometer devices allowed detailed experimental investigations of HOM interference [Ned07; Fre15] and enabled new paths to study fundamental questions of mesoscopic physics such as the Kondo effect [Kon64; GG98; Pot07; Tak14; Tak16]. The development of reliability criteria for electron two-path interference [Bau14b; Tak15] further opened up the way to reinvestigate long-standing questions that arose from unexpected results of early experiments in the field of electron two-path interferometry.

One long-standing puzzle in the field of electron two-path interferometry arose from observations of pioneering experiments investigating coherent transmission through a large quantum dot hosting hundreds of electrons [Sch97]. In this experiment, abrupt jumps were encountered in the transmission phase, which were suspected to occur in a universal manner. The first part of this thesis is devoted to re-investigate this long-standing question about such a universal transmission phase behaviour with a novel MZ-type electron interferometer in experiment. Our transmission phase measurements clearly show a non-universal phase behaviour and provide several indications for the theoretically expected parity-dependent transmission phase behaviour [Lee99; TB99]. Our findings put the observations of pioneering experiments on electron two-path interferometry in a new perspective and resolve the long-standing puzzle about a universal transmission phase behaviour [Edl17].

Besides transmission phase measurements and experimental investigations of fundamental physics, electron two-path interferometers have large potential for applications in emerging quantum computing approaches. DiVincenzo's criteria identified the transmission of quantum information between stationary nodes of computation as a central requirement for any useful implementation of a quantum computer [DiV00]. Several theoretical works developed this aspect further towards the idea of a quantum computing architecture with flying electrons [Ber00; IAU01]. To implement such proposals in experiment, basically three components are needed: a well-controllable source of single electrons, a coherent and adiabatic transport- and manipulation-medium and a detector of single flying electron qubits. MZ-type interferometer devices could now be employed to prepare and couple flying charge-qubit states in a single-electron circuit. To do so, it is necessary to go beyond the ballistic transport regime and to study quantum interference with solitary flying electrons in single-shot experiments. Such a single-

particle approach allows to investigate the behaviour of a completely decoupled electron and provides spatial and temporal control permitting the possibility to study the coherence and interaction of solitary flying electrons. To provide such a platform for quantum-optics-like experiments at the single-particle level, different approaches of single-electron sources have been developed in the last years. Let us highlight in the following three single-electron sources allowing repetition rates in the GHz regime: mesoscopic capacitors [Fèv07], tunable-barrier electron pumps [Blu07; Fle12; Gib12; Fri14] and Levitons [Dub13]. Employing these single-electron sources first quantum-optics-like experiments have been already successfully conducted with single flying electrons [Boc12; Boc13; Ubb14; Jul14].

In the quantum Hall regime, single electrons can be launched along edge-channels by an oscillating voltage signal that is applied on a mesoscopic capacitor [Fèv07]. This approach enabled the observation of anti-bunching of a single flying electron pair in a HBT [Boc12] or HOM setup [Boc13]. A conceptually different approach is the tunable-barrier electron pump where a quantum dot (QD) structure is used to shuffle an electron from one charge reservoir to the other [Blu07]. This single-electron source allows to adjust the energy of the emitted electron in a very controllable fashion. Due to the relatively high emission energy and the corresponding relaxation processes [Ema19], this single-electron approach is however not the best choice for quantum-computing approaches. With high magnetic fields [Fle12; Gib12] or serially connected and clocked emitters [Fri14], the single-electron pump provides though extremely stable quantised current plateaus having a relative uncertainty of about $1 \cdot 10^{-6}$ for very small currents $I = e \cdot f < 1$ nA. As consequence, this type of single-electron sources has large potential for future unit standards in the regime of small currents where the relative uncertainty of novel programmable quantum current generators (PQCGs) strongly increases. The tunable-barrier electron pump further allowed the realisation of HBT-like experiments which provided evidence for repulsive interactions in the partitioning process of single electron-pairs [Ubb14].

As third outstanding candidate, let us also highlight so-called Levitons [Lev96]. This kind of quasiparticle is a collective charge excitation of a single electron flying above the Fermi-sea. It can be formed by a Lorentzian voltage pulse applied via an ohmic contact to the 2DEG. The particularity of this pulse excitation is its exponential energy distribution leaving the Fermi-sea completely unaffected. Owing to the decoupling from the Fermi sea, Levitons are expected to have outstanding coherence properties. Demonstrating the reduction of shot-noise in a HOM setup, the presence of Levitons has been shown in a GaAs/AlGaAs heterostructure by Lorentzian voltage pulse excitation [Dub13]. Subsequently, such experimental realisations of Levitons were also successfully applied for quantum state tomography [Jul14][4].

[4]Quantum state tomography has been also performed with single-electron pumps [Fle19].

All of these experiments with mesoscopic capacitors, tunable-barrier electron pumps and Levitons are performed via analysing correlations in current measurements. For these single-electron-transport techniques, a detector or receiver of flying electrons is so far however missing[5]. The lack of a fast single-electron detector or receiver currently makes slower single-electron-transport approaches more promising for the first demonstration of quantum logic operations with flying electrons qubits. To trap and detect a single electron in a solid-state device, in the past mainly surface-gate defined QDs were employed [Fie93]. Successful transmission of an electron qubit has been recently shown in solid-state devices via arrays of such QDs [Fle17; Fuj17; Mor18] or via Heisenberg exchange interaction through a multielectron mediator [Mal19]. In these investigations, the focus was on the spin state of the propagating electrons[6]. There are also recent proposals to shuffle electrons through a dynamically controlled linear array of quantum dots [Mil19]. Within this experimental frame, electrons are transferred from one quantum dot to another like in a bucket brigade. An appealing alternative to the surface-gate controlled shuffling of single electrons are surface acoustic waves (SAWs) [For17; Bäu18].

Owing to the modulation of the shallow electric potential, SAWs allow the displacement of charge carriers in the 2DEG of a piezoelectric heterostructure such as GaAs/AlGaAs. Sending a SAW through a surface-gate-defined transport channel, the piezoelectric modulation of the sound wave forms a train of moving QDs. This SAW train allows now to transport a discrete number of electrons through such a quantum rail. Using stationary QDs as electron source and receiver, sequences of SAW trains can be moreover employed to send a single charge carrier back and forth several micrometer long tracks with promising efficiency [Her11; McN11]. The central advantage of such a SAW-driven single-shot-transfer experiment over the aforementioned single-electron sources is that the SAW-transported electron is completely isolated by the potential landscape from other electrons during propagation. Since a single electron is transported one-by-one to the receiver QD via a solitary SAW train in single-shot experiments, this transfer technique is particularly interesting for quantum processing approaches. Recently, SAW-driven transfer of individual spin polarized electrons has been reported [Ber16a]. These advances make SAW-driven single-electron transport a promising candidate for the transmission and manipulation of single flying electron qubits[7].

[5]Let us note, however, that single-shot detection was just recently also reported for single electron pumps with an overall fidelity of 99.6 % and a repetition rate of 24 Hz [Fre19].

[6]Let us note at this point an interesting aspect concerning flying spin qubits: The displacement of an electron allows to enhance its spin coherence time [Fle17]. There were also interesting proposals for the suppression of phonon-mediated spin relaxation[ZHH16].

[7]Recently, there were also theoretical proposals to use counter-propagating SAWs for standing-wave formation [Sch17]. These standing sound waves are envisioned as acoustic lattices enabling the trapping of single electrons in analogy to ion traps.

To realise a quantum logic architecture with flying electrons, one could employ SAWs to convey solitary flying electrons through a circuit of surface-gate defined quantum rails. If the coherence length of a flying electron in such a SAW-driven single-electron circuit is sufficiently long, such an architecture could enable the implementation of electron quantum optics experiments [Boc13; Dub13; Ubb14; Bäu18] and quantum computation schemes at the single-particle level [BSR00; AS17; For17]. To achieve such goals, it is necessary to develop highly efficient single-electron sources and detectors, synchronized transport along parallel quantum rails and a tunable beam-splitter structure that permits adiabatic and coherent propagation of the flying electron within the SAW train. In addition, it is necessary to show coherent interference phenomena with SAW-transported charge qubits and to test the coherence length with two-path interferometer structures of successively increasing size.

These tasks are in the focus of the second part of this thesis. We present two essential building blocks of a SAW-driven single-electron circuit: By tunnel-coupling highly efficient quantum rails, we realise a setup allowing us to partition a flying electron arbitrarily into two depleted transport channels. Implementing a triggered single-electron source, we further accomplish an important requirement to synchronise transport of flying electrons. Our results are supported by quantum mechanical simulations that deliver insight on the quantum state of the flying electron. Most of the presented single-shot experiments are performed with a transfer efficiency exceeding 99 %. Moreover, we address our observation of tunnel oscillations in the present beam-splitter setup and discuss the remaining challenges to perform coherent operations on flying charge qubits. With this work [Tak19], we meet important milestones to perform MZ- and HOM-type interference experiments with single SAW-transported electrons. We anticipate that the demonstrated building blocks will be of great importance for the first demonstration of quantum logic operations with single flying charge qubits.

CHAPTER 1

Transmission phase measurements with a large quantum dot

In 1997, pioneering experiments exploited the Aharanov–Bohm (AB) effect [ES49; AB59] to perform electron interferometry experiments with quantum dots (QDs) as a phase-shifting medium [Sch97]. Just after this experiment, the theoretical basis for the interpretation of the data was developed [Lee99; TB99]. It turned out that electron interferometry delivers in principle insights on the internal structure of a QD. The experimental observations of the pioneering work in this field [Sch97] and later experiments provided however data that was controversially discussed in the viewpoint of the theoretical findings. The observation of long sequences of transmission phase lapses was suspected as generic feature. This hypothesis triggered a lot of interest. Despite many theoretical efforts, the question about such a universal behaviour remained however puzzling for more than two decades.

Here we reinvestigate the puzzle about this universal behaviour of large QDs in experiment. For this purpose we employ a recently developed Mach–Zehnder type (MZ) electron interferometer [Yam12; Tak15]. In the following we first provide the historical background of AB interferometry, which led to the development of the employed electron interferometer. Secondly, we outlay the aforementioned incongruity which arose between early experimental observations of transmission phase lapses and the theoretically expected behaviour. Having introduced the question about a universal behaviour, we then provide a detailed description of the employed electron two-path interferometer and the measurement procedure. Finally, we present and discuss our experimental results with which we resolve the long-standing question about a universal transmission phase behaviour of large QDs[1].

[1] Selected findings of our experimental investigations were published under the title "Non-universal transmission phase behaviour of a large QD" in the journal Nature Communications [Edl17]. The present section thus contains contents of that paper.

1.1 Background[2]

The scientific field of electron interferometry in solid state devices is quite young. It started in 1995 with an electron interferometry experiment by Yacoby *et al.* [Yac95]. Fig. 1a shows a SEM image of that solid-state device. It is a two-path electron interferometer realised in a two-terminal geometry. Conducting paths and a QD are defined by surface gates on a GaAs/AlGaAs heterostructure. Transport through the QD takes place in the Coulomb blockade regime. Theoretically, it was expected that the wave function of a coherently transmitted electron experiences a gradual phase modification along a Coulomb blockade peak (CBP). Yacoby *et al.* attempted to measure this transmission phase in this early two-terminal interferometry experiment. As they gradually changed the magnetic field perpendicular to the surface, they made the ground-breaking finding of AB oscillations – see Fig. 1b and 1c. This result showed that electron transmission through a QD is partly coherent and that their goal of electron interferometry with a QD was within reach.

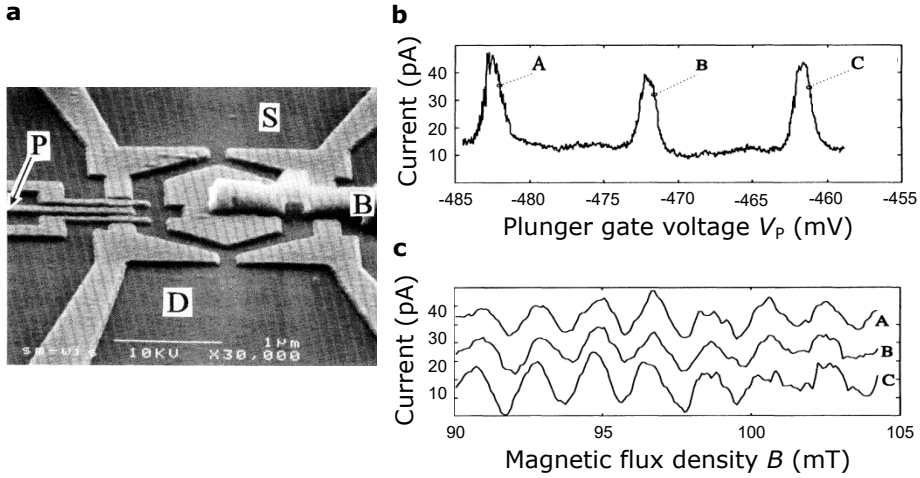

Figure 1: Observation of AB oscillations at electron transmission through a QD in a two-terminal interferometer. (a) SEM image of the electron two-path interferometer showing ohmic contacts for source (S) and drain (D), an air-bridge (B) providing electrical connection to the central island of the AB ring and the plunger gate (P). **(b)** Coulomb blockade peaks (CBPs): Measurement of the collector current as the voltage on the plunger gate, V_P, is swept along three QD resonances. **(c)** Measurement of AB oscillations at the positions A, B and C of the CBPs. Reprinted figure with permission from Yacoby *et al.* [Yac95]. Copyright (1995) by the American Physical Society.

[2]Parts of this section follow the content of the review article of G. Hackenbroich [Hac01].

1.1.1 Transmission phase of a quantum dot

Which course of the transmission phase did Yacoby *et al.* [Yac95] expect? Electron transmission through a QD is a double-barrier scattering problem. Here the amplitude and phase of electron transmission is typically derived by a scattering matrix approach. In this picture transmission through the QD is expressed by the scattering matrix element, S_{12}. This operator couples an incident wave from one side of a scattering object – that is a QD in the present case – to the other side. The scattering matrix element S_{12} is applied on the incident electron wave, which is generally expressed as a complex number. Since S_{12} causes a change in amplitude and phase of an incident wave, this operator itself has to be expressed as a complex number. Consequently, we define S_{12} as the transmission function:

$$t = S_{12} = |t| \cdot e^{i \arg(t)}. \tag{1}$$

This mathematical construct allows to compute the magnitude of transmission:

$$M = |t|. \tag{2}$$

We can further use it to calculate the phase modification of the electron wave function at resonant transmission through the QD, the so-called transmission phase, via the argument of this complex quantity:

$$\phi = \arg(t). \tag{3}$$

The electron scattering process at a QD can be understood in the vicinity of a CBP via a simplified picture: In analogy to the scattering process of an incident particle in an atom, we can model electron transmission through a QD by Breit–Wigner resonance theory. An incident electron gets captured in the QD and forms a metastable bound state that transmits or reflects the particle after decay – see schematic in Fig. 2a. In this picture of Breit–Wigner resonance theory, we describe a resonance in a double-barrier scattering problem as a Lorentzian distribution:

$$M(E_\mathrm{P}) = \frac{2 \cdot M_0}{\pi \cdot \Gamma \cdot \left[1 + 4 \cdot \left(\frac{E_\mathrm{P} - E_n}{\Gamma}\right)^2\right]}, \tag{4}$$

with the maximum transmission magnitude, M_0. Here n indicates the discrete index of the quantum state that is swept along the bias window. E_n is the eigenenergy of this state, which represents the center of the resonance. Γ indicates the full width at half maximum of the peak of coherent transmission. Γ is the coupling energy, which characterises the magnitude of the QD barriers to the leads. E_P indicates the electrostatic potential shift of the QD states that is introduced by the plunger gate.

Sweeping the voltage on the plunger gate, single electrons can be successively added to the bound states of the QD. Such a change causes a continuous rearrangement in the charge density distribution of the QD. The local charge configuration plays a central role for the scattering process of an electron wave at a QD. The scattering-phase shifts at the Fermi energy are related to the number of bound electron states by the Friedel sum rule [Fri52]. This rule is one of the few exact results of solid state physics [Ron06] and holds even in the presence of electron interactions [LA61]. According to the Friedel's sum rule, the transmission phase experiences a continuous shift of π as a metastable QD state is populated. The course of the phase shift is related in a cumulative way to the resonance shape. For a resonance of Lorentzian shape, we obtain thus an arctangent course of the transmission phase:

$$\phi = \arctan\left(\frac{E_\mathrm{P} - E_n}{\Gamma}\right). \tag{5}$$

Characteristic courses of the phase and magnitude of coherent electron transmission are plotted in Fig. 2b and Fig. 2c according to equation 5 and 4.

After this short excursion to the theoretically expected transmission properties along a CBP, let us now come back to the results of pioneering experiments. In the course of the Yacoby-experiment [Yac95] it was attempted to measure

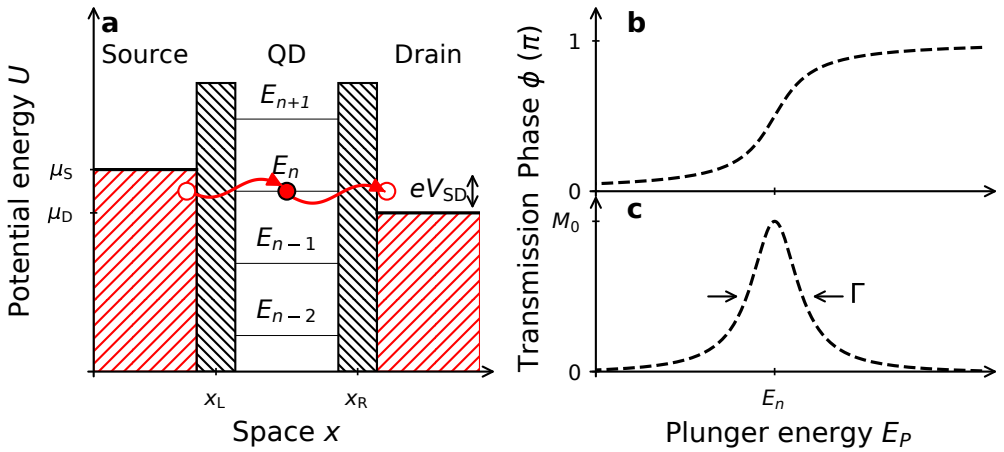

Figure 2: Schematics of electron transmission through a quantum dot according to Breit–Wigner resonance theory. (a) Idealised band diagram of a quantum dot (QD) inserted into two leads between which a bias voltage, V_SD, is applied. Quantum dot state energies, E_{n-2} to E_{n+1}, are indicated via horizontal black lines. Only a QD state with a potential energy lying inside the bias window leads to resonant transmission. **(b)** Characteristic arctangent shift of the transmission phase along a resonance according to equation 5. **(c)** Coulomb blockade peak of Lorentzian shape according to equation 4.

the characteristic transmission phase shift – see Fig. 2b – with a two-terminal electron interferometer. As they extracted the phase of the AB oscillation for several positions along a CBP, however, no arctangent phase shift was observed that is related to the width of the CBP. Instead, they encountered an abrupt jump from 0 to π. Shortly after this experiment it turned out that the employed type of electron interferometer suffered from a conceptual problem related to the number of leads that are connected to the AB-ring [LB95; Hac01]: Due to time-reversal symmetry and current conservation, the phase of the interference fringes in such a two-terminal geometry is restricted to either 0 or π at zero magnetic field. A derivation of this relation is provided in appendix A. As consequence of this so-called phase rigidity, a reliable measurement of the transmission phase with such a two-terminal interferometer was not possible.

In 1997 – two years after the Yacoby-experiment – Schuster *et. al* [Sch97] found a way to overcome this phase rigidity problem in a multi-terminal electron interferometer setup. A SEM image of the employed electron interferometer is shown in Fig. 3a. The transmission phase measurement was still done in a two-terminal setup, but additionally four grounded ohmic contacts were connected to the AB ring. The additional electrical connections to the AB ring strongly diminished the collector current signal. Despite this limitation, the multi-terminal electron interferometer allowed to measure the characteristic transmission phase shift (equation 5) via the AB effect. Fig. 3b shows measurements of the transmission phase from that pioneering experiment. The plot shows the phase shift, ϕ, of AB oscillations along a CBP. Fitting the resonance with a Lorentzian function (dashed line) they obtained the theoretically expected arctangent phase shift, which showed excellent agreement with the experimental transmission phase.

1.1.2 Occurrence of transmission phase lapses

As Schuster et al. [Sch97] scanned the transmission phase along multiple resonances, they observed a rather unexpected course: In between each successive resonance they encountered an abrupt phase lapse of π – see vertical arrows in Fig. 3c. Two years after this experiment a theoretical basis for the understanding of these transmission phase lapses was found. In this theory the occurrence of those lapses is related to the parity sequence of the quantum dot (QD) states [TB99; Lee99]. In this context, parity does not strictly describe spatial inversion symmetry of the wave function corresponding to a QD state, but simply the product of the wave-function sign at the two connections to the leads. Initially, the experimental results were only partially explainable with the implications of this theoretical work. A decade later, however, these theoretical investigations gained importance. In this regard, let us now introduce the theoretical background on the origin of transmission phase lapses.

The core of the theory of Lee [Lee99] and Taniguchi and Büttiker [TB99] is the internal spatial structure of the QD states. In order to introduce the relation of transmission phase lapses to the QD configuration, we have to define the parity of a QD state. In general, the parity of a QD state is defined as the spatial inversion symmetry of its wave function. Here we define the parity more specific as the product of the wave-function sign at the two connections to the leads. In section 1.1.1 we have mentioned that the scattering process of an electron wave on a QD sensitively depends on the local charge density distribution. Additionally, we have highlighted the importance of the Friedel sum rule in this context. Applying the Friedels sum rule for all transmission phases of the scattering matrix, it was shown that electron transmission through a QD is moreover affected by the parities of the wave functions that are attributed to the QD states.

Let us now qualitatively describe the central implications of the theoretical work of Lee [Lee99] and Taniguchi and Büttiker [TB99]. The theoretical investigation of E_P-intervals in between successive resonances has shown that, despite the characteristic arctangent phase shift along a resonance, further features can occur in the transmission phase, ϕ, that are moreover reflected in the magnitude of transmission, M. It was found that a sudden phase lapse of π appears in the valley between two consecutive resonances, if the involved QD orbitals have the same parity. Such a situation can particularly occur if the shape of the QD is not one-dimensional but two-dimensional. It is important to mention that

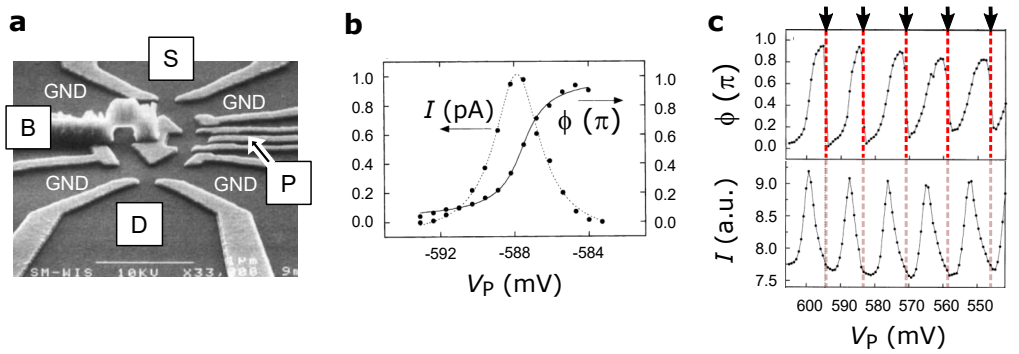

Figure 3: Transmission phase measurement with a multi-terminal interferometer. (a) SEM image of the multi-terminal interferometer showing ohmic contacts for source (S), drain (D) and ground potential (GND). An air-bridge (B) provides electrical connection to the central island of the AB-ring. The plunger gate (P) shifts the QD states in electrostatic potential. **(b)** Collector current, I, and transmission phase, ϕ, measured along a Coulomb blockade peak (CBP). **(c)** Transmission phase, ϕ, scanned along several CBPs. The data shows phase lapses of π between each of the investigated resonanes. Adapted by permission from Moty Heiblum: Nature, Schuster *et al.* [Sch97], Copyright (1997) by Springer Nature.

this phase lapse is accompanied by a point of vanishing transmission through the QD – a so-called transmission zero. This situation is schematically shown in Fig. 4 between the resonances E_{n-2} and E_{n-1} and the resonances E_n and E_{n+1}. Since the QD dot states have the same parity, a transmission phase lapse occurs as they cross the bias window. When successive QD states have on the other hand a different parity such a phase lapse is absent and the characteristic phase shifts just add up at the resonances. This cumulative behaviour gives rise to a phase plateau between two resonances as shown between the resonances E_{n-1} and E_n situation in Fig. 4. Analysing the sequence of transmission phase lapses and transmission zeros, it is thus possible to obtain information about the wave functions that are attributed to the respective QD states. The theoretical findings of Lee [Lee99] and Taniguchi and Büttiker [TB99] therefore show that the transmission measurements deliver in principle insights in the internal structure of a QD.

What is now the physical reason for transmission phase lapses? The answer to this question is unfortunately rather unintuitive. A transmission phase lapse of π

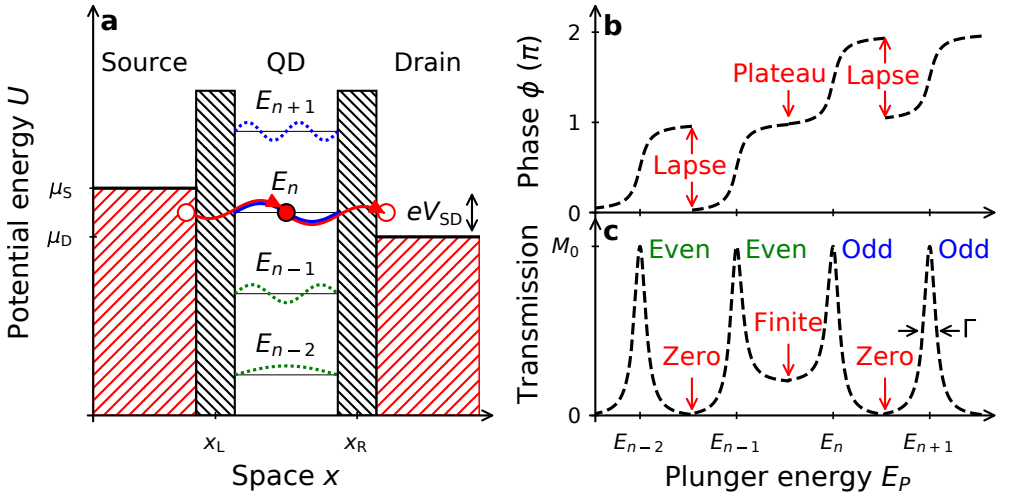

Figure 4: Schematics describing the occurrence of transmission phase lapses. **(a)** Idealised band diagram of a two-dimensional quantum dot (QD) as in Fig. 2. The blue and green, wavy lines on top schematically indicate an arbitrary sequence of QD state parities. Because the QD is not one- but two-dimensional, it is possible that successive QD states have the same parity as schematically indicated. **(b)** Transmission phase sequence that is theoretically expected for the parity sequence corresponding to the QD states shown in (a). Transmission phase lapses occur if the parity of successive QD states is the same. Else a transmission phase plateau is present. **(c)** Magnitude of coherent transmission that is theoretically expected for the sequence of QD states shown in (a). The transmission is expected to completely vanish when a phase lapse is present.

occurs as a singularity point is trespassed by the complex transmission function [TB99; Lee99]. Imagining a complex value, t, crossing the origin of the complex plane, it is obvious that the argument, $\phi = \arg(t)$, undergoes an abrupt jump of π and that the norm, $M = |t|$, vanishes. In our electron-transmission problem through a QD, a singularity point occurs now in the complex transmission function, t, in a similar way. An abrupt transmission phase lapse of π therefore also goes along with a transmission zero.

To gain a better physical understanding of the occurrence of phase lapses, let us go now a bit more in detail and consider the coupling mechanism of a transmitted electron wave to the quantum dot. In the following we introduce this relation with a simplified line of argumentation and refer for further literature to the generic lattice model in the weak coupling limit [LB00; Mol12]. The transmission phase, ϕ, exhibits an abrupt jump by π in the case where the complex transmission function, t, crosses a singularity point. The occurrence of such a singularity point between two subsequent QD states ψ_n and ψ_{n+1} depends now on the respective effective couplings at the left and right connection, $\gamma_{n/n+1}^{\mathrm{L/R}}$. A singularity point occurs now in the complex transmission function when

$$\gamma_n^{\mathrm{L}} \cdot \gamma_n^{\mathrm{R}} \cdot \gamma_{n+1}^{\mathrm{L}} \cdot \gamma_{n+1}^{\mathrm{R}} > 0. \tag{6}$$

In this case the transmission phase undergoes an abrupt phase jump of π that is accompanied by a transmission zero. Considering single mode leads connected to the QD, the effective coupling $\gamma_n^{\mathrm{L/R}}$ can be expressed by the sub-band wave function of the left and right lead, $\Phi_{L/R}(y)$, and the wave function of the nth QD state at the respective coupling position, $\psi_n(x_{L/R}, y)$:

$$\gamma_n^{\mathrm{L/R}} \propto \int \mathrm{d}y \; \Phi_{L/R}(y) \cdot \psi_n(x_{L/R}, y). \tag{7}$$

It is apparent that the sign of $\gamma_n^{\mathrm{L}} \cdot \gamma_n^{\mathrm{R}}$ is determined by the sign of the QD state ψ_n at the positions of the connections to the leads $x_{L/R}$. Consequently, we can identify the sign of this quantity as the aforementioned longitudinal parity of the QD wave function, $P_n = \mathrm{sgn}(\gamma_n^{\mathrm{L}} \cdot \gamma_n^{\mathrm{R}})$. With this definition we can now formulate the condition for a singularity point in different words: A singularity point occurs, if two successive QD states, n and $n+1$, have the same parity:

$$P_n \cdot P_{n+1} = +1 \quad \Rightarrow \quad P_n = P_{n+1} \tag{8}$$

Strictly speaking, this definition is only complete for spin-less particles. With electrons transmitted through non-degenerate QD states at low magnetic fields ranging from 0 to 200 mT, however, spin-effects have to be considered. For the observations in our experiments we thus have to define the condition for transmission phase lapses in a more comprehensive way.

1.1.3 Spin-related effects on electron transmission

So far we have considered the transmission phase of spin-less charges. In this section we go one step further and introduce the theoretically expected effects of the spin states on electron transmission for different regimes. The presented theories are partly underpinned by experimental results. We start this section with a short review of theoretical and experimental work on the Kondo effect in a single spin impurity that is realised in a surface-gate defined quantum dot (QD). This chapter of two-path electron interferometry already nicely showed the progress of transmission phase measurements with the next generation of electron interferometer structures. After this short review, we shift the focus on the theoretically expected spin-dependent phase evolution from the strong to the weak coupling regime. Besides the phase, the spin of a certain QD state is also reflected in the magnitude of coherent transmission. This aspect will be discussed at the end of this section. Thanks to these spin-related effects we have in principle quite a large set of tools allowing us to characterise the QD states in terms of their orbital and spin properties.

Kondo effect

Let us begin this section with a very interesting spin-related many-body-correlation phenomenon. Cooling down certain metal alloys to very low temperatures, a logarithmic increase of electrical resistance was observed. This behaviour was theoretically explained by J. Kondo in the middle of the 70s [Kon64]. The corresponding physical phenomenon, which was subsequently referred to as the Kondo effect, arises from the interaction of free electrons with a localised spin. This system can be described as a correlated many-body singlet ground state – the so-called Kondo cloud that gives rise to several fascinating quantum mechanical phenomena [Car12]. The Kondo effect can be also observed in the experimental frame of nanoelectronic devices in semiconductor heterostructures. Typically, it is obtained in the strong coupling regime of an electron-transmission setup through a QD [GG98; COK98; vdW00]. In this regime, the transmission phase shift is determined by the electron occupancy of the highest occupied level. When this level only hosts a single electron, its spin plays a predominant role. In such a configuration, an electron can be only transmitted if it has a spin state that is opposite to the electron which is bound to the QD. A characteristic signature of the Kondo effect is an increased conductance minimum in the valley between two resonances as the temperature is decreased. Below a certain temperature threshold, the electronic system forms the aforementioned strongly correlated many-body state – the Kondo ground state –, which theoretically leads to a $\pi/2$ phase shift across two consecutive resonances [Ger00].

First electron interferometry experiments [Ji00; JHS02; Zaf08] that aimed to

measure these $\pi/2$ transmission phase shifts along a Kondo valley employed a multi-terminal electron interferometer as in the pioneering work of Schuster *et al.* [Sch97]. Measuring the transmission phase along the two resonances next to a Kondo conductance valley, they measured – different than theoretically expected [Ger00] – a total phase shift of $1.5 \cdot \pi$ along the pair of resonances. It was argued that this phase behaviour arose from electron interactions. A clear explanation for the measured phase evolution has been however missing. Another possible hypothesis was that multi-path contributions of electrons that encircle the AB ring additionally affected the phase measurement.

The development of an enhanced quantum interferometer structure [Yam12] recently enabled reliable two-path interference by anti-phase AB oscillations in a two terminal measurement[3]. Employing this enhanced quantum interferometer, different to the preceding experimental investigations, the theoretically expected $\pi/2$ phase shifts where successfully measured along a the pair of resonances around a Kondo conductance valley [Tak14]. The main difference to preceding investigations was the development of a quality criterion in an effective three-terminal setup to establish reliable two-path interference. Therefore, it is very likely that the transmission phase measurements of early experiments using multi-path structures according to Schuster *et al.* [Sch97] significantly suffered from multi-path contributions of electrons that are encircling the AB ring.

Transmission phase lapses and spin

For weak coupling, on the other hand, a phase shift of π is theoretically expected to occur along a Coulomb blockade peak – see section 1.1.1. The course of this shift can be understood by Friedel's sum rule and follows the aforementioned Breit–Wigner profile. In this regime, a transmission phase lapse of π occurs between two resonances as the involved QD states that successively cross the bias window have the same parity – see section 1.1.2. In a one-dimensional QD, the parity changes between each successive QD state. Neglecting the spin of the transmitted electrons, a transmission phase lapse should therefore not occur at all. Considering the spin of the transmitted electron, the occurrence of phase lapses changes already for the one-dimensional system drastically and gets additionally affected by exchange and spin-orbit interaction. How does the transmission phase behave for a QD that is typically formed in experiment? Does the transmission phase evolve independently for the two spin species or are there interaction effects? The answer to this question strongly depends on the set of assumptions and is not straight forward. In the following we discuss a very specific situation of electron transmission through a two-dimensional QD taking into account the spin properties of the QD states. Note that we completely

[3] We will discuss this aspect in more detail in section 1.2.3.

neglect exchange and spin-orbit interaction in this discussion.

Electron interferometry experiments of small QDs hosting only a few electrons provided transmission phase data, which strongly contributed to a better understanding of these questions [AK05]. A QD that is formed in such an electron interferometry experiment, is extended in two dimensions with corresponding quantisation of eigenstates. With the connections to one-dimensional leads, such a QD is often referred to as quasi-one-dimensional. In this situation, it is possible that QD states that successively cross the bias window have the same parity with respect to the transmission direction. Modelling the QD of this experiment as an elliptical object, theoretical investigations of the transmission phase were partly able to explain the sequence of transmission phase lapses (up to the first five electrons) of the experimentally observed data [Ron10]. Here we assume however zero temperature ($T \Rightarrow 0$ K) and an extremely small coupling energy ($\Gamma \ll \mu_B B$). It is questionable if these assumptions hold in experiment. Let us in the following nonetheless review the expected tranmsission phase behaviour that is expected in this hypothetical picture. The theoretical investigations suggest that the transmission phase evolves basically independently for the two spin species up to a few electrons. It was also noticed, however, that electron interaction and asymmetries of the QD structure can strongly affect the transmission phase sequence that is measured in experiment. The extent of these effects basically scales with the number of electrons in the QD.

For the sake of completeness let us here introduce the proposed pattern for spin-filling sequence that is underpinned by numeric simulations [Ron10] for a specific example. A schematic picture of the QD and the orbital filling sequence of electrons is shown in Fig. 5a and Fig. 5b. We will pick-pick up this particular case also in the subsequent discussion of spin-scattering effects on the transmission magnitude. The discussed situation is a small QD which is elongated transverse to the transmission direction of the electrons. The extension of the QD along the transfer direction, a, is smaller then its transverse extension, b. The ground state is the elliptic s orbital. Since the energy shift of the spatially non-degenerate orbitals is proportional to $1 - a^2/b^2$, the subsequent states for this case $a < b$ are introduced into the p_y and then the p_x orbitals [Ron10].

The spin-dependent pattern for the occurrence of phase lapses follows the theoretical prediction of a parity-dependent behaviour [Lee99; TB99], however, separately for the two spin-species $\uparrow$ and $\downarrow$. A transmission phase lapse occurs, if the previously added electron of the same spin state was introduced in a orbital of the same parity. By sequentially filling the s, p_y and p_x orbitals in the $a < b$ case with respectively two electrons having spin $\uparrow$ and $\downarrow$, the sequence of phase lapses evolves as shown in Fig. 5c. The first two electrons are introduced into the s orbital and thus have the same (even) parity. Despite the sequence of equal parities, no transmission phase lapse occurs because their spin state is different.

When a third electron is added in the even p_y orbital of the QD, however, an abrupt lapse of π occurs in the transmission phase, because the previously added electron of the same spin species occupies an orbital having the same parity – namely the even s orbital. A similar situation is present as the fourth electron is added. The previous electron of the same spin species occupies an orbital of identical parity, which causes another transmission phase lapse. The fifth electron is added in the p_x orbital having odd parity with respect to the transmission direction. Due to the parity change no phase lapse occurs in this case and the transmission phase shift adds up. And similarly, we obtain another phase plateau as the sixth electron is added.

For such a transmission phase behaviour, which depends both on the parity of the QD orbitals and the spin-filling sequence, it is interesting to consider also the sequence of phase lapses for a elliptical QD elongated along the transmission direction ($a > b$). In this case the p_x orbital is filled before the p_y orbital leading to transmission phase sequence, where no phase lapses occur as the first six electrons are added to the QD. The transmission phase sequence would thus resemble the aforementioned hypothetical one-dimensional case. The observation of transmission phase plateaus along the six first resonances would allow to underpin the presently discussed transmission phase behaviour. An experimental investigation of a small QD elongated longitudinal to the transmission direction could thus significantly contribute to a better understanding of the spin-dependent occurrence of phase lapses in QDs.

Spin-scattering effects on the transmission magnitude

Before we have mentioned the Kondo effect – a spin-scattering effect that is reflected in the transmission phase of a quantum dot in the strong-coupling regime. Spin-scattering effects are however also expected for a QD in the weak-coupling regime. Particularly, when also single-level transport is present. Here the single-level energy spacing, δ, is larger then the resonance width, Γ. In the weakly-coupled QD configuration ($\delta > \Gamma$), it is theoretically predicted [Ake93; Ake99; KG01; KG02] that spin-scattering effects affect the distribution of transmission magnitude around a Coulomb blockade peak (CBP). The spin-occupancy of the resonant QD state determines basically how the magnitude of coherent transmission is distributed along a CBP. Since the spin-occupancy changes along a resonance, an asymmetric transmission distribution is expected along a CBP. Analysing the transmission magnitude distributions along CBPs, it is thus in principle possible to obtain additional information about the spin-filling sequence.

Coherent transport through the QD is directly linked to the magnitude of AB oscillations, M, in such a two-path-interferometry experiment. Spin-scattering effects should be thus reflected in the distribution of M along a CBP. Experimen-

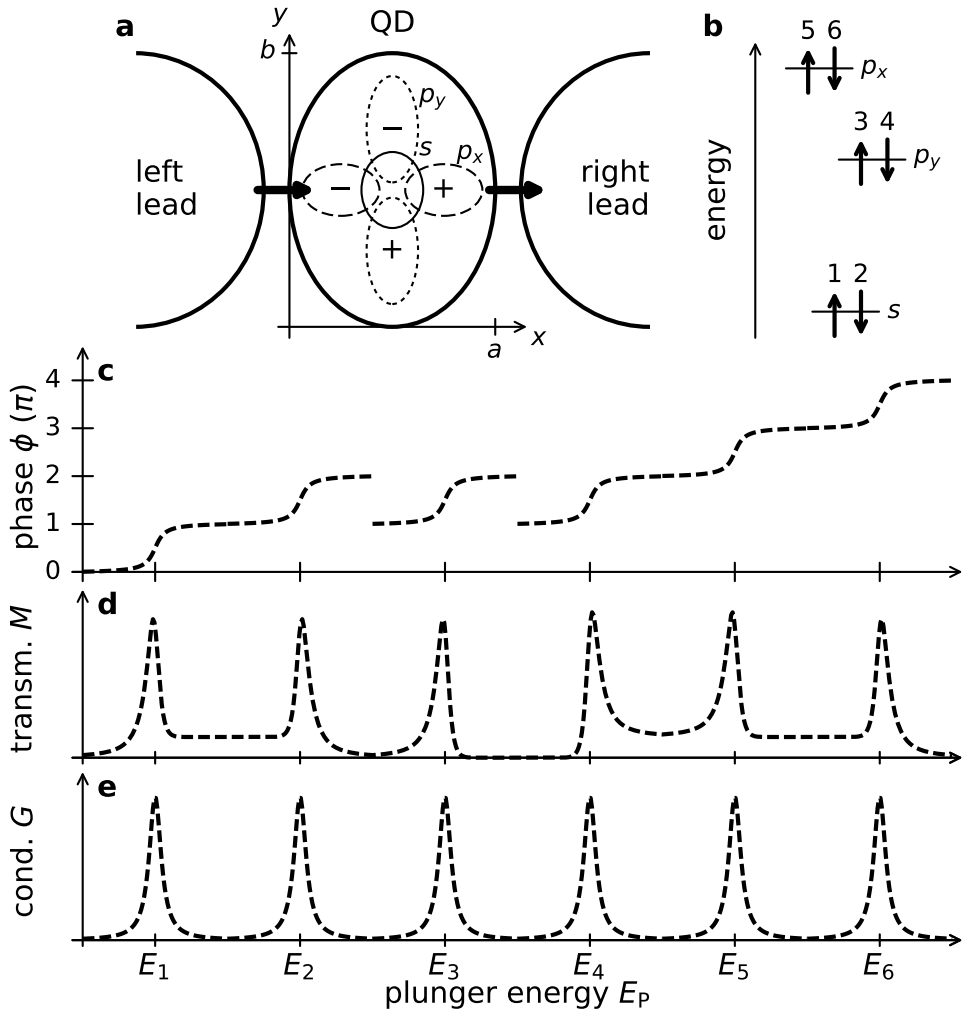

Figure 5: Transmission phase lapses and spin. Schematics showing the hypothetical course of transmission phase, ϕ, magnitude of transmission, M, and conductance, G, along the six first resonances for a small elliptic quantum dot (QD) extended transversal to the transmission direction. **(a)** Sketch of the QD and its connections to the leads. **(b)** Electron-filling sequence of the first QD orbitals. **(c)** Schematic of the expected course of the transmission phase, ϕ, along the first six resonances – according to the situation discussed by Rontani [Ron10]. **(d)** Schematic course of the magnitude of coherent transmission, M, showing asymmetric peaks due to spin-scattering according to the correspondingly expected sequence of transmission zeros. **(e)** Schematic of the first six CBPs.

tally, such characteristic asymmetries in the magnitude of AB oscillations have indeed been observed for double-quantum-dot systems [Aik04b; Ihn07]. Whenever M shows an asymmetric distribution around a resonance, in principle the sign of the present half-integral spin state of the QD can be deduced. It should be noticed, however, that also other effects – such as the Fano effect or the occurrence of transmission zeros – can lead to asymmetric distributions of M.

To make the spin-scattering effects on the transmission magnitude clearer, let us discuss two of the aforementioned CBPs that are shown in Fig. 5d-e. We now focus on the resonances at plunger gate energies E_2 and E_3. The course of M shown in Fig. 5d is schematically adjusted to the spin-filling sequence shown in Fig. 5b. As the second electron is added to the QD, the half-integer spin configuration changes to a integer spin state of the QD. Which processes now occur when we sweep the plunger energy along E_2? For $E < E_2$ the highest occupied orbital is hosting an electron of spin $\uparrow$. The metastable transmission state of spin $\downarrow$ now predominantly transmits $\downarrow$ electrons. Electrons with spin $\uparrow$ are on the other hand only transmitted as they undergo incoherent spin-flip processes what diminishes the magnitude of the AB oscillations, M. At the left side of the CBP at energy E_2, M is thus mitigated by such incoherent spin scattering events. For $E > E_2$ the QD is mostly occupied by an even number of electrons. This spin configuration reduces the incoherent spin-flip processes of spin-$\uparrow$ electrons at the right side of the peak. The gradual change of the spin occupancy thus causes an asymmetric distribution of M with reduced coherent transmission at the left side of the peak. *Vice versa* is now the situation for the subsequent resonance at the energy E_3. The integral spin configuration of the QD that is predominant at the left side ($E < E_3$) of the CBP allows coherent transmission of both spin species. Bringing the third metastable transmission state in a more and more stable occupation configuration ($E > E_3$), the total spin of the QD changes however to a half-integral value causing incoherent spin-flip processes of spin $\downarrow$ electrons. Consequently, we obtain an asymmetric distribution of M with reduced coherent transmission at the right side of the peak.

So far we have discussed a rather hypothetical spin-filling sequence where subsequently spin $\uparrow$ and $\downarrow$ electrons are added to the first bound orbitals of the QD at the zero temperature limit. Such a filling sequence could theoretically occur for a small number of electrons located in the QD. In this situation, the asymmetry of the distribution of M flips between each resonance. Referring to the electron interferometry measurements of Avinun-Kalish *et al.* [AK05], we indeed find such a tendency up to an electron number of five. For stronger evidence, however, a direct comparison to the CBPs needs to be performed and other possible effects causing such asymmetric distributions should be ruled out. For larger numbers of electrons we have to expect on the other hand less regular spin-filling sequences allowing subsequent M distributions with equal alignment.

1.1.4 A universal transmission phase behaviour?

Having discussed the origin of transmission phase lapses (section 1.1.2) and its relation to the spin-filling sequence of a QD (section 1.1.3), we expect a varying sequence of transmission phase lapses and plateaus for QDs that are defined via surface gates in a two-dimensional electron gas. This sequence basically reflects, with additional information from the transmission magnitude, the internal structure of the QD, which gets more and more complex as the size of the many-electron system increases. In this regard, however, the results of the pioneering experiment of Schuster *et al.* [Sch97] were quite unexpected. They investigated the transmission phase of a large QD hosting about 200 electrons with a multi-terminal electron two-path interferometer. In the course of their investigations they observed for the first time the characteristic arctangent transmission phase shifts along a Coulomb-blockade peak. Scanning the transmission phase along several subsequent resonances they further observed the occurrence of the aforementioned transmission phase lapses of π. But surprisingly, they encountered these lapses in between all of the investigated resonances and the question arose, if their measurements were performed in a particular regime where such phase lapses occur generically. Since the measured series of phase lapses was robust against changes in various QD properties, the transmission phase behaviour was called *universal*.

The puzzle about such a generic regime of transmission phase lapses attracted a lot of interest. Several theoretical models have been dedicated to explain the occurrence of phase lapses in a universal regime proposing different mechanism to make the appearance of a lapse more likely [Hac01]. One idea was that phase lapses stem from multi-level effects that are introduced by the finite temperature of the system [OG97; AuS98; Pat98]. Also shape deformation of the QD was considered as source for such multi-level effects [HHW97; VLM98]. Additionally, a combination of finite-temperature and shape-deformation effects was investigated [BG99]. As alternative to that, it was discussed that energy shifts between the QD and the leads give rise to a generic phase behaviour [SI00; LB00]. The tunneling of electrons through quantum dots was moreover discussed by means of stable bouncing–ball orbits [HM18], population-switching [GG06; Gol09], mean-field calculations [BG07] or Fano-type antiresonance [Kar07]. There were also discussions of interference effects that are rather related to the AB ring then to the QD itself [Wu98; Kan99]. Recent theoretical investigations addressed the role of the QD size for the emergence of long sequences of phase lapses [Mol12; Jal14; Jal17]. These investigations delivered insights on a mechanism that could lead to the emergence of very long, but non-universal sequences of transmission phase lapses. The aforementioned set theoretical studies shows up that there is at present no satisfactory explanation for a *universal* absence of phase plateaus that could apply on the experimental frame of pioneering investigations [Sch97]. Con-

sequently, the question about a universal transmission phase behaviour remains as a long-standing puzzle of mesoscopic physics.

Let us highlight at this point two of the aforementioned theoretical approaches. The numerical investigation of Karrasch *et al.* [Kar07] predicts a universal transmission phase behaviour for the particular regime where the average level spacing, δ, is smaller or comparable to the coupling energy, Γ, which is basically reflected in the resonance widths. The theory addresses the multi-level transport regime that we did not discuss so far in this section. In that work the cause for a generic sequence of phase lapses is identified by Fano-type antiresonances of the renormalized single-particle levels. A continuum of states mediates the coupling of two successive resonances that are shifted through the bias window. This mediation causes that the occurrence of phase lapses is no longer parity-dependent, but universal. They identify this continuum as a renormalized effective single-particle level that broadens so much that it reaches in the bias window. Experimentally one can estimate δ from Coulomb diamond measurements. Estimating Γ from the widths of the resonances one can in principle deduce if the condition $\delta \lesssim \Gamma$ is met in experiment.

A different, very interesting theoretical approach to the problem of a universal transmission phase behaviour was shown by Molina *et al.* [Mol12; Jal14]. In this work the quantum-dot size was identified as central leverage arm for the probability that transmission phase lapses occur. The basis of this investigation is the theoretical finding that for a semiclassical, completely ergodic system, the autocorrelation function of the wave functions can be expressed as a Bessel function, $\mathcal{J}_0$ [Ber77]. Applying this premise on a QD system in the Coulomb blockade regime, peak-height distributions, $P(G_{\max})$, were obtained [Nar01] in agreement with experimental observations [Fol96]. Having this strong indication for chaotic ballistic QDs in the semiclassical limit, Molina *et al.* derived the relation for the probability that no transmission phase lapse occurs:

$$\mathcal{P} \propto \frac{1}{k_F \cdot L} \tag{9}$$

where k_F is the Fermi wave vector and L the length of the QD along the transmission direction. Their investigation shows that the larger a QD gets, the higher is also the probability for the occurrence of a transmission phase lapse. Such a scenario could explain the results of pioneering and follow-up experiments in a way that the probability of phase-lapses occurring is not unity – but simply very high.

To see if these theoretical investigations indeed provide explanations for the experimentally obtained transmission phase data, additional electron interferometry experiments of large QDs need to be performed. These transmission phase measurements should additionally aim to characterise the QD via Coulomb diamond

measurements and peak-height distributions in order to compare the properties of a large QD to the scenarios of present theoretical investigations. This task is the scope of our experimental investigation that is presented in this chapter.

1.2 The electron two-path interferometer

To re-investigate the question about a universal transmission phase behaviour in experiment, we place a large quantum dot (QD) in the probing branch of a novel type of electron two-path interferometer. The structure of the nanoelectronic device is inspired by Mach–Zehnder (MZ) type interferometry that is mainly known from optics. A scheme of such an optical interferometer is shown in Fig. 6a. The basic idea of this approach is to divide an incident beam coming from a source (S) with a beam splitter in two branches serving as reference and probe. The beams passing along the two paths are then guided to a second beam splitter where they interfere before being projected on two screens. Due to energy conservation, the interference patterns that are apparent on the screens show complementary distributions. The phase of the intensity oscillations results from the optical path difference between the two branches. Inserting a phase-shifting material in the probing branch, the interference fringes on the screens are shifted by a phase ϕ according to the refractive index and size of the inserted medium. The concept of our electron interferometer is similar to this optical MZ setup. To guide the electrons, however, different components need to be employed and to observe the interference phenomena, a quantum mechanical effect of electrons is exploited.

The major difference of the electron two-path interferometer to its photonic counterpart are the paths along which the elementary particles are transferred. We employ a well-established Schottky gate technique that is realized in a semiconductor-heterostructure allowing to guide flying electrons in the ballistic transport regime. Applying a negative voltage on these Schottky gates, the below-lying two-dimensional electron gas (2DEG) is fully depleted. In between facing electrodes, however, several quantum channels remain, which form the transport paths of the interferometer. Figure 6b shows a schematic of the surface gates defining the ballistic transport-channel structure of our electron two-path interferometer (see red, dotted paths). The number of quantised transport channels can be typically deduced via the conductance plateaus that appear in the pinch-off characteristics.

We employ a tunnel barrier as electronic analogue to the beam splitter in an optical MZ setup. It is realised by an extremely narrow Schottky gate of 20 nm width – see electrodes TL and TR in Fig. 6b. Adjusting the negative voltage that we apply on this surface-electrode, we control the coupling of close-by transport channels via the in-between lying tunnel-barrier potential. Similar to the beam

splitter in an optical MZ setup, we use the tunnel barrier to partition an incident wave into the two paths of the interferometer and to make these waves interfere in a second coupling region. The tunnel-coupled wires play thus a key-role for the transmission phase measurement. In section 1.2.1 we will describe their function in more detail.

The electronic MZ setup further distinguishes itself from its optical counterpart by the mode of detection. In a semiconductor architecture, the interference pattern cannot be simply projected on a screen [KBS14]. Instead, the transported electrons are collected at certain terminals of the nanoelectric device via ohmic contacts (see crossed boxes) that provide electrical connection to the 2DEG. In order to observe interference of the two electron beams, we exploit the Aharonov-Bohm (AB) effect. This quantum mechanical phenomenon of electrons allows to induce a phase shift via the magnetic flux passing through the area encircled by the two paths along which the electrons are guided. Sweeping the magnetic flux density, B, perpendicular to the surface, we introduce a phase shift between the two paths of transportation[4]. This phase shift goes along with characteristic oscillations occurring on top of the currents, I_0 and I_1, that we measure at the detection terminals. Sweeping B, we can thus scan through the interference fringes of the reference and probe beam. The extent of the oscillations reflects the fraction of electrons that are coherently transported through the interferometer structure.

Finally, also the phase shifting medium of our electron two-path interferometer is different than in the optical MZ setup. Instead of the optical material properties, we aim to study the phase shifting properties of a QD that is inserted in the probing branch of the electron interferometer. In particular, we investigate – similar to the work of Schuster *et al.* [Sch97] – a large QD hosting hundreds of electrons. This QD causes the formation of a Coulomb blockade in the probing branch of the interferometer structure. Sweeping the voltage on the plunger gate, P, we can shift the eigenstates one after another through the bias window. When no eigenstate lies in the bias window, transport is blocked and current passes only through the reference branch of the device. Consequently, no interference is observable in this situation. As an eigenstate gets in resonance, however, electrons are transported through both paths leading to interference of the electron waves in the second tunnel-coupled region. When an electron is coherently transmitted through the QD, the wave function experiences a phase modification – see sections 1.1.1, 1.1.2 and 1.1.3. This transmission phase is now directly reflected in the phase shift of the AB oscillations which occurs in the currents that we measure in the two detection terminals.

[4]Note that different from the electronic MZ interferometer using edge states in the quantum Hall regime [Ji03; Rou08; Lit07] the present electron two-path interferometer is operated at low magnetic fields.

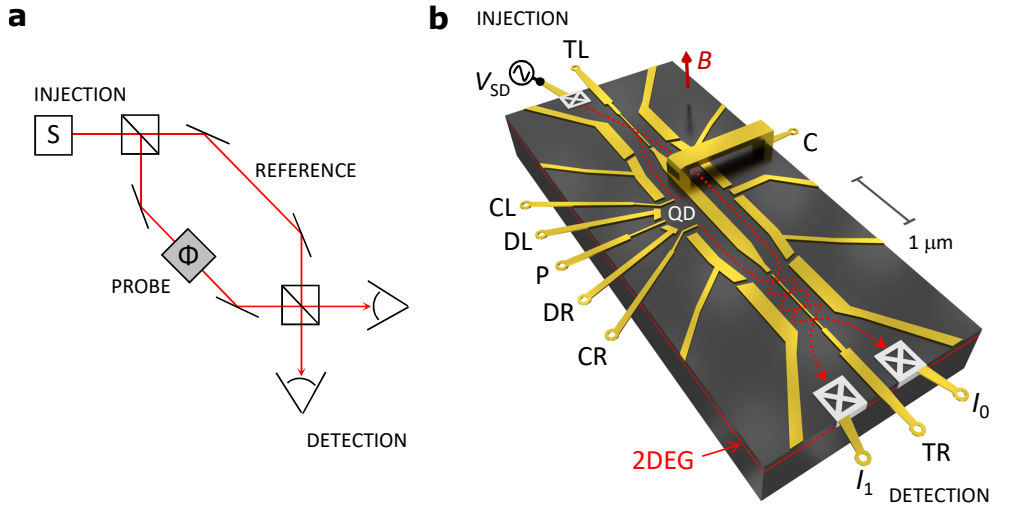

Figure 6: Scheme the electron interferometer and its counterpart from optics. (a) Shown is the principle of optical MZ interferometry – the photonic counterpart of our electron interferometer. **(b)** The figure presents a detailed three-dimensional view on the Schottky gates (golden) defining the conductive paths (red, dotted lines) and the interferometer structure in the two-dimensional electron gas (2DEG) located 110 nm below the surface. The ohmic contacts establishing electrical connection to the 2DEG are schematically indicated via the grey crossed boxes in the terminals of the interferometer. Adapted from our publication Edlbauer *et al.* [Edl17].

1.2.1 Experimental setup

The electron interferometer is realised with a standard Schottky gate technique in an GaAs/AlGaAs heterostructure hosting a two-dimensional electron gas (2DEG) with a density, $n \approx 2.7 \cdot 10^{11}$ cm^{-2}, and a mobility, $\mu \approx 10^6$ cm^{2}V^{-1}s^{-1}, that is located 110 nm below the surface[5]. The structure of the electron interferometer is defined by Schottky gates, which are realized via electron-beam lithography. The presently investigated sample was fabricated by Shintaro Takada [Edl17]. Figure 7 shows a scanning electron microscopy (SEM) image of these electrodes that are deposited on the surface of the chip. Applying a set of negative voltages, $\mathbf{V}$, on these electrodes we locally deplete the electrons in the below-lying 2DEG and define the conductive paths of our interferometer structure. In Fig. 7 we explicitly indicate only the surface gate voltages that are most important for the transmission phase measurement – we will refer to them in the following sections.

[5]With the initial value of the electron density, the conductance plateaus in the pinch-off characteristics were hardly visible. To enhance the visibility of these plateaus in the pinch-off characteristics, we illuminated the surface with a few light pulses stemming from a light-emitting diode that was directly installed on the chip carrier. This approach allowed to shift the pinch-off voltages by about −0.1 V what significantly enhanced the visibility of the quantised conductance modes.

Other, less important gates are directly labeled within the SEM image. The set of applied voltages, $\mathbf{V}$, is chosen such that only a few quantised conductance modes contribute to transport. The experiments are performed at a temperature of about 30 mK using a ^{3}He/^{4}He dilution refrigerator. Without sweeping the magnetic field, the base temperature is about 10 mK.

To achieve measurements of pure two-path interference effects, we implement the nanostructure as an effective three terminal device. We realize for this purpose an AB ring, which is connected to two tunnel-coupled wires on either side: The tunnel barrier at the injection side serves as a beam splitter guiding injected electrons into the two branches of the interferometer. At the detection side, a second tunnel-coupled wire guides the interfering electron waves – from the upper and lower interferometer branch – towards a pair of terminals where the currents, I_0 and I_1, are measured. Electrical connection to the 2DEG is established by ohmic contacts – see crossed, white boxes.

To increase the signal-to-noise-ratio of the detected signal in I_0 and I_1, a standard lock-in measurement is performed – details are provided in appendix B. The second ohmic connection at the injection side is put via a 100 Ω resistance to ground potential (cold ground) in order to collect eventually occuring backscattered electrons. Charge floating islands outside of the interferometer structure are prohibited via grounded ohmic contacts that are placed between the surface electrodes – see crossed, black boxes. In between surface electrodes where such grounded ohmic contacts are not present, we have chosen the spacing of the electrodes such that the charge floating islands are sufficiently far away from the two-path interferometer structure.

The Aharonov-Bohm (AB) ring is defined by the central electrode, C. In first realisations of such MZ-type electron two-path interferometers this central electrode was electrically connected via one of the tunnel-barrier electrodes (TL or TR) [Yam12; Tak14]. Here we establish electrical connection to this surface gate via a metal bridge that is placed over the upper interferometer branch [Tak15; Tak16; Tak17]. This electrode allows independent control of the tunnel barriers (TL and TR). The metal bridge is fabricated by two additional electron-beam lithography steps: First a pad of SU-8 photo-resist is deposited. This pad prohibits electrical connection of the metal bridge, which is deposited in the second step.

We form a QD in the lower interferometer branch with the electrodes C, CL, DL, P, DR and CR. The coupling of the QD to the two leads is controlled by the electrodes CL and CR. We can deform the QD transverse to the transmission direction via the voltages on the Schottky gates DL and DR. The narrow electrode P, which is sandwiched by DL and DR, serves as plunger electrode allowing to electrostatically shift the QD states in energy. Since the voltage stability on these electrodes defining the QD structure is critical for the transmission phase

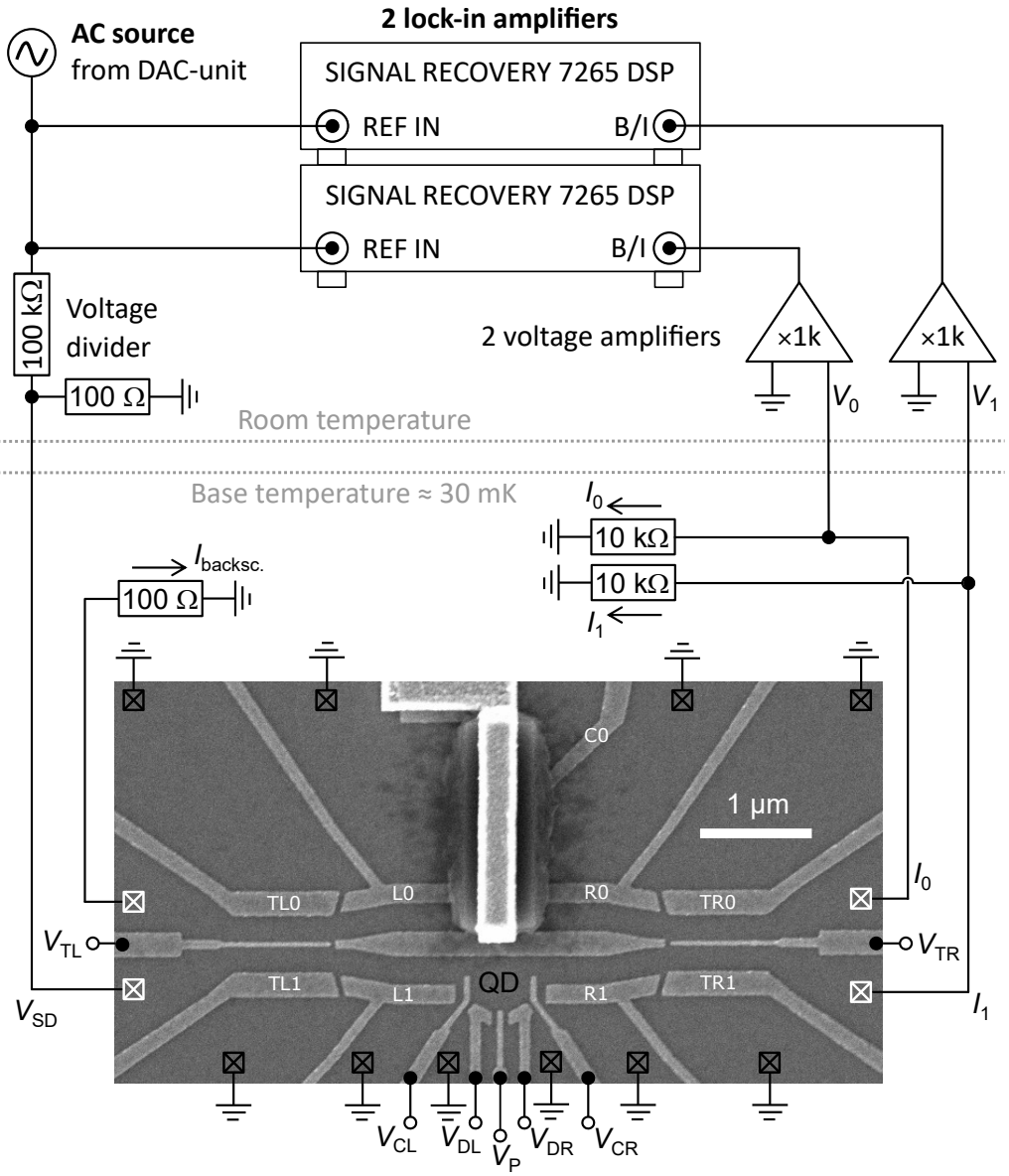

Figure 7: SEM image of the device and scheme of experimental setup. The terminals of the sample are electrically connected by ohmic contacts – see indication via crossed boxes. A modulated bias voltage, V_{SD}, is provided by a lock-in amplifier. The currents, I_0 and I_1, that are measured in the detection terminals are amplified and analysed by the lock-in amplifier. Voltage fluctuations above 100 Hz are filtered for the electrodes defining the QD (QD) structure.

measurement, we suppress voltage fluctuations above 100 Hz by additional low-pass filters that are placed at the electrical connections at room-temperature.

During the transmission phase measurements, which were performed in the course of this thesis, we slightly adjusted the voltages applied on the surface gates in order to compensate instabilities and electrostatic drifts. For the sake of completeness and reproducibility, we list the ranges of the applied voltages in table 1. Future experiments with similar surface gate structures and similar properties of the GaAs/AlGaAs heterostructures can use this data as a reference. The central island of the AB ring was kept at the same voltage for all of the conducted transmission phase measurements. A strongly asymmetric voltage set was only applied on the coupling gates of the QD (CL and CR). The asymmetry likely stems from the different quality of these narrow surface gates. We suspect that the tip of CL did not stick very well to the surface of the GaAs/AlGaAs heterostructure what demanded in turn a larger negative voltage to achieve a comparable effect as with the surface-electrode CR.

Table 1: Typical voltages applied on the electrodes of electron interferometer. Listed are the ranges of voltages, $\mathbf{V} = \{V_i\}$, that were applied on the surface gates of the present electron interferometer at the transmission phase measurements, which were conducted in the course of this thesis.

Index i	$\min V_i$ (V)	$\max V_i$ (V)	Description
C	-0.43	-0.43	Island gate of AB ring
L0	-0.51	-0.50	Top left gate of AB ring
C0	-0.57	-0.50	Top center gate of AB ring
R0	-0.53	-0.51	Top right gate of AB ring
L1	-0.52	-0.50	Bottom left gate of AB ring
R1	-0.52	-0.50	Bottom right gate of AB ring
DR	-0.89	-0.91	Right deformation gate of QD
DL	-0.89	-0.91	Left deformation gate of QD
CR	-1.07	-1.00	Right coupling gate of QD
CL	-1.58	-1.55	Left coupling gate of QD
P	-0.50	-1.00	Plunger gate of QD
TL	-0.71	-0.69	Tunnel barrier of left TCW
TL0	-0.51	-0.48	Upper side gate of left TCW
TL1	-0.53	-0.50	Lower side gate of left TCW
TR	-0.72	-0.70	Tunnel barrier of right TCW
TR0	-0.54	-0.52	Upper side gate of right TCW
TR1	-0.51	-0.48	Lower side gate of right TCW

1.2.2 Geometric and magnetic electron interferometry

The decisive factor for the interference of electrons is – as in an optical MZ setup – the phase lag that is acquired by the electron wave along the two interferometer branches. Owing to the charge of the electron, there are basically two ways to affect this phase lag of a ballistic electron in an two-path interferometer setup. The corresponding physical effects stem from the electromagnetic interaction of the electron with its environment. The phase shift of a plane electron wave, $\Psi \propto \exp\left(i(\vec{k}\cdot\vec{r}-\omega t)\right)$, that is acquired along two closed paths of transportation is generally expressed as:

$$\phi = \underbrace{\oint_{\partial A} \mathrm{d}\vec{r}\cdot\vec{k}}_{\text{geometric phase}} \underbrace{-\frac{e}{\hbar}\iint_{A} \mathrm{d}x\mathrm{d}y\, B}_{\text{AB phase}}. \tag{1}$$

The first term indicates the geometric phase. As in an optical interferometry setup, it basically depends on the length difference of the two interferometer paths. The momentum of the electron wave ($\hbar\vec{k}$), however, also depends on the number of quantised conductance channels along a certain path of transportation. For electrons, the geometrical phase change is thus a semi-classical effect. The geometric phase can be affected by any gate that is located along the two branches, whereas larger surface gates have a stronger effect.

The second term describes the Aharonov–Bohm (AB) effect that we have already mentioned several times in this chapter. This effect stems from the interaction of the flying electron with a vector potential that penetrates the two closed paths of transportation. The AB phase is determined by the magnetic flux passing through the area, A, that is enclosed by the two interferometer branches. Alternative to the geometric path difference, it is thus also possible to impose a phase shift by changing the magnetic flux that is enclosed by the two-path of transportation. Placing the electron-interferometer sample in the center of a coil, the magnetic field is basically constant along the whole interferometer structure. In this case one can easily perform the integral of the AB phase shown in equation 1 and express the periodicity of the AB oscillations, ΔB, with respect to the area, A, that is enclosed the by the two interferometer paths:

$$\Delta B = \frac{2\cdot\pi\cdot\hbar}{e\cdot A}. \tag{2}$$

From the periodicity of the AB oscillations that are observed in experiment, it is thus possible to deduce the actual area that is formed by the AB ring.

Let us now demonstrate these two interference effects by means of the presently investigated electron two-path interferometer. For the sake of simplicity, we prohibit the formation of a QD in the probing branch of the electron interferometer.

Putting V_{DL} and V_{DR} to quite negative voltages, while keeping V_{CL} and V_{CR} relatively positive, we obtain a situation where no QD is formed in the lower interferometer branch[6]. In this situation the phase, ϕ, that is acquired along the two path of transportation barely depends on the geometric phase difference and the AB effect as quoted in equation 1[7]. Figure 8 shows AB oscillations in I_0 and I_1 as function of the magnetic and geometric phase of the present electron two-path interferometer. Here we sweep the magnetic field slowly in order to avoid heating of the system. The data nicely shows the geometrical phase shift introduced by voltage changes on the surface gates L0 and R1 along the reference and probing branch of the electron interferometer. Since the gates are located at different interferometer branches, the AB oscillations are shifted in different direction of B. The magnitude of the AB oscillations typically corresponds to 5 to 15 % of the respective current signal. The sweep of the magnetic field needs to be performed rather slow in order to avoid unnecessary heating of the device via Eddy currents. From the AB oscillations shown in Fig. 8 we obtain $\Delta B \approx 3.75$ mT

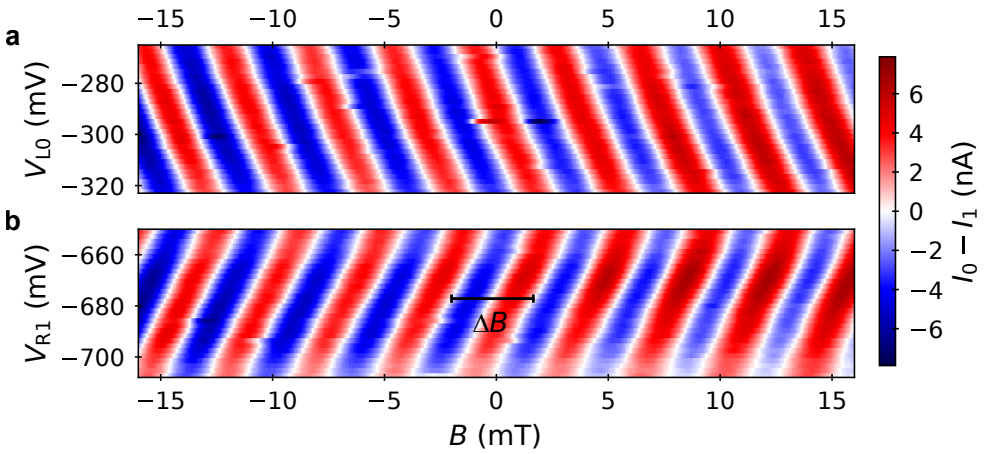

Figure 8: Geometric phase shift of anti-phase AB oscillations. Difference of the currents, $I_0 - I_1$, as function of the magnetic flux density, B, and a gate voltage along one of the interferometer branches. Here no Coulomb blockade is present in the probing branch. **(a)** AB oscillations as function of the voltage V_{L0} applied on a surface gate (L0) along the reference interferometer branch. **(b)** Here we sweep the voltage V_{R1} applied on the gate (R1) along the probing branch. ΔB indicates the periodicity of the AB oscillations.

[6]In the example presented in Fig. 8 we had $V_{\mathrm{DL}} = V_{\mathrm{DR}} = V_{\mathrm{CL}} = V_{\mathrm{CR}} = -1.2$ V, whereas the other outer gates surrounding the AB ring were set to ≈ 0.6 V. The island electrode of the AB ring was polarised to $V_{\mathrm{C}} = -1.2$ V.

[7]If a QD would be present in the probing branch of the interferometer, the phase lag ϕ would be additionally affected by the transmission phase of the quantum dot – see section 1.1.1. This transmission phase would appear as an additional term in equation 1.

giving $A \approx 2.2\ \mu\text{m} \times 0.5\ \mu\text{m}$ what is consistent with the lithographically defined structure of the device.

1.2.3 The role of anti-phase oscillations

Having described the basic experimental setup of the presently employed MZ-type electron interferometer, let us now introduce an important quality criterion that ensures two-path interference of the transmitted electrons. In an optical MZ interferometer it is clear that two-path interference is established, because photons hardly interact with its environment as they propagate though space – they are deflected via lenses and mirrors in a very controlled manner. A clear fingerprint of this behaviour are the complementary interference patterns which are projected on the screens of the two outputs of a MZ interferometer. In analogy to its photonic counterpart, two-path interference can be ensured in an electronic MZ-type interferometry setup by complementarity of the detected interference signals. In other words one can rule out multi-path contributions to the transmission phase of electrons that encircle the central island of the effective three-terminal device by establishing anti-phase behaviour of the interference patterns that are measured at the two detector terminals.

To observe the interference phenomena of the electron beams passing through the reference and probing branch of our nanostructure, we exploit the aforementioned AB effect. As we change the magnetic flux density, B, of a magnetic field perpendicular to the two-dimensional electron gas (2DEG), we observe AB oscillations in the currents, I_0 and I_1, that are measured in the two detection terminals of our device. By carefully tuning the tunnel barriers via the voltages, V_{TL} and V_{TR}, we can obtain the aforementioned anti-phase behaviour in the AB oscillations that we measure in I_0 and I_1. These anti-phase AB oscillations are now the characteristic feature to ensure reliable two-path interference as shown by analytical quantum mechanical calculations, computer simulations and experimental investigations [Yam12; Bau14b; Aha14; Tak15]. The anti-phase relation of the AB oscillations in I_0 and I_1 indicates the suppression of electrons that are coherently encircling the AB ring. In the following we will provide a set of arguments to justify this relation. For simplicity we consider again the situation where no QD is formed in the probing branch of our electron two-path interferometer. The presented anti-phase criterion applies however for any phase measurement in an effective three-terminal electron interferometer.

Let us briefly point out why anti-phase oscillations ensure a proper flow of electrons through the present interferometry setup. With a perfect anti-phase AB oscillation in I_0 and I_1 the current transmitted in the two terminals, $I_{\text{transm.}} = I_0 + I_1$, stays constant. Due to a constant bias, also the total current $I_{\text{tot.}} =$

$I_{\text{transm.}} + I_{\text{backsc.}}$ is constant. As consequence, $I_{\text{backsc.}}$ cannot show AB oscillations. This implies that there are no back-scattered electrons that coherently encircle the AB ring opposite to the transmission direction. Let us also consider the opposite situation of in-phase AB oscillation in I_0 and I_1. Due to current conservation, in this case also $I_{\text{backsc.}}$ must show AB oscillations. Thus, backscattered electrons encircle the AB-ring coherently in the backward direction. In this case the phase measurement can be additionally affected by multi-count contributions. We conclude that anti-phase AB oscillations are a requirement to prohibit electrons encircling the AB ring.

In order to achieve anti-phase AB oscillations and suppress in-phase behaviour in the currents, I_0 and I_1, one has to carefully tune the set of voltages, $\mathbf{V}$, that are applied on the involved surface gates. To find a configuration of the voltages

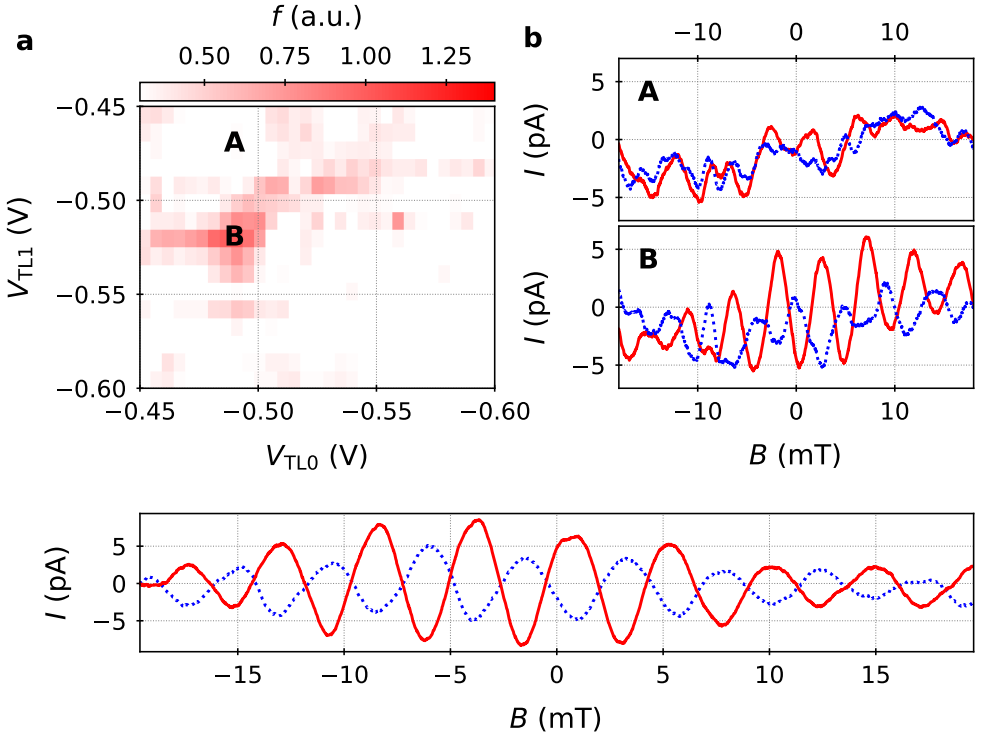

Figure 9: Optimising anti-phase behaviour of the AB oscillations. **(a)** Calculation of f via AB measurements that were conducted for different voltages on the gates TL0 and TL1. **(b)** AB oscillations in I_0 and I_1 with subtracted background for the voltage configurations A and B. **(c)** AB oscillations in I_0 and I_1 after a few cycles of manual optimisation. For the exemplary data shown here, a QD was formed on resonance in the probing branch of the electron interferometer.

on the surface gate leading to a robust anti-phase oscillation in I_0 and I_1, it is beneficial to define a optimisation function:

$$f = \int_{B_{\min}}^{B_{\max}} \mathrm{d}B\left(\frac{\partial^2 I_0(B,\mathbf{V})}{\partial B^2} - \frac{\partial^2 I_1(B,\mathbf{V})}{\partial B^2}\right) \tag{3}$$

where $B_{\min}$ and $B_{\max}$ indicate the borders of the sweeping range of B and $\mathbf{V}$ is the set of voltages applied on the surface gates of the device[8]. One can now measure f as respectively two voltages of the set $\mathbf{V}$ are varied. Doing so one obtains a map as exemplarily shown in Fig. 9a. Here we sweep the voltages on the side gates (TL0 and TL1) of the tunnel-coupled region at the injection side[9]. The regions with higher values of f indicate voltage configurations providing stronger anti-phase oscillations. Two exemplary traces of I_0 and I_1 with poor (A) and more pronounced (B) anti-phase behaviour of the AB oscillations are shown in Fig. 9b. We repeat such measurements systematically sweeping two voltage values of the set voltages applied on the surface gates, $\mathbf{V}$. After each step, we adapt the current voltage configuration to maximise f. Doing so, we can iteratively optimise the anti-phase behaviour and the strength of the AB oscillations. After several optimisation cycles, we obtain anti-phase AB oscillations as shown in Fig. 9c. The anti-phase behaviour extends with large current amplitude over many AB oscillations.

A suggestion for future transmission phase measurements: This optimisation procedure is particularly important when a QD is inserted in the probing branch of the electron interferometer. As the transmission phase is scanned along several resonances, it is at some point necessary to retune the interferometer configuration to maintain anti-phase AB oscillations. In the measurements that were performed in this thesis, we have performed this optimisation manually. Such optimisation was typically necessary after scanning through more than three to six resonances. For future investigation on related topics, it suggests itself to consider automatisation of this process. It should be staight-forward to implement a feedback loop between the measurement and data analysis process. Do do so, a more elaborate optimisation function would be necessary that is able to account for perturbations from switches and vibrations. Such a optimisation function could be for instance implemented using a Fourier transform of the AB-oscillation data with projection on the actual AB periodicity, ΔB, of the magnetic flux density:

$$f = \mathcal{F}_{\mathrm{B}}\left(\frac{\partial^2 I_0(B,\mathbf{V})}{\partial B^2} - \frac{\partial^2 I_1(B,\mathbf{V})}{\partial B^2}\right)\Big|_{B^{-1}=\Delta B^{-1}} . \tag{4}$$

[8] We calculate here the second derivative of the currents in order to force the inflection points of the signal to zero – what is similar to subtracting a slowly varying background signal.

[9] The surface gates TL0 and TL1 are also indicated in the SEM image shown in Fig. 7.

1.2.4 The measurement of the transmission phase

Let us now consider the situation where a quantum dot (QD) is embedded in the probing branch of the AB ring. It is operated in the Coulomb blockade regime meaning that the changing energy, E_C, and the bias energy, $e \cdot V_B$, between the leads is much smaller than the thermal energy $k_B \cdot T$. If a discrete state of the QD has in this situation an electron potential located in the bias window – so in between the chemical potentials of the two leads to which the QD is electrically connected –, the state is in resonance and electrons can be transmitted one-by-one. In the Coulomb blockade regime the phase of the wave function is modified as the electron is transferred. The extent of this transmission phase depends on the resonance condition[10].

The conductance through the QD and thus the resonance condition is controlled by the so-called plunger gate, P, that is embedded in the QD structure. This electrode affects the electrostatic potential of the QD and is used to bring a QD state in resonance with the leads. Comparing to the effect of smaller side electrodes such as C0, we find that a shift of the plunger gate voltage has a negligible effect on the geometric phase. Figure 10a shows a CBP – the electrical

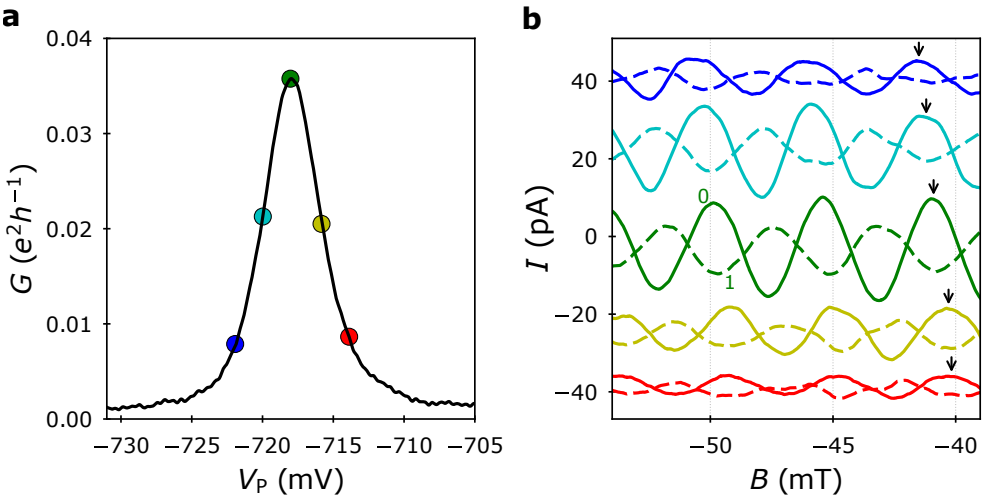

Figure 10: Anti-phase AB oscillations along a CBP. (a) Conductance through the QD, G, as the plunger gate voltage, V_P, is swept along a resonance. **(b)** Excerpts of the currents, I_0 (solid line) and I_1 (dashed line), as a function of the magnetic flux density, B, for five positions of V_P along the resonance. The V_P positions of the current traces are indicated via correspondingly colored data points in (a). The arrows indicate the shift of the AB oscillations. For clarity a continuous background is subtracted and an offset is added. Adapted from Edlbauer *et al.* [Edl17].

[10] For details to the transmission phase of a QD see section 1.1.1.

conductance through the QD as the plunger gate voltage, V_P, is swept along a resonance. For five positions along the resonance the corresponding anti-phase AB oscillations in I_0 and I_1 are shown in Fig. 10b. The magnitude of the oscillations is linked with coherent transmission through the QD and is hence stronger at the center of resonance. Off-resonance the transmission through the QD is blocked. As consequence, AB oscillations are hardly observable in the conductance valleys. As V_P is swept along the resonance, the anti-phase AB oscillations experience a phase shift (see arrows in Fig. 10b), which directly reflects the transmission phase of the QD.

1.2.5 Data analysis procedure

Here we perform the transmission phase measurement by scans of the electron interference fringes via sweeps of the magnetic flux density, B, for different steps of the plunger-gate voltage, V_P. An exemplary set of raw data along a resonance is shown in Fig. 11a. Shown is the difference of the currents, I_0 and I_1, that are measured at the two terminals at the detection side. The AB oscillations experience a characteristic shift as V_P is scanned along a resonance. To obtain the transmission phase quantitatively from the data, we perform a Fourier transform with respect to B.

The measured current signals, I_0 and I_1, contain a continuous background. To force the inflexion points of the AB oscillations to zero, we smooth the data and calculate the second derivative. This procedure is comparable to the subtraction of a continuous background and leads to similar results. By forcing the inflexion points to zero, the quality of the Fourier transform is however strongly enhanced. Therefore, this approach facilitates the detection of the AB periodicity.

Figure 11b shows the magnitude of the Fourier transformed data, $M = |f_0| + |f_1|$. The data clearly show a peak (see arrow) corresponding to the AB periodicity, ΔB. For further analysis we only process a slice of the data at $B = \Delta B$, which reflects the AB oscillation:

$$f_{0/1}^{\mathrm{AB}}(V_P) = \mathcal{F}_B\Big(\frac{\partial^2 I_{0/1}(B, V_P)}{\partial B^2}\Big)\Big|_{B^{-1}=\Delta B^{-1}} . \tag{5}$$

In order to perform a reliable phase measurement, two criteria have to be met. The first quality criteria ensures sufficient coherent transmission through the QD and thus a sufficient signal-to-noise ratio of the AB oscillations. The second quality criterion assesses the anti-phase relation of the AB oscillations in I_0 and I_1, which assures that multi-path contributions are eliminated as mentioned in section 1.2.3.

The coherent transmission criterion is implemented via a threshold for the magnitude of AB oscillation, M. Figure 11c shows a comparison of a slice of the

Fourier transformed data at the AB peak (blue data points) with the electrical conductance through the QD, G (black line). The shown conductance data, G, that is shown here is obtained from a separate measurement, where we guide the electrons only through the probing branch hosting the QD. G shows the CBP reflecting the total transmission probability through the QD. The slice of M on the other hand is based on the AB effect – a phase coherent quantum interference phenomena. Therefore, M merely describes the coherent transmission probability and serves as adequate quantity for the assessment criterion. In order to ensure sufficient visibility of the AB oscillations we set a coherent transmission criterion such that only data points above a threshold of $M > 0.5$ (arbitrary units) are kept – see blue, dashed line. By this approach only data points with a distinctive AB peak in the Fourier transform are kept. AB oscillations with a small signal-to-noise ratio are discarded.

The anti-phase criterion assesses the phase difference of the AB oscillation in the currents, I_0 and I_1. This AB phase can be directly calculated from the argument of the projected Fourier transform:

$$\phi_{0/1}(V_\mathrm{P}) = \arg\left(f_{0/1}^{\mathrm{AB}}(V_\mathrm{P})\right) . \tag{6}$$

Figure 11d shows the phase difference of the AB oscillations in the two terminals for the exemplary data set. The quality criterion is set such that only data points are accepted where the deviation from the anti-phase relation is below the threshold:

$$|\phi_0 - \phi_1| < \pi \pm 15\% . \tag{7}$$

Finally, the transmission phase, ϕ, is extracted only for V_P values where the data fulfils the two quality criteria (filled symbols) by evaluating the expression:

$$\phi = \arg\left(f_0^{\mathrm{AB}} - f_1^{\mathrm{AB}}\right) . \tag{8}$$

The phase data corresponding to the exemplary data set is shown in Fig. 11e. The red, filled triangles show data points fulfilling our quality criteria. These data points represent the transmission phase through the QD according to the employed quality criteria. Fitting the conductance, G, shown in Fig. 11c with a Lorentzian function we can construct the expected course of ϕ from Breit–Wigner resonance theory (dashed line). The data points fulfilling our quality criteria agree with the expected course, whereas the discarded data points (open triangles) strongly deviate. Employing the two discussed quality criteria, we have a useful measure to assess the quality of two-path interference in the present experiment.

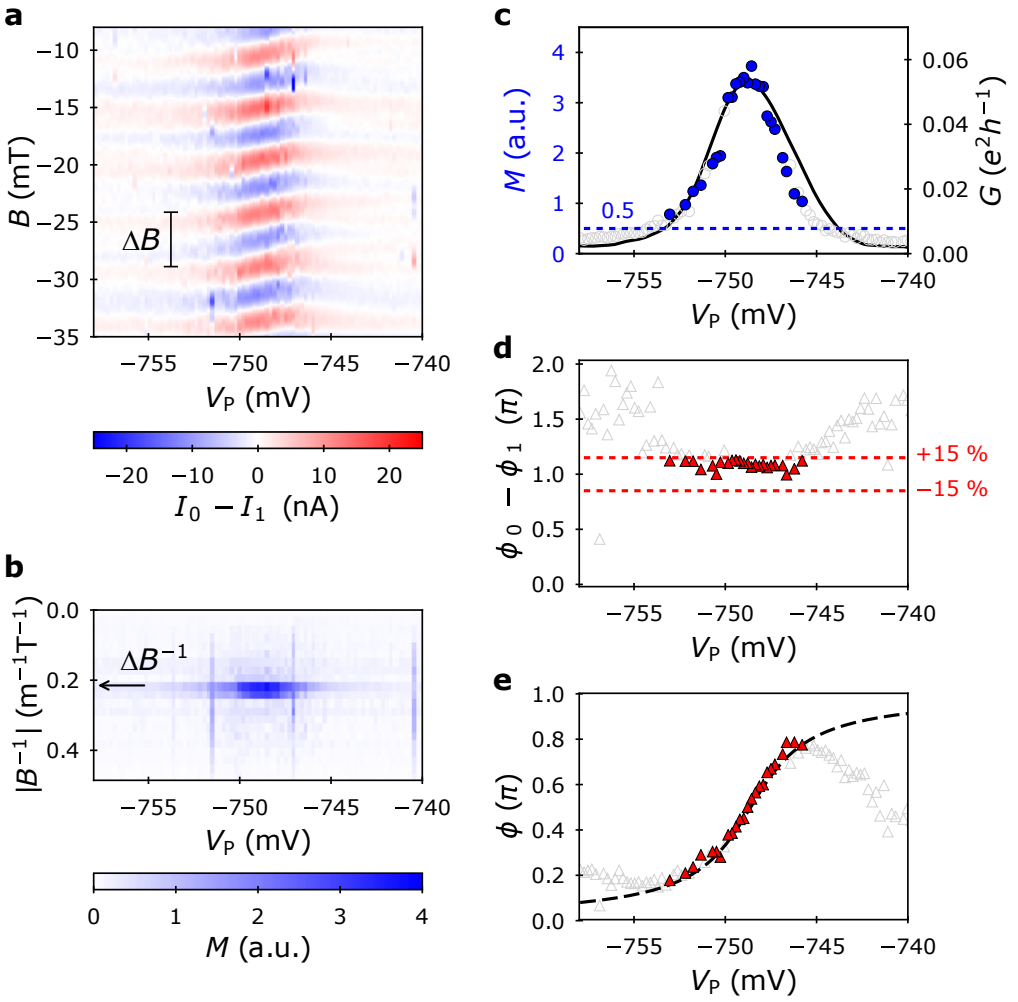

Figure 11: Exemplary set of raw data with analysis. **(a)** Difference of currents, $I_0 - I_1$, as a function of magnetic flux density, B, and the plunger gate voltage, V_P. **(b)** Magnitude of AB oscillation, M, obtained by Fourier analysis with respect to B. The arrow indicates the periodicity of the AB oscillation, ΔB. **(c)** Slice of M at ΔB (left axis; blue points) and electrical conductance through the QD (right axis; black line) as a function of V_P. **(d)** Difference of the AB phases, $\phi_0 - \phi_1$ – see equation 6. **(e)** Transmission phase, ϕ, (red points) as a function of V_P. The dashed line indicates the evolution expected from a Breit–Wigner profile based on a Lorentzian fit of G – see data (c). Data points not fulfilling our quality criteria are shown as open, grey symbols. The figures stem from our publication Edlbauer *et al.* [Edl17].

1.3 Experimental Results

Having introduced the background and working principle of our original Mach–Zehnder type (MZ) electron interferometer in the sections 1.1 and 1.2, let us now present the transmission phase measurements that were performed with this device. With our experimental investigations we particularly aim to address the question about a universal transmission phase behaviour in large QDs in the light of previous theoretical investigations[11]. Consequently, we have chosen to put a slightly larger QD as in the work of Schuster *et al.* [Sch97] in the probing branch of our interferometer structure. In the following we present data which puts the observations of these pioneering experiments in a new perspective.

In the following we show electron interferometry measurements that clearly indicate a non-universal transmission phase behaviour via the absence of phase lapses between certain resonances. Interestingly, we also observe characteristic features of a parity-dependent transmission phase behaviour in the magnitude of the AB oscillations. To underpin the non-universality of the sequence of transmission-phase lapses, we investigate the effects of QD deformation and magnetic field variation on our transmission phase measurements and find clear changes in the measured sequences of phase lapses and plateaus. Due to the difficulty of such electron interferometry experiments, transmission phase measurements of this kind are rare. Only a few groups have succeeded in performing such delicate measurements [Sch97; Sig04; Aik04a; AK05]. We thus anticipate that our findings set a milestone towards a comprehensive understanding of the transmission phase in the Coulomb blockade regime.

1.3.1 Properties of the investigated large quantum dot

The QD structure is defined via voltages on six Schottky gates: Transversal to the transmission direction the QD is confined by the central electrode (C) and two opposing gates (DL and DR). C depletes the two-dimensional electron gas below a central island to form the AB ring. The longitudinal QD confinement and the coupling to the conductive channels of the interferometer branch are defined by two narrow gates (CL and CR). The lithographic dimensions of the QD are approximately 0.5 μm in transverse direction and 0.6 μm in longitudinal direction. A scanning electron micrograph of the sample is shown in figure 7 of section 1.2.1. Assuming an underestimated homogenous electron density of $2.7 \cdot 10^{11}$ cm^{-2} and a circular QD shape with a radius of 190 nm, we can estimate that the present QD contains approximately 300 electrons.

Let us now introduce further properties of the investigated QD on the basis of a Coulomb diamond measurement. The presence of the QD causes Coulomb

[11] Compare section 1.1.4.

blockade of electron transport in the lower interferometer branch allowing characterisation of the QD. By increasing the tunnel barriers via the voltages V_{TL} and V_{TR}, electrons are steered only into the lower branch. In this configuration we can now measure Coulomb diamonds as shown in Fig. 12. Here we measure the differential conductance, dI_1/dV_{SD}, as we change the plunger gate voltage, V_{P}, for different values of the DC component of the source-drain voltage, V_{SD}. We estimate the charging energy, E_{C} from the Coulomb diamond height [Han07] as about 240 μeV.

The Coulomb diamonds show a width of $V_{\mathrm{C}} \approx 26$ mV. We obtain the voltage to energy conversion factor as $\eta = E_{\mathrm{C}} \cdot V_{\mathrm{C}}^{-1} \approx 0.01\ e$ from the spacing of the resonances in voltage. Approximating the resonances with a Lorentzian function, we obtain the coupling energy, $\Gamma \approx \eta \cdot \Delta V_{\mathrm{FWHM}}\ [\mathrm{V}] \approx 30 \sim 60\ \mu$eV, from the full width at half maximum, ΔV_{FWHM}. The energy spacing of the excited states, δ, is hardly resolvable. From the structures appearing at the resonances A11 to A14, we can however estimate the level spacing as $\delta \approx 60\ \mu$eV. Taking into account the gate geometry and the depth of the 2DEG, we can estimate the effective QD area as $A \approx 0.3\ \mu\mathrm{m} \times 0.4\ \mu\mathrm{m}$. With this information, we can alternatively approximate δ from the minimum level spacing of a two-dimensional particle in a box problem [Kou97]. We derive $\delta \gtrsim \hbar^2 \cdot \pi^2/(2 \cdot m \cdot A) \approx 50\ \mu$eV, where $\hbar$ is the reduced Planck constant and m is the effective electron mass in a GaAs crystal. The two estimates of δ are consistent. $\delta \approx \Gamma$ implies transport at the crossover from the single-level ($\delta > \Gamma$) to the multi-level ($\delta < \Gamma$) regime. For the investigated magnetic field range, the Zeeman energy is much smaller than the temperature fluctuation. We do not observe any enhancement of the valley conductance when lowering the temperature. Hence, we assume that the Kondo temperature is much lower then the electron temperature.

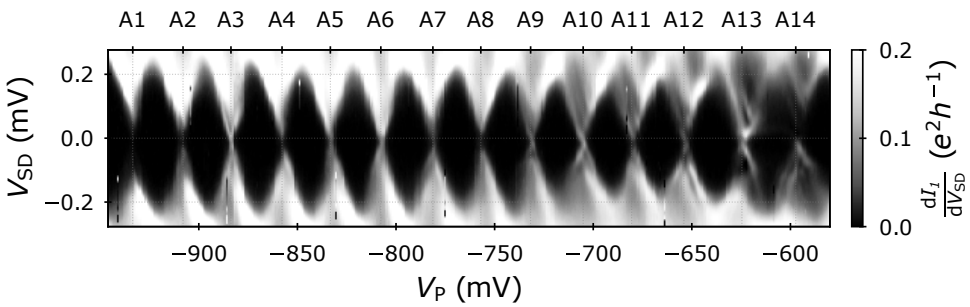

Figure 12: Coulomb diamonds. Transconductance measurement as the bias voltage, V_{SD}, and the plunger gate voltage, V_{P}, are swept. The investigated resonances, A1 to A14, occurring in the swept V_{P} interval are labeled at the upper axis. The figure stems from our publication Edlbauer *et al.* [Edl17].

1.3.2 Height distribution of Coulomb-blockade peaks

In section 1.1.4, we have introduced the question about a universal transmission phase behaviour in a large QDs. In the course of this discussion we have presented an explanation of long sequences of transmission phase lapses in such large-scale systems proposed by Molina *et al.* [Mol12]. In this theoretical investigation the probability for the absence of transmission phase lapses was reciprocally related to the QD size. This relation was obtained with the assumption of chaotic ballistic QDs in the semiclassical limit. For this kind of system, the height-distribution of the Coulomb-blockade peaks (CBP) theoretically follows a particular probability-density-distribution for zero and non-zero magnetic field [JSA92]:

$$P(\alpha|B = 0\ \mathrm{mT}) = \sqrt{\frac{2}{\pi \cdot \alpha}} \cdot e^{-2\cdot\alpha} \tag{1}$$

$$P(\alpha|B \neq 0\ \mathrm{mT}) = 4 \cdot \alpha \cdot \big(K_0(2 \cdot \alpha) + K_1(2 \cdot \alpha)\big) \cdot e^{-2\cdot\alpha} \tag{2}$$

Here K_0 and K_1 are modified Bessel functions. α is a dimensionless peak height that is defined by the coupling to the left and right leads,$\Gamma_{L/R}$:

$$\alpha = \frac{\Gamma_L \cdot \Gamma_R}{\bar{\Gamma} \cdot (\Gamma_L + \Gamma_R)} \tag{3}$$

where $\bar{\Gamma} = (\Gamma_L + \Gamma_R)/2$ is the average coupling energy. It is important to note, that this model applies for the single-level regime where $\delta \gg kT \gg \Gamma$. Moreover, effects of spin-scattering are ignored and independence of the leads is assumed. Four years after the theoretical prediction [JSA92], such a peak height distributions, $P(\alpha|B = 0\ \mathrm{mT})$ and $P(\alpha|B \neq 0\ \mathrm{mT})$, have been indeed experimentally observed for a large QD [Fol96]. Note that the size of that QD was larger (approximately 0.5 μm $\times$ 0.8 μm) and that the surface-gate geometry was more asymmetric than in our present experimental investigation.

Comparing δ to Γ for the experimentally investigated large QD, we have estimated that resonant electron transport is at the crossover from the single-level to the multi level regime – see section 1.3.1. Let us now nonetheless investigate the height-distribution of the CBPs for the present QD and compare if the results of the aforementioned distributions (equations 1 and 2) hold for the present QD. To obtain CBP data for statistically independent configurations, we repeated conductance measurements for different QD deformations – via V_{DL} and V_{DR} – and different values of the magnetic flux density, B. An exemplary set of CBPs is shown in Fig. 13a. Since QD deformation affects the coupling to the leads, we obtain $\bar{\Gamma}$ for a specific deformation-configuration by averaging over all variations in B. We fit each CBP that is resolvable in the present data with a hyperbolic secant distribution (sech $x = 1/\cosh\ x$). For simplicity we assume symmetric

coupling to the leads providing us the dimensionless peak height $\alpha = \Gamma/(2 \cdot \bar{\Gamma})$. Doing so we obtain 1,404 and 17,806 α-values for $B = 0$ mT and $B \neq 0$ mT.

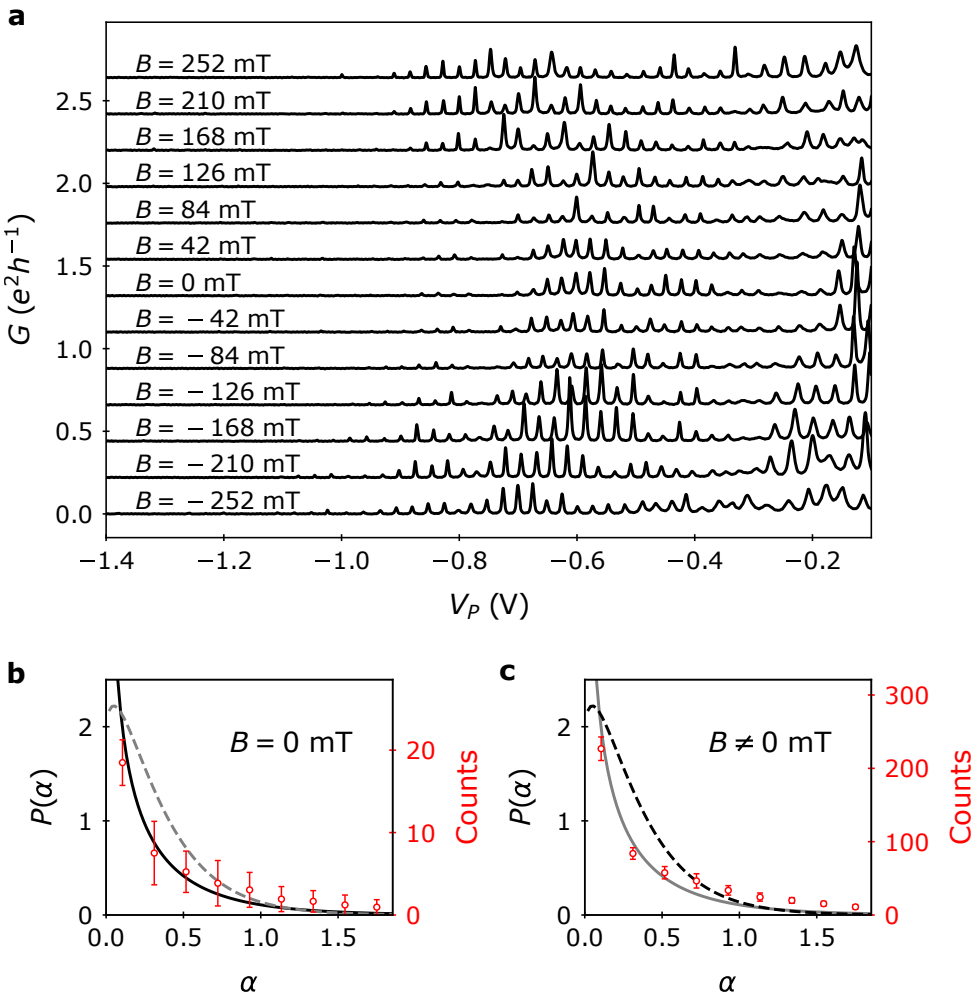

Figure 13: Height distribution of Coulomb-blockade peaks. **(a)** Exemplary set of Coulomb-blockade peaks for different magnetic flux density, B. The deformation configuration of the QD is defined via $V_{\mathrm{DL}} = -1.3$ V and $V_{\mathrm{DL}} = -0.7$. Such data sets were measured 41 times for the simultaneous deformation variation $\delta V_{\mathrm{DL}} = +0.4$ V and $\delta V_{\mathrm{DL}} = -0.4$ V. **(b)** Height distribution of Coulomb-blockade peaks for $B = 0$ mT (data points; right axis) compared to the theoretically expected probability distribution function, P, as function of the dimensionless peak-height, α (solid line; equation 1). The grey, dashed line shows $P(\alpha)$ for $B \neq 0$ mT. **(c)** Height distribution of Coulomb-blockade peaks for $B \neq 0$ mT (data points; right axis) compared to $P(\alpha)$ (dashed line; equation 2). The grey, solid line shows $P(\alpha)$ for $B = 0$ mT.

Averaging the data over 41 sets of deformation-configurations, we then obtain peak height distributions as shown in Fig. 13b-c. The error bars indicate the corresponding standard deviations. For $B = 0$ mT we find that the experimentally deduced peak height distributions strongly resemble the theoretically expected course (equation 1; solid line). Considering the case of $B \neq 0$ mT, however, we do not observe the theoretically expected change of the peak height distribution (equation 2; dashed line). The data rather stays unaffected and still holds qualitative agreement with equation 1. It could however well be that the accuracy of the conductance measurement was not high enough for the small conductance peaks. Furthermore, we cannot exclude that systematic deviations occur due to crosstalk from voltage variations. Looking at the peak widths in Fig. 13a for instance, we find a broadening of the peaks as the plunger gate V_{P} is made more positive which implies a changed coupling to the leads. The premise of statistically independent measurements is hence questionable and a comparison to the aforementioned theoretically predicted distributions has to be treated with care.

1.3.3 A non-universal transmission phase behaviour

To check the universality of transmission phase lapses in a large QD it is necessary to investigate a set of resonances that is as large as possible. When sweeping the plunger gate over a large voltage range, crosstalk between the different electrostatic gates defining the QD affects the visibility of the AB oscillations and renders the measurement more difficult. By adjusting voltages of the side gates of the reference branch and the tunnel barriers, however, one can increase the amplitude of the AB oscillations. To obtain the transmission phase along many resonances, we therefore have to split the measurement in several parts and compensate the loss of AB oscillation magnitude by retuning the interferometer configuration. For each part, we carefully fine-tune the voltages on the electrodes defining our interferometer and QD structure to obtain maximal visibility of the anti-phase AB oscillations along the scanned resonances.

To align the fine-tuned data sets, it is necessary that the measurements have overlapping V_P intervals. The data alignment regarding plunger gate voltage, V_P, is performed by overlapping the AB oscillation peaks. The alignment regarding phase is performed manually using a guide to the eye, that is constructed on the basis of CBPs. The CBPs were measured in the lower interferometer terminal in the same interferometer configuration in which the transmission phase measurements were performed[12]. Fitting each peak with a Lorentzian function, we obtain

[12] A CBP measurement with closed tunnel barriers, where the electrons are steered through the lower interferometer branch only, is not appropriate here. As the tunnel barriers are closed – a voltage change of approximately 300 mV – the QD states can be affected due to capacitive

the positions of the maxima, $V_{P,0}$, and an averaged value of the coupling energy Γ – compare equation 4. Using these fit parameters we then construct the phase shift for each resonance that is expected from Breit–Wigner resonance theory – see equation 5 on page 12. In between the resonances, phase lapses of π are introduced according to the phase plateaus that are observed in the transmission phase measurements.

Following this approach with six overlapping measurements along several resonances we can construct the course of the transmission phase along a set of fourteen successive resonances as shown in Fig. 14. Characteristic phase shifts of

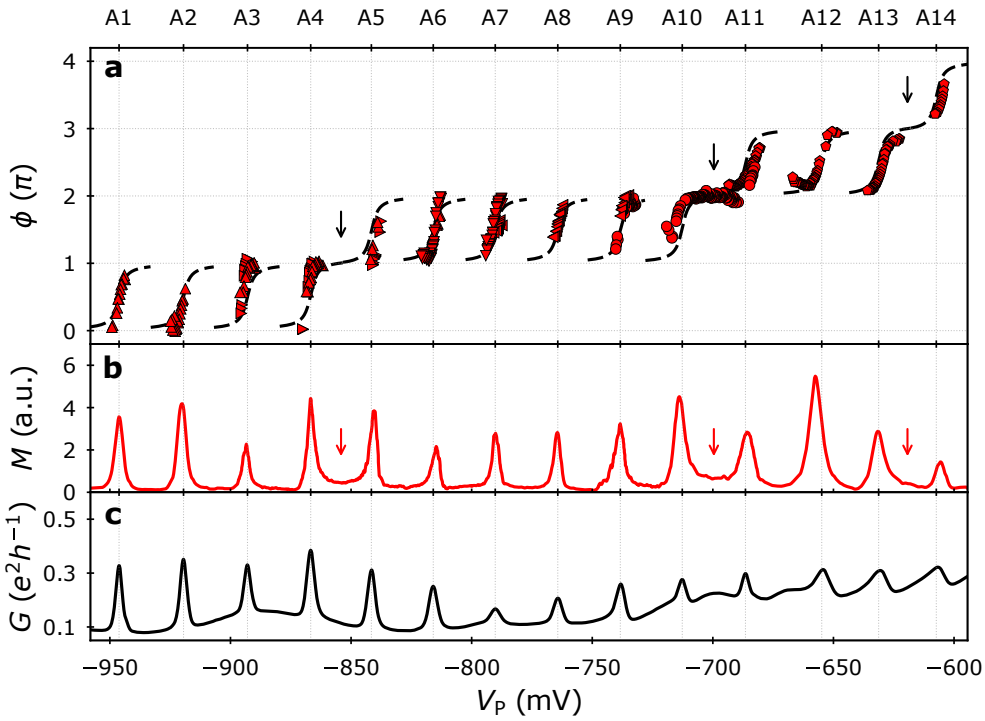

Figure 14: Transmission phase along fourteen resonances. (a) The red data points show the transmission phase, ϕ, measured along the resonances A1 to A14. The arrows indicate phase plateaus. A guide to the eye is shown as dashed line. It is constructed from electrical conductance, G (compare section 1.1.1). **(b)** The magnitude of the AB oscillation, M, is illustrated as red line. The red arrows indicate regions of enhanced AB oscillation. **(c)** The electrical conductance at the lower terminal of the interferometer, $G = I_1/V_{SD}$, is shown as black line. The figure stems from our publication Edlbauer *et al.* [Edl17].

crosstalk. Using such conductance data for the construction of the guide to the eye, consequently, would be misleading for comparisons to the AB oscillation magnitude and phase.

π (red data points) are apparent along all of the investigated resonances labelled as A1 to A14 at the corresponding peaks of conductance, G. Most importantly, however, the data show a significant signature of non-universal transmission phase behaviour: among the investigated fourteen resonances a lapse in the transmission phase is absent three times. The missing jumps of π lead to clear phase plateaus after the resonances A4, A10 and A13 (see black arrows in Fig. 14) where the transmission phase cumulates the characteristic shift of π. In between these plateaus, nonetheless, we also observe long sequences of phase lapses as in previous experimental investigations [Sch97].

Theoretically, the occurrence of phase plateaus is linked to a parity change of the QD states [Lee99; TB99] as discussed in chapter 1.1.1. For a simple one-dimensional problem, the parity should change when going from one orbital state to the next one. For a large QD, which has to be regarded as a two-dimensional system the situation is more complicated and it is indeed likely to occur that successive QD states have the same parity. In this case parity is defined by the coupling of the QD state to the two leads – compare equations 6 and 7 and see references [LB00; Kar07; Mol12]. For two successive QD states having the same parity a singularity point called transmission zero occurs that causes a phase lapse in between the resonances and a complete suppression of the AB oscillation in the conductance valleys. When the parity of two successive QD states changes, on the other hand, the magnitude of the AB oscillation in the conductance valley is enhanced.

This characteristic feature of enhanced AB oscillation in conductance valleys without transmission zero is clearly apparent in our experimental data. In congruency with a parity-dependent transmission phase behaviour, we find augmented magnitude of AB oscillation, M, in between resonances where a phase plateau occurs (see red arrows in Fig. 14). The enhancement of the AB oscillation is strongly pronounced in between the resonances A4 and A5 and A10 and A11. Our observation of this theoretically expected signature shows that transmission phase measurements indeed can be used to access the sign of the wave functions for the QD states at the connections to the leads.

1.3.4 Asymmetry in coherent transmission

Another interesting feature that we find in the present data is the asymmetry of the AB oscillation magnitude, M, with respect to conductance peaks. This asymmetry around a resonance could indicate spin-flip scattering processes which mitigate coherent transmission [Ake93; Ake99; KG01; KG02] as mentioned in section 1.1.3. By comparing M with respect to the conductance peaks, G, in principle the presence of an empty or partially occupied spin-degenerate level could be deduced [Aik04b; Ihn07]. If the region of reduced AB oscillation mag-

nitude is located at the positive side of the conductance peak regarding plunger gate voltage, V_P, a partially occupied spin-degenerate level is present. *Vice-versa* is the situation for an empty spin-degenerate level.

Such a feature is particularly strong at resonances where phase plateaus occur. Asymmetric peaks in M are also apparent at several other resonances. Nonetheless, we find no systematic correspondence to the occurrence of phase plateaus. Other effects such as the Fano effect [Kob02; Kob04; Aik04a] or the aforementioned transmission zero can also lead to an asymmetric AB oscillation magnitude around the resonances. The asymmetries of AB oscillation peaks and the sequence of phase plateaus point out the complexity of the internal structure of the present large QD. A detailed characterization of the spin-state sequence for the present data is out of reach. From the occurrence of phase plateaus, however, we can clearly observe changes in orbital parity.

1.3.5 Effect of quantum-dot deformation

According to a parity-dependent transmission phase behaviour [Lee99; TB99] one expects modifications of the phase lapse sequence as QD states change. If the QD shape is for instance distorted such that the QD states and, thus, the sequence of orbital parities changes, one should observe a modified sequence of phase lapses and plateaus. With the present experimental setup, we can readily investigate this assertion.

We deform the QD by changing the balance of the voltages V_{DL}, V_{DR} and V_P. As a starting point for the discussion we consider a reference QD configuration with $V_{DL} = V_{DR} = -0.92$ V. A set of transmission phase shifts measured along five consecutive resonances is shown in Fig. 15a. For this reference configuration a phase plateau occurs after CBP B2. We modify the QD shape by changing the voltages, V_{DL} and V_{DR}, to -1.08 V. At the same time we adjust the voltage V_P to keep the electron number constant.

Comparing the transmission phase measurements along the same set of resonances for the two situations – compare Fig. 15a and 15b – we find significant changes: We observe an alternation of the phase lapse sequence as the QD shape is modified. After deformation of the QD, the phase plateau occurs after resonance B3 instead of B2. This change is indicated via black arrows in Fig. 15a and 15b. The deviating intervals of V_P in Fig. 15a and Fig. 15b result from the different gate voltage applied to the gates V_{DL} and V_{DR} and have been chosen such that the same resonances, B1 to B5, are shown.

The data shows that QD deformation causes a change in the sequence of orbital parities what is directly reflected in the observed course of the transmission phase. According to the altered position of the phase plateau, augmented AB oscillation

magnitude, M, appears in the conductance valley between B3 and B4. The augmented AB oscillation magnitude at transmission phase plateaus is indicated via red arrows in Fig. 15a and 15b. This change clearly shows the correlation between those two theoretically expected features and indicates a parity change of the QD state that is moved through the bias window at resonance B3.

1.3.6 Quantum dot modification by magnetic field variation

As second approach affecting the QD states, we vary the magnitude of the magnetic flux density, B. The electron states in a QD are affected by an external magnetic field via their spin and orbital motion. As the magnetic field is swept, changes in angular momentum lead to a different order of the QD states in energy. Remeasuring the transmission phase after shifting the magnetic flux density B by approximately 200 mT, we find indeed a change in the sequence of transmission phase lapses – compare Fig. 15a and 15c. At higher magnetic field, a transmission phase lapse is also present in the conductance valley between CBP B2 and B3 – the quality of the phase shift data is however reduced. The transmission phase plateau between the resonances disappears as the magnetic flux density is changed. We find as second striking feature that the magnitude of coherent transmission, M, in now mainly located at the left side of the CBPs that are measured via the conductance G. This effect is likely related to spin-scattering effects as discussed in section 1.1.3. The change in the sequence of the transmission phase lapses could indicate that the parities of QD states corresponding to CBP B1 and B2 or to CBP B3, B4 and B5 have switched.

Tracing the positions of the CBPs, we observe shifts erratically changing their direction as B is increased – see Fig. 15d. Here the electrical conductance, G, is measured with completely closed tunnel barriers. Electrons are guided only through the probing branch of the electron interferometer that hosts the QD. By setting V_{TL} and V_{TR} approximately 300 mV more negative, therefore we slightly increase also the electrostatic potential of the QD what causes that the CBPs are located about 10 mV more positive than in Fig. 15b and Fig. 15c. Such movements in the CBP positions with B were already observed several times for a many-electron QD [Fol96; Lin02; Hel15]. Since the Landé g factor for bulk GaAs is -0.44 we expect a minor magnetic field dependence of the CBP position on spin. Rather we suspect that the fluctuations of the CBP positions are caused by effects of the magnetic field on the orbital wave functions of the QD. We speculate that strong level mixing occurs and that orbital energy anti-crossings cause erratic changes in the shifting direction of the CBPs.

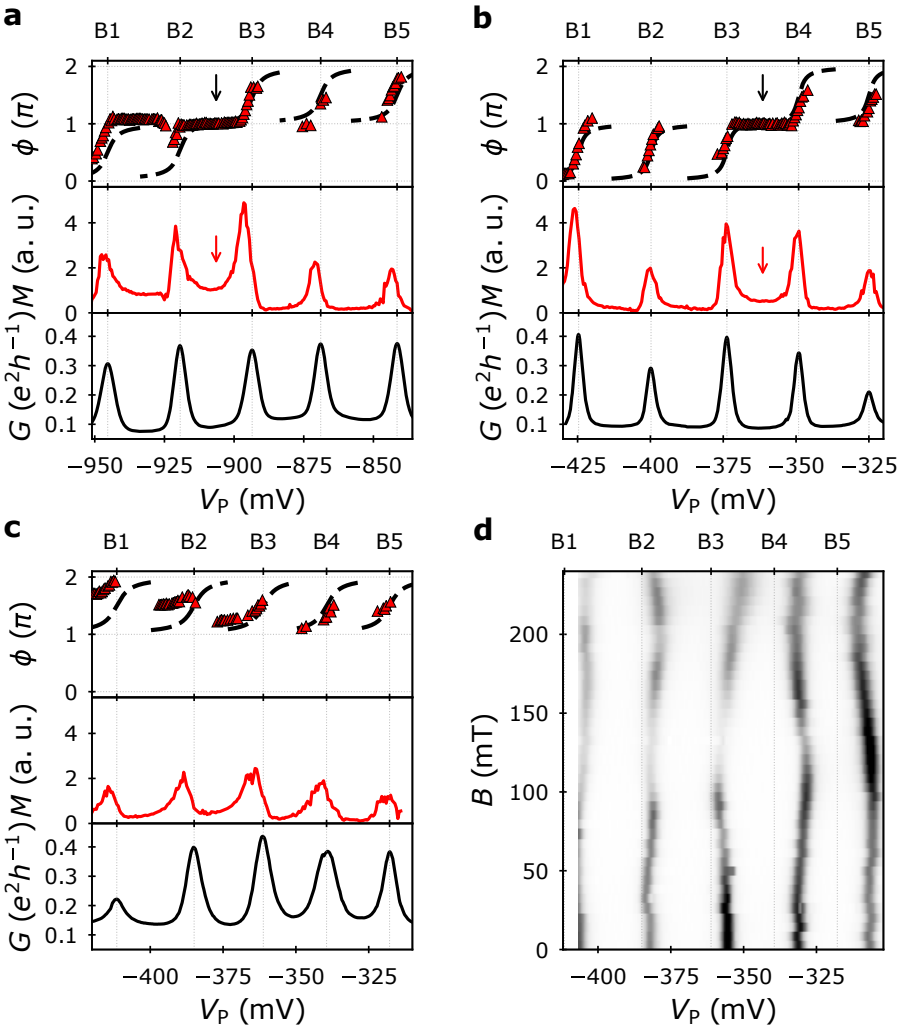

Figure 15: Effect of QD deformation and magnetic field variation. Transmission phase, ϕ, magnitude of AB oscillation, M, and electrical conductance at lower terminal, G, along the same set of resonances (B1 to B5) for different QD configurations: **(a)** Reference configuration with $V_{\mathrm{DL}} = V_{\mathrm{DR}} = -0.92$ V; $B \in [-15, 45]$ mT. **(b)** Deformed QD with $V_{\mathrm{DL}} = V_{\mathrm{DR}} = -1.08$ V. **(c)** Sweeping range of the magnetic flux density shifted to $B \in [200, 240]$ mT with $V_{\mathrm{DL}} = V_{\mathrm{DR}} = -1.08$ V. The dashed line underneath the phase data serves as guide to the eye and is constructed on the basis of conductance peak data shown in the bottom panel. **(d)** CBPs measured for different values of B. Here G is measured, while the electrons are guided only through the QD. The figures contain data of our publication Edlbauer *et al.* [Edl17].

1.4 Discussion and conclusion

In analogy to optical interferometry, an electron two-path interferometer represents a powerful tool to probe the wave properties of electrons via the Aharonov–Bohm (AB) effect [Yac95]. The invention of multi-terminal electron interferometers [Sch97; AK05] allowed to demonstrate coherent transport phenomena such as tunnel-oscillations and quantum gate operations of flying charge qubits in the ballistic transport regime [Yam12]. Moreover, it enabled transmission phase measurements that could provide insights on the internal structure of quantum dot (QD) states [Sch97; Lee99; TB99; AK05] and quantum physical phenomena such as the Kondo effect [Zaf08; Tak14]. Electron transmission through a quantum dot is yet however not fully understood and due to their experimental difficulty, investigations in this field are rather rare.

Here we have experimentally investigated the long-standing question about a universal transmission phase behaviour that arose from the observation of phase lapses in pioneering experiments of electron two-path interferometry [Sch97]. For this purpose we employed a recently developed Mach–Zehnder (MZ) interferometer structure that prohibits multi-count contributions to the transmission phase from electrons that encircle the AB ring. Measuring the transmission phase along a large set of CBPs, we observed – in line with previous experimental investigations of a QD having similar dimensions – long sequences of phase lapses [Sch97]. Scanning the transmission phase along a larger set of successive resonances, however, we encountered several times the absence of such a phase lapse giving rise to a phase plateau. These cumulative regions of the transmission phase came along with an augmented amplitude of the AB oscillations as theoretically expected for a phase behaviour that depends on the parity sequence of the QD states [TB99; Lee99]. Deforming the quantum dot and varying the sweeping range of the magnetic flux density, we further demonstrated changes in the sequence of phase lapses and plateaus.

Let us now put our experimental results in the context of two theoretical works that addressed the question about a universal transmission phase behaviour in QDs. A truly universal transmission phase behaviour has been only predicted for the case where the coupling energy of the QD, Γ, is larger than the level spacing of the excited states, δ [Kar07]. In experiment such a regime is however difficult to achieve. So far, all experimental works, including ours, have been done in a regime where $\Gamma \sim \delta$ or $\Gamma < \delta$. For these conditions, which are typically encountered in experiment, another set of theory predicts on the other hand that for larger QDs longer sequences of phase lapses appear, while the probability of finding a phase plateau remains finite [Mol12; Jal14]. The characteristic parameter within this theory is the quantity $k_{\mathrm{F}}L$, where k_{F} is the Fermi wave vector and L is the QD length along the transmission direction. Deriving the expression $\mathcal{P} \propto 1/k_{\mathrm{F}}L$ they find that longer sequences of transmission phase lapses are more likely to occur

for a large QD assuming the presence of a chaotic transmission through the large QD.

Such a very small but finite probability for phase plateaus would be in congruency with our observation of transmission phase plateaus. Estimating k_F from the electron density and L from the gate separation taking into account the depletion length, we can estimate the quantity $k_F L \approx 50 \sim 60$ for the large QD that is realised in our experiment. Considering spin-less particles this theory predicts a probability of $\mathcal{P} \approx 35 \sim 55$ % in such a situation [Jal14]. Out of 13 conductance valleys we observe three transmission phase plateaus. From these numbers we can perform a rough, insignificant estimation of the probability for transmission phase plateaus giving $\mathcal{P} \approx 0.23$. We suspect that the deviation to the aforementioned theoretical estimation arises from spin-effects as discussed in section 1.1.3. For significant probabilistic statements, however, much larger data sets of independent transmission phase measurements are necessary.

To measure the transmission phase along a larger set of resonances, it will be necessary to enhance the measurement approach. The transmission phase shift is in principle also apparent when scanning the interference fringes via the geometrical instead of the magnetic AB phase. A geometric scan of the interference fringes via a side gate, could provide much faster measurements. Using a side gate to scan the interference fringes, it will be necessary to cross-check the transmission phase measurements with results obtained from B-field sweeps. Additionally, I suggest the development of an automatic tuning system of the interferometer configuration by means of variables that do not affect the QD structure – this could be the tunnel-barriers or side-gates of the reference branch. Such tuning functionality could be accomplished by a cost function assessing the magnitude of the anti-phase oscillations as discussed in section 1.2.3. Achieving faster and automatised measurements, it should be possible to scan the transmission phase along hundreds of resonances for large QDs of different size. Such statistical investigations could show if the probability for transmission phase plateaus indeed decreases reciprocally with the size of the QD [Mol12].

In conclusion, our experimental investigation of the transmission phase of a large quantum dot with a novel MZ-type electron interferometer provided several results that are characteristic for a parity-dependent phase behaviour. Our findings thus firmly establish that even for the case of a QD containing a few hundred electrons the absence of phase lapses is possible and show that the occurrence of phase lapses is not a universal feature as previously claimed. Transmission phase measurements serve as useful tool to characterise the properties of single QDs and more sophisticated quantum systems. We anticipate that the present interferometry experiment opens up a path for further studies on the transmission phase of QD and on other fundamental topics, such as correlated electron systems [Tho96; Bau13; Iqb13].

CHAPTER 2

Sound-driven single-electron transfer in a beam-splitter setup

Surface acoustic waves (SAWs) represent a promising platform to transmit quantum information via electrons in solid-state devices [For17; Bäu18]. Owing to the modulation of the shallow electric potential on a piezoelectric substrate, SAWs allow transfer of a single electron along several micrometer long channels between distant quantum dots [Her11; McN11]. Recently, also SAW driven transfer of spin polarisation has been shown [Ber16a]. These advances support the idea of a SAW-driven quantum circuit enabling the implementation of electron quantum optics experiments and quantum computation schemes at the single-particle level [BSR00; AS17]. The central building block of such a quantum circuit is a tunable beam-splitter permitting coupling and partitioning of single flying electrons. The experimental implementation of such a device, however, is still missing.

Here we investigate the implementation of such a beam-splitter device for a single electron that is conveyed by sound. In the course of our investigations we achieve important milestones to realise a SAW-driven platform with flying qubits[1]: Firstly, we demonstrate a transfer efficiency exceeding 99 % and partition an electron on-demand into the two quantum rails of our beam-splitter device. Performing quantum-mechanical simulations of the experimental results, we deliver insight into the quantum state of the SAW-transported electron. Secondly, we demonstrate a voltage pulse trigger enabling synchronisation of the sending process – a central requirement to couple a pair of flying electrons – and characterise transport along the single-electron circuit. We address moreover the observation of probability oscillations and discuss the feasibility of quantum logic gates for a SAW-transported flying qubit.

[1] Selected findings of our experimental and theoretical investigations were published under the title "Sound-driven single-electron transfer in a circuit of coupled quantum rails" in the journal Nature Communications [Tak19]. The present section thus contains contents of that paper.

2.1 Background[2]

Around the millennium, several theoretical works investigated the feasibility of a quantum computer in solid-state devices. In the course of these investigations, the transmission of quantum information was identified as central requirement to realise quantum quantum computation approaches [DiV00]. This aspect was developed further into the concept of a so-called flying qubit architecture where electrons are continuously displaced through a circuit of quantum rails [Ber00; IAU01; BSR00]. Recently, SAWs have been considered as potential candidate to link quantum information between stationary nodes of computation [Van17]. In this section we provide the theoretical foundation of such a SAW-driven quantum computing architecture with flying charge qubits. First, we describe the central set of quantum logic gates in such an architecture and discuss their feasibility and expected limitations. Having explained the theoretical concept of a SAW-driven flying qubit, we introduce step-by-step the building blocks allowing transfer of a single electron with a sound-wave.

2.1.1 A flying qubit defined by charge

Similar to a charge qubit in a stationary double QD, we define the flying charge qubit simply by the presence of an electron in one of two tunnel-coupled transport channels. Let us assume a coherently transported electron occupying the lowest eigenstate in a tunnel-coupled wire of two SAW-driven transport channels. Having a closer look on a cut of the electron potential perpendicular to the transport direction, we find a double-well potential as shown in Fig. 16a. As the tunnel barrier is increased, the lower two eigenstates in the tunnel-coupled wire come closer in energy forming a symmetric and an antisymmetric state with energy splitting, $\Delta E = E_\mathrm{A} - E_\mathrm{S}$.

With these symmetric and antisymmetric states one can construct a different basis with states having probability distribution of the electron only at the left

$$\psi_0 = \frac{1}{\sqrt{2}}(\psi_\mathrm{S} + \psi_\mathrm{A}) \tag{1}$$

or right part

$$\psi_1 = \frac{1}{\sqrt{2}}(\psi_\mathrm{S} - \psi_\mathrm{A}) \tag{2}$$

of the double-well potential. These states that define the two-level system of the flying charge qubit are schematically shown for comparison with the eigenstates ψ_S and ψ_A in Fig. 16b. In such a non-degenerate two-level system, Rabi

[2]The present section introducing the background on SAW-driven single-electron transport follows over a wide range the review articles of C.J.B. Ford [For17] and C. Bäuerle *et al.* [Bäu18].

oscillations occur with a periodicity related to the coupling energy, ΔE:

$$\Delta t = \frac{\pi \hbar}{\Delta E} \tag{3}$$

A short derivation of this relation is presented in appendix C.

As starting point for this introduction of a flying charge qubit, we assume fully adiabatic and coherent transport of a single electron along two parallel transport channels. Let us further imagine that these transport channels can be coupled by a tunnel barrier. The quantum state of an electron that is flying through such a system can be represented on a Bloch sphere:

$$|\Psi\rangle = \frac{1}{\sqrt{2}}\left(\cos(\frac{\theta}{2}) \, |0\rangle + \sin(\frac{\theta}{2}) \cdot \exp(i\varphi) \, |1\rangle \right) \tag{4}$$

A visualisation of the quantum state Ψ in this representation is shown in Fig. 16c. The tunnel-coupling defined by ΔE causes a rotation, θ, around the y-axis. This transition occurs on a time scale according to equation 3. Increasing the tunnel barrier, the transition times get longer. As the two quantum wells are completely decoupled, this polar rotation is suppressed and the state vector rotates only azimuthal around the Bloch sphere according to the geometrical phase difference, φ, along the two paths of transportation.

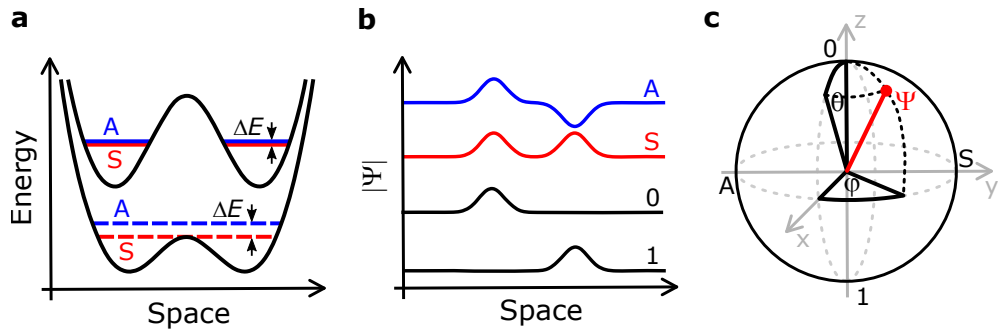

Figure 16: Definition of a flying charge qubit. Schematics showing the two-level system that constitutes the flying charge qubit. **(a)** Double-well potential for low and high tunnel barrier. The horizontal lines indicate the energies of the lowest two eigenstates with symmetric (S) and antisymmetric (A) wave function. **(b)** Amplitude of the wave functions of the two-level system represented in the eigenbasis (S and A) or in the basis of the transport channels (0 and 1). **(c)** Representation of a flying qubit state on a Bloch-sphere. The quantum state is defined by the angles θ and ϕ, which depend on the tunnel coupling and the evolution of the electron wave vector along the two transport channels. The presented potentials and eigenstates qualitatively are adapted from the thesis of T. Bautze [Bau14a] for the current purpose of presentation.

2.1.2 Quantum logic gates for flying qubits

Having introduced the definition of a flying charge qubit, let us now focus on two concepts for quantum logic gates allowing the modification of the mixing and the phase of the superpostion state, Ψ. The basic building block for these gates is the aforementioned tunable beam splitter. This device can be realised by a tunnel-coupled region of quantum rails as schematically shown in Fig. 17a. Two rails carrying the quantum information are coupled by a tunnel barrier (T) along a coupling region (C). As an electron is sent through the structure, there is a certain probability that the particle tunnels from one quantum rail into the other. The tunnel coupling causes a mixing represented via the polar angle θ on the Bloch sphere. Tuning the tunnel barrier of the beam splitter such that a 50-50 superposition is achieved, we project $|\Psi\rangle$ on the equatorial orbit of the Bloch sphere, if the electron was initially located in the electron state $|0\rangle$ or $|1\rangle$. This situation represented by $\Delta\theta = \pi/2$ is shown in Fig. 17b. Here the flying charge qubit that is defined on a track of two quantum rails exhibits a so-called Hadamard gate operation.

To affect the azimuthal phase, φ, of the flying qubit state $|\Psi\rangle$ in the Bloch sphere representation, a MZ-type interferometry setup can be employed. For this purpose we arrange two Hadamard gates ($\Delta\theta = \pi/2$) in a row as shown in Fig. 17c. In such a setup we can affect φ via the geometrical phase difference and the AB phase[3]. The discussed situation is similar to the ballistic electron interferometry experiments that we presented in chapter 1. Here we consider however single-shot transfer of a solitary electron. The geometrical path difference is controllable via the voltage on a side gate (G). To change φ, we can alternatively affect the AB phase via the magnetic flux density, B, in the AB ring which is defined by the two branches that are enclosed by the tunnel-coupled regions. In this interferometer setup, the final flying qubit state sensitively depends on the phase shift, $\Delta\varphi$. For $\Delta\varphi = 0$ the flying electron exhibits solely two $\Delta\theta = \pi/2$ rotations leading to a final projection on $|1\rangle$ for an initial flying electron state $|0\rangle$. As we increase $\Delta\varphi$, the projection on the charge qubit basis ($|0\rangle$ and $|1\rangle$) evolves as indicated by the horizontal red arrow in Fig. 17d. For $\Delta\varphi = \pi$ the flying qubit is projected back on its initial state as shown in Fig. 17e.

It is worthy to mention at this point also a two-qubit quantum logic gate: the controlled phase shifter [Bäu18]. This device completes the single qubit gates to a set of universal quantum gates meaning that any unitary quantum operation can be expressed as a sequence of gates from this set [IAU01]. Figure 18a shows the concept of the device. The idea is to couple two MZ-type electron interferometers with an additional barrier (CC) that is sufficiently high such that tunnel coupling is completely suppressed. At the same time, the barrier must be

[3]See equation 1 on page 31.

sufficiently narrow such that two synchronously propagating electrons experience their respective Coulomb potential when they trespass this Coulomb-coupling region.

Here two quantum rails form respectively one track for a flying charge qubit that are indicated as A or B. The input states for the controlled phase shifter are determined by the initial states of A and B and the configuration of the barriers T1 and T3. The value of these input states determines now if an additional phase shift of φ is imposed on the two flying qubits via Coulomb interaction. Expressing the functionality of this Coulomb-coupler device in the product basis of these two tracks, we obtain a matrix as shown in Fig. 18b. The states of the A⊗B two-qubit basis are written beside the matrix with additional schematic indication of the presence of the two electrons (red bars) in the four channels. As the probability to send the two electrons simultaneously through the CC region is sufficiently high, the flying qubits experience the additional phase shift of φ. This event corresponds to the $|10\rangle$ state. As the flying qubits enter the tunnel-coupling regions, T2 and T4, this phase shift affects the projections on 0 and 1

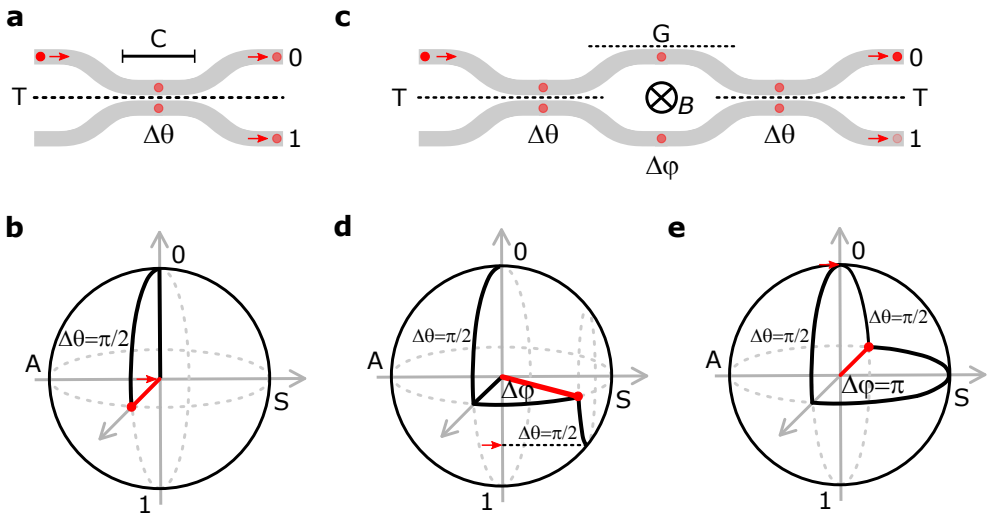

Figure 17: Quantum logic gate concepts for flying charge qubits. (a) Beam-splitter for single flying qubits realised by coupling two quantum rails (0 and 1) via a tunnel barrier (T) along a coupling region (C). **(b)** Effect of the Hadamard gate operation on an initial flying qubit state $|0\rangle$ represented on a Bloch sphere. The horizontal red arrow indicates the projection of the final state after the quantum logic operation. **(c)** MZ-type electron interferometer with side gate (G) and magnetic flux density, B, to tune the flying qubit phase φ **(d)** Effect of the phase shift, $\Delta\varphi$ on the final flying qubit state. **(e)** Back projection on the initial flying qubit state for $\Delta\varphi = \pi$.

according to the respective barrier heights (T1-T4) and the phase shifts along the two interferometer structures (φ_A and φ_B). The particular setting of the tunnel-couplings T1, T2, T3 and T4 and the phase shifts φ_A and φ_B determines thus the specific functionality of the device.

To point out how this SAW-driven two-qubit device works, let us discuss two specific examples starting with the aforementioned controlled phase shifter. In this particular example we exploit the state of one flying qubit to control weather a phase shift operation is performed on the charge state in the other track or not. Let us choose track A as control qubit. Doing so, we have to tune the qubit rotation of T1 and T2 to a multiple of 2π such that charge qubit A remains unaffected as it flies along the structure. For simplicity we assume that $\phi_A = \phi_B = 0$. Tuning the qubit rotation of T3 and T4 to $\pi/2$, the charge state in track B experiences a phase shift, φ, that is triggered by the state of qubit A. The extent of φ is determined by the strength and duration of Coulomb interaction.

Another fascinating application of this device addresses the generation of maximal entangled flying qubit states – so-called Bell states. To achieve such a state, all of the tunnel barriers (T1, T2, T3 and T4) act as Hadamard gates ($\Delta\theta = \pi/2$). The phase shift imposed by Coulomb interaction is now π. With this setup the input states are back-projected as discussed in the aforementioned single-qubit phase shifter – see Fig. 17e. The particularity of this setup is now that qubit A is maximally entangled with qubit B, if the input state is $|10\rangle$. This means that an additional gate operation after entanglement on qubit A will instantaneously

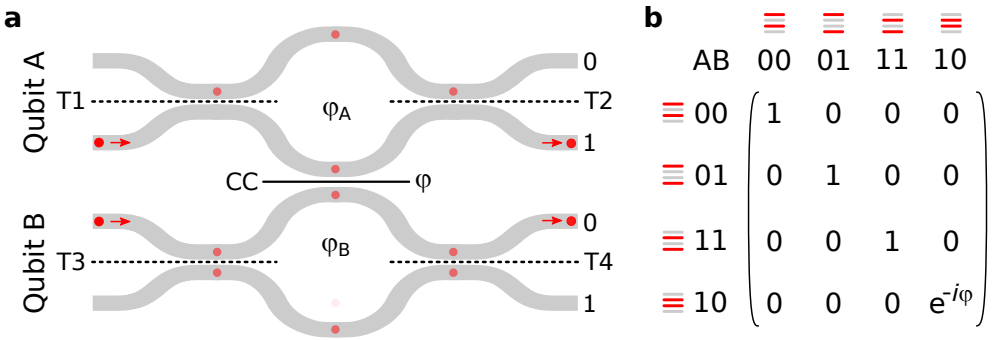

Figure 18: Concept of a quantum logic gate for two flying qubits. (a) Coupling two MZ-type electron interferometers via an additional Coulomb-coupling region (CC) a controlled phase shifter is formed. The Coulomb interaction of the electrons synchronously flying through the CC-region imposes a phase shift, φ, on the two charge qubits A and B. **(b)** Representation of the two-qubit gate operation as matrix in the two-qubit basis. The physical representation of states forming the two-qubit basis is additionally indicated via the red (electron) and grey (no electron) lines representing the presence of an electron in the four quantum rails of the two tracks.

affect qubit B.

These examples show the potential of quantum-optics like experiments with electrons in solid-state devices. The challenge is now to perform such quantum logic operations in a controllable way at the single particle level. The experimental realisation of such a system requires the achievement of the following points:

1. Efficient source of a single flying electron
2. Efficient receiver/detector of a single flying electron
3. Tunnel-coupled quantum rails serving as beam-splitter
4. Synchronised electron transport along parallel tracks
5. Adiabatic transport in a two-level system
6. Coherence length sufficient to execute quantum logic operations

There is so far no platform that fulfils all of these points. The QDs employed in SAW-driven single-electron transport, however, provide a very efficient single-electron source and receiver. As a result of highly-efficient electron transfer along the surface surface gate defined quantum rails, one should be able to guide the SAW-transported electron also through more complicated structures such as tunnel-coupled regions without perturbing the flying qubit state. The crucial questions are now if SAW-driven single-electron transport can be performed adiabatically in a true two-level system and if the coherence time of the flying charge qubits is sufficiently long.

2.1.3 Decoherence of a flying charge qubit

A charge qubit undergoes population- and phase-relaxation due to interaction of the electron with its environment. The central decoherence mechanisms root from electron-scattering, charge noise, electrical noise in the surface gates and electron-phonon interaction [FHH04]. The decoherence of a charge qubit is characterised in analogy to spin-qubits via the relaxation times T_1, T_2^* and T_2. For the sake of completeness let us quickly review the measurement procedures to obtain these quantities for the envisioned flying charge qubit. To measure the population relaxation time, T_1, for a spin-qubit, one typically performs a $\Delta\theta = \pi$ pulse and reads out the charge state after a certain waiting time. For a flying charge qubit, the propagation time is however fixed. From this perspective, such an approach is not feasible. Instead one can however just gradually change the coupling time as depicted in Fig. 19. Due to population relaxation, it will not be possible to perform full projections on the eigenstates of the qubit basis as

the coupling time increases. Such a measurement might be however additionally affected via the geometric and magnetic phase evolution along the two paths. The actual outcome of such a measurement would thus provide a lower bound of the population relaxation time, T_1.

To measure the phase relaxation of a qubit state one typically performs a Ramsey interferometry experiment as schematically shown in Fig. 20. In this type of experiment first a $\Delta\theta = \pi/2$ pulse is performed to project the qubit state on the equatorial orbit of the Bloch sphere. Waiting for a certain time in this state, phase decoherence takes place that affects a subsequent projection on the complementary qubit state via second $\Delta\theta = \pi/2$ pulse. Performing such an experiment for different waiting times between the two pulses, one can deduce the

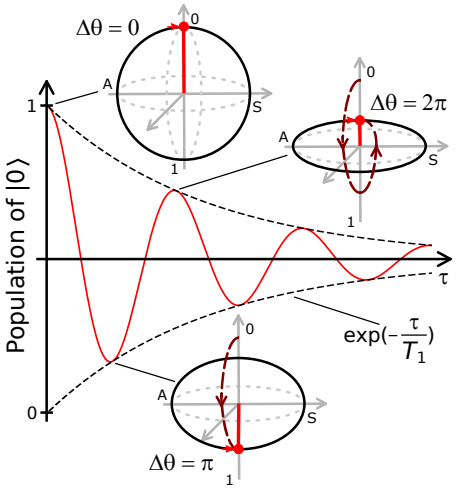

Figure 19: Schematic showing process of population relaxation for a flying charge qubit. Turning on the tunnel coupling for a certain time, τ, the flying qubit undergoes Rabi oscillations between in the two-level system of eigenstates. Due to population relaxation, the Rabi oscillations show an exponential decay. The time constant related to this decay, T_1, can be used to characterise the population relaxation process of the flying charge qubit.

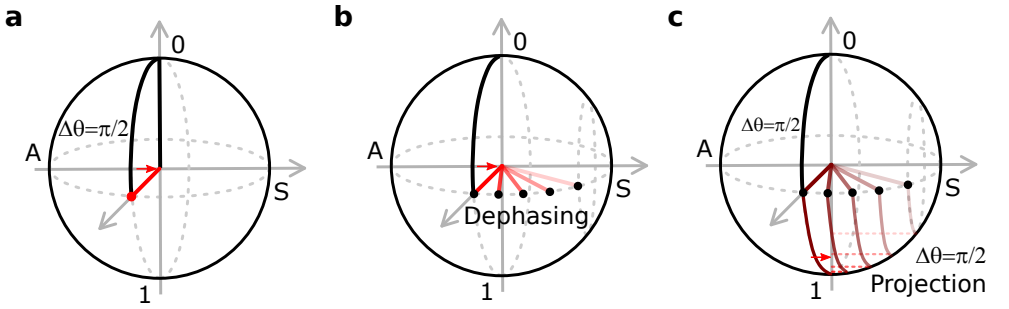

Figure 20: Schematic showing the pulse sequence of for Ramsey interference. (a) A $\Delta\theta = \pi/2$ pulse brings the charge qubit in on the equatorial orbit of the Bloch sphere. **(b)** Phase relaxation processes cause dephasing for a certain waiting time. **(c)** A second $\Delta\theta = \pi/2$ pulse projects the qubit on eigenstate that is complementary to the initial value. The extent of the projection is mitigated depending of the strength of phase relaxation. It exponentially decays with a characteristic time, T_2^*.

extent of dephasing and characterise the relaxation time T_2^* via the exponential decay of the projection.

Phase decoherence can be corrected to a certain extent by applying a so-called Hahn echo [Hah50]. Figure 21 shows a schematic of the approach. As in the aforementioned T_2^* measurement, here a $\Delta\theta = \pi/2$ pulse is performed to project the qubit state on the equatorial orbit. After waiting for a certain duration $\tau/2$, however, a $\Delta\theta = \pi$ pulse is additionally applied to bring the dephased state on the other hemisphere in the Bloch sphere representation. Waiting now again for a duration $\tau/2$, the dephasing occurs in the opposite direction (an echo) what causes to a certain extent a refocussing on the original state. Performing another $\Delta\theta = \pi/2$ pulse, the refocussed state is projected back on the initial state of the experiment. Increasing the waiting time, τ, of this experiment, the dephasing occurs now slower than in the aforementioned Ramsey interference experiment. Analysing the exponential decay of the projection back on the initial state, one can quantify the corrected phase relaxation time, T_2.

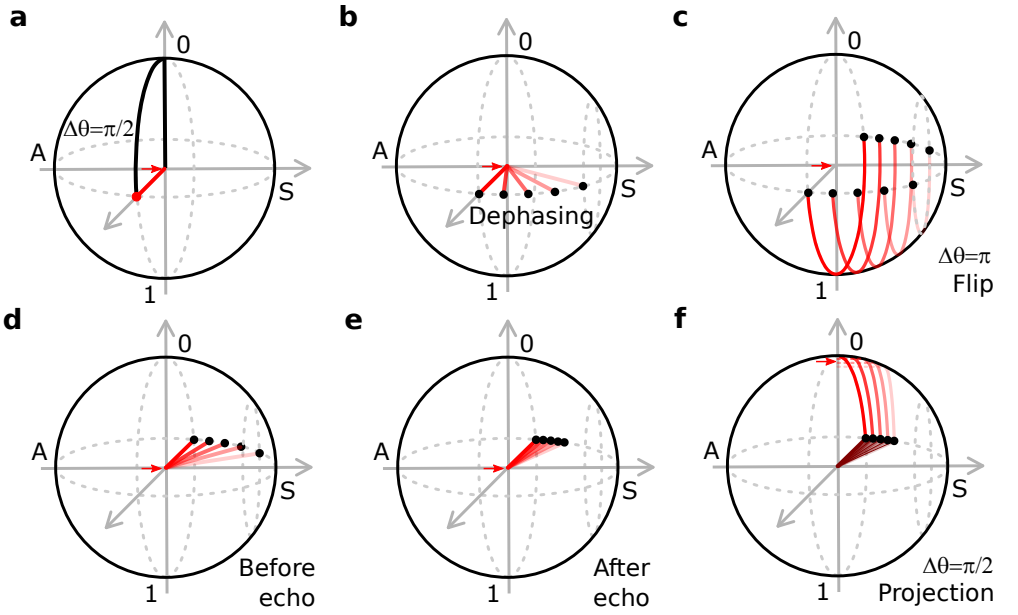

Figure 21: Schematic showing the pulse sequence of for Ramsey interference with Hahn echo. (a) A $\Delta\theta = \pi/2$ pulse brings the charge qubit in on the equatorial orbit of the Bloch sphere. **(b)** Phase relaxation processes cause dephasing for a certain waiting time, $\tau/2$. **(c)** To obtain the Hahn echo a $\Delta\theta = \pi$ is used to flip the states on the Bloch sphere. **(d,e)** Waiting again for the time τ_2, the qubit state is refocussed to a certain extent on the evolution of the original state. **(f)** Performing a second $\Delta\theta = \pi/2$ pulse, the refocussed state is projected back on the original state. Performing the pulse sequence for different waiting times, $\tau/2$, the exponential decay of this back-projection can be characterised by the phase relaxation time T_2.

To assess coherence in such solid-state implementations, let us mention at this point the stationary counterpart to the investigated flying qubit structure that is a charge qubit in a double QD [Hay03; Pet04; Pet10; Sto17]. In later experimental investigations of such a system, a phase relaxation time (T_2) of several nanoseconds was observed what is in the order of the population or charge relaxation time (T_1). Charge relaxation was thus assumed as central mechanism limiting coherence [Pet10]. In piezoelectric host materials such as GaAs, electron-phonon coupling was suspected as major origin of charge relaxation processes [Sto17]. Since the SAW velocity typically is in the order of μm/ns, we can expect that charge coherence in principle can be maintained for SAW-driven single-electron transport over several micrometers. Let us consider a specific example: In a GaAs/AlGaAs heterostructure the typical SAW-velocity is about 2.7 μm/ns. Assuming a coherence time of 10 ns – based on the experimental findings from stationary double QDs – we thus obtain a coherence length of 27 μm for a SAW-transported electron. Electron interferometer structures as schematically shown in Fig. 17c are typically realized with state-of-the-art electron beam lithography machines below that length scale [Bau14b; Tak16; Tak17; Edl17]. The demonstration of the aforementioned quantum gate operations should be thus feasible with SAWs as medium of electron transport.

2.1.4 Surface acoustic waves

Surface acoustic waves (SAWs) are sound waves that propagate along the surface of any elastic material. First studies on these transverse sound waves were performed by John W. S. Rayleigh in the 19th century. Accordingly, SAWs are often referred to as Rayleigh waves. A typical example of a SAW is a water wave. Different than Love waves (named after Augustus E. H. Love), that only have transverse strain components with respect to the propagation direction, SAWs have also a longitudinal component causing an elliptical motion of the displaced atoms. Figure 22 schematically shows a snap-shot of this SAW-introduced displacement of atoms near to the surface of a crystal. The extent of the strain decays in the bulk ($-z$ direction) over a length scale that corresponds to the wavelength of the SAW. The time-dependent profile of a SAW can be electrically detected in piezoelectric materials by a fork-like structure of surface electrodes. The cross-section of surface gates of such a detector is schematically indicated in Fig. 22. The signal is detected on the central electrode that is connected to a fast oscilloscope, whereas the outer fingers are connected to ground potential. The strain modulation of the SAW creates surface charges via the piezoelectric effect leading to a time-dependent electrical potential on the central surface electrode. The magnitude of this electrical signal now directly reflects the SAW amplitude. To obtain the original SAW profile one has to deconvolve the measured amplified signal with a function that is determined by the detector geometry.

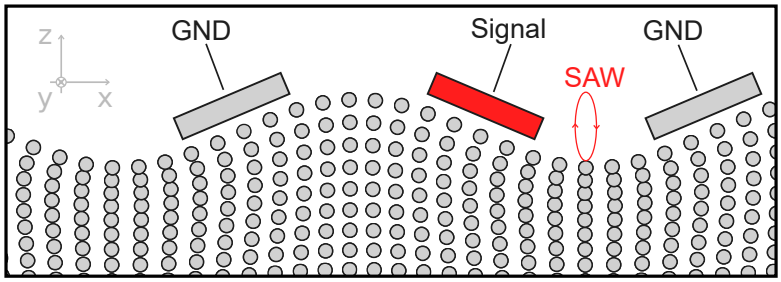

Figure 22: Schematic showing surface acoustic wave and cross-section of surface electrodes. The schematic shows the displacement of atoms introduced by a surface acoustic wave (SAW). The amplitude of the wave is strongly exaggerated. The SAW introduces a strain field that displaces the atoms on an elliptic orbit. The rectangles on the surface indicate surface electrodes of an interdigital transducer (IDT). Depending on the geometry of this IDT, one can perform a time-dependent measurement of the SAW profile via the piezoelectric effect or generate a SAW that propagates along the surface via the inverse piezoelectric effect. The figure is adapted from the PhD thesis of Tobias Bautze [Bau14a] for the current purpose of presentation.

The inverse piezoelectric effect can now be exploited in a similar way for the generation of a SAW. To transduce an electrical signal into a SAW, typically a set of interdigitated surface electrodes is used that resembles two interlocked combs [Cam89]. Applying an alternating voltage signal between the two interlocked surface electrodes of such an interdigital transducer (IDT), elementary strain waves are introduced below each IDT finger. Hitting the resonance frequency of this device with the applied RF signal, these elementary waves constructively add up and form a SAW propagating through the material. The design of the IDT fingers is now the key to efficiently couple the RF signal into a SAW. The dimensions of the employed IDT geometry determine the efficiency and frequency range of of the electro-acoustic transduction. Also the electrical properties of the IDT play an important role for the efficiency of SAW transduction.

The main application of IDTs is found in modern mobile telephones. Dozens of IDTs can be found in fact in the current generation of smartphones for instance. In this commercial field, IDTs are mainly employed as sensors, delay lines, pulse-compression filters or band-pass filters [Mor10]. IDTs and SAWs are also in the focus of current research. Examples of applications are acousto-electric current generation in graphene [Lio17] or enhanced coherent photon scattering from single-photon sources based on semiconductor QDs [Vil17]. SAWs are also employed to study the physics of novel materials such as graphene [Lio17; Fan18]. And recently, it was shown that SAWs could have interesting applications in quantum information processing with superconducting qubits [Man17; And18]. Owing to this zoo of applications, there is an enormous amount of IDT designs available. In the following we highlight two IDT designs – single finger and double

finger IDTs – that were previously employed for charge transport in a piezoelectric semiconductor heterostructure [Her11; McN11; Ber16a]. Schematics of these IDT designs are shown in Fig. 23.

The geometrically simplest form of a SAW source is an IDT with single interlocked fingers as shown in Fig. 23a. For the purpose of SAW generation, this simple design is however not optimal. Since the single fingers are aligned with a spacing coinciding with the wave nodes, this IDT also strongly acts as a SAW cavity. This property makes the device suffering from internal reflections diminishing the amplitude of the transduced SAW. One strategy to reduce these internal reflections is a double-finger design as shown in Fig. 23b. The arrangement of the fingers is chosen such that the elementary waves of one comb-shaped IDT electrode show less overlap with the SAW nodes. This arrangement of IDT fingers allows now to mitigate internal reflections. Avoiding a Bragg-mirror-like structure one can strongly enhancee the amplitude of the transduced SAW signal.

Figure 24a shows an experimental setup to measure the time-dependent SAW-profile for an IDT that consists out of 111 interlocked double-fingers having a periodicity of 1 μm. The detector is a broadband IDT that consists only out of three interlocked double fingers having again a periodicity of 1 μm. The central double finger is used to measure the signal, whereas the outer fingers are connected to ground potential. Applying a resonant RF signal on the IDT, a SAW is launched along the surface of the piezoelectric GaAs crystal. Additionally to the SAW, however, evanescent electromagnetic (EM) waves propagate along the device when the RF signal is applied on the IDT. Since these modes travel with the speed of light, they arrive much earlier at the detector IDT what allows to clearly distinguish them from the acoustic wave. Figure 24b shows the amplified signal that is measured that the detector. One can clearly see the parts corresponding to the evanescent EM waves and the SAW. When employing IDTs to transfer charge carriers in a piezoelectric heterostructure, it is necessary to prohibit the propagation of these evanescent EM waves. The suppression of these EM modes can be achieved by grounded metal shields surrounding the SAW propagation path[4].

The length and amplitude of this SAW train depends now on the duration of the RF signal and the length of the IDT itself. The travelling time of the first elementary strain wave from the outer left part of the outer right part is $T_{\mathrm{IDT}} = L/v_{\mathrm{SAW}}$ where L is the length of the IDT and v_{SAW} is the speed of the SAW. For the presently discussed IDT that is realised on a GaAs substrate we obtain $T_{\mathrm{IDT}} = 40$ ns. Applying a resonant RF signal with the frequency $f_{\mathrm{SAW}} = v_{\mathrm{SAW}}/\lambda$, the elementary strain waves constructively interfere what gradually increases the amplitude of the SAW train until the saturation time T_{IDT}. Figure 24c shows measurements of the SAW profile for three resonant RF signals on the IDT having

[4] A particular implementation of these shields will be presented in section 2.2.1.

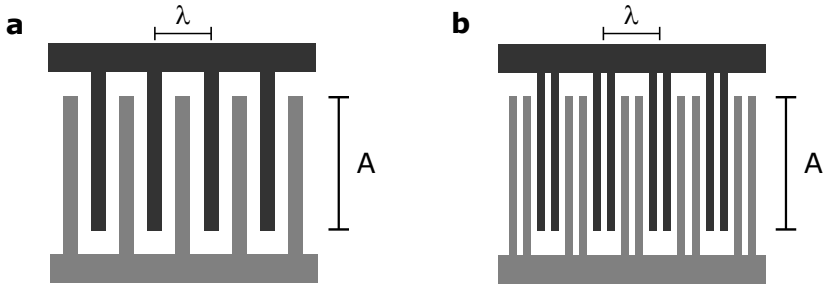

Figure 23: Exemplary set of interdigital transducers. Shown are the schematic geometries of the surface electrodes of an interdigital transducer (IDT) having **(a)** single fingers and **(b)** double fingers with indications of the wavelength, λ, and the aperture, A. The split surface electrodes of the double finger IDT allows that the nodes of the transduced SAW show less overlap with the positions of potential modulation introduced by the RF signal.

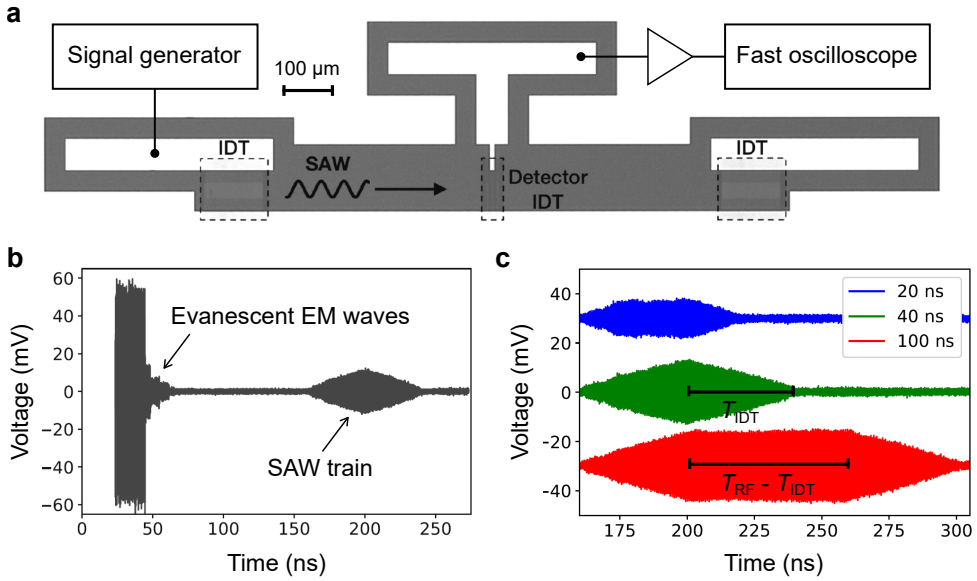

Figure 24: Time-dependent measurement of SAW profile. **(a)** Experimental setup to perform a time-dependent measurement of the SAW profile. Shown is an optical microscopy image of the IDT and fork-like double-finger detector with schematic indications of the of the employed signal generator, voltage amplifier and fast oscilloscope. **(b)** Time dependent measurement of the SAW profile with contributions from the evanescent electromagnetic (EM) crosstalk at times below 70 ns. **(c)** Time dependent measurement of the SAW profiles for different durations of the RF signal, $T_{\mathrm{RF}} \in \{20\ \mathrm{ns}, 40\ \mathrm{ns}, 100\ \mathrm{ns}\}$, that is applied on the IDT. The presented data stems from Junliang Wang [Wan18] and is adapted for the current purpose of presentation.

a duration T_{RF} of 20 ns (blue), 40 ns (green) and 100 ns (red). For a shorter RF signal one does not exploit the full capacity of the device and a plateau occurs in the SAW-profile until T_{IDT}. This can be nicely seen in the exemplary trace for 20-ns-long resonant RF signal (blue). Since the duration of the RF signal is shorter than T_{IDT}, the SAW amplitude saturates already after 20 ns (T_{RF}). The saturation persists until the total length of the SAW train reaches 40 ns (T_{IDT}). Subsequently, the SAW linearly decays over a duration of 20 ns (T_{RF}). If the duration of the RF signal matches, the travelling time of a strain wave along the IDT ($T_{\mathrm{RF}} = T_{\mathrm{IDT}}$), the SAW profile follows a diamond shape just reaching the maximal possible amplitude. In the presently discussed example this situation corresponds to the 40-ns-long RF signal (green). Sending an even longer RF signal – for instance 100 ns (red) – the amplitude starts to saturate after 40 ns. Having a RF signal, T_{RF}, that is longer than T_{IDT}, one generally obtains a trapezoidal SAW profile having a total length of $T_{\mathrm{RF}} + T_{\mathrm{IDT}}$ and a plateau of saturated SAW amplitude along a duration of $T_{\mathrm{RF}} - T_{\mathrm{IDT}}$. This shows that the shape of a SAW can be well predicted to a certain extent from the IDT geometry and the employed RF signal.

The amplitude of the generated SAW scales now with the length of the IDT, T_{IDT}, and the aperture, A. To feed the IDT with a strong electric signal, it is however also necessary to reduce possible reflections from the signal generator along the transmission line to the interdigitated surface electrodes. Since the transmission lines are typically designed with a 50 Ω impedance, it is necessary to match the impedance of all additional components to this value [Lac10]. The most critical parts are typically the bonding wires to the chip and the impedance of the IDT itself. One simple approach to reduce the bottleneck at the bonding wires is to put many parallel connections to the IDT electrodes. Only increasing T_{IDT} and A one will also create an impedance mismatch that effectively reduces the efficiency of SAW transduction. To bypass this problem one can engineer tank circuits, transmission lines or a proper geometry of the IDT fingers and bonding pads and wires.

2.1.5 Continuous acoustically driven single-electron transfer

As a starting point, let us discuss how one can use a continuously applied surface acoustic wave (SAW) to transfer single electrons through well defined depleted channels. The strain oscillation of a SAW forms a periodic potential modulation in a piezoelectric material [WW57]. In a high mobility heterostructure such as GaAs/AlGaAs, this SAW-introduced potential wave can displace charge carriers in the 2DEG [WKW86]. Implementing a quantum point contact (QPC) via two opposing surface electrodes that are polarised with a sufficiently negative voltage, one can form a narrow depleted potential constriction through which by default

no charge carriers can flow. As one continuously sends a SAW through such a QPC structure, however, the dynamic potential modulation of the sound wave allows to drag electrons from one side of the Fermi sea over the depleted channel to the other side [Shi96].

In such a setup, the dynamic potential resembles a train of moving QDs that is formed by the SAW propagating along the QPC. Such a SAW train is schematically shown in Fig. 25a. Pinching-off such a QPC via a negative voltage on these surface electrodes, the current characteristic shows quantised plateaus at multiples of $e \cdot f$, where f is the frequency of the SAW. At the flattest part of such a quantised conductance plateau, a single electron is transported on average in each moving QD of the SAW [Tal97]. This situation is schematically shown in Fig. 25b. The SAW-driven quantisation of current through a QPC was discussed as interesting candidate for the implementation of future standard for currents below 1 nA [Pek13]. To use the quantisation of SAW-driven electron transport for a quantum standard of current, it will be however necessary to measure the current with a relative uncertainty smaller than 10^{-7} at a

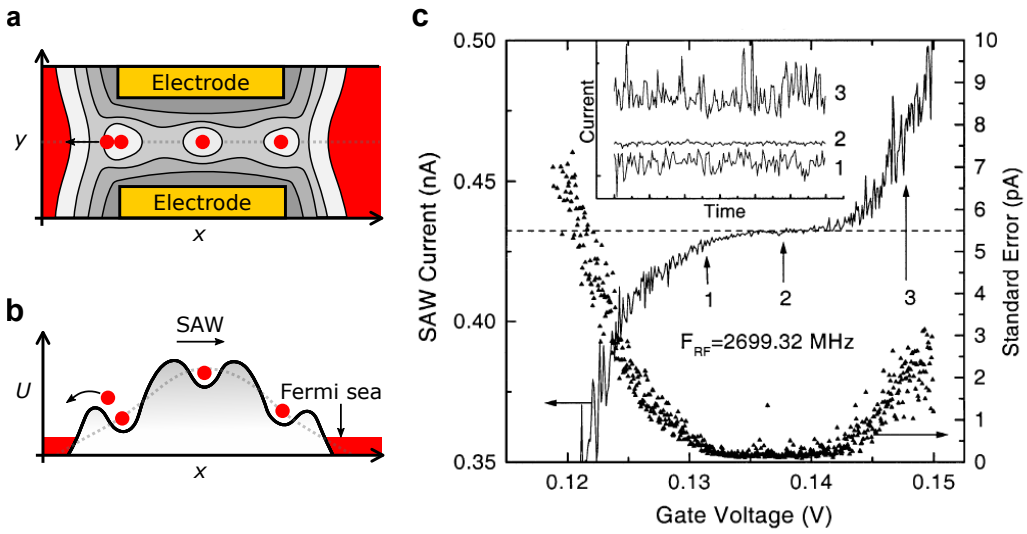

Figure 25: Continuously SAW-driven single-electron transport through a depleted one-dimensional channel. **(a)** Schematic of the potential landscape (greyscale) with SAW modulation along the transport channel that is defined by the potential of two surface electrodes forming a quantum point contact (QPC). The red region indicates the Fermi sea. A red dot indicates an electron. **(b)** Schematic cut of the electron potential, U, along the quasi-one-dimensional channel. The dashed line indicates the potential landscape without SAW modulation. **(c)** Quantised conductance plateau of SAW-driven single-electron transport through a QPC. Reprinted from Janssen and Hartland [JH00] with permission from Elsevier.

preferably large conductance plateau that is very robust against the variation of experimental parameters. The so far highest relative accuracy that was reported for the measurement of a SAW-driven quantised current plateau is $5 \cdot 10^{-6}$ at a current of about 0.5 nA [JH00]. Figure 25c shows original data from that work. The major limitation to increase the accuracy of the SAW-driven single-electron pump is tunnelling of electrons within the train of moving quantum dots (QDs) that is formed by the SAW within the transport channel. In this hindsight, the recently developed SAW-generation technique using higher harmonics of split 52 IDTs [Sch15; Nys17], represents a promising candidate to enhance the visibility of acoustoelectric quantised conductance plateaus further. We will address this SAW generation technique in more detail in section 2.5.1.

Employing continuous SAW-driven single-electron transport, quantum phenomena of single SAW-transported electrons have been already demonstrated in the past. Kataoka *et al.* [Kat09] succeeded to show tunnel-oscillations of a continuous stream of single-SAW transported electrons into an electron reservoir that was coupled to the quantum rail by a narrow potential barrier. Due to the continuous measurement principle of such an experiment, it is however relatively difficult to study the behaviour of the single-propagating electrons in more detail. It is therefore also from this perspective an appealing idea to perform SAW-driven charge transport in single-shot experiments where an electron in transferred by a finite SAW train. In the following we describe the central tool – a surface-gate defined quantum dot – allowing to achieve this type of single-shot experiments.

2.1.6 Single-electron detection in a quantum dot

The possibility to transport a single electron on-demand between gate defined quantum dots (QDs) is a central requirement for the implementation of quantum logic gates for flying electron qubits that are defined by charge or spin. In order to achieve such single-shot experiments with SAWs as transport medium, a surface-gate defined QD is placed at each end of the transport channel. Figure 26a shows a schematic of a QD that is coupled to a quantum rail. Such a QD geometry can serve now as a source or receiver of a single electron that is transferred on-demand with a SAW burst. The steep potential barriers of these QDs prohibit the transfer of charge carriers from the Fermi see even when a SAW is propagating along the device.

To trace the presence of an electron in a QD, typically a QPC is employed as very sensitive electrometer [Fie93]. Placing such a QPC next to the QD as shown in Fig. 26, one can sense a single electron entering or leaving the QD. The QPC is a narrow conductive transport channel in which only a few discrete conductance modes contribute to transport. The bias voltage applied between the two ohmic contacts of the QPC is typically below 1 mV. As one sweeps the voltage V_{QPC}

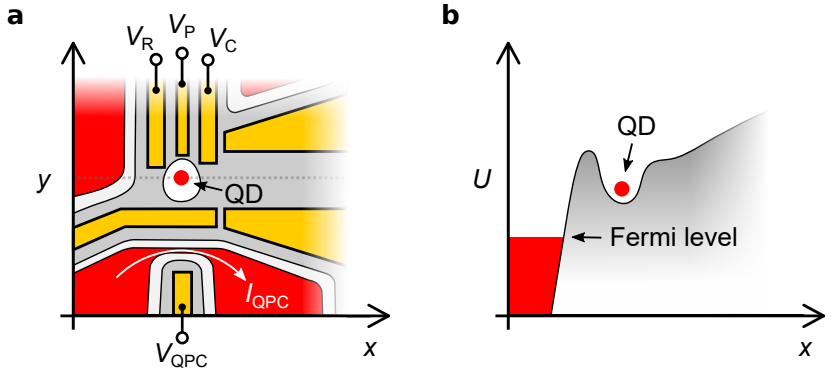

Figure 26: Geometry of a quantum dot with charge sensor. **(a)** Schematic of the two-dimensional potential landscape (greyscale) showing the quantum dot (QD) with close-by quantum point contact (QPC). A red dot indicates an electron that is loaded into the QD. The QD can be controlled via the voltages on the reservoir gate, V_R, the plunger gate, V_P, and the coupling gate to the transport channel, V_C. The presence of the electron within the QD is traced via discrete jumps in the QPC current, I_{QPC}. **(b)** Schematic cut of the electron potential, U, along the quantum dot. The red region indicates the Fermi sea.

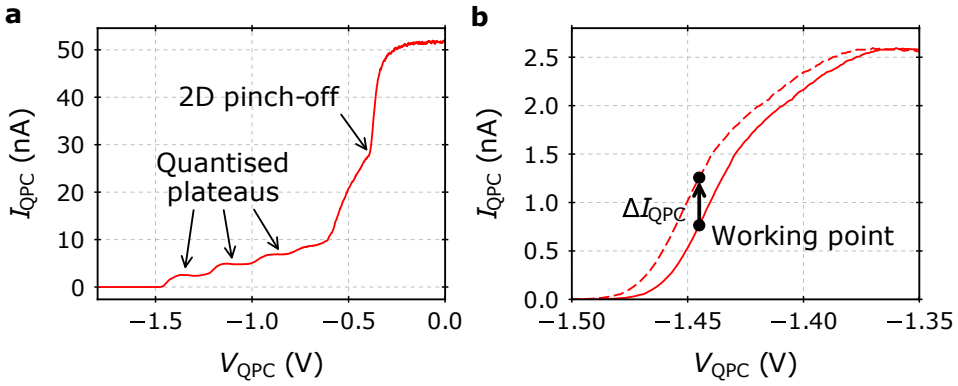

Figure 27: Exemplary pinch-off characteristic of a quantum point contact. **(a)** Pinch-off characteristic of the quantum point contact (QPC). Measurement of the the QPC current as function of gate voltage, V_{QPC}. The data shows the 2D pinch-off transition and quantised current plateaus. **(b)** Zoom in the region of the first quantised current plateau. A slight potential change close to the QPC causes a shift of the pinch-off characteristic. Setting the working point of the QPC at the steepest slope of the current characteristic, small charge fluctuation can be sensed such as an electron that is loaded into a close-by quantum dot (QD).

applied on the QPC, one obtains a characteristic pinch-off curve of the current as shown in Fig. 27a. At small negative values of V_{QPC}, the electron gas undergoes the so-called two-dimensional pinch-off transition, where the 2DEG in the constriction region is transformed in a quasi-one-dimensional channel. Making V_{QPC} more and more negative, conductance plateaus appear that correspond to the remaining quantised transport modes in the channel. The abrupt transitions between these plateaus can now be used to sense the presence of an electron in the neighbouring QD[5]. Figure 27b shows the shift of the pinch-off characteristic for a small potential fluctuation in the vicinity of the QPC. At a sensitive working point of the QPC, a single-electron that enters (or leaves) a close-by QD causes a jump in the QPC current, ΔI_{QPC}, that is typically a fraction of a nanoampère. Due to this sensitivity one can easily trace the charge state of a QD via the current passing through a QPC which is located a few hundred nanometers beside the dot with state-of-the-art current amplifiers.

To control the QD, it is typically sufficient to perform a fast sequence of voltage movements on the surface gates that define the coupling to the reservoir (V_{R}) and the transport channel (V_{C}). With such a sequence of voltage movements in V_{R} and V_{C} one can empty the QD, load an electron into the QD or isolate a single electron as schematically shown in Fig. 26b. To find proper voltage configurations for these operations one typically investigates so-called stability diagrams. Figure 28a shows an example of such a stability diagram for the presently discussed QD structure with a slice of the data to visualise the discrete jumps in I_{QPC} that are introduced by electrons entering the QD. Tracing I_{QPC} as one varies V_{R} and V_{C}, one observes abrupt jumps on top of a gradual change in current that is caused by additional electrostatic changes of the QPC potential by the voltage movements on the surface gates. To clearly show charge transitions in the QD, therefore, one typically plots the derivative of I_{QPC} with respect to V_{R} for a two-dimensional scan of the voltages V_{R} and V_{C} – see Fig. 28b. The distinct lines in the stability diagram indicate changes in the charge occupancy of the QD.

Let us now discuss what these lines indicate and why they fade out in the stability diagram as we make V_{R} more negative. Fixing the reservoir gate voltage, V_{R}, at a relatively positive voltage such as -0.8 V, one can couple the QD to the Fermi sea and load a discrete number of electrons in the dot simply by a changing the voltage on the coupling gate to the channel, V_{C}. For more negative voltages of V_{R} the coupling to the Fermi sea is reduced what is indicated by a fade-out of charge degeneracy lines in the stability diagram. In this region the charge transitions are no longer visible since the electrons are well isolated by the depleted potential landscape well above the Fermi see. In Fig. 26b we showed already a schematic

[5] As alternative to a QPC, one can employ Coulomb blockade peaks (CBP) in a QD to sense the charge occupation of another QD. The slopes of the CBPs are typically steeper what provides better charge sensitivity.

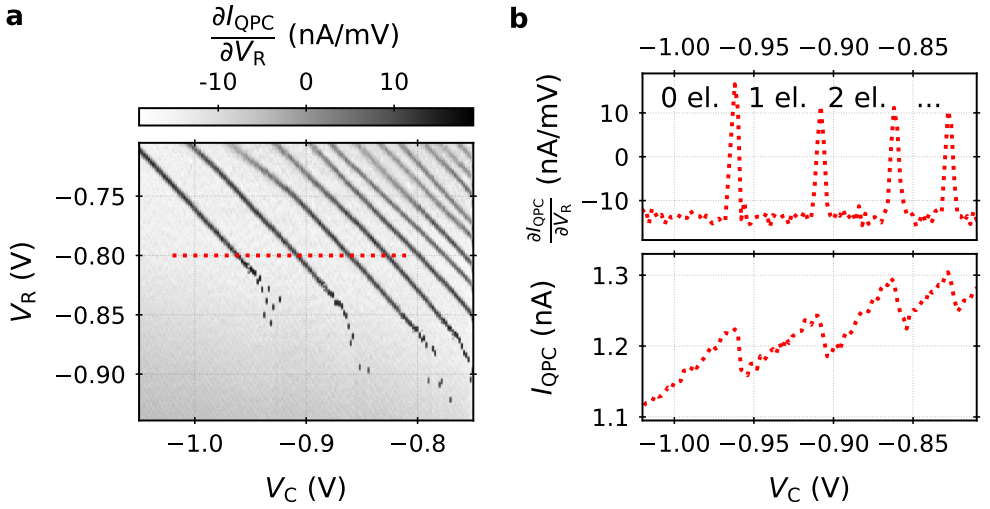

Figure 28: Charge stability diagram of a quantum dot. (a) The data shows the derivative of I_{QPC} with respect to V_{R} for a two-dimensional scan of the voltages on the reservoir gate, V_{R}, and the coupling gate to the channel, V_{C}. **(b)** Slice of the data showing the distinct peaks with indications of the corresponding QD occupation with electrons. In the lower part also the raw data of I_{QPC} is shown.

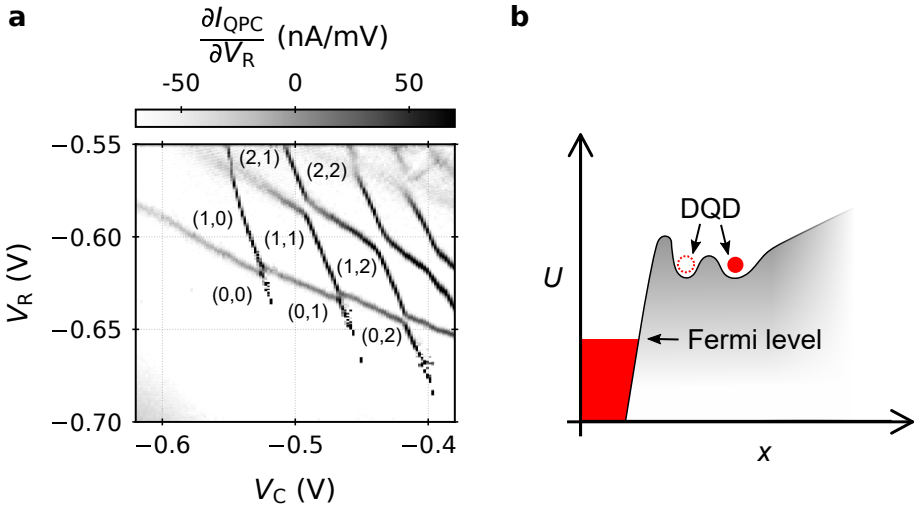

Figure 29: Charge stability diagram of a double quantum dot. (a) The data indicates charge degeneracy lines for different electron configurations within a double quantum dot (DQD). **(b)** Schematic of the electric potential, U, along the direction of the transfer channel. The DQD is formed by an additional potential minimum at the end of the transfer channel.

of this situation. As one changes in such a metastable position V_C to more negative values, one can transfer the electrons that are trapped in the isolated QD one-after-another back to the Fermi sea. Since the potential of the QD is above the Fermi level, loading is not possible in this metastable region. By the measurement of a stability diagram, we can therefore clearly identify the different voltage configuration regions for loading, isolation and initialisation, which allow us to control the QD.

With the presently employed QD structure it is also possible to form a double QD (DQD) with an additional QD formed at the end of the transfer channel. One encounters in such a situation a stability diagram as shown in Fig. 29a. In such a diagram one can clearly identify the charge configuration in two QDs that are located close to the reservoir and the transport channel. Here we indicate the charges via a tuple (N_R, N_C) where N_R and N_C indicates the number of electrons in the respective QDs. The schematic shown in Fig. 29b shows the metastable charge configuration (0,1). The reason for the formation of such a DQD behaviour in the presently discussed geometry of surface electrodes is the potential barrier that is formed by the gate that controls the coupling to the transport channel. Having such a DQD behaviour one can also control the spin states of a pair of electrons [Han07].

2.1.7 Sound-driven single-shot electron transfer

Having described the formation of a QD via a specific geometry of surface electrodes, let us now quickly sum up the procedure to transfer a single-electron from one QD with a SAW to another distant QD. A more detailed description of the precise voltage movements on the QD gates will be provided at a later point in section 2.2.4. Let us consider a device geometry as sketched in Fig. 30a. Using surface electrodes on top of a GaAs/AlGaAs heterostructure, we form a depleted transport channel whose ends are respectively equipped with surface-gate defined QDs serving as source and receiver of a single electron. To trace the number of electrons in the QDs, we employ a QPCs as charge sensor as discussed in section 2.1.6. Such a device structure has been successfully employed in pioneering experiments [Her11; McN11] to demonstrate SAW-driven single-shot electron transfer between distant QDs.

To perform single-shot transfer of an electron, the SAW is not applied continuously, but along a finite time window that is typically in the order of tens of nanoseconds. Compared to continuous SAW-driven electron transport, there is therefore much less heating that is introduced by phonons what allows the usage of higher SAW amplitude. At the beginning of a single-shot-transfer experiment there is thus no SAW present. During that time, all QDs are first emptied. After this initialisation process, a single electron is loaded via controlled voltage move-

ments on the respective surface gates into the source QD as shown in Fig. 30b. In this loading process, the potential of the source QD is lowered such that a single electron can tunnel from the Fermi sea into the QD. Raising the QD potential back above the Fermi level the electron remains in the QD as shown in Fig. 30c. In this metastable configuration that we introduced in section 2.1.6 the electron is completely isolated by the stationary potential landscape that is formed by the surface gates. The electron is then brought in a sending configuration, where the electron is still well isolated, but where a SAW train can easily pick up the particle. Launching a SAW train in this configuration, the electron is trapped by a certain moving QD that is formed via the potential modulation wave in the transfer channel. The propagating SAW train then transports the electron along the depleted transport channel as shown in Fig. 30d. Setting the voltage configuration of the receiver QD in a proper catching configuration as shown in Fig. 30e, the flying electron is finally trapped at the end of the transport channel.

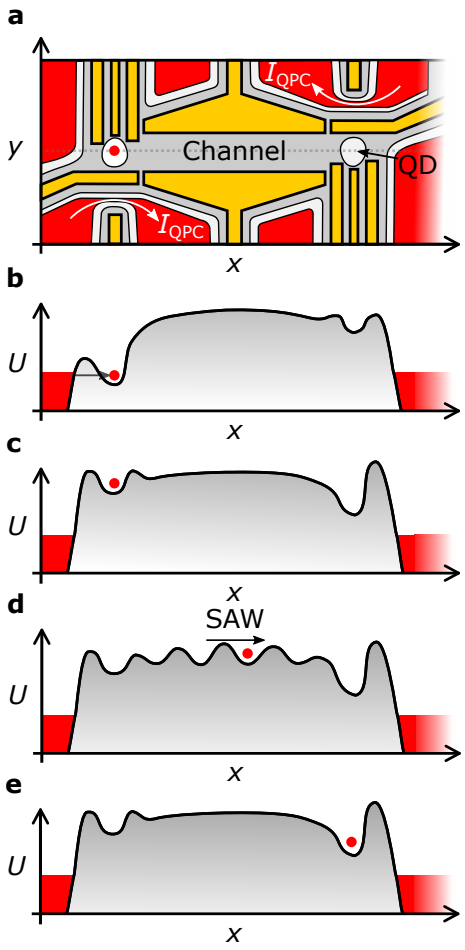

Figure 30: Schematics showing SAW-driven transport of an electron. **(a)** Depleted potential landscape (grey regions) without SAW modulation along the transport channel. The red region indicates the Fermi sea. A red dot indicates an electron that is loaded in the source quantum dot (QD). The receiver QD is empty. Next to each QD a quantum point contact (QPC) is placed to sense the presence of an electron. **(b)** Cut of the electron potential, U, along the quasi-one-dimensional channel for the situation when a single electron is loaded from the Fermi sea into the stationary source QD. **(c)** After loading, the electron is brought in an isolated configuration far above the Fermi sea. **(d)** Sending a finite SAW train, the electron is transferred with the first sufficiently strong wave period along the depleted channel. **(e)** Having the receiver QD in a catching configuration, the electron gets trapped when the SAW train passed by the device.

With this measurement approach, pioneering experiments already showed that SAW-driven single-electron transfer can be performed with an efficiency of about 92 % [Her11]. Sending a single electron back and forth along a 4 μm transport channel, a single electron was transported along a cumulative distance of 0.25 mm [McN11]. The QD structure in the sample geometries that were employed in these experiments also allowed the formation of a double QD as introduced before in section 2.1.6. Exploiting this behaviour for the preparation and readout of spin states, further SAW-driven transfer of spin information has been demonstrated along such a quantum rail [Ber16a]. Also the injection mechanism from the stationary QD into the moving train of QDs that is formed by the SAW along the transport channel was studied in experiment [Ber16b]. It was found that the injection process is characterized by an activation law with a sending threshold depending on the SAW amplitude and the dot-channel potential gradient. If the potential between the quantum dot and the transport channel is to steep, an initially loaded electron cannot escape the stationary QD or is dragged back in the injection part of the transport channel when a SAW train passes by. The design of the surface gates and the corresponding set of applied voltages, hence, play a crucial role for efficient transport.

2.2 The single-electron beam splitter

Let us now focus on a more complex SAW-driven single-electron circuit which we experimentally investigate in the second part of this thesis. If coherent electron transport is maintained over a sufficiently large distance, SAWs could be employed to demonstrate MZ- and HOM-type interference with single flying electrons in a highly controllable way. Enabling the manipulation of a quantum state of a flying electron, these experiments could be furthermore used to demonstrate quantum mechanical phenomena such as spatial entanglement of flying electrons as introduced in section 2.1.2. Achieving these goals, SAW-driven single-electron transport could find interesting applications for quantum computation approaches in solid-state devices. The central building block for the realisation of such SAW-driven single-electron circuits is a tunable beam splitter [IAU01; BSR00; Bäu18]. Inspired by the success of electron interferometry experiments in the ballistic transport regime [Liu98; Oli99; Hen99] and first tunnel-coupling experiments with continuous SAW-transport of single electrons [Kat09], we decided to implement such a beam-splitter device for a SAW-transported electron by coupling two quantum rails via a surface-gate defined tunnel barrier.

Figure 31a shows a schematic of this SAW-diven single-electron beam splitter. The device is realised via the electric potential that is induced by surface electrodes in a Si-δ-doped GaAs/AlGaAs heterostructure. The single-electron circuit consists out of two surface-gate defined quantum rails that are bent towards a tunnel-coupled region. A very narrow surface gate forms a tunnel barrier allowing the coupling of a flying electron between the two quantum rails. The ends of each quantum rail are respectively equipped with surface-gate defined QDs serving as source or receiver of a single electron as introduced in section 2.1.6. To transfer an electron in this circuit of quantum rails from one QD to the other, we use a finite SAW train, which is launched from an IDT that is placed beside the nanostructure.

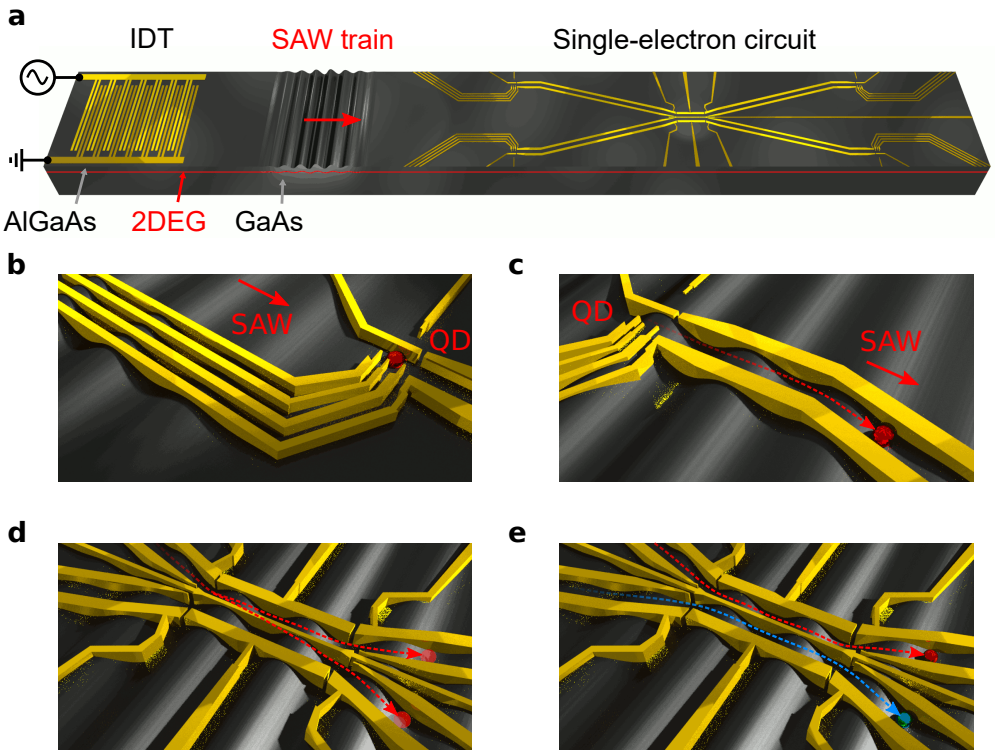

Figure 31: Schematics showing the SAW-driven single-electron circuit and with possible applications. **(a)** Schematic showing a cut of the GaAs/AlGaAs chip with the interdigital transducer (IDT) launching a SAW train towards the single-electron circuit. **(b)** Image of the source QD structure just before the arrival of the SAW train. An electron is prepared for transfer. **(c)** Source QD structure after the SAW picked up the initially loaded electron. In reality the electron is located in the quantum well below the surface. **(d)** Region of the tunnel-coupled quantum rails with a SAW-transported electron getting partitioned in flight between the two transport paths. **(e)** Image of the tunnel-coupled region for the scenario of two flying electrons that interact in flight.

After loading an electron at the source QD, we launch a SAW train from the IDT to transfer the electron along the quantum rail. A sketch of this process is schematically shown in Fig. 31b and Fig. 31c[6]. The electron is then transferred with a certain SAW minimum along the injection path to the tunnel-coupled region. Tuning the voltage on the tunnel-barrier electrode, it is in principle possible to partition or couple on-demand single flying electrons in such a beam-splitter setup. Setting the tunnel barrier sufficiently low, the wave function of the electron can be partitioned between the two quantum rails as schematically shown in Fig. 31d. If the electron was adiabatically transported in the lowest eigenstates of the potential and if the coherence length of such a SAW-transported electron is sufficiently long, one can use this partitioning to prepare a flying charge qubit state where the electron is in a superposition of being in the upper and lower quantum rail. Such a state represents the basis for two-path interference experiments as discussed in section 1. Investigating interferometer structures of different size[7], one can characterise the coherence length for a SAW-transported electron.

To perform HOM interference or to entangle flying charge qubits, it is necessary to couple a pair of SAW-transported electrons in such a beam-splitter setup. Figure 31e shows a sketch of two SAW-transported electrons that interact as they fly by the tunnel-coupled region. Here an electron is initially loaded respectively at each of the two source QDs of the single-electron circuit. For HOM interference it is important that the tunnel-barrier is sufficiently low such that the overlap of the respective electron wave functions is large enough for Pauli repulsion. To entangle two flying qubits such a strong coupling is on the other hand not necessary, since the mere presence of Coulomb potential stemming from the control qubit is sufficient to cause a geometrical phase shift of the quantum state. The coherence length must span however over several beam-splitter entities to make the effect of charge entanglement observable.

To make the pair of flying electrons interact, it is essential that the particles are synchronously transferred with a SAW train along the circuit of transport channels. The pair of electrons must be therefore simultaneously sent from the respective stationary source QDs into a specific position of the SAW train and the electrons must additionally remain in this specific moving QD as they propagate along the tunnel-coupled circuit of quantum rails to the receiver QD. To achieve this requirement for the coupling of single flying qubits, it is necessary that the sending process is triggered by a certain mechanism. Furthermore, the potential landscape along the transport channels must be sufficiently smooth such that the

[6] For simplicity we show here the electron above the surface. The amplitude of the SAW is strongly exaggerated. In reality the electron is located in a depleted region in the 2DEG of the GaAs/AlGaAs heterostructure.

[7] Compare measurement of the coherence length in the quantum Hall regime with MZ-type electron interferometers [Rou08].

electron stays at its location within the SAW train. Achieving these requirements for synchronisation of SAW-driven transport, one can experimentally investigate the repulsive interaction of a flying pair of electrons.

In this chapter we will investigate the feasibility of such a beam-splitter setup for SAW-driven single-electron transport in experiment. In the following sections, we present a first implementation of such a SAW-driven single-electron circuit. We begin by introducing the central parts of the device and the experimental setup for SAW transduction and synchronised control of picosecond pulses. We then describe in more detail the procedure to transfer a single electron with a SAW in such a beam-splitter setup by means of measurements that are performed on the implemented device.

2.2.1 Experimental setup

We realise the SAW-driven beam splitter for a flying electron via surface electrodes forming a depleted potential landscape in the two-dimensional electron gas (2DEG) of a GaAs/AlGaAs heterostructure. Figure 32a shows a SEM image of the single-electron circuit. The 2DEG is located at the GaAs/AlGaAs interface 100 nm below the surface and has an electron density of $n \approx 2.7 \times 10^{11}$ cm^{-2} and a mobility of $\mu \approx 10^6$ cm^{2}V^{-1}s^{-1}. The wafer (# 13734) was provided by Prof. A. D. Wieck from the Ruhr-University Bochum in Germany. It is introduced by a Si-δ-doped layer that is located 55 nm below the surface. All components are realised by Ti/Au electrodes (Ti: 5 nm; Au: 20 nm) that are written by electron-beam lithography on the surface of the wafer. The presently investigated sample was fabricated by Shintaro Takada [Tak19]. The device consists out of two quantum rails, which are coupled along a region of 2 μm by a 20-nm-wide tunnel-barrier electrode. Applying a set of negative voltages on the surface electrodes, different than in chapter 1, we completely deplete the 2DEG along the quantum rail.

The ends of each quantum rail are respectively equipped with surface-gate defined QDs, which we use to send and catch a SAW-transported electron as introduced in sections 2.1.6 and 2.1.7. Figure 32b shows a scanning-electron-microscopy (SEM) image of a source QD with schematic description of the electrical connections. The bias and pinch-off voltages, V_B and V_Q, of the sensor QPCs are tuned for maximum visibility of charge transitions in the respective QD. Achieving a sufficiently sensitive working point, we are able to clearly detect an electron leaving or entering the QD via a jump in QPC-current, I_QPC. To measure, I_QPC, we employ a current amplification circuit as schematically indicated in the upper part of Fig. 32b. The SAW-driven single-shot transfer experiments were typically performed with a amplification factor of 10^8. To send the electron in a specific position of the SAW train, we employ a voltage-pulse trigger. The voltage pulse

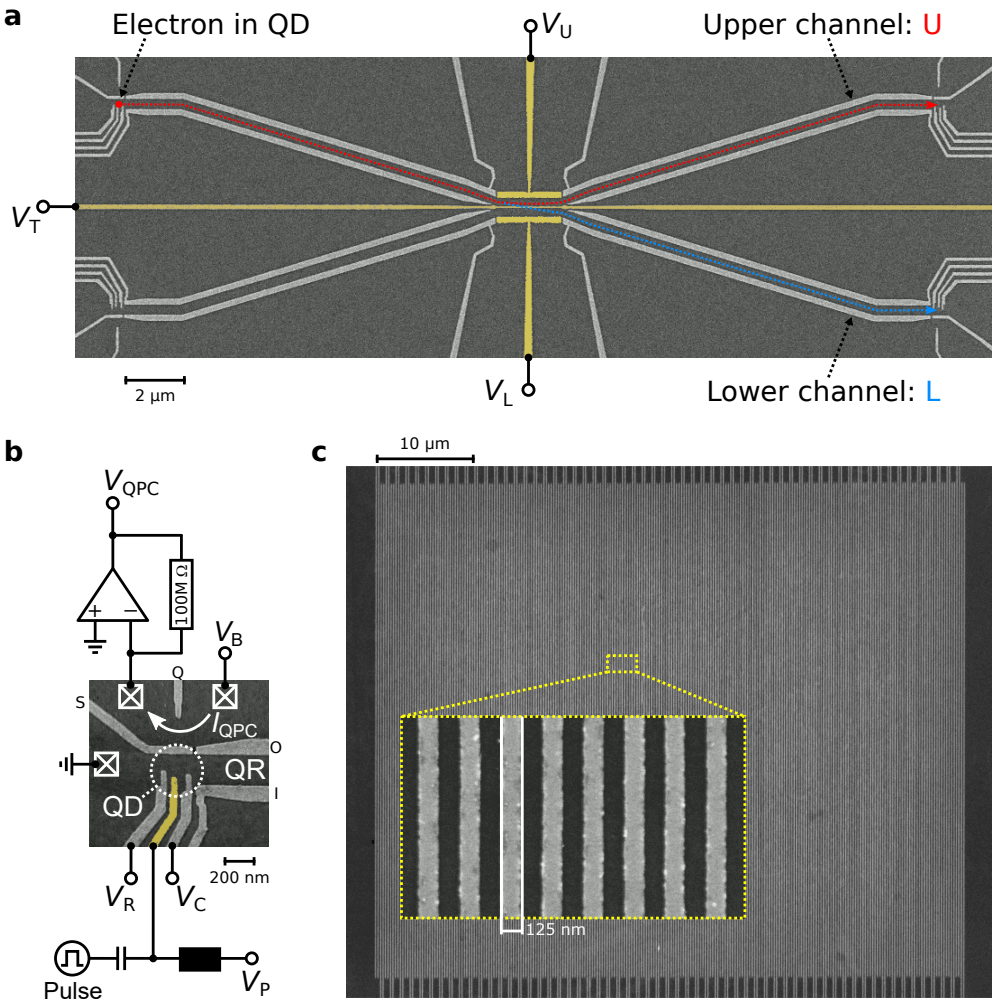

Figure 32: Experimental setup of the SAW-driven single-electron circuit. **(a)** SEM image of the SAW-driven single-electron circuit. An electron loaded at the upper source QD can be sent with a SAW through the circuit of quantum rails as indicated by the red and blue dashed lines. The flying electron can end up at the upper (U) or lower (L) receiver QD. **(b)** SEM image showing the upper source quantum dot (QD), coupled to the quantum rail (QR). Electrical connections to the ohmic contacts of the 2DEG are schematically indicated. The QPC-current, I_{QPC}, is used to trace the presence of an electron in the QD. It is measured via the voltage $V_{\mathrm{QPC}} \approx 100\,\mathrm{M\Omega} \cdot I_{\mathrm{QPC}}$ through a current amplifier circuit. The electron reservoir of the QD (left) is connected to ground. Using a bias tee we can couple a fast voltage pulse on the potential $(e \cdot V_{\mathrm{P}})$ of the plunger gate – highlighted in yellow. **(c)** SEM image of the 125 nm wide double fingers of the employed IDT structure. The inset shows a zoom on eight IDT fingers.

is sent from an arbitrary waveform generator of the type "Tektronix AWG7122b" through a bias tee on the plunger gate of the QD structure. The bias tees must provide a proper bandwidth for pulse transmission. Here we have employed bias tees of the type "Anritsu K250" and "SHF BT45".

The source of the finite SAW trains is placed on a grounded island of 2DEG outside of the central mesa – at a distance of about 1.6 mm beside our beam-splitter nanostructure. To reduce internal reflections, we employ a double-finger interdigital transducer (IDT) for SAW generation as introduced in section 2.1.4. A SAW train that is launched from the IDT allows to transport a single electron from one gate-defined QD along the circuit of tunnel-coupled quantum rails to one of the receiver QDs. The IDT consists out of 120 interdigitated double-fingers with a finger-spacing and -width of 125 nm leading to a SAW wavelength of $\lambda = 1$ μm. A SEM image of the IDT fingers is shown in Fig. 32d. The inset shows the IDT fingers in more detail. The aperture of the IDT is 50 μm.

We operate the device with a pulse modulated, sinusoidal voltage signal oscillating with a frequency, f_{SAW}, for resonant SAW generation. The power on the signal generator was set to 25 dBm. The RF signal for the IDT is attenuated by 6 dB at the 1 K stage and by 3 dB on the cold plate (at about 50 mK) of the ^{3}He/^{4}He dilution refrigerator setup. Additionally, there is about 3 dB attenuation of the IDT signal along the bonding wire that electrically connects the pad of chip carrier to the interdigitated surface electrode. To choose proper values for the resonance frequency f_{SAW} and and the length of the SAW train, we investigate sending experiments with a single electron that we loaded at the source QD. Figure 33 shows an example of such a sending measurement. To synchronize the employed signal generators in the present setup, it is important that the SAW frequency is a multiple of the 10 MHz clock frequency. We will address this point in more detail when introducing the pulsing setup in section 2.2.3. The exact value of f_{SAW} can

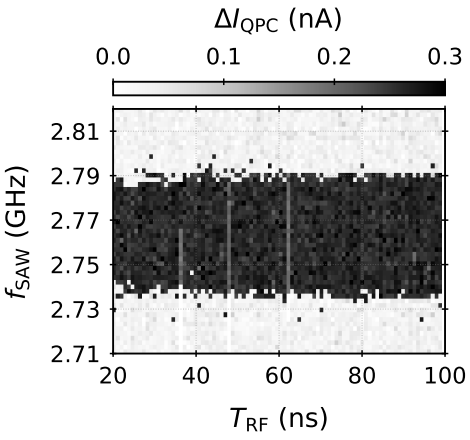

Figure 33: Investigation of the RF signal for resonant SAW transduction. Here we initially load an electron at the source QD and investigate the success of the SAW-driven sending process into the transfer channel for varying frequency of the RF signal, f_{SAW}, and duration, T_{RF}. The plot shows the jump in QPC current at the source QD, ΔI_{QPC}, after sending a surface acoustic wave (SAW). A black pixel indicates successful sending event.

actually vary over a certain range. Sweeping f_{SAW} we observe a clear window where we can send the electron. Here we have chosen the resonance frequency to be $f_{\mathrm{SAW}} = 2.77$ GHz. The propagation time of an elementary strain wave along the IDT is thus $T_{\mathrm{IDT}} \approx 21.7$ ns. In all of the present experiments the duration of each oscillation pulse on the IDT was set to $T_{\mathrm{RF}} = 30$ ns. Such a oscillation pulse causes a SAW train of about 143 μm length with a trapezoidal amplitude profile having a saturated maximum amplitude for about 8 ns in the center of the wave.

The experiments are performed at a temperature of about 10 mK using a ^{3}He/^{4}He dilution refrigerator. The electrical connections of the presently investigated SAW-driven single-electron circuit includes 38 DC lines and 4 RF lines. One RF line is used to transmit the resonant voltage oscillation signal on the IDT. The other three RF lines are used to couple a fast voltage pulse from an AWG into the electric potential on the plunger gates of the two source QDs and the upper receiver QD. The experimental setup was once adapted to perform also pulsing experiments at the lower receiver QD. A detailed list of the voltages that were applied on the surface gates of the investigated sample is provided in appendix F with information on the electrical connections on the chip carrier and additional notes on the conducted experiment.

2.2.2 Shielding of evanescent electromagnetic waves

From the RF signal that is applied on the interlocked electrodes of an IDT only a fraction is transduced into a SAW. Having an impedance mismatch between the RF connection and the IDT, a part of the RF signal is reflected back along the RF line. Another typically non-negligible part of the RF signal couples capacitively via an evanescent electromagnetic (EM) field to the 2DEG. This evanescent EM wave leads to a parasitic current that was already discussed in previous works [FSS11; Bau14a]. As in pioneering experiments on SAW-driven single-electron transport [Her11], we suppress the propagation of these evanescent EM waves from the IDT via metal shields. We place these shields fully around the propagation path of the SAW and connect them electrically to the ground potential. This approach allows to reduce propagation of evanescent EM waves. To achieve a strong effect, the shields must be placed sufficiently close to the IDT. The distance of the the grounded metal shields to the IDT should be smaller than the distance of the IDT to the closest surface electrode belonging to the single-electron circuit.

When performing SAW-driven charge transport experiments, typically two grounded metal shields are placed as shown in Fig. 34. A large copper shield is placed on top of the chip-carrier. This top-shield (TS) is mounted on the cold-finger (CF) in the dilution refrigerator setup as shown in Fig. 34a and Fig. 34b. Counterbor-

ing the chip in the chip carrier (CC), TS has approximately the same distance to the surface of the chip as to the ground-plane of the chip carrier. For the measurements performed in the course of the present thesis, this distance was about 0.5 mm. Due to the small spacing between TS and CC, the bonding wires of the electrical connections to the chip need to be very flat. To verify that no bonds touch to ground, the impedance of each electrical connection is carefully checked before each cool-down at room temperature and 4 K.

We place a second set of metal shields directly on the GaAs/AlGaAs heterostructure as shown in appendix F. These on-chip shields (CS) are deposited on the surface with the deposition steps of ohmic contacts and the surface gates defined by laser lithography steps. CS consist out of an annealed NiGeAu alloy covered with TiAu. CS is grounded via bonding wires connecting to CC. They are placed such that the whole area beside the propagation path of the SAW is covered. In commercially available SAW filters crosstalk between the IDTs is typically strongly reduced by a proper grounding setup of the RF setup [EPC12]. Crosstalk can be mitigated by a common ground of the employed IDTs. Here we connect thus one of the IDT electrodes respectively to a common ground via CS. Additionally, we place each IDT on an island of 2DEG that is connected also to ground potential via ohmic contacts established also by CS.

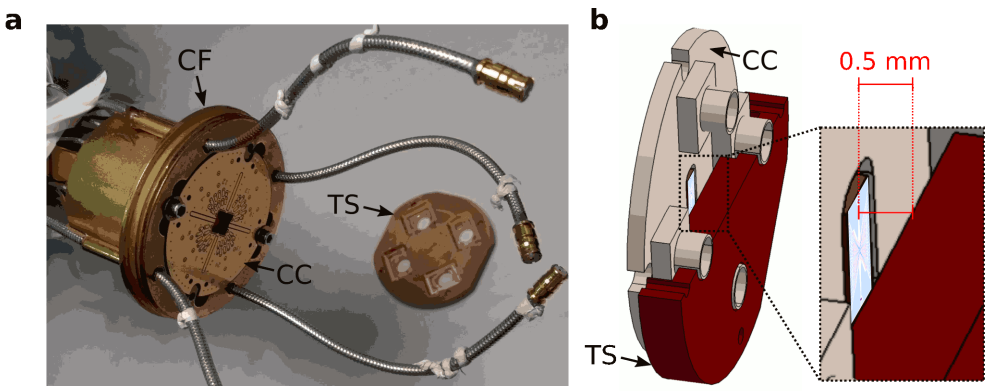

Figure 34: Arrangement of grounded metal shields to avoid the propagation of evanescent electromagnetic (EM) waves from an interdigital transducer (IDT). (a) Picture of the so-called cold-finger (CF) carrying the chip-carrier (CC) and the top-shield (TS) that is mounted on CC. **(b)** Schematic showing TS mounted on CC. TS is cut here to expose the position of the chip (center). The final distance of the the chip to TS is about 0.5 mm as indicated in the zoom. The figures stem from the thesis of T. Bautze [Bau14a] and are modified for the present purpose of presentation.

2.2.3 Setup for transmission of picosecond voltage pulses

To reliably repeat SAW-driven single-electron-transport experiments with ultrafast voltage pulses, it is essential that the pulse and signal generators are properly set up. Here we aim to use an ultrafast voltage pulse particularly to send a single-electron within a specific SAW minimum. Thus, we have to verify that the jitter of the fast voltage pulse with respect to the IDT signal is much smaller than a SAW period – that is about 360 ps in the current experiment. To verify this requirement, a sufficiently fast oscilloscope must be employed to test the setup of signal and pulse generators.

The experimental setup of the devices that are used for our pulsing experiments is shown in Fig. 35a. Basically two devices are employed: Firstly, we use a signal generator of the type "Rhode & Schwarz SMA100A" to send pulse modulated voltage oscillations to the IDT for SAW generation. Secondly, a fast pulse generator of the type "Tektronix AWG7122b" allows to send voltage pulses that are controllable on the picosecond scale. As reference oscillator of the signal generator (REF IN) we use the precise clock of the fast pulse generator (via the REF OUT connector). This clock provides a stable frequency of $f_{\mathrm{Clock}} = 10$ MHz. To achieve a RF setup that does not dephase, the frequency on the signal generator, f_{SAW}, needs to be set to an integer factor of this clock frequency. In other words, $f_{\mathrm{SAW}}/f_{\mathrm{Clock}}$ must be an integer value. Here we have thus chosen therefore $f_{\mathrm{SAW}} = 2.77$ GHz. The main trigger for each experiment is sent to the signal generator via the PULSE EXT input from the FPGA unit. This trigger basically launches a pulse modulated voltage oscillation that is sent towards the IDT for SAW generation.

The SAW signal of the employed generator experiences a jitter on the nanosecond scale with respect to the FPGA trigger. Since we aim for temporary voltage pulse control below the time scale of a SAW period ($\Delta t_{\mathrm{SAW}} \approx 361$ ps), the extent of this jitter represents a fundamental problem for our measurements. To bypass this problem, we impose the jitter of the SAW signal also on our picosecond voltage pulses. For this purpose, we use the pulse modulation of the signal generator (via the PULSE VID output) as trigger for the fast pulse generator (via the TRIG IN connector). This approach allows to drastically reduce the jitter of the fast voltage pulse with respect to the SAW signal.

We characterise the jitter between the picosecond voltage pulse and the SAW signal using a fast sampling oscilloscope of the type "LeCroy waveMaster 830Zi". Measuring the SAW signal (RF OUT) and the picosecond voltage pulses (negative analog output at AWG channel 2) in this setup, we obtain time traces of the SAW signal and the fast step pulse as shown in Fig. 35b. Let us define the delay between the AWG pulse and the SAW signal by the respective rising edges at about 50 % maximum amplitude – see red dotted vertical lines in Fig. 35b. Due

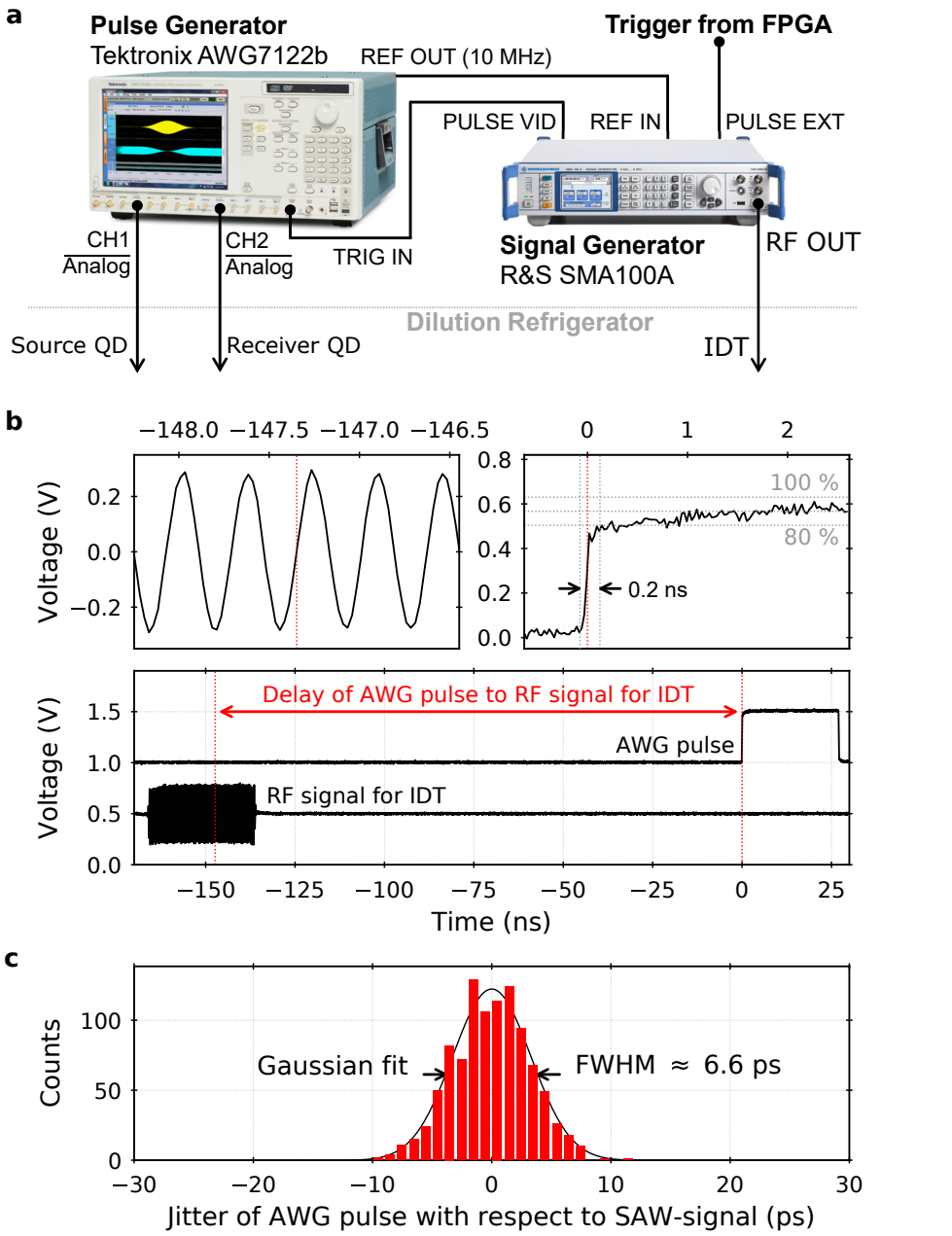

Figure 35: Characterisation of the signal generation setup. (a) Experimental setup for pulse triggered, SAW-driven single electron transfer. The images of the signal generators are from vendor websites [AWG; RuS]. **(b)** Time traces of a voltage oscillation burst for SAW generation and of a fast step pulse. We measure the delay between the two signals via fixed phases that are determined by 50 % amplitude of the respective signals – see redly dotted vertical lines. **(c)** Histogram of the variations in the delay of the AWG pulse to a fixed point in the train of the SAW signal.

to effects of higher harmonics in the generation of the SAW signal that mainly affect the oscillation burst at its edges, it is beneficial to choose the rising edge for the SAW signal in an arbitrarily chosen oscillation in the middle of the wave train. By this approach a precise measure of the AWG pulse delay with respect to a fixed phase of the SAW is obtained (see red arrow in Fig. 35b). Figure 35c shows a histogram of a thousand measurements of this pulse delay. The distribution of the data visualises the jitter of the fast AWG pulse with respect to the SAW. Fitting the data with a Gaussian distribution we obtain a full-width-at-half maximum (FWHM) of about 6.6 ps. Measuring a jitter of our fast voltage pulses that is about 54 times smaller than the SAW period, we verify the applicability of the present setup for our purpose of a pulse triggered SAW-driven single-electron source.

2.2.4 Tracing sound-driven electron transport

To send a single-electron with a SAW from one surface-gate defined quantum dot (QD) to the other, we perform a fast sequence of voltage movements on the QD gates. In each single-shot-transfer experiment, we perform basically three steps to execute a SAW-driven single electron transfer: initialisation, loading and preparation to send and catch. Between each step we go to a well protected measurement configuration where we readout the current passing through the quantum point contact (QPC). To trace the path of the electron, we monitor the QPC current at all involved QDs as the steps of the transfer procedure are executed. The jumps in QPC current then basically show whether an electron enters, stays or leaves a stationary QD.

To demonstrate the procedure of SAW-driven single-electron transfer, let us focus on an exemplary data set. Figure 36 shows traces of QPC current measured at the source (diamonds) and receiver (circles) QD of the upper quantum rail. To keep it simple, we only show data points in the read-out frames of QPC current of the fast sequence. After initialisation no electrons are present in the source and receiver QD. Subsequently to the loading procedure, we observe a change in QPC current, ΔI_{QPC}, indicating successful trapping of a single electron from the Fermi sea. During the sending time frame, we then move the source and receiver QD respectively in a sending and catching configuration. Launching subsequently the SAW train during the sending window, we finally execute the single-electron transfer which causes respectively jumps in QPC current. In this example a single electron that is initially loaded at the source QD is successfully transported by a SAW train along the upper quantum rail to the receiver QD.

The duration of a single-electron-transfer experiment is determined by the time-of-flight of the electron with the SAW (ns), the duration of the surface-gate operations (μs) and readout of QPC current (ms). The repetition rate of the

single-shot electron transfers, is thus mainly limited by the readout duration. This bottleneck could be strongly reduced by an RF reflectometry setup [Are16]. But also with faster charge readout, a repetition rate above the kHz regime can not be easily achieved in the present setup, because the surface-gate operations are performed sequentially. For the present purpose, hence, a conventional charge detection via a jump in QPC current is sufficient.

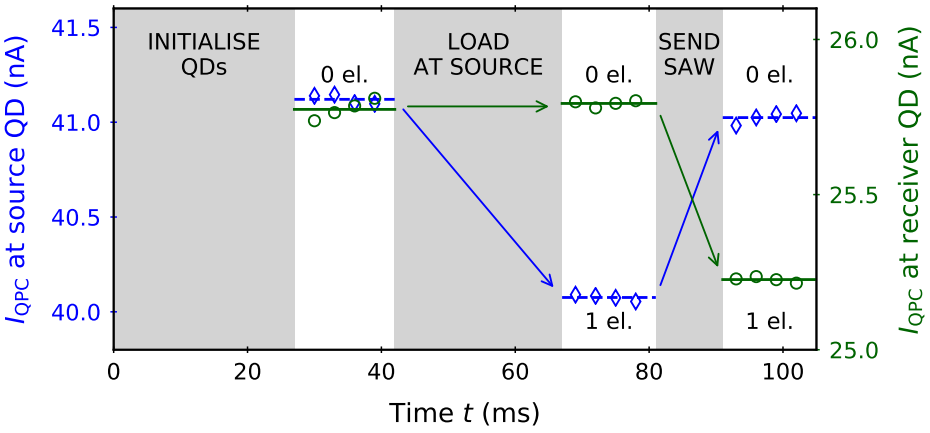

Figure 36: Trace of QPC current for a successful SAW-driven single-electron transport experiment. Shown is a time trace of the QPC current, I_{QPC}, at the source (blue diamonds; left axis) and receiver (green circles; right axis). The grey regions show the time frames where voltage movements are performed on the surface gates of the respective QD to initialise, load and transfer the electron. In between these operations we record several data points of I_{QPC} at the source and receiver QD. Averaging over these data points (see horizontal lines) we obtain a value that clearly indicates the presence of an electron.

2.2.5 Initialisation and loading at the source

It is now time to go in more detail and specify the three steps – initialise, load and send – that are executed in the fast sequence of voltage movements at the source QD before launching the SAW train. The fast sequence basically involves voltage movements on the reservoir (R) and coupling (C) gates of the respective QDs as indicated in the SEM image shown in Fig. 37a. In between each step we go to a protected measurement configuration (M) and read out the current through the quantum point contact (QPC) as indicated in the charge stability diagram shown in Fig. 37b. We obtain this diagram by sweeping the reservoir gate voltage, V_{R}, for different steps of the coupling gate voltage, V_{C}. To keep the working point of the QPC in a sensitive position, we linearly adjust the QPC voltage, V_{QPC}, for each step in V_{C}. We obtain the sweeping range for V_{QPC} via the working

points of two pinch-off characteristics that we measure for the boundaries of the sweep of V_C. Plotting the derivative of QPC current, $\partial I_{QPC}/\partial V_R$, we obtain data showing so-called charge degeneracy lines which indicate a change of the charge state of the QD. Based on these diagrams we can identify possible regions for initialisation (I), loading (L) and sending (S).

When we execute the fast sequence, we go to a protected measurement configuration (M) and read out the current through the quantum point contact (QPC) in between each step. Comparing the QPC current before and after each step, we can deduce if an electron entered or left the QD. To initialise the system, we remove all electrons electrons from the QDs by visiting configuration I. We then load a single electron at the source QD. For this purpose, we go to the QD configuration L, wait for 10 ms such that an electron can tunnel from the Fermi sea into the QD and return to the measurement position, M. Fig. 37c shows jumps in QPC current at different loading configurations (L) that are visited after initialisation via voltage variations from the measurement position, M. The data show that, depending on the voltage variations of the reservoir (δV_R) and coupling gate (δV_C), different numbers of electrons can be efficiently loaded from the electron reservoir to the left into the source QD.

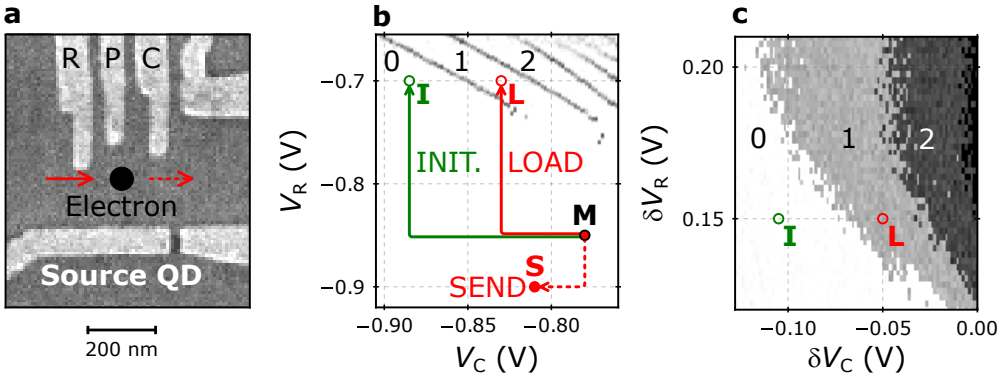

Figure 37: Voltage steps to prepare SAW-driven single-electron transfer. **(a)** SEM image of a source QD with indication of surface electrodes. **(b)** Charge-stability diagram showing example source-quantum-dot configurations for QPC measurement (M), initialisation (I), single-electron loading (L) and sending (S). Here we plot $\partial I_{QPC}/\partial V_R$. The data show abrupt jumps in QPC current indicating charge-degeneracy lines of the QD. **(c)** Loading map showing configurations I and L. Each pixel represents the difference in QPC current, ΔI_{QPC}, before and after visiting the respective loading configuration. The greyscale reflects the electron number in the QD. Here the reference configuration is the measurement position M. The figures are adapted from our publication Takada *et al.* [Tak19].

Based on such a loading map we choose a proper loading position (L) where a single-electron electron can be efficiently loaded from the electron reservoir into the source QD. Repeating the initialisation and loading procedure several thousand times, we can estimate the efficiency of the loading process. The voltage ranges for efficient loading configurations of the QD can vary even for similar implementations of QDs in a GaAs/AlGaAs heterostructure as the present in the order of 100 meV. We suspect that this variation mainly stems from fluctuations in the surface-gate quality and the corrugated background potential stemming from the positions of the active Si sites in the δ-doped layer. Additionally, we encountered hysteresis effects that can render the execution of a fast sequence more complicated. Having accomplished the loading process, we go to a sending configuration (S) where the electron can be picked up by the SAW. At the same time as we prepare the source QD for sending, we bring the receiver QD into a configuration allowing the electron to be caught. We then launch a SAW train to execute the transfer of the loaded electron. Comparing the QPC currents before and after the SAW burst, we can assess whether the electron was successfully transported.

2.2.6 Configuration of the sending process

In order to find a source QD configuration where the SAW can pick up a loaded electron with high efficiency into a moving QD of the SAW train that propagates along the quantum rail, we investigate so-called sending maps. In these maps the QPC currents before and after launching a SAW train are compared. Typical examples are shown in Fig. 38. The jump in QPC current, ΔI_{QPC}, is measured both at the source and receiver QDs for various sending configurations that are visited via voltage variation on the reservoir gate, δV_{R}, and the coupling gate, δV_{C}, of the source QD. Here the greyscale is chosen based on the histograms of the jumps in QPC current such that a black pixel indicates the presence of an electron.

Figure 38a shows a sending map that is measured at the source QD whereas no SAW train is launched here. The plot shows that the loaded electron can be simply removed from the source QD by the voltage variations, δV_{R} and δV_{C}. The sending map basically shows two transitions: At the horizontal transition (see dashed arrow in Fig. 38a) the loaded electron is pushed back into the electron reservoir. Crossing the vertical transition (see solid arrow in Fig. 38a) on the other hand, the electron is pushed into the quantum rail. Tracing the QPC current at the receiver QD as shown in see Fig. 38b, we observe no electron entering, since there is so far no SAW train launched from the IDT.

These transitions shift as we launch a SAW train after bringing the electron at the source QD into the sending configuration (S) – see Fig. 38c. The change in

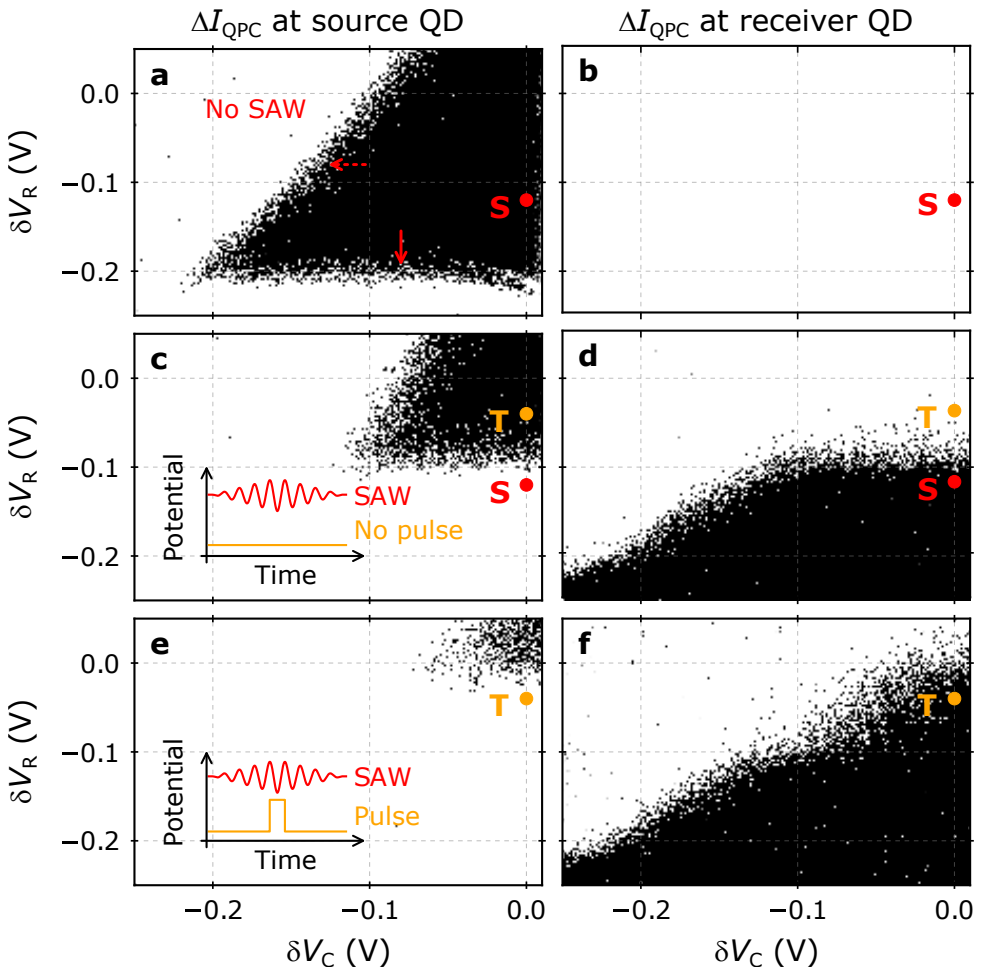

Figure 38: Example of sending maps. The plots show jumps in QPC current, ΔI_{QPC}, after a sending configuration is visited via the voltage variations δV_{R} and δV_{C} on the source quantum dot (QD). Here the reference voltage configuration ($\delta V_{\mathrm{R}} = \delta V_{\mathrm{R}} = 0$) at the source QD is $V_{\mathrm{R}} = -1.0$ V and $V_{\mathrm{C}} = -0.88$ V. The color-scale of the plots is chosen such that the black data points indicate events where an electron is present after visiting this position. The voltage configurations S and T indicate possible sending positions without (S) and with (T) additional voltage pulse applied on the plunger gate. **(a)** ΔI_{QPC} measured at source QD without any SAW launched during the sending time frame. **(b)** ΔI_{QPC} measured at receiver QD without SAW. **(c)** ΔI_{QPC} measured at source QD with a 30 ns SAW train launched during the sending time frame. **(d)** ΔI_{QPC} measured at receiver QD showing electron transport by SAW. **(e)** ΔI_{QPC} measured at source QD with additional 360 ps voltage pulse applied at the plunger gate in time with the SAW arrival. **(f)** Corresponding measurements of ΔI_{QPC} at the receiver QD.

the sending map occurs because the SAW allows the electron to overcome the potential barriers more easily. Investigating ΔI_{QPC} at the receiver QD – see Fig. 38d –, we observe now an electron entering whenever it was successfully transported by the SAW. The sending position, S, is now chosen such that the electron is only sent to the receiver when a SAW burst is applied. The sending threshold sensitively depends on the SAW amplitude and the dot-channel potential gradient [Ber16b].

To send the electron in a specific moving QD of the SAW train, we use a picosecond voltage pulse applied on the plunger gate of the source QD. Figure 38e and Fig. 38f show measurements of ΔI_{QPC} at the source and receiver QD for the case where a 360 ps long voltage pulse is applied on the plunger gate (P) of the source QD in time with the arrival window of the SAW. For this pulse, a clear shift of the sending transition is apparent. Applying this fast voltage pulse, the potential barriers are further reduced. Consequently, we can choose a sending position, T, where sending is triggered only by the voltage pulse. Reducing the pulse length down to 90 ps we can make the sending fringes visible meaning that we can see the SAW-related phases where transfer is blocked or activated. As we make make the pulse shorter, however, we also shrink the region of possible pulse-triggered sending positions, T. Therefore, the most critical factors for the efficiency of the voltage pulse trigger are the abruptness of the sending transition and the attenuation of the fast pulse along the transmission line.

2.2.7 Configuration of the catching process

A very important part of the transfer procedure is the catching process of the electron at the receiver QD. To characterise the catching process we usually measure so-called "holding" and "catching" maps that are very similar to the aforementioned sending maps. This kind of investigation allows us to verify that a transferred electron is indeed caught in the receiver QD and to find configurations of high trapping probability. Figure 39a and Fig. 39b show typical examples of such holding and catching maps. In both of those investigations we compare the QPC-current at the receiver QD, before and after a SAW-train is sent along the structure. In a holding map we load a single electron directly at the receiver QD before we launch the SAW – see Fig. 39a. In a catching map on the other hand an electron is initially loaded at the source QD, transferred by the SAW and eventually trapped at the receiver QD – see Fig. 39b. As we temporarily visit different configurations of the receiver QD during the transfer time frame via voltage variations on the reservoir and channel gate, $\delta V'_{\mathrm{C}}$ and $\delta V'_{\mathrm{R}}$, we can now identify regions were the electron is well trapped. Differences in the holding and catching maps might indicate that the received electron is located in the quantum rail and not in the receiver QD.

In Fig. 39a and Fig. 39b it is apparent that the regions with high trapping probability are distributed in the same way – both for the holding and catching event. The similarity of the holding and catching map shows that the transferred electron is indeed caught in the receiver QD and not at a different position such as the end of the transfer channel. The data further shows that the trapping probability significantly increases as we make the reservoir gate, $\delta V_{\mathrm{R}}'$, more negative and the coupling gate, $\delta V_{\mathrm{C}}'$, more positive. To trap an electron efficiently we raise the potential barrier to the electron reservoir and strongly couple the QD to the transport channel during the sending time frame of the SAW. The optimization process of the catching efficiency involves the potential variations on the gates of the QD as well as on the nearby channel. A further indication for a receiver configuration where the electron is stuck in the transfer channel are two-electron catching events.

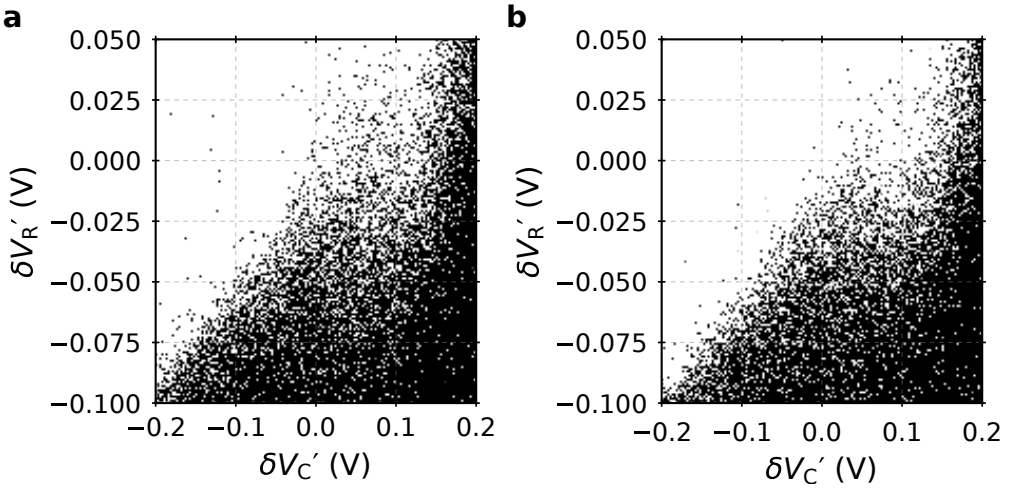

Figure 39: Holding and catching a single electron at the receiver quantum dot (QD). Shown is the SAW-introduced jump in QPC-current measured at the receiver QD, $\Delta I_{\mathrm{QPC}}'$, for different temporary configurations that are visited via voltage the variations, $\delta V_{\mathrm{C}}'$ and $\delta V_{\mathrm{R}}'$, while a SAW-burst is sent. Here the reference voltage configuration ($\delta V_{\mathrm{R}}' = \delta V_{\mathrm{R}}' = 0$) at the receiver QD is $V_{\mathrm{R}}' = -1.0$ V and $V_{\mathrm{C}}' = -0.65$ V. Note that the voltage applied V_{C}' is relatively small here, since we have the plunger gate polarised at $V_{\mathrm{P}}' = -0.44$ V. A black point indicates the presence of an electron. **(a)** Holding map. An electron is directly loaded at the receiver quantum before the SAW is launched. **(b)** Catching map. An electron is loaded at the source QD and transported with the SAW to the receiver QD, where it its caught or not.

2.3 Experimental Results

Having introduced the experimental frame of our SAW-driven single-electron circuit of coupled quantum rails, let us now focus on more elaborate measurements that were performed with this device. We begin this section by demonstrating the efficiency of SAW-driven single-electron transport. Secondly, we couple the two quantum rails and investigate the ability of this device to act as a directional coupler where the electron is partitioned into the two output-channels of the device. To gain a better understanding of our experimental results we comparte them to quantum-mechanical simulations of SAW-driven electron transport in a comparable model system. Then we demonstrate a picosecond-voltage-pulse trigger allowing us to send the electron at a specific position of the SAW train. Applying a similar pulsing approach at the receiver dot, we measure moreover the time-of-flight and characterise SAW-driven single electron transport through the present beam-splitter setup.

2.3.1 Transfer efficiency

Sufficiently high efficiency of loading, sending and catching is essential for single-shot experiments with flying electrons. In order to achieve highly efficient single-electron transfer, it is necessary to tune the different processes of a SAW-driven transport experiment. This optimisation includes initialisation, loading and the preparations to send and catch. Additionally it is important to chose a proper set of voltages applied on the electrodes along the 22-μm-long transport channel of the employed sample in order to establish a smooth potential landscape along the transport paths[8]. To ensure sufficiently depleted transport channels, the sum of the voltages on a pair of channel gates should be in general about 200 mV below the pinch-off voltage. In the experiments that are presented in this thesis, we started from a homogenous set of voltage values that were used in previous investigations (-0.8 V to -0.9 V). Adjusting the voltages in the tunnel-coupled region, we then were able to transfer an electron from the receiver quantum dot to the source. The success of the catching process strongly depends of the quality of the realised quantum dots and may vary from case to case. In the presently investigated sample, catching at the lower receiver QD worked from the beginning and optimisation was straight forward. For the upper receiver QD, however, initially no electrons were trapped and the catching process required also tuning on the channel gates. Varying the voltages of the channel gates in pairs – one after another –, one can step-by-step enhance the transfer efficiency. For the presently investigated sample, we found that a relatively asymmetric distribution of the voltages along channel electrodes led to a relatively good result.

[8] It can be advantageous to launch a SAW before the initialisation process in the early stage of optimisation, because electrons can pile up within the transfer channels.

In order to quantify the efficiency of the processes of the transfer sequence, we repeat the following two experiments: We first load a single electron at the source QD, send a SAW-burst and measure the jump in the QPC-current, ΔI_{QPC}, both at the source and receiver QD. Then, we do not load an electron at the source QD and run the same experiment. Since we load an electron at the source in the first experiment, we expect an electron to arrive at the receiver QD after launching a SAW-burst if the efficiencies of sending, transfer and catching are sufficiently high. In the second step we expect on the other hand no electron to arrive at the receiver QD after launching the SAW train, since we initially load no electron at the source QD. If in the first transfer-experiment the electron is dragged back in subsequent SAW minima, leaves the SAW and gets stuck in the transport channel, the electron will not arrive at the receiver QD. Repeating the transfer experiment without initial loading, the electron that got stuck along the transport path will be recovered however in this reference experiment at the receiver QD if the catching efficiency is sufficiently high. Thus, this approach allows to probe if the transport channel is smooth enough such that no electron gets stuck during transport. It requires however a certain degree of preceding enhancement of SAW-driven single-electron transport. Repeating this procedure we can now quantify the efficiency for sending, transfer and catching.

Figure 40 shows exemplary data for one thousand repetitions of these two steps. Whenever an electron is loaded at the source QD it is picked up by the SAW causing a positive jump in QPC current – see blue data points in Fig. 40a. If the loading or sending process fails, such a positive jump in QPC current does not occur. Due to a sufficiently smooth potential landscape along the quantum rail and an optimized catching configuration, the transferred electron also arrives at the receiver QD. As consequence of the successful transfer, we observe a negative jump in QPC current at the receiver QD – see green data points in Fig. 40b. The distinct peaks in the histograms of the events with (coloured) and without (grey) initial loading at the source QD – see Fig. 40c-d – show that the presence and absence of an electron in the QD is clearly distinguishable. The peak separation, which is a necessary requirement for the characterisation, is achieved due to a relatively large bias voltage of about 1 mV and a steep pinch-off characteristic of the QPC. Focussing now on the ΔI_{QPC} data points measured at the receiver QD, we observe three out of thousand events where no electron is caught – see red circles in 40b – despite the particle having successfully left the source QD. If the electron is recovered in the step subsequent of these error events, then the electron was likely stuck in the channel. Else – successful sending, but no electron reception – we interpret the event as a catching error. Repeating this kind of experiment 70,000 times at a specific optimised working point, we obtain a loading error of 0.07 % and a catching error of 0.18 %. Consequently, we deduce the transfer efficiency in the present configuration as 99.75 %.

The employed circuit of tunnel-coupled quantum rails has significantly higher complexity than first SAW-driving single-electron devices of pioneering experiments [Her11; McN11; Ber16a]. Consequently, the single-shot transfer efficiency along the 22-μm-long quantum rails exceeding 99 % represents a remarkable result that shows that SAW technology can be employed for single-electron transport on a relatively large scale. Achieving the ultimate goal of adiabatic and coherent SAW-driven transport of a single-electron in a certain moving QD of the SAW train, this novel transport technique opens up the route for several fascinating experiments as introduced in section 2.1.2. As next step, it is essential to investigate SAW-driven electron transport in more detail and optimize the propagation of an electron within a certain SAW train. It is further of central importance to investigate to which extent this efficiency changes as a SAW-transported electron is coupled in different directions of a circuit of tunnel-coupled quantum rails. These aspects will be in the focus of the following chapters.

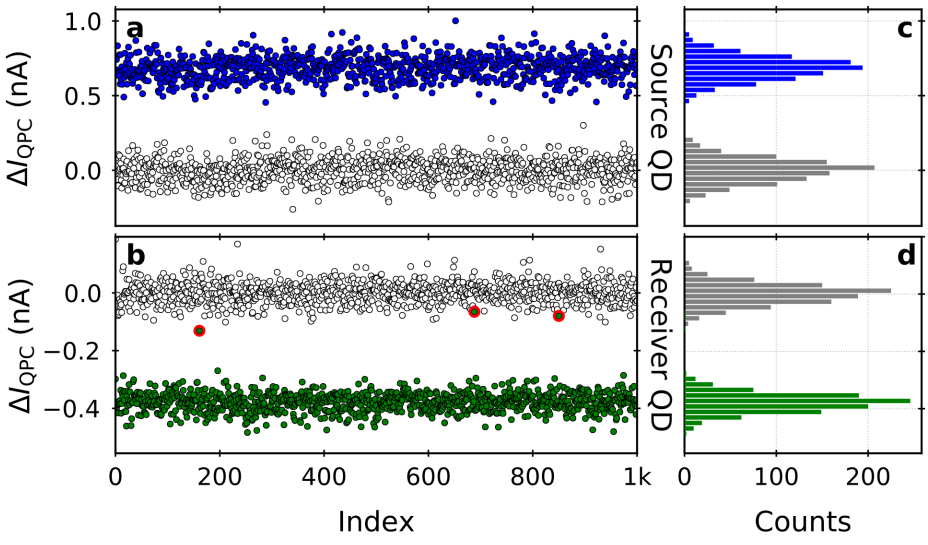

Figure 40: Characterisation of optimised SAW-driven single electron transport. The data points show the difference of QPC current, I_{QPC}, before and after lauching a SAW train at the **(a)** source and **(b)** receiver QD without (grey) and with (coloured) an electron initially loaded at the source. Error events are highlighted with red circles. **(c,d)** Histograms of the data. The figure contains data of our publication Takada *et al.* [Tak19].

2.3.2 Directional coupler operation

Having established highly efficient single-electron transport, next we couple the two channels to partition an electron in flight between the two quantum rails. The aim of this tunnel coupling is to prepare a superposition state of a flying charge qubit as discussed in section 2.1.2. In future investigations, two of such devices will be arranged in a MZ-type interferometry setup to test the coherence properties of a charge qubit that is surfing on a sound-wave. Here we investigate the feasibility of a single beam-splitter device for an electron that is transported by a SAW. We first investigate if we can maintain a high transfer efficiency as we partition the electron from one quantum rail into the other. Comparing our experimental results to time-dependent simulations of SAW-driven electron propagation in such a device, we then discuss the quantum state of the flying electron.

We find that we can finely control the partitioning of the electron, by detuning the voltages applied to the side electrodes of the coupling region, V_{U} and V_{L}, while keeping V_{T} constant at a sufficiently low value. The effect of this potential detuning on the double-well potential in the tunnel coupled wire is schematically shown in Fig. 41a. Figure 41b shows a schematic top view on the tunnel-coupled region with indications of the surface gates and the moving QDs that are formed by the SAW train in the transport channel. Having a potential detuning of $\Delta = V_{\mathrm{U}} - V_{\mathrm{L}} = 0$ V, the quantum rails are aligned in electric potential and the device serves as a 50-50 beam splitter. Setting a voltage configuration where $\Delta < 0$ V, the potential of the lower quantum rail (L) is decreased with respect to the upper path (U). For $\Delta > 0$ V, the situation is reversed. To achieve a 50-50 partitioning at exactly $\Delta = 0$ V, the sum $V_{\mathrm{U}} + V_{\mathrm{L}}$ has to be slightly adjusted. Deducing the transfer probabilities to the receiver QDs from a thousand single-shot experiments per data point, we measure the partitioning of the electron for different values of Δ as shown in Fig. 41c. Here we sweep V_{U} and V_{L} in opposite directions from -1.26 V to -0.96 V while keeping $V_{\mathrm{T}} = -0.75$ V. The data shows a gradual transition of the electron transfer probability from the upper (U) to the lower (L) detector QD while the total transfer efficiency stays at (99.5 ± 0.3) %.

A very striking feature of the observed probability transition is that its width (about 200 mV) is relatively large. It is further interesting that the measured probability data follows the course of a Fermi function:

$$P_{\mathrm{U}}(\Delta) \approx \frac{1}{\exp(-\Delta/\sigma) + 1} \tag{1}$$

Fitting the experimental data with such a function (see lines in Fig. 41c), we can quantify the width of the probability transition via the corresponding scale parameter, σ. To test the dependencies of the directional coupler transition on the different properties of the device, we investigated if the width of the directional

coupler transition changes as we sweep the gate voltage configurations on different surface electrodes of the nanostructure. The voltages on the injection channel and source QD left the directional coupler transition unaffected. Also as we decrease the amplitude of the SAW, we didn't find a significant change on the width of the measured probability transition. We found however a significant effect of the exit potential in the tunnel-coupled region and the tunnel-barrier electrode. Figure 41d shows the width of the probability transition, σ, as function of the tunnel-barrier voltage, V_T. Increasing the tunnel-barrier potential, we find a significant narrowing of the probability transition.

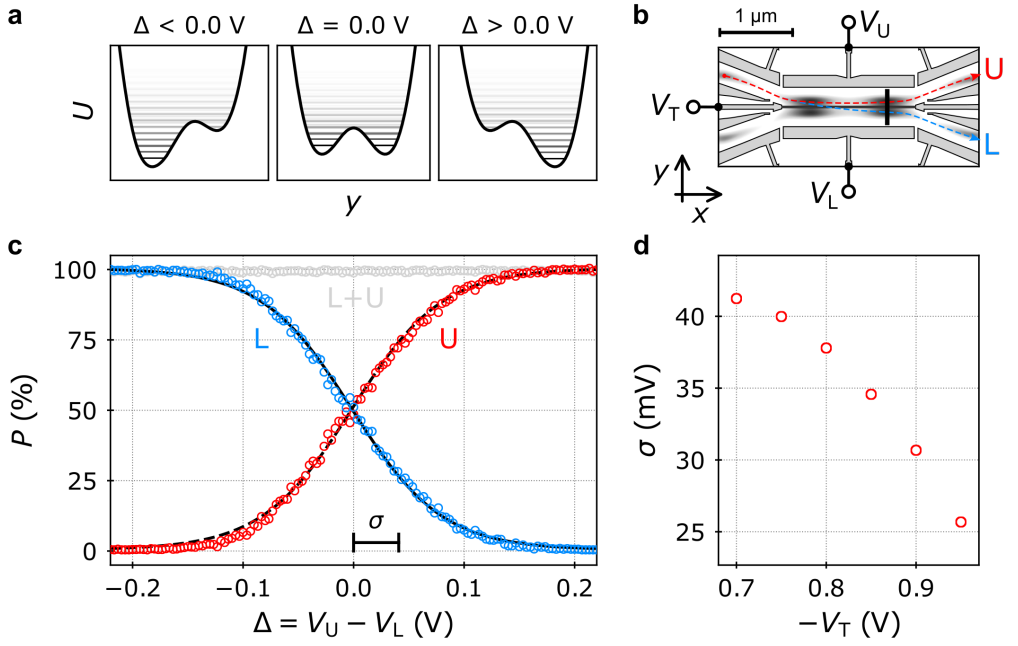

Figure 41: Partitioning a SAW-transported electron in flight. (a) Schematic showing slices of the electric potential, U, along the double-well potential for different values of potential detuning, Δ. The horizontal lines indicate the eigenstates in the moving QD. **(b)** Schematic of the electric potential in the tunnel-coupled region modulation from a SAW train. The black spots represent the moving QDs that are formed by the SAW. The vertical bar indicates the position of the aforementioned potential slice. To control the partitioning of the electron, we sweep the potential detuning via $\Delta = V_U - V_L$ while keeping V_T constant. **(c)** Probability, P, for a single electron to end up in the upper (U) or lower (L) quantum rail for different values of potential detuning, Δ. The lines show a fit with a Fermi function allowing to extract the width of the probability transition, σ, according to equation 1. **(d)** Transition width, σ, of directional coupler measurements for different values of the tunnel-barrier voltage, V_T. Adapted from our publication Takada *et al.* [Tak19].

2.3.3 Simulations of electron partitioning

To understand the experimentally observed transition in the transfer probabilities, P_U and P_L, as function of potential detuning, $\Delta = V_U - V_L$, we employ two independent models. First (model A), we perform a stationary investigation of the eigenstates in the tunnel-coupled region. The calculations have been performed in collaboration with Xavier Waintal from the CEA in Grenoble (France). Secondly (model B), we simulate the time-dependent propagation of the electron within a certain SAW minimum through our device. The time-dependent simulations were developed and performed by Hugo Lepage from the Cavendish Laboratory in Cambridge (United Kingdom). The collaboration was built in the course of the SAWtrain network [SAWtr]. Model A is a minimum model to understand our data. Model B is more elaborate and accounts for the actual partitioning mechanism.

The two models are applied on a potential landscape that we calculate with the commercial Poisson solver NextNano [Bir07]. Knowing the sample geometry, the electron density in the 2DEG and the set of applied voltages, we calculate the electrostatic potential of the gate-patterned device using a frozen charge layer and deep boundary conditions [Hou18]. The central premise is that the charge density in the 2DEG is constant. With this assumption, we deduce a donor concentration of about $1.6 \cdot 10^{10}$ cm^{-2} in the doping layer and a surface charge concentration of about $1.3 \cdot 10^{10}$ cm^{-2}. We superimpose the dynamic SAW modulation with an amplitude of 15 meV estimated from Coulomb-blockade measurements – for details see appendix G. With this approach we can approximate the dynamic potential landscape that the flying electron experiences as it propagates along the quantum rails of the single-electron circuit.

Figure 42 shows the static potential landscape along the tunnel-coupled region of the presently investigated device with various slices of the potential. Figure 42a shows a comparison of the static electric potential along a quantum rail (solid blue line) to the situation where a SAW with 15 meV amplitude is superimposed (dotted black line). The comparison shows that the dynamic changes along the potential landscape can significantly alter the actual depth of the moving QDs that are formed by the SAW along the quantum rails at different positions along the tunnel-coupled wire (TCW). A significant modification of the moving quantum dots is apparent at the injection and exit position of the TCW – compare moving QDs at $x \approx -1$ μm, $x \approx 0$ μm and $x \approx +1$ μm. Along the center of the TCW, however, the change of the static potential is very smooth leaving the potential of the moving QDs basically unchanged.

Since the potential changes at the injection and exit of the TCW seem to be most critical, let us now also investigate vertical slices of potential (along the y direction) for different positions at the entrance to the tunnel-coupled region.

Figure 42a shows the electric potential at $x = -950$ nm (solid red line), $x = -860$ nm (dashed red line) and $x = -700$ nm (dotted red line). The plots show that the potential drops down by more than 10 meV along a length that corresponds to a travelling time of 90 ps for a SAW-transported electron. If the energy separation of the qubit state is not sufficiently far from excited states, such a rapid transition could introduce transitions into higher energy states.

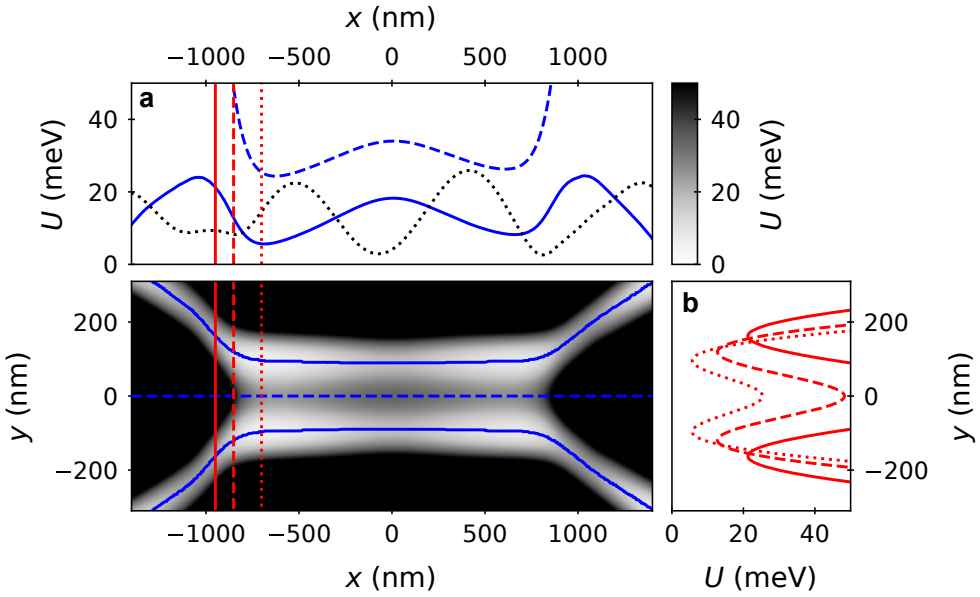

Figure 42: Potential landscape of the tunnel-coupled region. The two-dimensional plot shows the calculated stationary potential landscape with symmetric potential detuning of the tunnel-coupled quantum rails with the experimentally employed set of gate voltages. **(a)** Slices of the electrostatic potential along the potential minima of the quantum rails (solid blue lines) and at the position of the tunnel barrier (dashed blue line). To give an impression of the effect of the SAW modulation, we additionally show the potential slice along the quantum rail with superimposed SAW train having an amplitude of 15 meV (dotted black line). **(b)** Vertical cuts along the potential landscape at three positions, $x \in \{-950\text{ nm}, -860\text{ nm}, -700\text{ nm}\}$, at the entrance to the tunnel-coupled region. The data shows the abrupt change of the electrostatic potential that corresponds to a time frame of 90 ps for a SAW-transported electron.

Model A

As starting point for the stationary theoretical investigation, we consider a one-dimensional cut of the double-well potential in the tunnel-coupling region. In this region we have a sufficiently flat potential landscape, $U(\mathbf{r}) \approx U(y|\boldsymbol{V}) + U_{\mathrm{SAW}}(x,t)$, such that the eigenstate problem becomes separable in the x and y coordinates.

In this region, the electronic wave function $\phi_i(y)$ along the transverse y direction satisfies the 1D Schrödinger equation:

$$\frac{\hbar^2}{2m}\frac{\partial^2\phi_i(y)}{\partial y^2} + U(y|\boldsymbol{V})\cdot\phi_i(y) = E_i\phi_i(y) \tag{2}$$

where $U(y,\boldsymbol{V})$ is the electrostatic double-well potential defined by the surface-gate voltages $\boldsymbol{V}$ containing V_U, V_L and V_T. $U(y,\boldsymbol{V})$ has been obtained from solving the corresponding Poisson problem by the aforementioned approach. m indicates the effective electron mass in a GaAs crystal.

To obtain the probability of finding the electron in the upper or lower potential well, we can now simply sum up the contributions from the wave functions of the eigenstates for the respective regions of interest. To obtain the probability of finding the electron in the upper quantum rail, we integrate the square of the wave function over the respective region:

$$P_\mathrm{U} = \sum_i p_i \int\limits_{y>0\ \mathrm{nm}} \left|\phi_i(y, U(y|\boldsymbol{V}))\right|^2 \mathrm{d}y \tag{3}$$

where p_i is the occupation of the eigenstate ϕ_i. Remind that the spatial dimension y is perpendicular to the propagation direction, x, of the SAW. For a fixed tunnel-barrier height we can now detune the double-well potential as in experiment by varying Δ. It is now straightforward to calculate the directional coupler transition, $P_\mathrm{U}(\Delta,\boldsymbol{V})$, for the experimental setting with any imaginable occupation of the eigenstates.

Ground state occupation

Let us first consider the situation where only the ground state is occupied. We evaluate equation 3 with mere ground state occupation ($p_0 = 1$) and fixed tunnel-barrier height ($V_\mathrm{T} = -0.7$ V) for different values of potential detuning, Δ, that are changed as in experiment. Evaluating the stationary model for different values of Δ, we obtain a probability transition that follows the course of a Fermi distribution – see equation 1 on page 94. Qualitatively, this course strongly resembles the experimental data. Assuming pure ground-state occupation, the simulation shows that we have to expect an extremely abrupt transition in transfer probability as shown in Fig. 43a. We can characterise the width of the probability transition by the scale parameter, σ. For pure ground state occupation, the width of the probability transition, σ, is in the order of a few microvolts. Increasing the tunnel barrier, we increase the confinement in the double-well potential what makes the transition continuously narrower as shown in Fig. 43b. For $V_\mathrm{T} \approx -0.9$ V the transition width reaches already a scale of picovolt. With

state-of-the art equipment this transition thus would be hardly resolvable in experiment. It would appear as an abrupt jump of transfer probability from 0 % to 100 %. In our experimental investigations we observe on the other hand a width of such a directional coupler transition that is in the order of tens of millivolt. We conclude that the SAW-transported electron is not adiabatically transported in the ground state, but must occupy excited states to a certain extent.

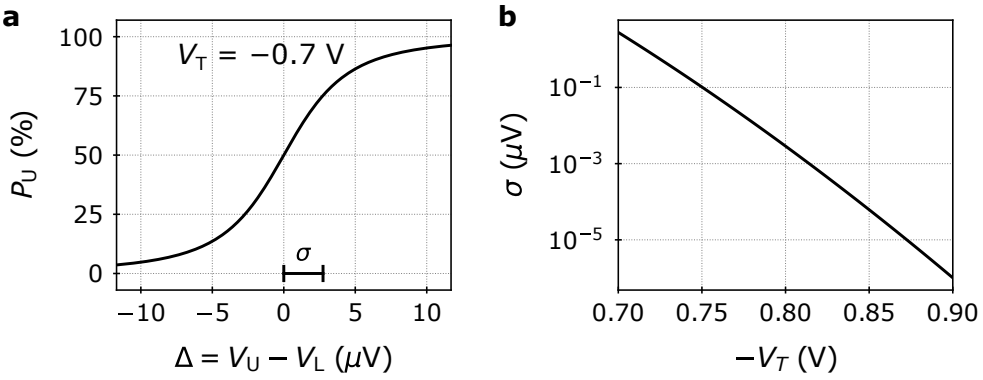

Figure 43: Partitioning a ground-state electron in the present double-well potential. **(a)** Probability, P_U, to find the electron in the upper quantum rail ($y > 0$ nm) as function of potential detuning, $\Delta = V_U - V_L$, for fixed tunnel-barrier height ($V_T = -0.7$ V). The transition width σ is obtained via the fit of a sigmoid function, $P(\Delta) = 1/(\exp(-\Delta/\sigma) + 1)$. **(b)** Width of the probability transition, σ, for different tunnel-barrier heights defined via V_T.

Occupation of excited states

How does the situation change as we populate successively excited eigenstates of the double-well potential? To investigate this question, we define the occupation of the eigenstates, ϕ_i, with eigenenergies, E_i, via an exponential distribution:

$$p_i \propto \exp\big(-\frac{E_i - E_0}{\varepsilon}\big) \tag{4}$$

where ε is a parameter determining the occupation of higher energy eigenstates. E_0 denotes the energy of the ground state for a certain potential configuration. With this approach we can keep the course of the probability transition that resembles the experimental data as we successively occupy excited states.

Increasing ε, we find a broadening of the probability transitions as exemplarily shown in Fig. 44a for a tunnel barrier voltage $V_T = -0.9$ V. Setting the occupation parameter as $\varepsilon \approx 3.5$ meV, we obtain simulation results of $P_U(\Delta)$ (black solid

line) showing very good agreement with the transition that we observe in experiment (red data points). Figure 44b shows the course of the transition width, σ, as function of the tunnel-barrier voltage, V_T, for fixed value of ϵ. As in experiment (red data points), we observe a narrowing of the transition width, σ. The raised tunnel-barrier potential increases the confinement within the potential wells and causes a rearrangement of the eigenstates. Since the absolute value of the excitation energy remains basically unaffected when increasing the tunnel-barrier, the occupation of the eigenstates changes. This shows that the transition width, σ, reflects the occupation of excited states and thus indirectly the confinement in the double-well potential. The transition width of such a directional coupler measurement thus gives information about the extent of excitation of the SAW-transported electron. Besides this qualitative and quantitative agreement we find however that the functional relation that is predicted by the simulation strongly differs from experiment. Instead of a concave relation of the simulation we observe in experiment a convex trend. We suspect that this difference stems from uncertainties in the calculation of the potential landscape. We cannot exclude however that there are additional effects that are not taken into account in the present discussion.

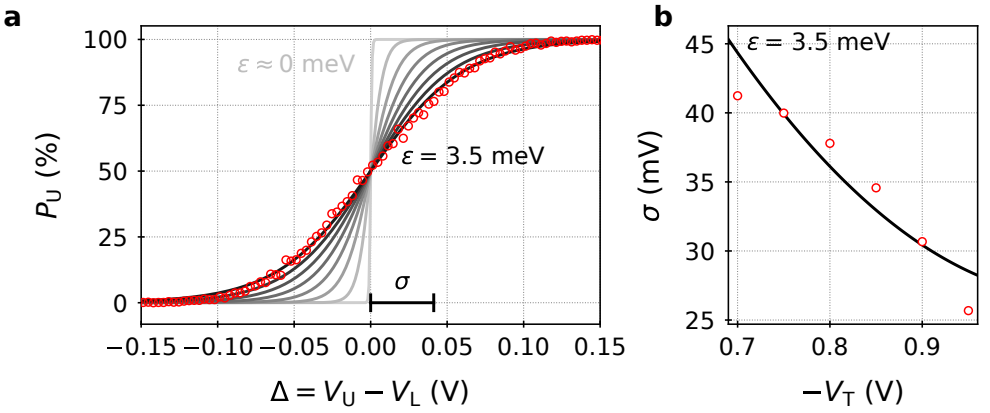

Figure 44: Simulation of electron partitioning with excitation. (a) Probability, P_U, to find the electron in the upper quantum rail ($y > 0$ nm) as function of potential detuning, $\Delta = V_\mathrm{U} - V_\mathrm{L}$, for fixed tunnel-barrier height ($V_\mathrm{T} = -0.9$ V). Here we evaluate the stationary model A given by equation 3. The red points show data from experiment. The lines show evaluations of equation 3 for different values of the excitation parameter, ε. **(b)** Course of the simulated transition width, σ, for different values of the tunnel-barrier voltage, V_T and a fixed value of the occupation parameter, $\varepsilon = 3.5$ meV. The red points show the transition width of corresponding measurements from experiment.

Model B

Let us now introduce the time-dependent simulation of SAW-driven electron propagation. For this purpose we consider the full two-dimensional potential landscape, $V(\boldsymbol{r},t)$, of our beam-splitter device with a 15 meV peak-to-peak potential modulation of the SAW having a wavelength of 1 μm. We calculate the evolution of the particle described via the electron wave function, $\psi(\boldsymbol{r},t)$, by solving the time-dependent Schrödinger equation:

$$i\hbar\frac{\partial\psi(\boldsymbol{r},t)}{\partial t} = \hat{H}\psi(\boldsymbol{r},t) = \left[-\frac{\hbar^2}{2m}\nabla^2 + U(\boldsymbol{r},t)\right]\psi(\boldsymbol{r},t) \tag{5}$$

where $\hat{H}$ describes the Hamilton operator, $U(\boldsymbol{r},t)$ is the two-dimensional dynamic potential encountered by the electron and m is the effective electron mass in a GaAs crystal. We numerically solve the equation using the finite-difference method [MLP00] and discretise the wave function both spatially and in time. In one dimension, the single-particle wave function becomes:

$$\psi(x,t) = \psi(m\cdot\Delta x, n\cdot\Delta t) \equiv \psi_m^n \tag{6}$$

where m and n are integers and Δx and Δt are respectively the lattice spacing in space and in time. In the time-dependent simulations that we show in the following, we have chosen the values of the discretisation parameters in the 2DEG of the simulated GaAs/AlGaAs heterostructure as $\Delta x = \Delta y = 1$ nm and $\Delta t = 0.1$ fs. Following the numerical integration method presented by Askar and Cakmak [AC78], we evaluate the leading term in the difference between staggered time steps:

$$\psi_m^{n+1} = e^{-i\Delta t\hat{H}/\hbar}\,\psi_m^n \simeq \left(1 - \frac{i\Delta t\hat{H}}{\hbar}\right)\psi_m^n \tag{7}$$

Consequently, we can write the relation between the time-steps ψ_m^{n+1}, ψ_m^n and ψ_m^{n-1} as:

$$\psi_m^{n+1} - \psi_m^{n-1} = \left(e^{-i\Delta t\hat{H}/\hbar} - e^{i\Delta t\hat{H}/\hbar}\right)\,\psi_m^n \simeq -2\left(\frac{i\Delta t\hat{H}}{\hbar}\right)\psi_m^n \tag{8}$$

By splitting the wave function in its real and imaginary parts, $\psi_m^n = u_m^n + iv_m^n$, where u and v are real functions, we can evaluate the entire wave function in the same time step. Using the Taylor expansion to estimate the second order spatial derivative, $\frac{\partial^2\psi}{\partial x^2} \simeq \frac{\psi(x-\Delta x)-2\psi(x)+\psi(x+\Delta x)}{\Delta x^2}$, the system of equations to solve becomes:

$$u_m^{n+1} = u_m^{n-1} + 2\left(\frac{\hbar\Delta t}{m\Delta x^2} + \frac{\Delta t}{\hbar}U_m^n\right)v_m^n - \frac{\hbar\Delta t}{m\Delta x^2}\left(v_{m-1}^n + v_{m+1}^n\right) \tag{9a}$$

$$v_m^{n+1} = v_m^{n-1} - 2\left(\frac{\hbar\Delta t}{m\Delta x^2} + \frac{\Delta t}{\hbar}U_m^n\right)u_m^n + \frac{\hbar\Delta t}{m\Delta x^2}\left(u_{m-1}^n + u_{m+1}^n\right) \tag{9b}$$

By this approach we do not need to obtain the eigenstates of the dynamic QD potential for each time step. Instead, we calculate the eigenbasis only at the beginning of the simulation to form the initial wave function based on an exponentially decreasing occupation of the eigenstates as presented in equation 4 on page 99. Solving the system of equations 9 for each successive time step, we then calculate the evolution of the wave function in the dynamic potential landscape that is given by the electrostatic potential defined by the surface gates and the potential modulation of the moving SAW train. We solve the time-dependent Schrödinger equation over the entire tunnel-coupled region using Dirichlet boundary conditions. The boundaries are sufficiently far away from the position of the wave function such that no reflections are observed. To obtain the occupation of the eigenstates after a certain propagation time of the wave-packet, t_P, we calculate the eigenstates of the SAW-modulated potential landscape only for the present time step (t_P) and decompose the wave function in that basis. The method we use is shown to be convergent and accurate [MLP00].

To find possible sources of excitation leading to the occupation of eigenstates at higher energies, we simulated the time-dependent propagation of the electron along different sections of our beam-splitter device. Simulating electron propagation along the injection channel, we find no significant excitation in this part of the quantum rail. As we prepare the electron directly after the source QD initially in the ground state, we find that the wave function basically remains in that state after propagation to the entrance of the tunnel-coupling region. We observe only 3 % excitation due to a change in momentum along the angled part of the injection channel.

At the entrance to the tunnel-coupled region we find however an abrupt change in electrostatic potential confinement as pointed out in Fig. 42 on page 97. Performing time-dependent simulations of the injection process of the SAW-transported electron into the double-well potential, we observe significant excitation of the electron state. Figure 45a shows an exemplary trace (red) of the electron wave function for this situation. The abrupt change in potential confinement causes Landau-Zener transitions into excited states at higher energies. The excitation causes that a small part of the wave function couples to the lower quantum rail since it encounters a sufficiently high tunnel-coupling energy.

To approximate the experimentally observed data with the two-dimensional time-dependent simulations, we assume on the other hand an equal spreading among the two quantum rails with exponentially decreasing occupation of the eigenstates[9]. The black trace shows the time-dependent propagation for such a state. Comparing the red and the black traces we find thus a significant difference in

[9]Compare equation 4 of the one-dimensional model on page 99. To have a similar outcome as in the one-dimensional stationary model, we have to increase the initial excess energy to $\varepsilon \approx 7$ meV in the two-dimensional time-dependent simulation.

the spreading of the electron wave function among the two channels. In the experimentally observed behaviour we observe equal partitioning ($P_U = 50$ %) at zero potential detuning ($\Delta \approx 0$ V). We suspect that the deviation to experiment stems from an overestimated scale of the potential calculation. Decreasing the

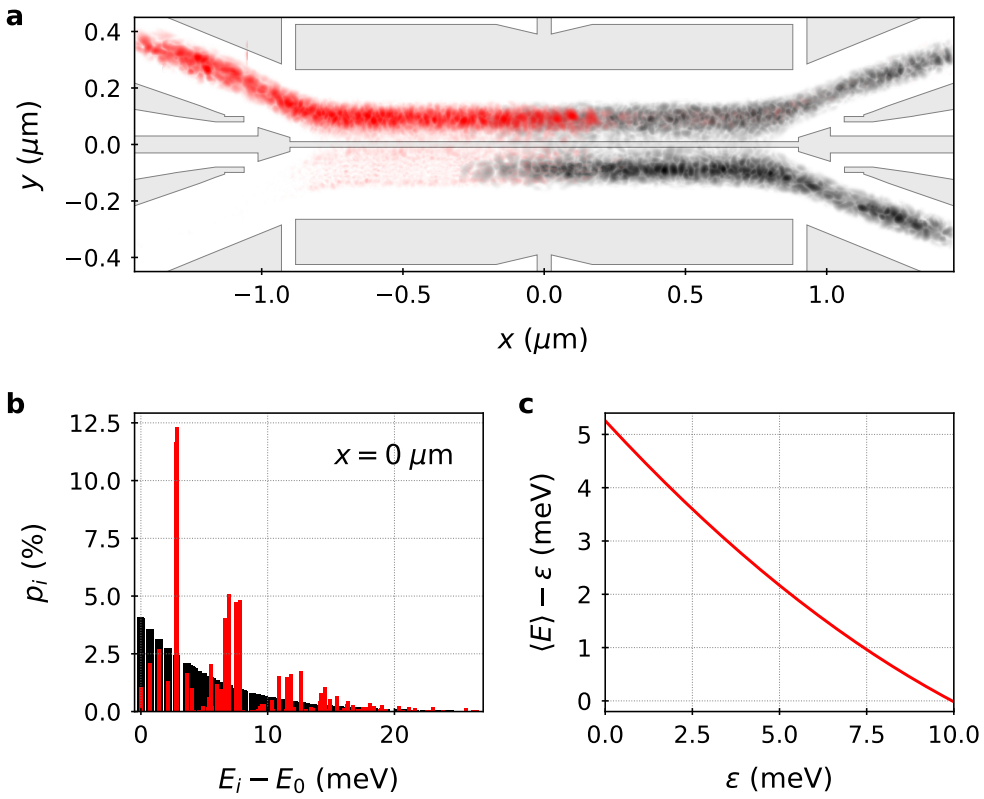

Figure 45: Comparison of time-dependent simulations of electron transport. **(a)** Propagation of the electron wave function with a moving QD of the SAW along the tunnel coupled region with symmetric potential detuning ($\Delta = 0$ meV) for two-scenarios: The black trace shows electron propagation from the center ($x < -1$ μm) to the exit of the tunnel-coupled region ($x > 1$ μm). The initial extent of excitation was chosen via an occupation parameter $\varepsilon = 7$ meV. In this configuration the time-dependent simulation reproduces the experimental measurement. The red trace shows on the other hand electron propagation from the injection channel ($x < -1$ μm) to the center of the tunnel-coupled region ($x = 0$ μm). Also for this exemplary trace the initial configuration is defined via $\varepsilon = 7$ meV. Here the tunnel-barrier voltage is set to $V_T = -0.85$ V. **(b)** Comparison of the eigenstate-occupation distribution, p_i, of the aforeshown red and black traces as function of eigenstate energy, E_i, with respect to the ground state (E_0) at the center of the tunnel-coupled region. **(c)** Increase of the expected electron energy, $\langle E \rangle$, due to excitation as function of initial state occupation, ε. Assuming an initial occupation with $\varepsilon \approx 10$ meV, the expectation energy is predicted to remain constant after propagation to $x = 0$ μm.

tunnel barrier voltage to $V_T = -0.6$ V in our simulations, we find equal partitioning among the two-channels as in experiment. We will address this aspect by the end of this section. Let us note at this point that the employed theoretical model does not take into account relaxation mechanisms. The presence of such energy dissipation processes could allow the electron wave function to occupy lower energy states much faster than in the present simulations. Since relaxation from a certain eigenstate further opens up subsequent occupation from other parts of the electron wave function, we suspect that energy dissipation could be an additional reason faciliating the spreading of the wave function into both sides of the double-well potential.

Let us now investigate the aspect of charge excitation at injection into the TCW in more detail and compare the eigenstate-occupation of the moving QD that carries the electron in the center of the tunnel-coupled region (red) to the situation that approximates the experimental partitioning results (black). Figure 45b shows a histogram of the eigenstate occupation for the two aforementioned traces at this position ($x = 0$ μm). Comparing the final eigenstate occupation of the red trace to the initial exponential distribution of the black trace, we find strong overlap of the two distributions. This indicates qualitatively that the presence of energy relaxation likely causes an occupation of the eigenstates that exponentially decreases with energy.

Performing the time-dependent simulation of electron propagation from the injection channel to the middle of the coupling region for different initial expectation energies, ε, we find an increase of energy as shown in Fig. 45c. Assuming initial ground state occupation in the injection channel, we obtain an increase of the electron energy of about 5 meV after propagation to the center of the tunnel-coupled region. This value is about 2 meV smaller than the excitation energy that we need to assume to approximate the experimental data. For a larger initial excess energy, ε, the extent of the excitation decreases. It is therefore possible that there is already a certain degree of energy increase from additional sources of excitation before the entrance into the tunnel-coupled region. There are two-possible scenarios. Firstly, there might be a corrugated potential background from the Si ions in the δ-doped layer which might cause a continuous potential fluctuation for the SAW-transported electron. Secondly, there might be excitation at the sending process at the source QD. The deviation could however also be simply related to the incompleteness and uncertainties of the employed model what would coincide with the aforementioned concerns. Since the simulation does not provide a complete image of the experimentally present situation, we cannot give an exact estimation of the total excitation energy and the increase in energy at the entrance into the tunnel-coupled region. The simulations provide however an estimate of the extent of charge excitation in the tunnel-coupled region that is in the order of a few meV and allow to clearly identify a major problem in the

presently employed beam-splitter setup.

Considering uncertainties in the potential calculations, it makes sense to vary the model parameters to mimic the experimental situation. For this purpose, we adjust in the following the height of the tunnel-barrier from $V_T = -0.85$ V to $V_T = -0.6$ V. This change allows us to achieve an equal spreading of the wave function of the flying electron at injection into the tunnel-coupled region as observed in experiment. Changing the simulation parameters in this model system, we can obtain new insights that are useful for experimental follow-up investigations. In the following we will particularly address changes of the SAW amplitude. To quantify adiabatic transport of the flying charge qubit, we define the qubit fidelity, F, as projection of the electron wave function on the two lowest eigenstates of the moving QD potential that is formed by the SAW along the coupled quantum rails. Figure 46a shows courses of the qubit fidelity, F, of a flying electron state that propagates along the tunnel-coupled region for different values of peak-to-peak SAW amplitude, A. For the present experiment we estimate A as 17 meV. For this value (red solid line) the simulation data shows an abrupt reduction of the qubit fidelity, F, due to the aforementioned excitation of the SAW-transported electron at injection from a single quantum rail into the tunnel-coupled region. In congruence with the experimental observation, in this case the electron wave function spreads out over both sides of the double-well potential as shown in Fig. 46b.

Let us now investigate if we can reduce the probability for charge excitation by increasing the longitudinal confinement via the SAW amplitude. For $A = 30$ meV – see red dashed line in Fig. 46a –, charge excitation is already strongly mitigated. The qubit fidelity vanishes however also in this case, since the electron still occupies low-energy states above the two-level system we are striving for. Despite non-adiabatic transport, we can already recognise coherent tunnel oscillations when looking at the trace of the wave function. This shows that also excited electron states can undergo coherent tunneling processes as previously expected in magnetic-field-assisted experiments on continuous SAW-driven single-electron transport through a quantum rail that is tunnel-coupled to an electron reservoir [Kat09]. Increasing the SAW amplitude further to $A = 45$ meV (blue solid line), the transport of the electron gets nearly adiabatic and clear coherent tunnel oscillations occur as shown in Fig. 46c. The simulations show that stronger SAW confinement can indeed prohibit charge excitation and maintain adiabatic transport. In experiment one can increase the SAW confinement via many ways such as reduced attenuation of the IDT signal, longer IDT geometries, impedance matching or the implementation of more advanced SAW generation approaches [Sch15; Eks17; Dum19].

Simulating the entrance of the SAW-transported electron into the coupling region, we showed up a major source of charge excitation that significantly affects the

intended functionality of the present beam-splitter device. Having understood the underlying processes of charge excitation, we can engineer enhanced geometries of tunnel-coupled quantum rails to remedy this problem in future devices. Enhanced calculations of the electric potential and time-dependent simulations of electron propagation will help to achieve a proper design of the surface gates allowing a sufficiently smooth potential landscape. To reduce the effect of charge excitation it will be equally important to increase the confinement of the electron within the SAW train. Comparing the transition width of the directional coupler operation to the present experiment, we can assess the success of the implemented changes. In this perspective, we anticipate that adiabatic transport of a flying charge qubit is feasible in the present semiconductor framework.

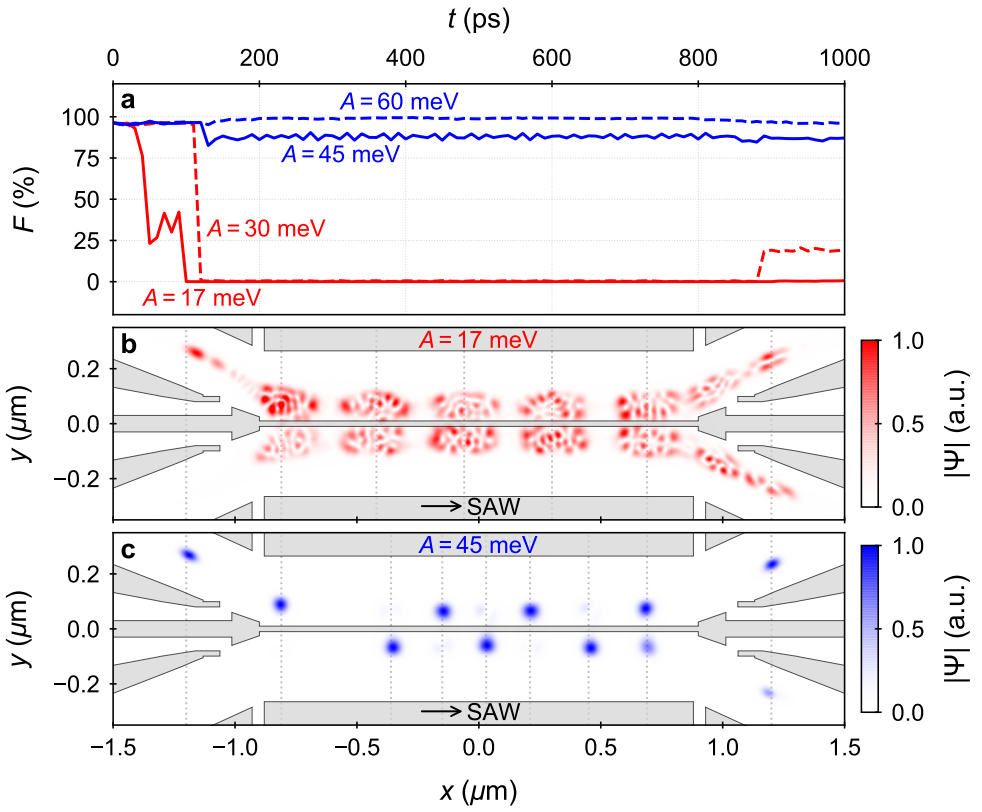

Figure 46: Time-dependent simulation of electron propagation. (a) Course of the qubit fidelity, F, for SAW-driven single-electron transport along the coupling region for different values of SAW amplitude, A. **(b)** Trace of the electron wave function, Ψ, along the coupled quantum rails for $A = 17$ meV at selected times, t, indicated via the vertical dashed lines. The grey regions indicate the surface gates. **(c)** Trace of Ψ for $A = 45$ meV. From our publication Takada *et al.* [Tak19].

2.3.4 Synchronisation via voltage-pulse triggering

The extremely high transfer efficiency makes SAW-driven single-electron transport a promising candidate to couple a pair of electrons in a beam-splitter setup such as the present device. In the long run, this electron-coupling could enable entanglement of quantum information at the single-particle level as discussed in section 2.1.2. In order to achieve this goal, electrons must be however sent simultaneously from different sources in a specific position of the SAW train. Sending an electron from a stationary source QD only by a SAW, the particle is typically transferred with one of the first sufficiently strong potential modulation minima of the SAW train. To accomplish synchronised transfer of single electrons along parallel quantum rails, it is thus necessary to address a specific location in the SAW train to transfer the electron.

In the following, we demonstrate a voltage-pulse triggered single-electron source that meets this requirement. The implemented approach is a proposal from a pioneering work of SAW-driven single-electron transport [Her11]. The idea is to bring an electron in a configuration where it can almost be picked out by the SAW. Applying a short voltage pulse in the right moment during the arrival window of the SAW, the electron is then brought in a temporarily unprotected configuration allowing the particle to escape at a specific location of the potential modulation train accompanying the SAW – see schematics in Fig. 47a and Fig. 47b. To demonstrate that the loaded electron is really sent in a specific position of the SAW, it is necessary that the duration of this short pulse is sufficiently small – shorter than the periodicity of the SAW.

We can assess the feasibility of this voltage-pulse trigger first by means of the aforementioned sending maps – see Fig. 38c-f on page 88. Let us focus on the vertical transition that occurs with a voltage sweep on the reservoir gate, δV_{R}. And let us further keep the voltage on the coupling gate constant ($\delta V_{\mathrm{C}} = 0.0$ V). As we push the initially loaded electron towards the transport channel via more negative value of δV_{R}, at some point the electron is in a configuration where it can be picked up by the SAW. Applying an additional voltage pulse on the pulsing gate of the source QD during the arrival window of the SAW, this transition region is shifted. The extent of this shift determines the region of possible pulsed sending configurations. Thus, the pulse amplitude is crucial for the implementation of a voltage-pulse triggered single-electron source. The pulse-introduced shift in the sending map sensitively depends on the strength and duration of the pulse and also on the geometry and voltage configuration of the surface gates defining the QD.

To accomplish an efficient triggering process, an abrupt holding-to-sending transition in δV_{R} is preferable. With such a feature, also for smaller shifts of the sending map transition, a sending trigger can be implemented. Obtaining a suffi-

ciently strong effect of the voltage pulse, a proper sending position for the desired triggering functionality can be chosen as shown in the temporary configuration T in Fig. 38e-f: In this sending position, electron transport is not possible as only the SAW-train propagates through the source QD and no picosecond voltage pulse is present. As a short voltage pulse is additionally applied with a delay that is in time with the arrival window of the SAW, however, the electron is transferred in the respective moving QD that accompanies the SAW.

Here we send the voltage-pulse trigger via the plunger gate of the source QD to provoke single-electron transfer – see highlighted surface gate in Fig. 47a. The measurement scheme to demonstrate the feasibilty of the sending trigger is shown in Fig. 47b: to transfer a single electron from the source QD into a specific potential modulation minimum of the SAW, the delay (τ) of a sufficiently short voltage pulse is adjusted with respect to the IDT signal to an appropriate position in the temporal arrival window of the SAW. To demonstrate the feasibility of this trigger, we use now an ultrashort voltage pulse of 90 ps what corresponds to a quarter SAW period [Rou18][10].

Sweeping the delay of this pulse, τ, over the arrival window of the SAW, we observe distinct fringes of transfer probability, P, as shown in Fig. 47c. For each measurement point of the transfer probability 800 repetitions were performed. The data shows clearly distinguishable fringes of high transfer probability that appear along a time frame of about 20 ns. Comparing the envelope of these transfer fringes to the actual length of the SAW train – that is about 52 ns for a 30 ns long RF signal on the IDT –, we find that the voltate pulse trigger starts to work at relatively high SAW amplitude. Sweeping the delay of the voltage pulse in finer steps of 10 ps along four SAW periods where transfer is activated by the trigger, we obtain a zoom into the central part of the fringes as shown in Fig. 47d. The data clearly shows that the fringes are exactly spaced by the SAW period. This periodicity indicates that there is a particular phase along the SAW train where a picosecond pulse can efficiently transfer an electron from the stationary source QD into a specific SAW minimum. As the voltage pulse overlaps in time with this phase, transfer is activated and the efficiency rapidly goes up from (2.7 ± 0.5) % to (99.0 ± 0.4) %.

Let us now try to quantify the threshold of the SAW amplitude to make the voltage pulse trigger work. For this purpose we analyse the envelope of the transfer-probability fringes shown in Fig. 47c. Figure 48 graphically shows the approach of the estimation. The fringes of transfer probabilty shown in Fig. 47c

[10] To send the electron in a specific SAW-minimum one can in principle also use a much longer pulse. With a pulse duration exceeding one SAW period, however, it is not possible to show that the electron is really sent at a specific position of the SAW train. Here a 180-ps-long pulse would have been actually better, since the rise time of the voltage pulse is 200 ps to 80 % of total amplitude.

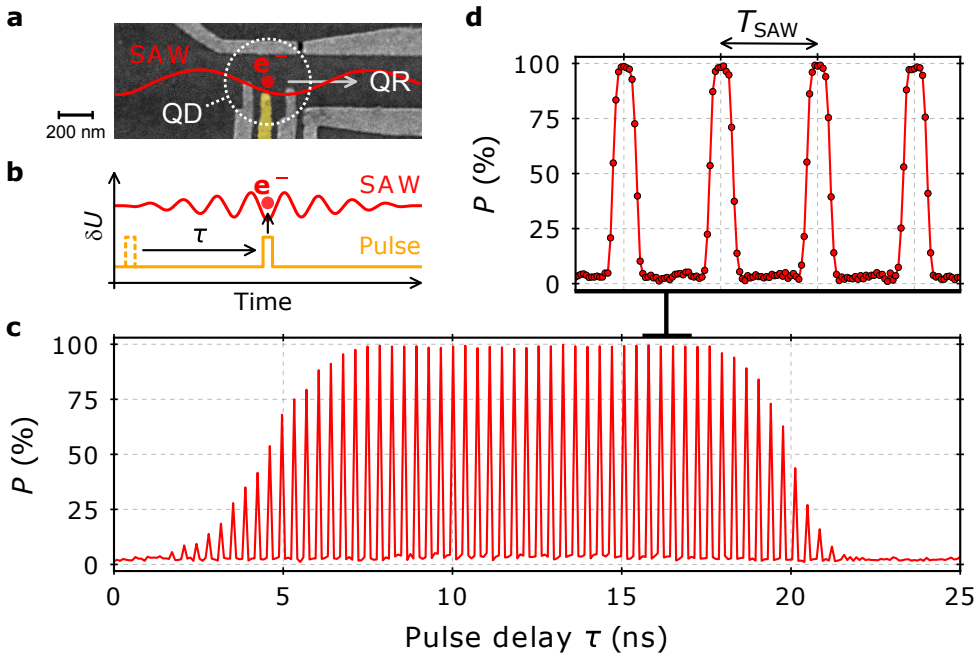

Figure 47: Pulse-triggered single-electron transfer. **(a)** SEM image of the source quantum dot (QD) showing the pulsing gate highlighted in yellow. A fast voltage pulse on this gate allows to trigger SAW-driven single-electron transport along the quantum rail (QR). **(b)** Measurement scheme showing potential modulation, δU, at the stationary source QD: The delay of a fast voltage pulse, τ, with respect to the IDT signal is swept along the arrival window of the SAW at the QD. **(c)** Measurement of probability, P, to transfer a single-electron with the SAW from the source to the receiver QD for different values of τ. **(d)** Zoom in a time frame of four SAW periods, T_{SAW}. From our publication Takada *et al.* [Tak19].

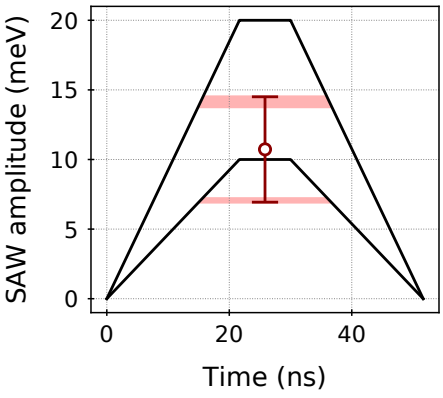

Figure 48: Estimation of the sending threshold of the SAW modulation with additional voltage pulse. The solid lines show the boundaries of the expected SAW profile in terms of peak-to-peak potential modulation amplitude. The red areas indicate the correspondingly estimated frames of time and SAW amplitude. From the limits of these regions we can estimate the sending threshold – shown here as errorbar.

are visible over a range of (21 ± 1) ns. For a resonant RF signal of duration $T_{\mathrm{RF}} = 30$ ns launched from the presently employed IDT ($T_{\mathrm{IDT}} \approx 22$ ns), the amplitude profile of the SAW follows a trapezoidal shape reaching maximum amplitude for $T_{\mathrm{RF}} - T_{\mathrm{IDT}} \approx 8$ ns. Additionally, we can estimate the peak-to-peak amplitude of the SAW from experimental investigations of CBP broadening[11]. Doing so, we deduce the SAW amplitude as as (15 ± 5) meV for the presently applied transducer power. With this information we can draw now the expected boundaries of the SAW profile as shown as solid lines in Fig. 48. Spanning now the regions of the sending (red area) below these trapezoids, we can roughly estimate the sending threshold as (11 ± 4) meV – see errorbar shown in Fig. 48. This investigation shows that a relatively large amplitude of the SAW modulation is necessary activate voltage-pulse triggered single-electron transfer with the presently employed setup.

In the present demonstration of a SAW-driven single-electron transfer that is triggered by a fast voltage pulse we have a sending background (about 2.7 %) and did not achieve maximum of the transfer efficiency (only 99.0 %). We anticipate however further enhancements in trigger efficiency by reduction of pulse attenuation and improvement of the QD structure allowing to exploit the full efficiency of single-electron transport also with sending trigger. The most critical factor for an efficient voltage-pulse-triggered sending process, is the aforementioned abruptness of the holding-to-sending transition of the sending map. This feature can be also enhanced simply by tuning the voltages applied on the QD gates. The present pulsing configuration is however sufficient to demonstrate the triggered single-electron source enabling a synchronised SAW-driven sending process.

2.3.5 Time of flight measurements

In the previous section we have demonstrated voltage-pulse-triggered transfer of a single electron from the source QD into a specific position of the SAW train. As a next step, we investigate the question whether the transferred electron stays in the addressed moving QD as the SAW train propagates along the 22 μm long quantum rail structure of the present beam-splitter setup. To obtain such information, we can measure the time of flight of the transported electron. For this purpose, we apply a pulsing approach at the receiver QD that is similar to the aforementioned triggered single-electron source. For the present setup, it turned out that a picosecond voltage pulse is not a good option to probe the arrival time of the electron, since the measured catching distribution is artificially biased by the SAW-duration[12].

[11] The SAW-introduced CBP broadening is presented in appendix G.

[12] Such a picosecond voltage pulse can be used, however, to probe the arrival of the SAW at the receiver QD when an electron is directly loaded at a receiver QD – see appendix H.

To reliably probe the arrival time of a flying electron at the receiver QD, it is necessary to use a pulse shape following a Heaviside step function. The principle to measure the time of flight is schematically shown in Fig. 49a. The sending process at the source QD is triggered by a short voltage pulse such that the electron is picked up by a specific moving QD of the SAW train. For the time-of-flight measurement, we keep the delay of this source pulse fixed. The delay of the step pulse at the receiver QD is chosen on the other hand such that it initially lies outside of the arrival window of the SAW. Here we have chosen to make the step initially occurring before the SAW such that the catching probability is high in the initial receiver QD configuration[13]. Turning off the step pulse, the catching probability decreases and we can obtain the contrast of the time of flight measurement in the transfer probabilty[14]. We then increase the delay of the step pulse and scan the transfer probability over the arrival window of the SAW. As we do so, the moving QDs of the SAW arrive one after the other in a configuration where catching at the receiver QD is no longer possible. If the exposed moving QD contains no electron, this has no effect on the measured catching probability. If the exposed moving QD on the other hand contains an electron, the catching probability decreases corresponding to the effect of the voltage step.

Let us consider first the hypothetical situation where the electron is always transferred in one specific SAW minima along the whole quantum rail. Let us further assume that the shape of the step pulse is a perfect Heaviside step function. For this ideal case, the transfer probability abruptly jumps down as the receiver step pulse delay is swept over the arrival time of the moving QD carrying the electron. In the case that the arrival time of the electron is distributed over several SAW-minima on the other hand a gradual diminution of the catching probability is expected. The transition that is measured in this way basically represents the convolution of the step pulse with the distribution of electrons in the SAW when it passes through the receiver QD. Mathematically, the convolution of a Heaviside step function with a certain function represents the integral of that function. With a step pulse we can thus obtain the approximate arrival distribution of the flying electron in the SAW by calculating the derivative of the measured transfer probability with respect to the delay time of the step pulse.

In experiment we realise the step function by a long voltage pulse that completely

[13]The catching configuration determines whether the initial catching probability is high or low. Depending on this choice and the profile of the sending maps, one has to set the sign of the step pulse such that maximum visibility of the time of flight measurements is achieved. Here we chose an initial receiver configuration where the electron is initially caught with high probability.

[14]The contrast of the time of flight measurements is basically determined by the form of the catching maps – see for instance Fig. 39 on page 90. As for the triggered single-electron source discussed in section 2.3.4, an abrupt transition is preferable. Since such an abrupt transition was not apparent in our catching maps, we had to work at a gradual transition what caused a relatively low contrast of about 75 %.

covers the arrival window of the SAW. Investigations with a fast sampling oscilloscope showed a rise time of about 200 ps to 80 % of the total pulse amplitude – see section 2.2.1. With this rise time, the calculated arrival distribution of the flying electron gets slightly broadened by the step pulse via the convolution of the two functions. Since the rise time of the step function is only about a fifths of a SAW period, this effect should be however negligible. With the present setup it should be thus possible to resolve the arrival probability for each SAW minimum.

We first employ this step pulse to measure the arrival distribution of a flying electron that is transferred only by a SAW – no pulse trigger is used at the source QD now. Doing so, we obtain data as shown in Fig. 49b. We can fit the transfer-probability transition by the integral of a Poisson distribution as shown by the black line. Calculating the derivative of this fit we obtain the approximate arrival distribution of the SAW-transported electron – see red line on the right axis. Interestingly, we find that no electrons arrive in the first ten periods of the SAW train. The data shows that the arrival distribution of the electron is spread out mainly over 14 SAW minima (FWHM) in the middle of the SAW train. Since the SAW amplitude does now increase along this part of the SAW train, the data clearly indicate that the transferred electron is dragged back in subsequent SAW minima as it travels along the quantum rail of the present beam-splitter setup.

Let us now investigate how the arrival distribution changes, as a voltage pulse is used to trigger transport at the source. The time-of-flight measurement for this situation is shown in Fig. 49c. The arrow indicates the arrival-time that is expected, if the flying electron stays in the SAW minima in which it was initially transferred at the source QD by the voltage pulse trigger. If the electron that is sent at this SAW position is not dragged in subsequent SAW minima, an abrupt jump would appear at this location in the transfer probability data. Contrary to this, we observe subsequently after this position a gradual reduction of the transfer probability that ranges over a time frame of about 5 ns. Compared to the SAW-only situation, we find a narrowing of the arrival distribution to 9 SAW minima (FWHM) with additionally activated pulse triggered source. Comparing the location of the distribution of the transferred electron in the SAW train to the expected arrival time (arrow), we obtain another indication that the electron is dragged into subsequent SAW-minima during transport.

We can now further remeasure the arrival distribution of the electron for different delay times of the pulse trigger at the source QD. So we perform the same procedure as presented in Fig. 49c, but change the initial position of the electron in the SAW train for each time-of-flight measurement. Doing so, we obtain a probability distribution of the arriving electron as shown in Fig. 50a. The transfer probability data is shown by the grey two-dimensional data map. The corresponding arrival distribution is shown by the red contour lines. The dashed, red line indicates the arrival time of the flying electron that is expected for the

hypothetical case that it remains in its initial position in the SAW train during transport. The data shows that the arrival distribution follows the delay of the sending trigger at the source QD. We further see that the electron is dragged back, but remains within the SAW train for pulse delays at the source shorter than 435 ns.

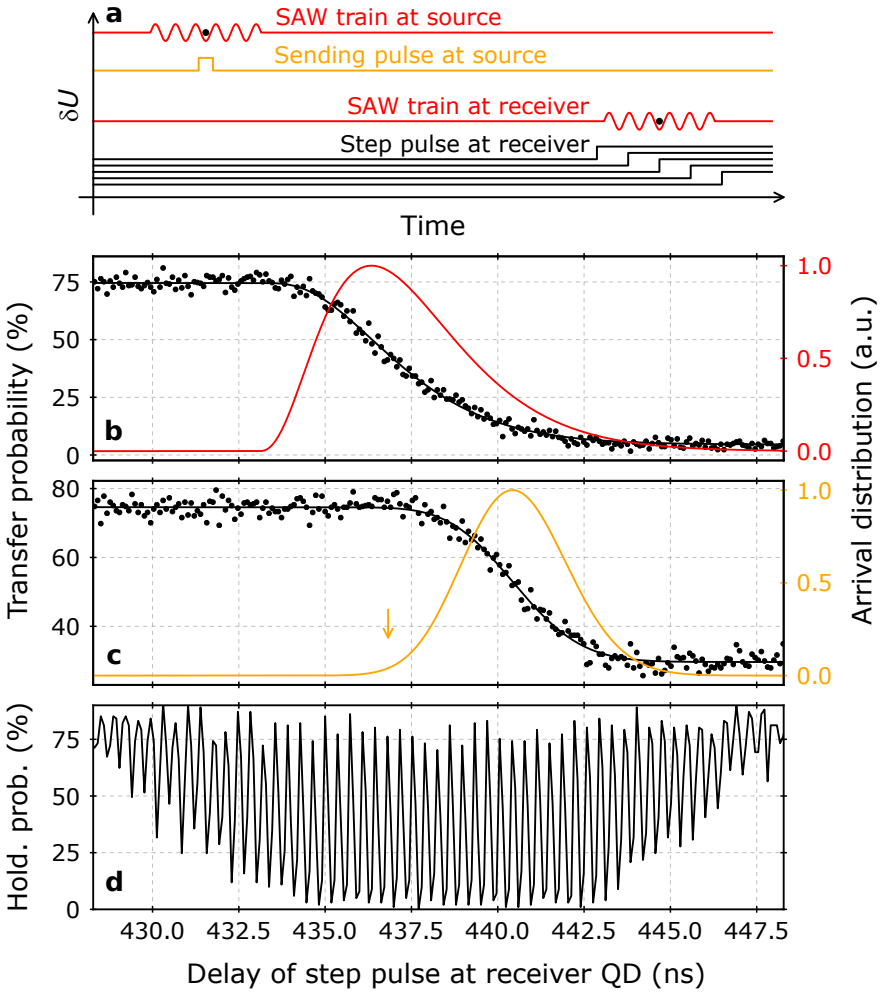

Figure 49: Measuring the arrival distribution at the receiver. (a) Schematic showing the measurement procedure. **(b)** Measurement of transfer probability as the delay of a step pulse is swept over the arrival window of the SAW at the receiver quantum dot (QD). The black curve shows a fit to that data. The derivative of this fit represents the arrival distribution show in red on the right axis. Here an electron is sent from the source side only by a SAW. **(c)** Transfer probability (black) and fit (orange, right axis) as in subplot (b). Here additionally a pulse trigger is present at the source QD. The accordingly expected arrival time of the electron is indicated by the orange arrow. **(d)** Reference plot showing the arrival window of the SAW measured via the holding probability – see appendix H.

We can now also perform this time-of-flight measurement for diagonal transfer across the single-electron circuit of tunnel-coupled quantum rails. Let us discuss the situation where we measure the time-of-flight for SAW-driven transfer of an electron from the upper source QD to the lower receiver QD. Lowering the tunnel-barrier, we can exploit transversal energy detuning (Δ) to send the electron diagonal along the beam-splitter device from the upper source QD to the lower receiver QD. Remeasuring the time of flight for this situation we obtain data as shown in Fig. 50b. The data shows an electron delay that is consisted with the measurement along the upper quantum rail. But we see that the cut-off time of the source delay where we loose the electron during transport occurs about 3 ns (8 SAW periods) earlier. Having a closer look, we further find that the electron distribution is about two SAW-periods wider. This finding underpins that the delay of a SAW-transported electron is sensitive to the potential in the tunnel-coupled region.

Previous time-of-flight measurements of SAW-driven single-electron transport in a straight 4-μm-long channel showed that the arrival distribution of the electron is smaller than 3 successive SAW minima[15]. Follow-up investigations of SAW-driven transport of spin qubits in such a linear structure recently underpinned that the electron stays in a certain SAW minimum for transport along a straight quantum rail[16]. The major differences of the present beam-splitter setup to a straight channel are the kinks along the bended quantum rails and the changes in electrostatic potential at the transitions of the quantum rails to the tunnel-coupled region. Our time-dependent simulations of SAW-driven single-electron transport along a bended channel – see section 2.3.3 – showed that the potential is sufficiently smooth along a kink such that the electron remains in the position of the SAW train during transport. Simulating electron propagation into the tunnel-coupled region, however, we found significant excitation that likely allows the electron to escape in subsequent position of the SAW train, particularly at the exit of the TCW. Considering the extent of the estimated charge excitation, it is not surprising that the electron is dragged back in subsequent positions within a SAW train when the electron trespasses the tunnel-coupled region. This would explain, why we also observe a strong dependency of the directional coupler transition on the exit potential of the TCW. The different delays for straight and diagonal single-electron transfer along the tunnel-coupled region additionally underpin this hypothesis. Based on the outcome of time-dependent simulations and the effects of the tunnel-barrier potential on the width of the directional coupler measurement, we thus identify the abrupt transition in the potential landscape from the injection channel into the tunnel-coupled region as major

[15] In these time-of-flight measurements it was not possible to resolving each SAW minimum because the duration of the voltage pulse that was limited to 1 ns for the employed signal generator.

[16] The investigations were conducted as the present thesis at the Institute Néel in Grenoble.

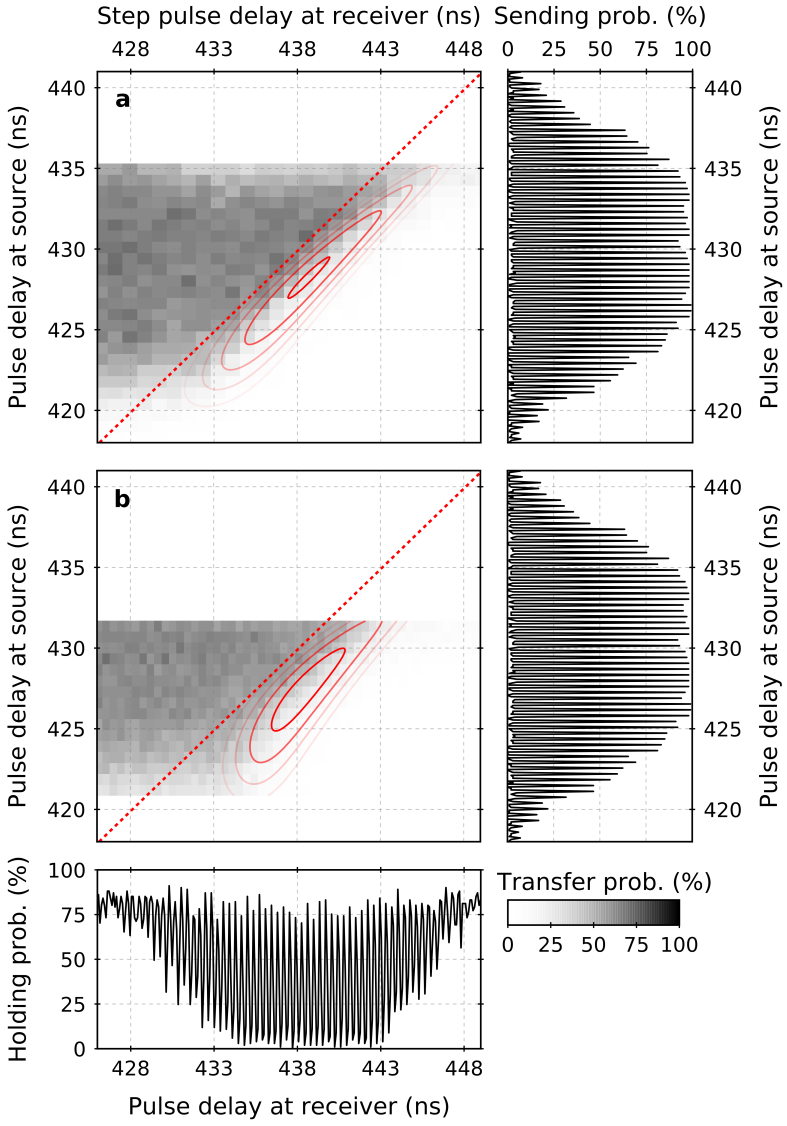

Figure 50: Arrival distribution for different delay time of the sending trigger. The two-dimensional data shows the transfer probability as function of the pulse delay at the source QD (vertical axis) and step-pulse delay at the receiver QD (horizontal axis) for **(a)** straight and **(b)** diagonal transfer along the beam-splitter setup. The red contour lines show the electron distribution obtained from the derivative of the fit of the transfer probability with respect of the receiver delay (horizontal axis) – compare Fig. 49 on page 113. The dashed line indicates the expected arrival time of the electron assuming that it the moving QD of the SAW-train with which it was initially sent with. The plots to the right and bottom serve as guide to the eye and indicate the arrival of the SAW train at the source and receiver QD – for details see appendix H .

source of excitation. Having understood the central limiting process in the present system, we should be able to engineer an experimental frame allowing to perform adiabatic SAW-driven transfer of a single-electron in a two-level system.

Let us finally mention possible strategies for reducing charge excitation and thus the electron-delay in a SAW-driven flying electron circuit: One idea that suggests itself is to realise gradually bending channels that smoothly guide the electron in the tunnel coupled region. Such a geometry prohibits abrupt changes in the channel direction, but still suffers from the changes in potential landscape at the connections to the tunnel-coupled region. A rather simple but appealing idea going beyond this concept is inspired by ballistic electron interferometry experiments as discussed in section 1. The idea is to have a completely linear device where the electron encounters coupling between the quantum rails at specific positions along the structure. Spanning this idea further with dynamical tunnel-barrier control on the picosecond scale, one should be able to probe electron coherence and quantum logic gate operations in a very systematic way. A more detailed discussion of this proposal is presented in section 2.5.2. Another approach to remedy the blockage of the SAW-transported electron could simply be to increase the amplitude and the confinement of the transported electron in the SAW. Investigations in this direction will be in the focus of future investigations of SAW-driven single electron transport in a beam-splitter setup. An increased amplitude of the SAW could be already simply achieved by reducing the attenuation of the IDT signal along the RF line. Additional approaches for enhancement of SAW confinement are presented as perspective in section 2.5.1 of this thesis.

2.3.6 Probability oscillations with tunnel barrier potential

With the presently investigated SAW-driven circuit of tunnel-coupled quantum rails, we aim to convey a flying charge qubit state and to manipulate this quantum mechanical object in flight. As a flying electron occupies the lowest eigenstate in the double-well potential, we expect the electron wave function to tunnel from one quantum rail to the other if the potential barrier is sufficiently low. In this situation, we should observe complementary tunnel oscillations in the transfer probabilities, P_{U} and P_{L}, as we decrease the voltage on the tunnel-barrier electrode, V_{T}. These probability oscillations should become gradually faster with reduced tunnel barrier height (smaller V_{T}) since we increase the coupling energy, ΔE[17]. Moreover, the oscillating features in P_{U} and P_{L} should flip as we switch the injection channel. The probability oscillations are additionally expected to be extremely sensitive on energy potential detuning, Δ, of the tunnel-coupled region[18].

[17] See equation 3 on page 55.

[18] A simplified derivation of these expected features is provided in appendix I.

Our investigations of SAW-driven single-electron transport have shown that adiabatic transport in a two-level system is at the current stage not achievable due to charge excitation in present setup. In previous experimental investigations of a continuous SAW-driven electron transport along a quantum rail that is coupled to an electron reservoir it was nevertheless shown that also excited electron states can experience coherent oscillations and tunneling [Kat09]. In the presently investigated device we have observed oscillations in the transfer probabilities that correlate with a change of the barrier potential and that could be thus interesting in that perspective.

As we sweep the tunnel-barrier voltage, V_T, over a large range, we have to compensate the changes in transverse confinement and absolute potential via the side gates, V_U and V_L, in order to maintain the flying electron in the SAW during transport. Sweeping the tunnel-barrier voltage, V_T, with symmetrically compensating voltages of the side gates, V_U and V_L, according to:

$$\begin{bmatrix} V_\mathrm{T} \\ V_\mathrm{U} \\ V_\mathrm{L} \end{bmatrix} = \begin{bmatrix} -1.2 \\ -0.8 \\ -0.68 \end{bmatrix} + \alpha \begin{bmatrix} +0.90 \\ -0.45 \\ -0.45 \end{bmatrix} \text{ (V)}, \; \alpha \in [0, 1], \tag{10}$$

we observe no tunnel oscillations, but independent transitions in the transfer probabilites, P_U and P_L, which occur over a rather large voltage range of about 100 meV – see Fig. 51. The onset of the transition at $V_\mathrm{T} \approx -1$ V linearly depends on the sum of the side gate voltages, $V_\mathrm{U} + V_\mathrm{L}$, and the potential of the injection channel. The change in the transfer probabilities at $V_\mathrm{T} \approx -0.55$ V on the other hand sensitively depends on the exit potential of the tunnel-coupled region. There is no indication that this transitions is related to the tunnel effect. The absence of clear tunnel oscillations in a two-level system is likely related to the excitation of the SAW-transported electron.

To better understand SAW-driven single-electron transport in such a tunnel-coupled setup, we investigate how P_U and P_L behave as we change the injection channel. Differently speaking, we investigate the effect of sending a single-electron from the lower instead of the upper source QD. Let us discuss in the following a

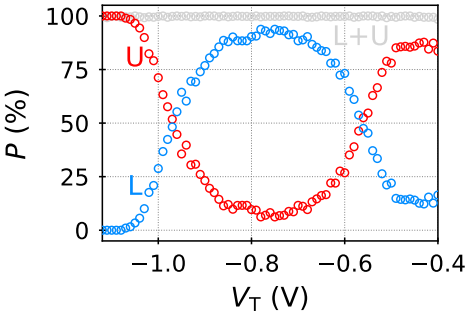

Figure 51: Probability transitions occurring with gradual change of tunnel barrier and symmetric compensation of side gates. Normalised probability to transfer a single electron to the upper (U) or lower (L) receiver QD for different voltages V_T applied on the tunnel-barrier electrode. Here the voltages V_T, V_U and V_L are linearly changed according to equation 10.

tunnel barrier sweep with asymmetric compensation of confinement by the side gates[19]:

$$\begin{bmatrix} V_\mathrm{T} \\ V_\mathrm{U} \\ V_\mathrm{L} \end{bmatrix} = \begin{bmatrix} -1.20 \\ -0.97 \\ -0.80 \end{bmatrix} + \alpha \begin{bmatrix} +0.90 \\ -0.28 \\ -0.50 \end{bmatrix} \text{ (V)}, \ \alpha \in [0, 1] \tag{11}$$

Figure 52 shows the course of P_U and P_L for this voltage change for SAW-driven transport of a single electron that is initially loaded at the upper (open symbols) or lower (filled symbols) source QD. For a high barrier ($V_\mathrm{T} < -0.85$) the values of P_U and P_L flip as we switch from the upper to the lower injection channel. Here the tunnel-barrier is sufficiently high such that the electron basically remains at the injection side of the tunnel-coupled region. For a lower barrier ($V_\mathrm{T} > -0.85$) on the other hand the observed features in P_U and P_L get completely independent of the choice of the injection channel. This finding suggests that for smaller tunnel barrier potential ($V_\mathrm{T} > -0.85$) the electron wave function basically spreads out over both quantum rails in the center of the tunnel-coupled region. In this range of V_T the exit potential plays the decisive role for guiding the electron into the upper or lower channel.

Sweeping the side electrodes, V_U and V_L, very asymmetric with V_T, we observe an interesting oscillation-like behaviour of the transfer probability as we tune the exit potential just to the threshold of the transition from the upper to the lower

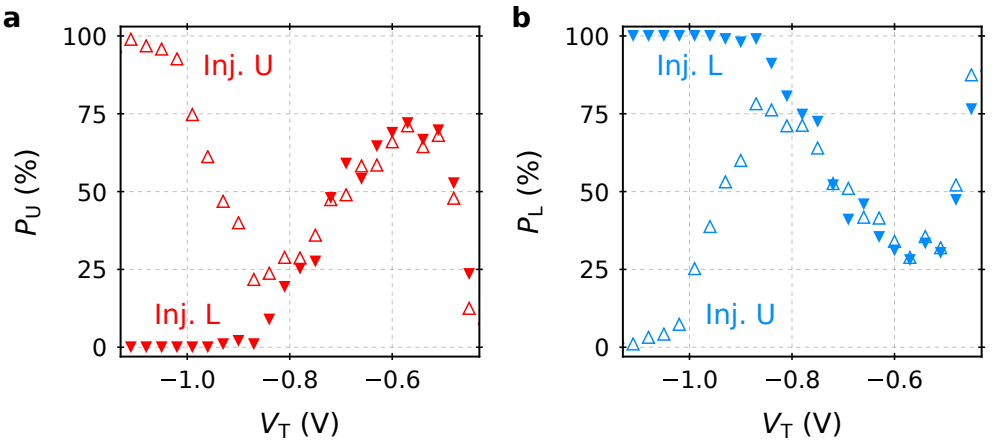

Figure 52: Comparison of transfer probability transitions for switched injection channel. Shown are exemplary traces of normalised transfer probabilities to the **(a)** upper and **(b)** lower receiver QD, P_U and P_L, as the tunnel-barrier voltage, V_T , is changed with asymmetric compensation of the side gates, V_U and V_L. Open (filled) symbols represent data with electron injection from the upper (lower) channel.

[19]For the present discussion it is not important how the compensation of confinement is performed by the side gates.

channel. Fig. 53a shows transfer probability data for the voltage sweep:

$$\begin{bmatrix} V_\mathrm{T} \\ V_\mathrm{U} \\ V_\mathrm{L} \end{bmatrix} = \begin{bmatrix} -1.20 \\ -0.95 \\ -0.60 \end{bmatrix} + \alpha \begin{bmatrix} +0.90 \\ -0.21 \\ -0.91 \end{bmatrix} \text{ (V)}, \ \alpha \in [0, 1] \tag{12}$$

The interesting part of the behaviour in P_U and P_L occurs for $V_\mathrm{T} > -0.8\,V$. As we switch the injection side and flip the gate movements of the side gates, we observe a qualitatively similar trend as shown in Fig. 53b. Here we move the voltages as:

$$\begin{bmatrix} V_\mathrm{T} \\ V_\mathrm{U} \\ V_\mathrm{L} \end{bmatrix} = \begin{bmatrix} -1.20 \\ -0.65 \\ -0.99 \end{bmatrix} + \alpha \begin{bmatrix} +0.90 \\ -0.72 \\ -0.17 \end{bmatrix} \text{ (V)}, \ \alpha \in [0, 1] \tag{13}$$

We can now test if the oscillation-like behaviour in P_U and P_L for $V_\mathrm{T} > -0.8\,V$ correlates with the movement of the tunnel-barrier voltage. For this purpose we performed the following measurement: We compare measurements along specific regions for the situations where we sweep V_T with V_U and V_L to the situation where we keep V_T constant and only change the side gates. Such a comparison is shown in Fig. 54. Sweeping V_T with V_U and V_L, we observe the oscillation-like behaviour. As we fix V_T and only sweep the side gates, on the other hand, we just observe a continuous probability change in P_U and P_L. This test shows that the

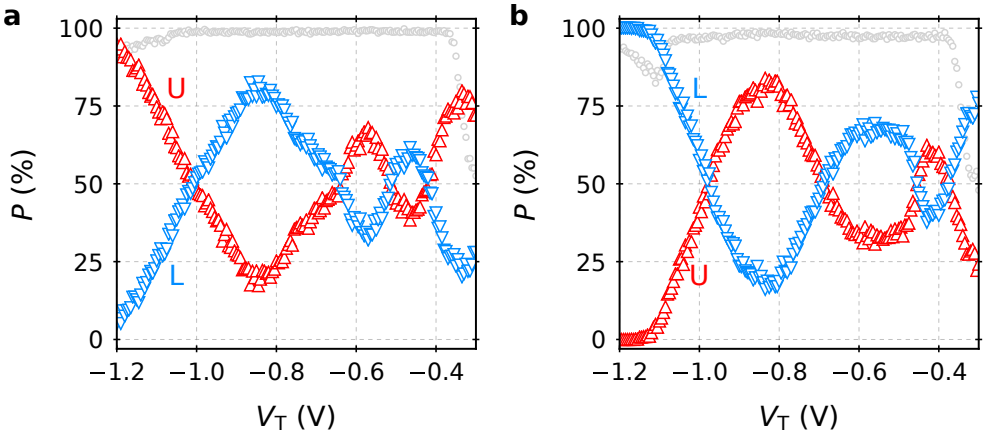

Figure 53: Probability oscillations occuring with change of tunnel-barrier height. Shown is the normalised transfer probability to the upper (U) and lower (L) receiver QD. The grey data points indicate the total transfer efficiency for each configuration. **(a)** Injection from the upper branch with voltage compensation according to equation 12. **(b)** Injection from the lower branch with correspondingly flipped voltage compensation as shown in equation 13.

oscillation-like behaviour for $V_T > -0.8\ V$ correlates with the movement of the tunnel-barrier voltage. The correlation of the oscillation-like behaviour with the tunnel-barrier movement does however not imply that the observed features in the transfer probability are caused by a tunnelling of the electron wave function. It is however one hypothesis that so far cannot be fully ruled out.

Let us now discuss one possible scenario. From our investigations of section 2.3.2, we have found that the electron is excited in a superposition of eigenstates of the double-well potential as it enters from the injection channel into the tunnel-coupled region. The reason for this excitation is related to an abrupt change in the potential landscape that goes along with an abrupt change of the eigenstates in the moving QDs that are formed by the SAW. Due to this change, an electron that is initially transferred in the ground state abruptly encounters many states that are subsequently occupied. Considering the speed of the SAW, we find that his process happens in less than 100 ps. At the end of the tunnel-coupled region we have now again such a change in the potential landscape, but in the opposite direction. The abrupt increase of potential confinement at the exit of the tunnel-coupled region could cause another non-adiabatic transition of the superposition state in an occupation of only a few eigenstates that experience tunnel-coupling for a very short time. The short coupling duration could explain why the oscillating features in the transfer probabilities occur over for a relatively large voltage sweep on the tunnel-barrier electrode. This is however only one possible hypothesis that requires more experimental as well as theoretical investigations.

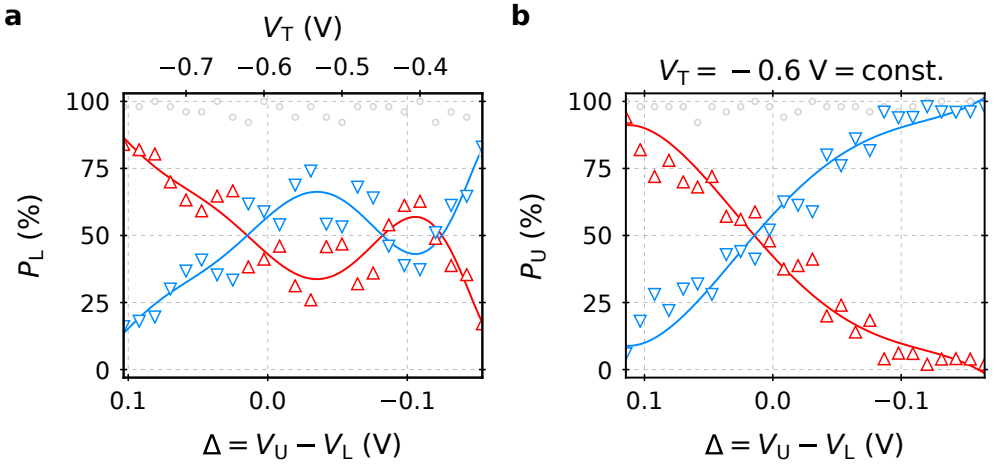

Figure 54: Correlation of oscillation-like features to tunnel-barrier movement. **(a)** Shown is transfer probability data similar to Fig. 53b for $V_T > -0.85$ V. **(b)** Here only the side gates, V_U and V_L, are swept while the tunnel-barrier height is kept constant with $V_T = -0.6$ V. The lines in the background are guides to the eye.

2.4 Discussion and conclusion

The emergence of nanostructured quantum devices such as QDs, QPCs and one-dimensional transport channels enabled novel techniques to trap, displace and manipulate single electrons in solid-state devices. This progress opened up the way to realise quantum mechanical experiments with single stationary and flying electrons. Having control over the quantum state of a flying electron, the realisation of quantum logic gates can be envisioned for spin and as well as charge qubits that are propagating through a circuit of transport channels. These prospects of quantum-optics-like experiments with single flying electrons stimulated the idea of a flying qubit architecture in which quantum information is not only transferred, but also manipulated on the fly between stationary nodes of computation [DiV00; Van17; Bäu18]. Owing to electron confinement during transport and the availability of highly efficient single-electron sources and receivers, SAWs represent a particularly promising candidate to deliver the first quantum logic gate for flying electron qubits [Ber00; IAU01; Bäu18; Yam12; Bau14b].

Here we have experimentally investigated the feasibility of the central building blocks of quantum-logic gates with flying electron qubits using SAWs as transport medium, namely a tunable beam splitter and a single-electron source that is adapted to synchronisation. In the course of our investigations we have achieved important milestones to tread the path towards coherent control of flying electron qubits that are surfing on a sound wave. Firstly, we have demonstrated highly efficient SAW-driven single-electron transport along a 22-μm-long circuit of tunnel-coupled quantum rails. Secondly, we have successfully demonstrated the capability of the present device to partition a single electron from one quantum rail into the other while maintaining highly efficient transfer. Performing quantum mechanical simulations of our experimental data, we moreover showed that the width of the directional coupler transition directly reflects the excitation energy of the flying electron state. This quantity can thus serve as useful criterion to assess the occupation of eigenstates by the flying electron in future experiments. Performing time-dependent simulations of SAW-driven electron propagation, we further identified abrupt transitions in the potential landscape as major source of charge excitation. Investigating the effects of increased SAW-amplitude in the time-dependent simulations, we further found a feasible approach to make the flying charge qubit system more robust against potential fluctuations.

Using a voltage-pulse trigger, we additionally demonstrated a powerful tool to synchronise the SAW-driven sending process of single electrons from the source QDs. With this achievement we fulfil a central requirement to couple a pair of single electrons in a beam-splitter setup. Employing this pulsing technique also at the receiver side, we conducted time-of-flight measurements, which showed that the aforementioned excitation of the flying electron causes transitions of the wave function in subsequent SAW minima. This experimental finding is in

congruency with the simulation results which show that the expectation energy due to charge excitation is in the order of the SAW amplitude. Increasing the confinement of the flying electron in the SAW, we anticipate that the coupling of single electrons in a SAW-driven beam-splitter setup is readily achievable with the demonstrated sending trigger technique. For very specific asymmetric configurations of the double-well potential in the tunnel-coupled region, we further observed oscillation-like features in the transfer probabilities that could indicate the occurrence of coherent tunnelling processes.

Most of our results on SAW-driven single-electron transport along the present 22-μm-long tunable beam-splitter setup were performed with a transfer efficiency exceeding 99 %. This property shows that SAW-driven single-electron circuits are feasible on a relatively large scale. Since SAWs propagate along macroscopic distances without significant damping, there is basically no limit on the distance to transfer a single electron. At the same time, we find that there are a few obstacles to realise flying charge qubits that are coherently conveyed by a sound wave. We anticipate, however, that these obstacles are vincible in future SAW-driven quantum experiments with single flying electrons.

Due to Coulomb repulsion, the effect of anti-bunching could be even observable if the transport of the electron pair is incoherent. In the present experimental investigations, the main obstacle to observe the repulsion of two flying electrons was insufficient confinement of the electron in a specific SAW minimum during transport. Charge excitation at the entrance into the tunnel-coupled region enabled transitions of the flying electron in subsequent potential modulation minima of the SAW. Having the electron distributed over many SAW-minima, the probability to find the two particles at the same position of the SAW train is strongly reduced. There are several ways to overcome this problem. The simplest approach to enhance the confinement of the electron in the SAW is the reduction of signal attenuation along the RF line that is connected to the IDT. Doing so, one has to be however careful not to introduce significant heating on the investigated nanoelectric device. Additionally, one could enhance SAW generation by employing for instance higher IDT harmonics or chirp pulses[20]. Overcoming the remaining challenge of insufficient SAW confinement, the coupling of single SAW-transported electrons is readily achievable with the sending trigger that was demonstrated in this thesis.

A greater challenge will be presumably the realisation of MZ-type interferometry experiments with single SAW-transported electrons. The limiting factor for such experiments is the coherence length of a SAW transported charge qubit. There were a few reports on the coherence time of stationary charge qubits in double QDs ranging up to several nanoseconds [Hay03; Pet04; FHH04; Pet10; Sto17]. From this perspective, it seems feasible to transport a single electron with a SAW

[20] We will discuss these approaches in more details in the perspectives section 2.5.1.

through a circuit of quantum rails while maintaining coherence. Charge excitations, as encountered in the current experiment, could however strongly mitigate coherence of the electron state in flight. The increase of electron confinement in the SAW is therefore also a critical factor for maintaining coherence during SAW-driven transport, since a large confinement directly increases the energy spacing of the eigenstates in the moving train of QDs that is formed by the SAW along the transport channels. A larger energy splitting of the eigenstates strongly reduces the probability to transition in energetically nearby states. An increased SAW amplitude therefore facilitates the realisation of a flying charge qubit that is truly defined by the lowest two eigenstates of a dynamic double-well potential.

From this perspective, the maximisation of the SAW amplitude and the development of novel SAW generation techniques has high priority. To prohibit charge excitations during SAW-driven single-electron transport along a circuit of tunnel-coupled quantum rails, it is equally important to establish an electric potential landscape that changes slowly enough along the paths of transportation such that adiabaticity is maintained. In the presently investigated beam-splitter setup, we found that the potential transition into the tunnel-coupled region occurs so abrupt such that the electron state exhibits Landau-Zener transitions in excited eigenstates. We conclude that changes in the potential landscape can occur, but they must happen gradual enough such that adiabatic transport in the ground-state is maintained. For future experiments on this topic the design of the surface gates plays thus a key role to demonstrate coherent control of flying charge qubits[21].

In conclusion, we have demonstrated two essential building blocks for a SAW-driven single-electron circuit of quantum rails that are important for the coupling and partitioning of flying electrons among parallel paths of transportation. A detailed analysis of our experimental results allowed to identify abrupt changes along the potential landscape and insufficient trapping of the electron within the SAW as remaining challenges to perform MZ- and HOM-type electron interference experiments with the present single-electron circuit of coupled quantum rails. We anticipate that an optimised surface-gate geometry as well as stronger SAW confinement [Sch15] will allow for coherent propagation and coupling of single electrons in flight in a true two-level state as previously demonstrated in stationary charge qubits [Hay03; Pet04; FHH04; Pet10; Sto17]. Our results thus pave the way for the realisation of quantum logic gates[Ber00; IAU01] and demonstrations of HOM interference and entanglement [Bäu18] with single flying electrons.

[21] In section 2.5.2 we will present a proposal of a linear MZ-type interferometer for a single SAW-transported electron with dynamic tunnel-barrier control.

2.5 Perspectives

With the presently investigated single-electron circuit of coupled quantum rails we have achieved important steps towards SAW-driven quantum-optics-like experiments with solitary electrons. Our investigations also showed up the remaining challenges to convey and manipulate a SAW-transported charge qubit in flight. In the following we present three possible directions to enable coherent manipulations of flying electrons that are transported by a SAW. In the first part we discuss possible approaches to enhance the confinement of the electron in the SAW. Secondly, we present a single-shot interferometer design, which provides in principle a sufficiently smooth potential landscape and allows to characterize population and charge relaxation of a flying charge-qubit state in a systematic way. Finally, we present a novel route of SAW-driven single-electron transport in a undoped GaAs/AlGaAs heterostructure. Such an undoped architecture would bring additional advantages for the homogeneity of the electron potential and opens up a link of SAW-driven single-electron circuits to photonics.

2.5.1 Enhancing acoustic confinement

Comparing our experimental results on the directional-coupler operation (section 2.3.2) to time-dependent simulations of SAW-driven single-electron propagation (section 2.3.3), we found that the electron is far off from being in a true two-level system due to excitation that goes along with insufficient confinement within the SAW during transport. One promising way to reduce the probability for such charge excitation, is an increased longitudinal confinement potential within a SAW train. In a semiconductor heterostructure such a GaAs/AlGaAs SAWs have a linear dispersion relation ranging up to a frequency of several GHz. Consequently, the phase and group velocity match over a wide frequency range. A SAW that is generated by any combination of frequencies from this linear range shows therefore no dispersion. This property makes Fourier transform an appealing tool to form an arbitrary SAW shape by design. In the following we discuss two promising SAW generation techniques that employ this mathematical concept to strongly increase the confinement potential within a SAW train.

Fourier synthesis of IDT harmonics

One promising approach to achieve a train of arbitrary SAW pulses employs the Fourier synthesis of higher IDT harmonics. Mixing the first four harmonics of a so-called split-52 IDT geometry one can generate for instance a train of distinct δ-peaks that are separated by the periodicity which is given by the base frequency of the IDT. This δ-function pulse shape is particularly interesting for the purpose of SAW-driven single-electron transport, since the pulse width is much narrower

than the wavelength of the SAW. A schematic of a split-52 IDT is shown in Fig. 55. The feasibility of such Fourier synthesis of split-52 IDT harmonics was already demonstrated with a base frequency of 144 MHz [Sch15]. The width of the generated SAW pulses was deduced as approximately 850 ps (FWHM).

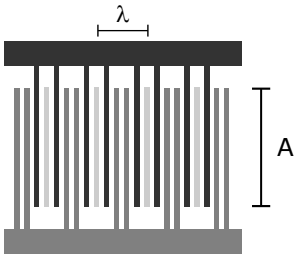

Figure 55: Schematic of a split-52 IDT. Here five fingers are placed with equal spacing along the period defining the fundamental frequency. Four of the five fingers are arranged as in the aforementioned double-finger IDT design. The fifth finger, however, is floating and placed in between one of the two double-fingers.

The Fourier synthesis of split-52 harmonics represents thus one interesting route to increase the confinement in SAW-driven quantum optics experiments with single electrons. To have an advantage with respect to previously employed SAW generation methods, one has to achieve however a pulse width going well below 360 ps. Keeping the set of amplitudes and phases for the employed harmonics constant, the width of the generated pulses scales linearly with the base frequency of the IDT. To generate a train of sufficiently narrow SAW peaks, split-52 IDTs must be operated with a base frequency in the order of GHz. Having a base frequency of 1 GHz one can in principle employ such a split-52 IDT to generate pulses having a width of about 122 ps (FWHM)[22].

To investigate if the realisation of such devices is feasible, we fabricated split-52 IDTs having a wavelength of $\lambda = 2.75$ μm and investigated the visibility of the higher harmonic resonances in S12 transmission measurements. The IDTs were fabricated and characterised in collaboration with Shintaro Takada during my secondment at AIST in Tsukuba (Japan) in April 2019. With the fabricated IDT devices, resonances were observable up to the 4th harmonic at about 4 GHz – see Fig. 56. This finding shows that the Fourier synthesis of IDT harmonics in the GHz regime is in principle feasible for the purpose SAW-driven single-electron transport. Sending a synthesised signal of these four harmonics with identical amplitudes and optimised phases on a 1 GHz split-52 IDT, one can in principle generate a SAW train of distinct minima as shown in Fig. 57. The Fourier synthesis of IDT harmonics for δ-peak generation provides distinct SAW peaks having high amplitude and narrow width. Due to large potential barrier between subsequent δ-peaks of the SAW train, electron transitions in subsequent δ-peaks are strongly mitigated compared to a conventional sinusoidal SAW train. To flatten the signal in-between the δ-peaks, one could work at lower base frequency for instance 500 MHz but synthesise more than four harmonics. We

[22] Taking the result of Schülein *et al.* [Sch15] as reference, we can calculate the expected width for a base frequency of 1 GHz as 850 ps $\cdot$ 144 MHz / 1 GHz $\approx$ 122 ps.

anticipate that the Fourier-synthesis of δ-SAW-peaks will be particularly interesting when working with continuous single-electron transport. Employing this approach to transfer continuously single-electrons through a QPC, we anticipate enhanced quantised acoustoelectric conductance plateaus due to increased SAW confinement.

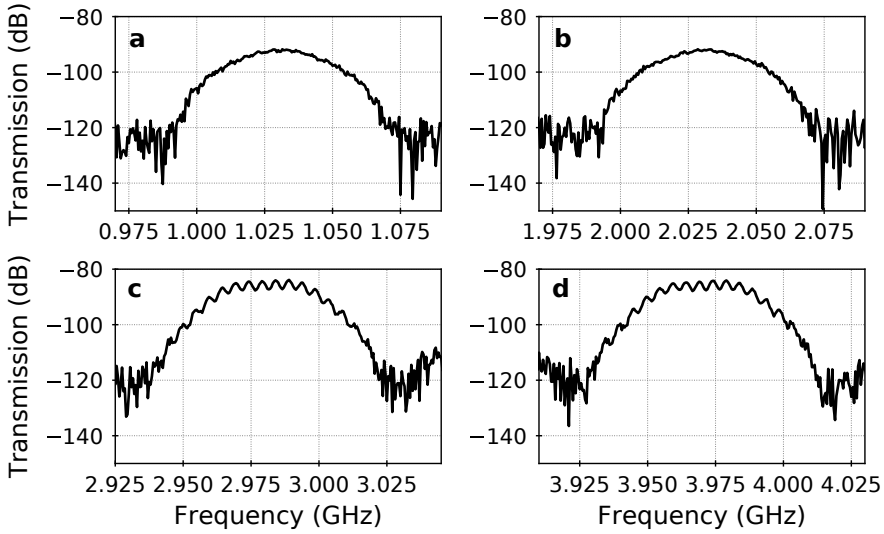

Figure 56: Transmission between a pair of split-52 transducers. The investigated IDT has an aperture of is $A = 50$ μm, and 21 interdigitated split-52 fingers having a periodicity of $\lambda = 2.75$ μm. The SAW-related transmission data is extracted by filtering of the electromagnetic crosstalk occurring at times well below the SAW flight-time after Fourier transform. The data clearly shows the **(a)** first, **(b)** second, **(c)** third and **(d)** fourth harmonic of the split-52 IDT.

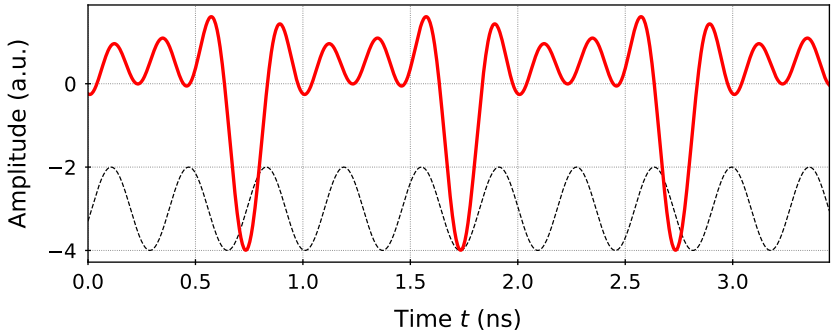

Figure 57: Comparison of a synthesised to a conventional SAW. The red line shows the course of a SAW that is expected when mixing the first four harmonics of a split-52 IDT having a base frequency of 1 GHz. The amplitudes of the mixed harmonics are identical (1 a.u.). The phase offsets are tuned to maximise the peak depth. For comparison also the course of a conventional SAW with base frequency of 2.77 GHz is shown – having also an amplitude of 1 a.u..

SAW generation by chirp pulses

A conceptually related but different approach for the generation of SAW pulses are so-called chirp signals. Using a continuum of frequencies, Fourier transform can be employed to design an IDT structure and signal allowing the generation of SAW pulses having arbitrary shape. The chirp IDT design detaches itself from a strictly periodic finger spacing – see sketch in Fig. 58. The continuously changing finger spacing allows the superposition of many elementary SAWs that interfere to a specific pulse shape. For the purpose of single-electron transfer we are particularly interested in the generation of a single SAW minimum that preferably has a very small wavelength and high amplitude. Applying a frequency modulated chirp signal with a range covering the linear part of the GaAs phonon-dispesion curve, one can transduce an acoustic wave spectrum interfering to a single non-dispersive SAW minimum.

First investigations of single-electron transport by such chirp generation of SAW pulses are presently performed in our group by Junliang Wang [Wan18]. Preliminary time-dependent measurements of such chirp SAW pulses provided data that

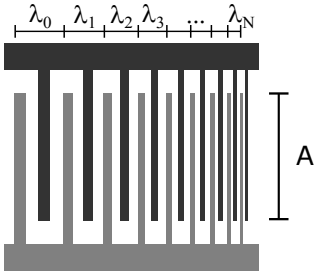

Figure 58: Schematic of a chirp IDT. The spacing and width of the interdigitated electrodes decreases linearly towards the transmission direction – giving a set of wavelengths $\{\lambda_1, ..., \lambda_N\}$. To form a single SAW minimum by this set of elementary waves, the corresponding resonance frequencies, $\{f_1, ..., f_N\}$, must be addressed at the right timing one after another.

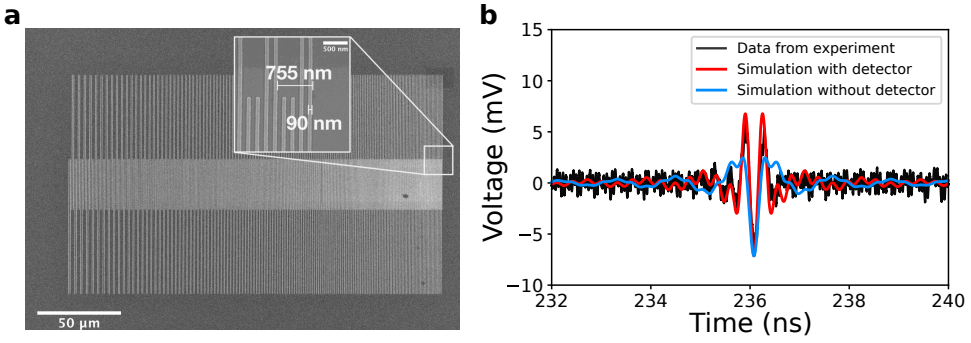

Figure 59: Generation of a single SAW minimum by the chirp IDT approach. **(a)** SEM images of the chirp IDT showing the gradually decreasing width of the interdigitated double-finger electrodes. **(b)** Time-dependent measurement of the profile of a single SAW minima realised by a chirp pulse that is applied on the interdigitated electrode of the IDT. The presented data stems from Junliang Wang [Wan18].

is very promising for the purpose of single-electron transfer. Figure 59 shows a prototype of such a chirp IDT and a time-dependent measurement of the corresponding SAW profile. The data shows that the a chirp IDT is indeed capable of generating a single non-dispersive SAW peak that is tunable by the properties of the transducer. The crucial variables for transport experiments with single electrons are the amplitude and the width of the chirp pulse. These variables can be adjusted by the length of the IDT and the maximum frequency. Making the IDT longer and the frequency maximum higher, one can increase the amplitude and reduce the width of the SAW peak. Adjusting the IDT design, we can thus generate a well-predictable SAW pulse. Having this control-by-design we can engineer chirp pulses allowing us to cope with the aforementioned remaining challenges.

2.5.2 Flying qubit operations via dynamical tunnel control

In order to avoid charge excitations of a SAW-transported flying electron, besides an increase of the SAW confinement, one can design smooth transitions in the potential landscape along the circuit of tunnel-coupled quantum rails. This approach should allow to convey a flying charge qubit adiabatically via transport by a SAW train. Imagining such a SAW-driven circuit of quantum rails, it is in principle possible to observe coherent interference phenomena over several micrometer distance. So far there are however no investigations on the coherence of SAW-transported charge qubits. To study this aspect, we will further need an experimental setup allowing a systematic characterisation of qubit relaxation as discussed in section 2.1.3 in terms of population and phase relaxation.

In the following we present a SAW-driven single-shot electron interferometer device that is very promising to meet both of these requirements[23]. The device geometry mitigates rapid potential changes and therefore related charge excitation and provides a flexible experimental frame to study coherence of a SAW-transported flying charge qubit. The proposed single-electron circuit of quantum rails is conceptually simple and provides a well controllable experimental setup. It is inspired by the success of the sending trigger that we demonstrated in section 2.3.4. Thinking about future quantum optics experiments with single SAW-tranported electrons, it suggests itself to use this pulsing approach in different components of the SAW-driven single-electron circuit. To systematically investigate the coherence properties of a SAW-transported charge qubit, it is now a particularly appealing idea to employ fast voltage pulses also for dynamic control of the tunnel-barrier potential in a very long region of coupled quantum rails.

The central idea is to have a tunnel-coupled region that is extended over a length

[23]The idea for this device structure arose from discussions with Shintaro Takada and my colleagues of the Quantum Coherence group at the Institute Néel in Grenoble.

of several tens of micrometers. By default, a sufficiently large tunnel barrier is present such that the two paths of transportation are completely decoupled. The dynamic control of the tunnel-barrier allows now to introduce tunnel-coupling on-demand between the two transport channels as the electron propagates with the SAW along the nanostructure. This coupling can be accomplished by a positive voltage pulse that is applied via a bias tee on the tunnel-barrier electrode for a certain pulse duration. Using a modern AWG, such dynamic tunnel-barrier control can be performed on a time scale of picoseconds. Consequently, one can choose the timing, region and strength of the tunnel-coupling in the double-well potential. Such dynamic tunnel-coupling control would thus open up a fruitful platform for a large set of experimental investigations.

To highlight the potential of this experimental frame, let us consider a simple test case, namely a T_2^* measurement. The measurement procedure consists out of two Hadamard operations which are separated by a certain waiting time, τ. Figure 60a shows a schematic of this exemplary case. To realise the Hadamard operations, we employ two positive voltage pulses. The duration, τ_C, of the two pulses is tuned such that the flying charge qubit performs a $\Delta\theta = \pi/2$ rotation. For zero waiting time between the two pulses, a flying electron undergoes a tunnel-transition from the upper to the lower quantum rail with 100 % probability assuming ideal coherent transport in a two-level system. Increasing the waiting time, τ, between the two Hadamard operations, phase decoherence causes an exponential decay of this projection that is characterised by the phase relaxation time, T_2^*[24]. If T_2^* is much smaller than the separation time of the two pulses, τ, one obtains the classical result, where the electron ends up the the upper and lower transport channel with 50 % probability.

Besides this example that we reviewed a bit in detail, we can employ this device with different sequences of tunnel-coupling pulses to characterise the population relaxation time, T_1, and the corrected phase relaxation time, T_2, as discussed in section 2.1.3. For the measurement of a lower bound of T_1 we would simply characterise the exponential decay of coherent oscillations as we vary the coupling duration, τ_C. A measurement of the corrected phase relaxation time, T_2, would require an additional $\delta\theta = \pi$ pulse between two Hadamard operations.

Having a profound understanding of the coherence properties of a SAW-transported charge qubit, one could further investigate the occurrence of AB oscillations arsing from the sweep of a perpendicular magnetic field. Since there are no abrupt changes in the geometrical structure of the quantum rails along the single-electron circuit, it is unlikely that the electron is dragged back in subsequent minima of the SAW during transport. Employing a voltage pulse trigger as demonstrated in section 2.3.4, we should thus be able to synchronise transfer of

[24]Here we assume that there is no accumulation of a geometric or magnetic phase when the flying charge qubit is projected on the equatorial orbit of the Bloch sphere.

two electrons along the upper and lower quantum rail and to demonstrate the repulsive interaction of a pair of single electrons that is transported with the SAW. Therefore, the proposed experimental setup is further promising for the coupling

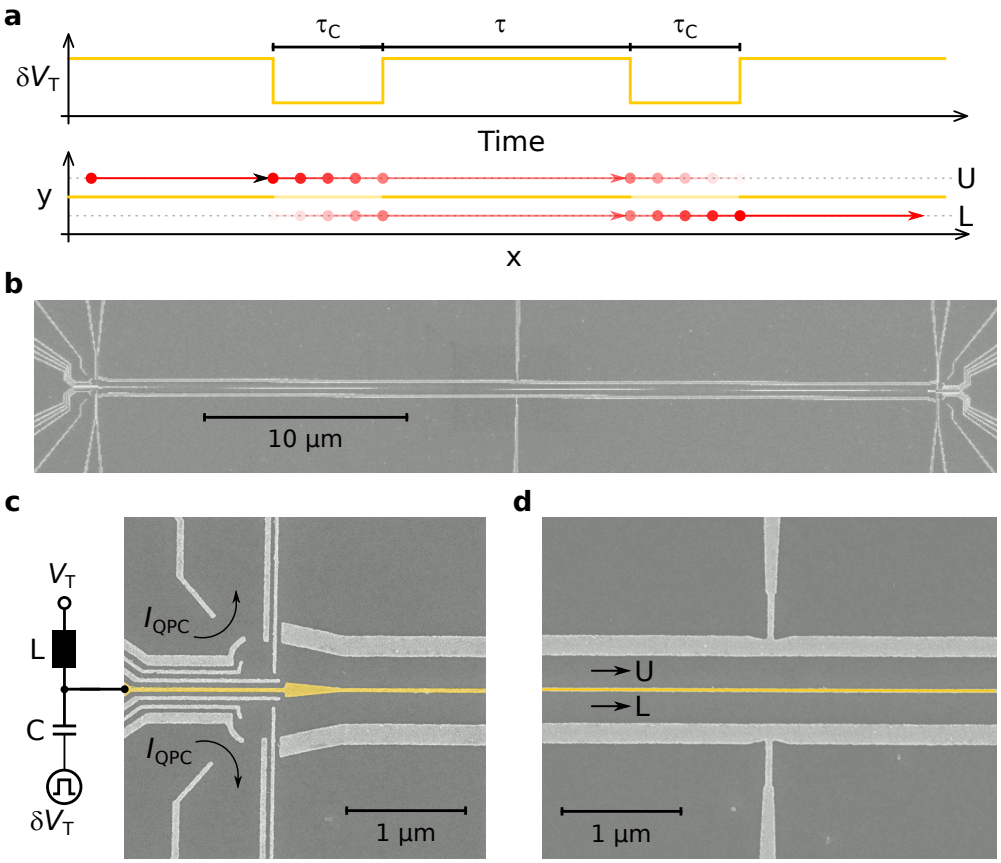

Figure 60: Prototype of a linear SAW-driven single-electron circuit with dynamical tunnel-barrier control. **(a)** Schematic showing effect of dynamic tunnel-barrier control. Shown is a sequence of two pulses with duration of τ_C that introduce a $\delta\theta = \pi/2$ shift of the flying charge qubit state. Assuming a phase coherence time, T_2^*, that is much longer then pulse sequence and no accumulation of a geometric or magnetic phase between the two pulses, the two Hadamard operations introduce a transition of the flying electron from the upper quantum rail (U) via a 50-50 superposition state on the lower quantum rail (L). **(b)** SEM image of the linear interferometer structure for single SAW-transported electrons. The tunnel-coupled region spans over a length of 40 μm. **(c)** Zoom in the region of the source QDs. To place two quantum dots at the end of the tunnel-coupled region, one ohmic connection of the QPC is also employed as electron reservoir for the source QD. The schematic electrial circuit shows a bias tee allowing pulse variation, δV_T, of the static gate voltage, V_T. **(d)** Zoom in the center of the tunnel-coupled wire of quantum rails.

of two SAW-transported electrons. Loading the electrons in different positions of the SAW, one could additionally investigate effects of long-range Coulomb interaction in neighbouring SAW minima and short-range Pauli repulsion.

A preliminary implementation of such a SAW-driven single-electron circuit with dynamic tunnel-barrier control is shown in Fig. 60b. The device was fabricated under guidance of Shintaro Takada [Tak19]. The SEM image shows a 40 μm long tunnel-coupled wire that is equipped with surface-gate defined QDs at the respective ends of the track. To realise such a linear tunnel-coupled single-electron transport device, we have to change the QD design that is typically employed for SAW-driven single-electron transport. In the beam-splitter device that we introduced in section 2.2.1, we place the QPC opposite to the surface gates of the QD. Bringing the QD of the two quantum rails close-by, such a design is obviously not possible to implement in such a linear structure.

One approach to bypass this problem, is inspired by triangular-arrays of solid-state spin qubits [Fle17]. Here one ohmic connection of the QPC is shared as electron reservoir for the QD. Figure 60c shows an implementation of such an arrangement of surface gates on a prototype sample. Verifying the homogeneity of the surface gates along the device, we find that such a structure can be indeed implemented with the dimensions of the tunnel-coupled region presented in section 2.2.1. Let us now assess the quality of the tunnel-coupled wire of quantum rails. Figure 60d shows a zoom in the tunnel-coupled region showing the quality of the surface gates. We have realised such a surface-gate structure with a 40-μm-long coupling region. The SEM images show that the fabrication of a very long linear SAW-driven single-electron circuit is definitely feasible.

2.5.3 An undoped heterostructure – a link to photonics

In this thesis we focussed so far mainly on the charge properties of SAW-transported electrons in a GaAs/AlGaAs heterostructurs with a Si-δ-doped layer. SAW-driven electron transport is however also feasible in an undoped GaAs/AlGaAs heterostructure with an accumulation-gate approach. In such a semiconductor architecture one can perform quantum experiments involving electrons and also electron holes. Recently, it was shown that this property can be exploited to realise a SAW-driven single-photon source [Hsi19]. In that work, single electrons are shuffled with a continuous SAW through a constricted channel from a Fermi sea of electrons into a region of electron holes (p-region). As a SAW-transported electron enters the p-region, it recombines with one of the holes emitting a single photon. Analysing the counting statistics of the emitted photon stream, it was found that such a setup basically serves as single-photon source that is locked to the frequency of a continuous SAW. By realising such a SAW-driven single-photon source with spin-polarized electrons, it could be possi-

ble to realise a link between flying spin qubits and polarisation-encoded photonic qubits.

Besides this conceptual aspect, realisations of SAW-driven electron transport in undoped semiconductor architectures have advantages for the homogeneity of the electric potential at the position of the 2DEG. One inevitable property in a Si-δ-doped GaAs/AlGaAs heterostructure is the basically random background potential in the 2DEG stemming from the positive ions in the doping layer. The corrugation of this background potential introduces potential fluctuations, which might represent an additional limiting factor for coherent transport of a flying charge qubit. Assuming a random distribution of the Si dopands, one can estimate the potential fluctuations at the position of the 2DEG simply by summing up the contributions of the Coulomb potential. Looking on a relevant length scale of 250 nm, we find a background potential that superimposes a corrugation in the order of several meV on the potential landscape that is formed by the surface gates. Due to the corrugation of this parasitic corrugated potential landscape, the experimental characteristics of two similar the nanoelectric devices can differ even for a perfectly set of identical surface gates. To bypass this problem, SAW-driven single-electron transport between surface-gate defined QDs in a undoped GaAs/AlGaAs heterostructure represents an interesting alternative route. Here electrons or holes are accumulated from ohmic contacts towards the nanostructure where the quantum experiments are performed.

QPCs, QDs and double QDs have been already demonstrated with a top-gate approach in an undoped GaAs/AlGaAs heterostructure for electrons [Li14] and holes [THR14]. Due to the large surface-to-interface distance and screening and mass-loading effects, however, this approach is not suitable when using SAWs. In the course of this thesis, we have performed investigations on an alternative approach where no top gate is present. For this purpose we have started a collaboration with Antonio Rubino from the group of Prof. Chris Ford at the Cavendish Laboratory in Cambridge. Details on the working principle and first measurements on a prototype sample are presented in appendix J. In the course of our investigations we found that charge up below surface gates makes the control of experiments at the single-particle level so far relatively difficult. In undoped semiconductor architectures there are several aspects that require systematic investigations. To achieve the controlled isolation and detection of single electrons in a SAW-compatible architecture, it is necessary to enhance the quality of the ohmic connections and to perform experiments on different QPC and QD designs.

Summary and overall conclusion

Owing to the advances of nanofabrication and measurement techniques, mesoscopic experiments in Si-δ-doped AlGaAs/GaAs heterostructures represent nowadays a great platform to study quantum mechanical phenomena of electrons. Since this field of research is relatively young, there are many fascinating measurements that can be envisioned in this experimental frame having large potential in future technologies. Especially entanglement [Ned07] and teleportation [Dup19] of quantum information is in the focus of modern experimental research in this field. In this thesis we discussed two types of electron-quantum-optics experiments at the single-particle level. Firstly, we experimentally investigated the phase modification of the electron wave function at transmission through a large quantum dot (QD) in a two-path interferometry setup. Secondly, we went beyond the ballistic transport regime and employed surface acoustic waves (SAWs) to convey a single electron through a circuit of tunnel-coupled quantum rails between distant QDs.

In the first part of this thesis, we employed an original MZ-type electron two-path interferometer to perform transmission phase measurements through a QD in the ballistic transport regime. In this electron interferometry experiment, the single-electron aspect came into play from a large QD that was inserted as phase-shifting medium in the probing branch of the interferometer structure. Our transmission phase measurement showed several clear indications of a transmission behaviour that reflects the internal structure of eigenstates within the QD. We did not observe a universal transmission phase behaviour for the presently investigated large QD hosting hundreds of electrons. In congruency with a paritiy-dependent transmission phase behaviour [Lee99; TB99], we observed however several times the absence of such a phase lapse that was respectively accompanied by augmented coherent transmission in the conductance valleys. We underpinned the non-universal character of the transmission phase by demonstrating changes in the sequences of phase lapses via QD deformation and magnetic field variation. Our experimental findings put the observations of pioneering experiments [Sch97] in a new perspective and solve the long-standing question about a universal transmission phase behaviour in large QDs [Edl17]. Our results thus set an important milestone towards a comprehensive understanding of the transmission phase of QDs.

In the ballistic transport regime, electron interferometer structures are readily available to study the quantum mechanical phenomena with flying electrons. We expect that our demonstration of a non-universal transmission phase behaviour with a large QD will motivate further measurements on large QDs allowing statistical statements on the occurrence of transmission phase lapses [Mol12; Jal14]. We anticipate moreover that the employed MZ-type electron interferometer will allow to test the implications of a parity-dependent transmission phase behaviour by further investigations on small quantum dots. To check the spin-related effects on the transmission phase, it is particularly interesting to study a few-electron QD that is elongated in the transmission direction, since for such a system, no phase lapses should occur along the first six resonances due to the spin-filling sequence of the s, p_x and p_y orbitals [Ron10]. Besides the study of the internal properties of quantum dots, the employed MZ-type electron interferometer will be applicable in investigations of quantum criticality in highly-correlated electron systems such as the two-channel Kondo effect, which are important for the understanding and design of complex materials and unconventional high-temperature superconductors of the future [Pot07; Car12; Kel15].

The second part of this thesis was dedicated to the realisation of a quantum interferometer device for a single electron that is transported by a SAW. For this purpose, we investigated the feasibility of the central building block of such a SAW-driven single-electron circuit, that is a tunable beam splitter. Besides the realisation of MZ-type interferometry experiments, such a beam-splitter setup can be employed to realise HBT/HOM interference experiments with a pair of SAW-transported electrons. Demonstrating these kind of interference phenomena, it is in principle possible to realise quantum logic operations and entangled states with SAW-transported flying charge qubits. To realise such kind of quantum experiments, it is necessary to partition a flying electron into a track of tunnel-coupled quantum rails and to synchronise SAW-driven single-electron transport along parallel tracks.

Here we first addressed the partitioning of a SAW-transported electron. Using the energy potential detuning between a pair tunnel-coupled quantum rails, we achieved controlled partitioning of the SAW-transported electron among two paths of transportation while keeping the transfer efficiency above 99.6 % whereas we identified the catching process as central limitation. Performing quantum mechanical simulations of the experiments, we identified a major source of charge excitation. As the SAW-transported electron enters the tunnel-coupled region, it encounters an abrupt change in potential confinement causing Landau-Zener transitions in higher energy states. The simulations predict an excitation energy that is in the order of a few meV what is comparable to the SAW amplitude. Performing time-dependent simulations of SAW-driven single electron transport through a our circuit of tunnel-coupled quantum rails with increased SAW-amplitude,

we furthermore provided a clear-cut strategy to overcome the problem of charge excitation in follow-up investigations.

Secondly, we demonstrated a SAW-driven single-electron source that is adapted to synchronisation. Employing a voltage pulse trigger, we demonstrated control of the SAW-driven sending process on a picosecond scale. Using this trigger, we were able to address on-demand a specific position of the SAW to send the electron along a quantum rail. Employing a similar pulsing technique at the receiver side, we also performed time-of-flight measurements which showed, in agreement with the aforementioned excitation, that the flying electron is dragged back in subsequent minima of the SAW train – particularly at the exit of the tunnel-coupled region. In agreement with the aforementioned central source of charge excitation, we observed dependencies of the delay of the SAW-transported electron on the tunnel-coupled region.

Finally, we presented probability oscillations that occurred with a change of the tunnel-barrier potential in a specific asymmetric potential configuration. We showed that the oscillating features correlate with the voltage on the tunnel-barrier electrode. We have so far however not enough indications that the observed features in the transfer probabilities indeed stem from a coherent phenomenon. Based on our findings, we proposed a new experimental setup for systematic investigations of charge coherence of a single SAW-transported electron. Overcoming the remaining challenges in such SAW-driven single-electron circuits, this single-electron transport technique is readily available for the demonstration of quantum mechanical phenomena with a single-flying electrons [Tak19].

Due to the availability of single-electron receivers, SAWs represent a transport medium that is very promising for the demonstration of quantum logic gates with flying electron qubits. Employing a set of experimental investigations combined with quantum mechanical simulations, we gained a better understanding of SAW-driven single-electron transfer in the presently investigated circuit of tunnel-coupled quantum rails. Based on these insights, we provided a clear route to realise a flying charge qubit that is conveyed by sound. Overcoming the remaining challenge of charge excitation, we anticipate that adiabatic transport of an charge qubit is feasible in a circuit of tunnel-coupled quantum rails. We expect that the implementation of novel SAW generation techniques such as the chirp approach in combination with linear electron interferometer structures with dynamic tunnel-barrier control will allow to systematically study coherent phenomena of a single-electron that is surfing on a sound wave.

Appendix

A Phase rigidity in a two-terminal interferometer

The physical basis for phase rigidity in a two-terminal device is time reversal symmetry. It occurs because both magnetic field, $\vec{B}$, and momentum, $\vec{p}$ negate upon time reversal. Let us derive the phase-rigidity relation by modelling the transmission through a two-terminal conductor via a scattering matrix approach:

$$\vec{b} = \hat{S}(B) \cdot \vec{i} \tag{A.1}$$

where $\vec{i} = (i_1, i_2)$ is a vector of incident waves and $\vec{b} = (b_1, b_2)$ is a vector of backscattered waves at the two terminals. A schematic of the discussed two-terminal electron interferometer is shown in Fig. 61.

$\hat{S}(\vec{B})$ is a B-field dependent scattering matrix containing transmission and reflection coefficients, $t(\vec{B})$ and $r(\vec{B})$.

Applying the time reversal symmetry operator on equation A.1 the magnetic field, $\vec{B}$, and the momenta of the incident and backscatter waves, $\vec{i}$ and $\vec{b}$, invert and we obtain:

$$\vec{i}^* = \hat{S}(-B) \cdot \vec{b}^*. \tag{A.2}$$

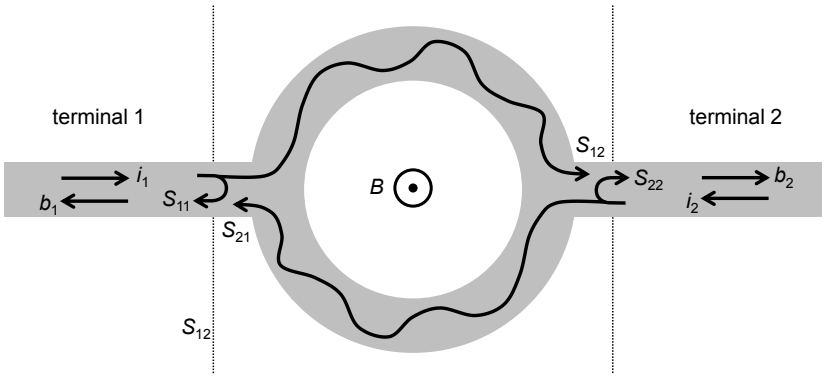

Figure 61: Schematic of a two-terminal electron interferometer in a perpendicular magnetic field. The directions of the incident and backscattered waves are indicated via arrows. The roles of the scattering parameters are also indicated via arrows.

In this time-reversed picture $\vec{b}^*$ represents the incident wave and $\vec{i}^*$ the backscattered wave since the role of the waves exchanged. The B-field dependent scattering object $\hat{S}(B)$, however, remains unaffected.

Combining equation A.1 with the complex conjugate of equation A.2 we obtain the system of equations:

$$\hat{\zeta}(B) = \begin{bmatrix} \zeta_{11}(B) & \zeta_{21}(B) \\ \zeta_{12}(B) & \zeta_{22}(B) \end{bmatrix} = \hat{S}(B) \cdot \hat{S}^*(-B) = \hat{1} \tag{A.3}$$

Due to conservation of current, the scattering matrix $\hat{S}(B)$ further has to be unitary:

$$\hat{S}^\dagger(B) \cdot \hat{S}(B) = \hat{1} \tag{A.4}$$

To meet this condition, $\hat{S}(B)$ requires to suffice the general form of a unitary matrix:

$$\hat{S}(B) = \begin{bmatrix} S_{11}(B) & S_{21}(B) \\ S_{12}(B) & S_{22}(B) \end{bmatrix} = \begin{bmatrix} r(B) & t(B) \\ -t^*(B) & r^*(B) \end{bmatrix} \tag{A.5}$$

The unitary relation must also hold for inverted magnetic field:

$$\hat{S}^\dagger(-B) \cdot \hat{S}(-B) = \hat{1} \tag{A.6}$$

As we additionally consider the relation:

$$T + R = t \cdot t^* + r \cdot r^* = 1 \tag{A.7}$$

we have all the necessary premises to continue with our derivation.

Let us explicitly write down some of the equations of system A.3:

$$\zeta_{11} = \quad r(B) \quad \cdot \quad r^*(-B) \quad - \quad t(B) \quad \cdot \quad t(-B) \quad = 1 \tag{A.8}$$

$$\zeta_{12} = \quad -t^*(B) \quad \cdot \quad r^*(-B) \quad - \quad r^*(B) \quad \cdot \quad t(-B) \quad = 0 \tag{A.9}$$

$$\zeta_{21} = \quad r(B) \quad \cdot \quad t^*(-B) \quad + \quad t(B) \quad \cdot \quad r(-B) \quad = 0 \tag{A.10}$$

Now we can substitute equation A.9 in A.8 and obtain with A.7:

$$-\frac{t^*(-B)}{t(B)} + t^*(B) \cdot t^*(-B) - t(B) \cdot t(-B) = 1 \tag{A.11}$$

Realising that also $\hat{\zeta}(-B) = 1$, we can combine equation A.10 with the complex conjugate of equation A.9, invert the magnetic field and obtain:

$$r(B) \cdot r^*(-B) = r^*(B) \cdot r(-B) \tag{A.12}$$

As we insert A.12 in A.8 we find that:

$$t^*(B) \cdot t^*(-B) = t(B) \cdot t(-B) \tag{A.13}$$

what brings us via A.11 to the relation:

$$t^*(-B) = -t(B) \tag{A.14}$$

Combining equation A.14 with the complex conjugate of A.8 and equation A.7 we obtain the important intermediate result:

$$r(B) = r(-B) \tag{A.15}$$

Finally, we can evaluate the expression for the transmission coefficient, T, and obtain:

$$\begin{aligned} T(B) = t(B) \cdot t^*(B) &\overset{\text{A.14}}{=} -t^*(-B) \cdot t^*(B) \overset{\text{A.9}}{=} \\ &\overset{\text{A.9}}{=} t^*(-B) \cdot t(-B) \cdot \frac{r(B) \cdot r^*(B)}{r(-B) \cdot r^*(-B)} \overset{\text{A.15}}{=} \\ &\overset{\text{A.15}}{=} t(-B) \cdot t^*(-B) = T(-B) \end{aligned} \tag{A.16}$$

Applying the Landauer/Büttiker formalism, we find that this relation is directly mapped on the conductance:

$$G(B) = G(-B) \tag{A.17}$$

We conclude that the conductance through our two-terminal device does not change as the magnetic flux is inverted.

Let us now consider a two-terminal two path interferometer as shown in figure 1. In this setup Aharonov-Bohm (AB) oscillations can be observed in the electrical conductance, G, as a magnetic field perpendicular to the AB-ring, B, is gradually changed:

$$G(B) \propto \cos\left(\delta - \frac{e}{\hbar} \iint\limits_A \mathrm{d}x\mathrm{d}y\ B\right) \tag{A.18}$$

where δ is the phase offset of the AB oscillations at zero magnetic field.

Combining equation A.18 with equation A.17 we get the relation:

$$\cos\left(\delta - \frac{e}{\hbar} \iint\limits_A \mathrm{d}x\mathrm{d}y\ B\right) = \cos\left(\delta + \frac{e}{\hbar} \iint\limits_A \mathrm{d}x\mathrm{d}y\ B\right) \tag{A.19}$$

From this result we immediately see that the phase offset δ must be 0 or a multiple of π. In other words: If the conductance through our two-terminal electron interferometer undergoes AB oscillations, then it must be symmetric at $B = 0$ T to satisfy current conservation.

B Lock-in measurement

To measure the currents, I_0 and I_1, flowing in the detecting terminals of the MZ-type electron two-path interferometer discussed in chapter 1, we performed a lock-in measurement. In the following we describe the corresponding experimental setup and measurement approach in more detail. We employ two lock-in amplifiers of the type "SIGNAL RECOVERY 7265 DSP". On these devices we measure the following quantity:

$$V_{lock-in} = \sqrt{2}\frac{1}{2\pi \cdot f \cdot T}\int_0^T U(t) \cdot \sin(2\pi \cdot f \cdot t)\, \mathrm{d}t. \tag{B.1}$$

Here f denotes the lock-in frequency. $U(t)$ is the time-dependent input signal at the lock-in amplifier. The integration time is typically much larger than the lock-in periodicity ($T \gg f^{-1}$) . The factor $\sqrt{2}$ stems from the conversion factor of the root-mean-square analysis of the lock-in measurement. Here we have chosen the modulation frequency as $f = 23.3$ Hz.

We bias the electron interferometer using a square-wave AC signal that is provided by the DAC-unit. The periodicity of this AC signal is chosen according to the modulation frequency, f. We use this signal also as reference for the lock-in amplifiers. The actual bias voltage, $V_{\mathrm{SD}}(t)$, which is applied on the ohmic contact of the injection terminal of the sample, is obtained from the same AC signal by a voltage divider, giving:

$$V_{\mathrm{SD}}(t) = \frac{V_{\mathrm{SD}}}{D} \cdot \mathrm{sgn}\big(\sin(2\pi \cdot f \cdot t)\big), \tag{B.2}$$

where V_{SD} indicates the amplitude of the voltage oscillation that is provided by the DAC unit and D is the division factor. Here we have chosen $D = 1000$. The bias causes a current:

$$I_{0/1}(t) = \frac{V_{\mathrm{SD}}(t)}{R_{\mathrm{S}} + R} \tag{B.3}$$

that flows via the sample (resistance R_{S}) and an additional series resistance, $R = 10$ kΩ, to ground – see simplified equivalent circuit shown in Fig. 62.

We obtain $I_{0/1}(t)$ via the voltage drop across R. For this purpose we employ voltage amplifiers with a gain of $G = 1000$ and sufficiently high input resistance. With this devices we obtain the input signal that we feed to the lock-in amplifier:

$$U_{0/1}(t) = G \cdot R \cdot I_{0/1}(t) \tag{B.4}$$

The lock-in amplifier then deduces the modulation with the reference signal according to equation B.1. Putting all the building blocks together we obtain the

expression:

$$V_{0/1}^{lock-in} = \sqrt{2} \cdot \frac{G \cdot R}{D} \cdot \underbrace{\frac{V_{\mathrm{SD}}}{R_{\mathrm{S}} + R}}_{=I_{0/1}} \cdot \underbrace{\frac{1}{2\pi} \int_0^{2\pi} \mathrm{sgn}\big(\sin(2\pi \cdot f \cdot t)\big) \cdot \sin(2\pi \cdot f \cdot t)\, \mathrm{d}\tau}_{=2/\pi} \tag{B.5}$$

To obtain the current through our electron interferometer in Ampère, we multiply the voltage signal that we measure on the the lock-in amplifier by the factor:

$$F = \frac{I_{0/1}}{V_{0/1}^{lock-in}} = \frac{\pi}{2\sqrt{2}} \cdot \frac{D}{G \cdot R} \tag{B.6}$$

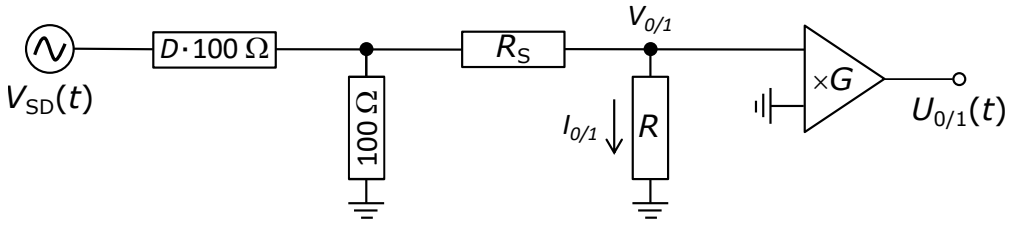

Figure 62: Equivalent circuit of the measurement setup. The input signal for the lock-in measurement, $U_{0/1}(t)$, is amplified by a factor of G. Due to the resistance of the ohmic contacts, the sample resistance R_{S} is in the order of 1 kΩ or larger. To avoid a second mitigation of the bias voltage $V_{\mathrm{SD}}(t)$, the cold ground resistance R must be much larger than R_{S}. Here we have chosen thus $R = 10$ kΩ.

C Rabi oscillation periodicity in a charge qubit

Let us consider a pure quantum mechanical two-level system, defined by the lowest eigenstates in a double-well potential. Assuming that the system is initially prepared in state ψ_0, how much time does it take to tunnel to the state ψ_1? The tunnel transition basically corresponds to an evolution in the quantum mechanical time operator:

$$\hat{U} = \exp\big(-\frac{i}{\hbar} \int \hat{H}(\vec{r}, t)\, \mathrm{d}t\big) \tag{C.1}$$

Applying this operator for a time-invariant Hamiltonian, we obtain the relation:

$$\psi_i(\vec{r}, \Delta t) = \hat{U}\psi_i(\vec{r}, t = 0) = \exp\big(-\frac{i}{\hbar} \cdot E_i \cdot \Delta t\big) \cdot \psi_i(\vec{r}, t) \tag{C.2}$$

Assuming no perturbation and that higher excited eigenstates are sufficiently separated in energy, we can constitute the total electron wave function merely by ψ_S and ψ_A:

$$\begin{aligned}\Psi(\vec{r},\Delta t) &= \exp\big(-\frac{i}{\hbar}\cdot E_S\cdot\Delta t\big)\cdot\psi_S+\exp\big(-\frac{i}{\hbar}\cdot E_A\cdot\Delta t\big)\cdot\psi_A\propto\\ &\propto\psi_S+\exp\big(-\frac{i}{\hbar}\Delta E\cdot\Delta t\big)\cdot\psi_A\end{aligned}\tag{C.3}$$

We can calculate now the probability to find the electron at a time t' at position $\vec{r}$:

$$\begin{aligned}P(\vec{r},\Delta t) &= |\Psi^*(\vec{r},\Delta t)\Psi(\vec{r},\Delta t)|^2=\\ &=\psi_S^2+\psi_A^2+2\cdot\cos\big(\frac{\Delta E\cdot\Delta t)}{\hbar}\big)\cdot\psi_S\cdot\psi_A\end{aligned}\tag{C.4}$$

As the system evolves in time, the electron state oscillates between ψ_S and ψ_A in time intervals of:

$$\Delta t=\frac{\pi\hbar}{\Delta E}\tag{C.5}$$

Accordingly, the quantum state oscillates between ψ_0 and ψ_1. We identify the level-splitting $\Delta E = E_A - E_S$ as the coupling energy between the left and the right quantum rail. As we increase the tunnel barrier, we reduce ΔE what increases the tunneling time Δt.

D Note regarding ground loops

On the employed ^{3}He/^{4}He dilution refrigerator setup (Mélusine) the measurement of QPC current was significantly disturbed by 50 Hz noise. This noise appeared due to different ground potentials of the computers and the ^{3}He/^{4}He dilution refrigerator setup. To mitigate this problem, we forced the ground potential of the analog-to-digital converter card to the ground potential of the dilution refrigerator setup. Let us highlight that this solution is not sustainable for more complicated setups. The cross-connection of ground potentials can lead to electrostatic charge-up and consequently also to discharges that can affect the measurements. For future investigations of SAW-driven single-electron transport on new measurement setups, we thus strongly recommend to think about a proper, for instance star-shaped setup of the ground potentials to avoid the occurrence of ground loops.

E Directional coupling of a flying electron pair

Let us now discuss how this directional coupler transition looks like, when we perform the measurement as discussed in section 2.3.2, but load initially two electrons at the source QD. Employing only the SAW to send the electrons, the two particles are stochastically distributed over the first sufficiently strong periods of the SAW. Having high loading and catching probability at the source and receiver QDs we obtain three two-electron-transfer events as shown in Fig. 63. Here the voltages on the side gates, V_U and V_L, were swept in opposite directions from -1.0 V to -1.3 V. In the presented case the symmetric partitioning configuration ($P_{11} \approx 50$ %) does not coincide with $\Delta = 0$ V, because the sum $V_U + V_L$ was not sufficiently adjusted. Shifting the sweeping range 0.1 V more positive we would have $P_{11} \approx 50$ % at $\Delta = 0$ V. The data shows that the directional coupler operation can be performed with a transfer efficiency of (96.7 ± 0.7) % having two electrons sent by the SAW. One obtains a similar catching distribution as one electron is respectively sent from the upper and the lower source QD as in a HOM-type experiment.

We see that the probability to catch respectively one electron at the two receiver QDs (P_{11}) does not exceed 50 %. This indicates that the partitioning process of the two electrons basically occurs independent of the repulsive interaction of the electron pair. As shown by our time-of-flight measurements – see section 2.3.5 – the electrons are not located at the same position of the SAW train as they trespass the coupling region. Transferring the two electrons with the same SAW minimum along the whole single-electron circuit, the electrons should show anti-bunching because of Coulomb and eventually Pauli repulsion in the tunnel-coupled region. Such anti-bunching effect would be reflected by an increase of P_{11} exceeding 50 % at $\Delta = 0.0$ V.

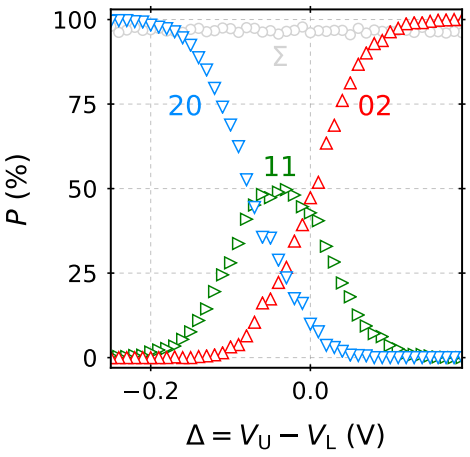

Figure 63: Partitioning two electrons in a beam-splitter setup. Normalised probability to partition two electrons among two tunnel-coupled quantum rails. 02 (20) indicates the probability to catch two electrons at the upper (lower) receiver QD. 11 represents the probabilty to catch respectively one electron at both QDs. The grey data points in the background indicate the total tranfer probability (Σ) that is used for normalisation.

F Additional notes on the sound-driven setup

In the following we present notes that can be helpful for reproduction of the SAW-related experiments that were performed in the course of this thesis or for follow up experiments. First, we address particularities in the set of voltages that we applied on the surface gates of the implemented single-electron circuit and important procedures that guaranteed stable measurements. Secondly, we describe the electrical connections of the surface electrodes of the GaAs chip to the pads of the chip carrier that was mounted in the ^{3}He/^{4}He dilution refrigerator setup. A list of the ranges of the voltages that were typically applied on the surface gates of the investigated device is shown in table 2. Figure 64 shows the larger surface gates and the ohmic contacts (dashed regions) and the 2DEG (light red regions) with schematic indications and labels of the electrical connections. In the following we will use several times the nomenclature that is introduced in Fig. 64.

Initial polarisation procedure of the surface gates

To avoid that electrons are trapped in the depleted potential landscape along the circuit of quantum rails after the first polarisation of the surface gates when starting up the experiment, it is important to polarise the surface gates in the right sequence. For this purpose we polarise the surface gates one after another with -1.6 V when starting up the experiment. First, we start with the tunnel barrier electrode, T. Subsequently, we polarize the side gates, U and L. Then we set the voltage of the inner channel gates, US-I, LS-I, UR-I and LR-I, followed by the outer channel gates, US-O, LS-O, UR-O and LR-O. Finally, we polarise the surface electrodes of the QDs.

Voltage configuration on the upper receiver quantum dot

At the upper receiver QD, it was difficult to achieve strong confinement of an electron with the investigated sample. As consequence, an efficient catching process of a SAW-transported electron was hardly achievable. In early measurements we bypassed this problem by making the inner channel gate very positive and the outer very negative. This explains the large voltage variations on the gates UR-I and UR-O. Doing so, the electron is actually trapped in the end of the upper quantum rail and not in the receiver QD after transport with the SAW train. In this configuration, we evacuated the transferred electron from the channel by polarising the inner channel gate (UR-I) very negatively after each transfer experiment in the fast sequence of voltage movements. At a later point, a bias tee was installed on the pulsing gate of this QD. Balancing the static voltages on the pulsing and coupling gates, V_P and V_C, it was possible to overcome this problem.

By applying a voltage of −0.4 V on the pulsing gate and reducing the coupling voltage C to −0.65 V, we were able to achieve a high catching efficiency also for this QD.

Cross-connection of ohmic contacts

Due to the limited amount of DC lines on the ^{3}He/^{4}He dilution refrigerator setup, we had to reduce the number of employed electrical connections. For this purpose, we have chosen to connect four ohmic contacts respectively at the upper and lower side of the chip together as shown in Figure 64. The cross-connected ohmic contacts were also used to bias the QPCs that are used for charge sensing.

Table 2: Typical voltages applied on electrodes of the beam-splitter device. Listed are typical ranges of voltages, $\mathbf{V} = \{V_i\}$, that were applied on the surface gates of the beam-splitter structure for SAW-transported single electrons. The indices of the gates are chosen according to the labels in Fig. 64.

QUANTUM RAILS

Index i	min V_i (V)	max V_i (V)	Index i	min V_i (V)	max V_i (V)
T	-1.20	-0.30	U,L	-1.51	-0.60
US-O	-0.95	-0.65	UR-O	-0.95	-0.85
US-I	-1.00	-0.85	UR-I	-0.75	-0.60
LS-O	-0.95	-0.71	LR-O	-0.98	-0.75
LS-I	-0.98	-0.95	LR-I	-0.85	-0.75

QUANTUM DOTS AND QUANTUM POINT CONTACTS

Index i	min V_i (V)	max V_i (V)	Index i	min V_i (V)	max V_i (V)
US-Q	-1.46	-1.36	UR-Q	-1.36	-1.20
US-S	-1.09	-0.99	UR-S	-1.02	-0.90
US-R	-0.95	-0.80	UR-R	-1.10	-1.00
US-P	-0.45	-0.00	UR-P	-0.44	-0.00
US-C	-1.00	-0.40	UR-C	-0.99	-0.65
LS-Q	-1.39	-1.30	LR-Q	-1.55	-1.40
LS-S	-0.99	-0.93	LR-S	-0.87	-0.81
LS-R	-1.50	-0.90	LR-R	-1.03	-0.72
LS-P	-0.45	-0.00	LR-P	-0.45	-0.00
LS-C	-0.90	-0.45	LR-C	-0.89	-0.59

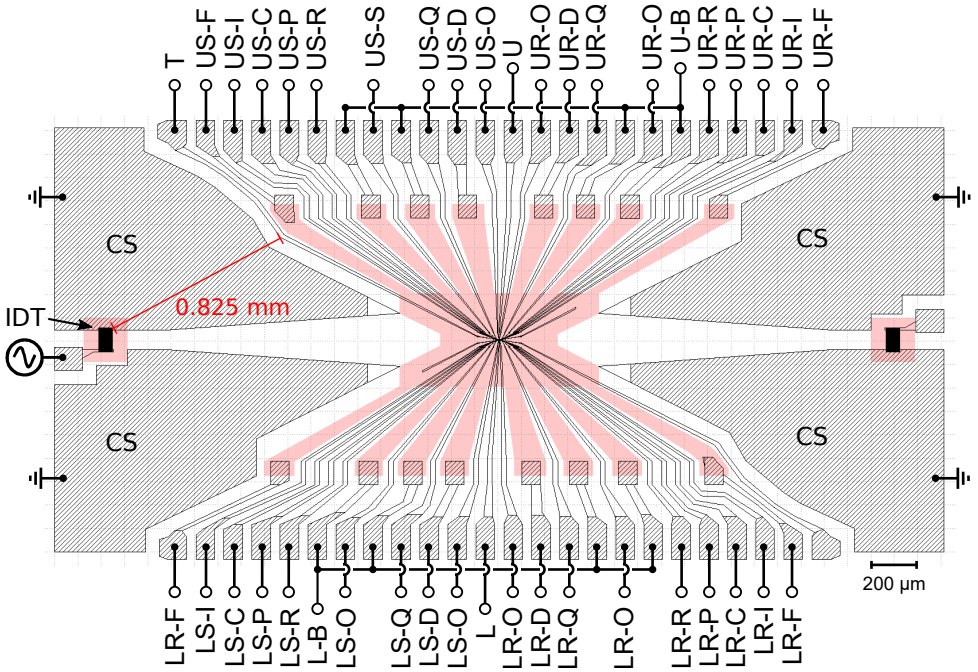

Figure 64: Electrical connections and geometry of the chip. Shows is the geometry of the surface gates (black borders), the ohmic contacts (dashed regions) and the mesa (light red regions). The electrical connections that are established on the chip carrier are schematically indicated according to the following nomenclature:

U / L	Upper (U) or lower (L) side gate of the tunnel-coupled region.
T	Surface gate defining the tunnel (T) barrier.
U-B / L-B	Ohmic contacts that are cross-connected at the upper (U) or lower side (L) of the chip. They are also used as QPC bias.
US-D / LS-D	Ohmic contacts at the upper (U) or lower (L) source QD that are equipped with an IV-converter to measure QPC current.
US-D / LS-D	Ohmic contacts at the upper (U) or lower (L) receiver QD that are equipped with an IV-converter to measure QPC current.
CS	Grounded on-chip shield to prevent the propagation of EM modes from the IDT.
US-X / LS-X	Gate X at the upper or lower source QD.
UR-X / LR-X	Gate X at the upper or lower receiver QD. $X \in \{Q, S, R, P, C, I, O, F\}$
Q	Surface gate to pinch-off QPC.
S	Separation gate between QD and QPC.
R / P / C	Reservoir, plunger or coupling gate of QD.
O / I	Outer or inner channel gate
F	Ohmic contact to electron reservoir for loading into the QD.

G Measuring the amplitude of a surface acoustic wave

Besides their application as single-electron sources, quantum dots (QDs) can be moreover employed as very sensitive electrometers. Consequently, a QD can be used to measure the amplitude of potential modulation that is introduced by a SAW in piezoelectric materials[Sch06]. The measurement approach is based on the broadening of discrete energy levels in quantum dots by SAW modulation. Due to the piezoelectric coupling, a SAW passing through a quantum dot leads to a periodic modification of the quantum dots chemical potential. This causes that the discrete energy states of the quantum dot oscillate with respect to the bias window. During this process – as for the situation of a classical swing – the quantum dot states remain most of the time close to turning points of the oscillation. Repeating Coulomb-blockade-peak measurements with increased SAW amplitude, the conductance peaks split according to the amplitude of the periodic potential modulation. The two lobes in which such a Coulomb blockade peak splits indicate the two energies at which a quantum dot state stays on average most of the modulation time. Stressing again the classical picture of a swing, thus, one can estimate the peak-to-peak amplitude of the SAW-introduced potential modulation by determining the energy difference between those two lobes of the split peak.

In order to obtain this peak-to-peak amplitude in meV, however, the voltage-to-energy conversion factor η has to be known. This quantity can be determined from Coulomb diamond measurements as exemplary shown in Fig. 65a. Knowing η, one can measure the broadening of the Coulomb blockade peaks with rising amplitude of the SAW introduced potential modulation, A. Figure 65b shows an exemplary data set showing the broadening of Coulomb blockade peaks with increasing transducer power, P. The splitting of resonances is indicated by the dashed red lines. At $P \approx 1$ dBm the side peaks of two neighbouring Coulomb blockade peaks start to overlap. At the intersection position, the peak-to-peak amplitude of the SAW is equal to the charging energy of the quantum dot, E_C. The peak-to-peak amplitude of the SAW introduced potential modulation, A, is related to the transducer power, P, by the relation [Bau14a]:

$$A\ [\mathrm{eV}] = 2 \cdot \eta \cdot 10^{\frac{P\ [\mathrm{dBm}] - P_0}{20}}, \tag{G.1}$$

where P_0 is a fit parameter accounting for power losses.

Since these measurements are performed in continuous-wave mode, we trace the broadening of the Coulomb-blockade peaks only up to a transducer power of -5 dBm in order to avoid unnecessary heating. Fitting equation G.1 to the data we estimate the SAW amplitude for the typically applied transducer power of 25 dBm with 30 ns pulse modulation. Figure 65c shows the SAW amplitude data (zoom in inset) and the extrapolation to 25 dBm (grey area) for measurements on

the present beam-splitter device. The extrapolation indicates a SAW introduced peak-to-peak modulation of about (15 ± 5) meV in the single-electron transfer experiments. Consequently, we modelled the SAW modulation driving single-electron transport in the present beam splitter setup with 15 meV peak-to-peak amplitude.

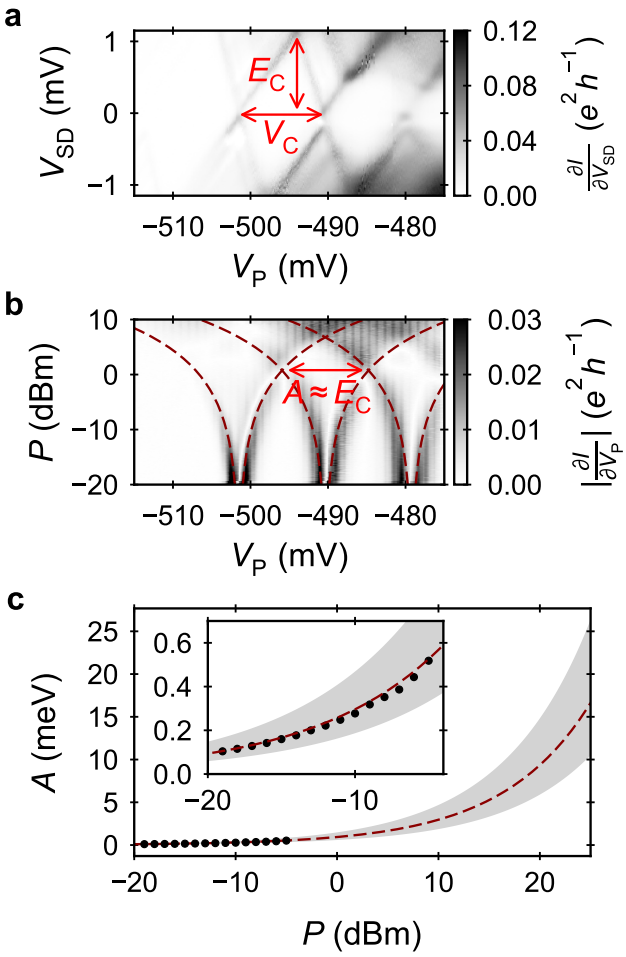

Figure 65: Estimation of the SAW amplitude. (a) Exemplary Coulomb-diamond measurement allowing the extraction of the voltage-to-energy conversion factor $\eta = E_C/V_C$. **(b)** Broadening of the corresponding Coulomb-blockade peaks with increasing transducer power, P. **(c)** Amplitude of SAW introduced potential modulation. The dashed line shows a fit of equation G.1 to the experimentally obtained data. The confidence region (grey area) is roughly estimated from variations of measurements on four QDs on a similar sample. The plot shows an extrapolation of this region to the typically employed transducer power of 25 dBm. The inset shows a zoom into the data points. The figure stems from our publication Takada et al. [Tak19].

H Comparison of SAW profiles at source and receiver

Similar to the voltage-pulse triggered sending process presented in section 2.3.4, a short voltage pulse can be used to probe the arrival of the SAW: Different than for the source side, where the electron is transferred in the transport channel, in this situation the electron is transferred from the receiver QD back into the Fermi sea. Measuring the holding probability of such a directly loaded electron at the receiver side as the delay of the short voltage pulse is swept along the expected arrival window of the SAW, we obtain fringes in the data as discussed in section 2.3.4. Comparing the voltage pulse-triggered sending distribution at the source QD – see Fig. 66a – with the voltage pulse-triggered holding distribution that we measure at the receiver QD – see Fig. 66b – we observe that the SAW arrives after about 8.1 ns as expected for SAW propagation along the present 22.5 μm long transport channel considering a SAW velocity of 2.77 μm/ns. The probability profiles shown in Fig. 66 serve as reference in Fig. 49 and Fig. 50 of section 2.3.5.

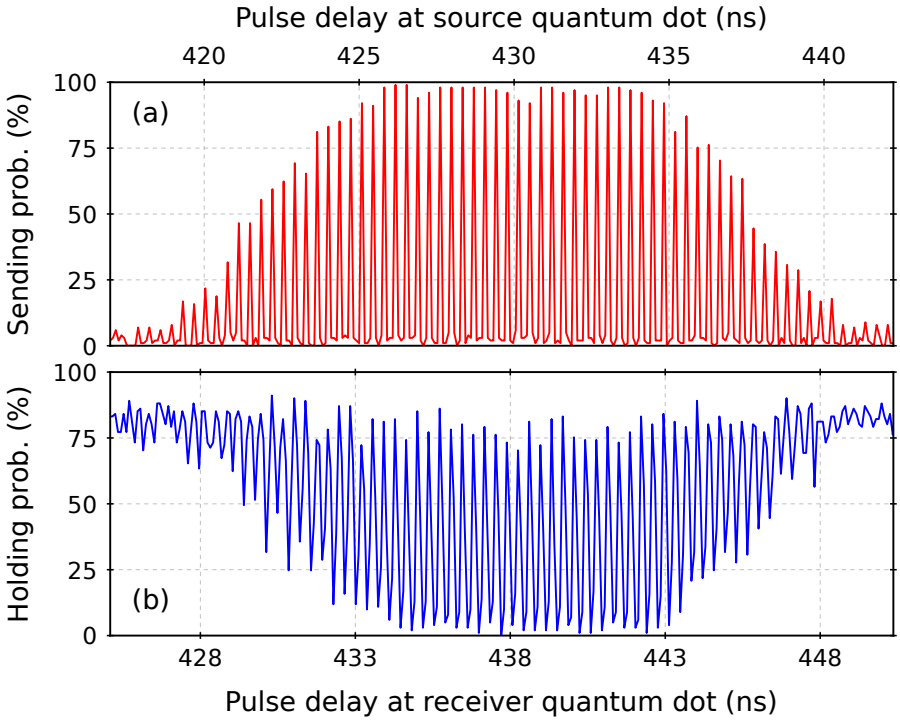

Figure 66: SAW-profiles represented by sending and holding probability. (a) The data shows the sending probability as a 180 ps pulse is swept over the arrival window of the SAW at the source QD **(b)** Here an electron is only loaded at the receiver QD. The data shows the holding probability as the pulse delay is swept over the arrival window of the SAW at the receiver QD.

I Tunnel oscillations of a flying charge qubit

Let us briefly derive the principal tunnel behaviour of an electron in a double well potential.[25] Assuming a homogenous tunnel-coupled region, the Hamiltonian of a flying electron occupying the two lowest eigenstates in a double-well potential is given by:

$$\hat{H} = \hat{H}_{\text{kin}} + \hat{H}_{\text{pot}} \tag{I.1}$$

where $\hat{H}_{\text{kin}}$ and $\hat{H}_{\text{pot}}$ describe the kinetic and potential energy terms. Assuming translational invariance along the propagation direction, x, the problem becomes separable in the spatial coordinates, x and y, allowing us to focus on the solution of the potential energy term. Describing the two-level system of the lowest eigenstates in the double-well potential by a Hubbard model we can express the potential energy term of the Hamiltonian in the basis of the states $|0\rangle$ and $|1\rangle$ as:

$$\hat{H}_{\text{pot}} = \begin{bmatrix} E_0 & -\Delta E/2 \\ -\Delta E/2 & E_1 \end{bmatrix} \tag{I.2}$$

where $\Delta E = E_{\text{AS}} - E_{\text{S}}$ is the coupling energy and E_0 and E_1 are the on-sight energies of being in the left or right quantum rail.[26] The eigenenergies of this Hamiltonian are:

$$E_{\pm} = \underbrace{\frac{E_0 + E_1}{2}}_{=\varepsilon} \pm \sqrt{\Big(\underbrace{\frac{E_0 - E_1}{2}}_{=\delta}\Big)^2 + \Big(\underbrace{\frac{\Delta E}{2}}_{=\gamma}\Big)^2} \tag{I.3}$$

where we can identify ϵ as an energy offset determined by the on-sight energies, Δ as the potential detuning between the two quantum rails and γ as the coupling energy. With these definitions we can write the eigenenergies and eigenstates of this Hamiltonian as:

$$E_{\pm} = \varepsilon \pm \sqrt{\delta^2 + \gamma^2} \tag{I.4}$$

$$|\psi_{\pm}\rangle = \frac{\gamma}{\sqrt{\gamma^2 + A_{\pm}^2}} \Big(|0\rangle + \frac{A_{\pm}}{\gamma} |1\rangle \Big) \tag{I.5}$$

where $A_{\pm} = \delta \mp \sqrt{\delta^2 \mp \gamma^2}$.

For a certain propagation time, t, of the flying electron one can now obtain the

[25] The following derivation is based on the PhD theses of Shintaro Takada and Grégoire Roussely

[26] To understanding the nomenclature of symmetric and antisymmetric states see section 2.1.1.

final state by applying the time-evolution operator:

$$|\psi(t)\rangle = \hat{U}(t)\,|\psi(0)\rangle = \exp\Big(-\frac{i}{\hbar}\hat{H}_{\mathrm{pot}}t\Big)\,|\psi(0)\rangle \tag{I.6}$$

$$= \sum_{\pm} \exp\Big(-\frac{i}{\hbar}E_{\pm}t\Big)\,|\psi_{\pm}\rangle\,\langle\psi_{\pm}|\,|\psi(0)\rangle \tag{I.7}$$

Assuming an initial state prepared in the upper channel, $|\psi(0)\rangle = |0\rangle$, we can calculate the probability to find the electron in the initial state:

$$P_0 = |\,\langle 0|\,\hat{U}(t)\,|0\rangle\,|^2 \tag{I.8}$$

After quite a lot, but straight-forward algebra we arrive at the expressions:

$$P_0 = 1 - \frac{\gamma^2}{\delta^2+\gamma^2}\sin^2\Big(\frac{\sqrt{\delta^2+\gamma^2}\cdot t}{\hbar}\Big), \tag{I.9}$$

where the the complementary probability is $P_1 = 1 - P_0$. Depending on the tunnel coupling, γ, and the potential detuning, δ, the electron state experiences Rabi oscillations between the states $|0\rangle$ and $|1\rangle$. Besides the application on charge qubits, this model of a two-level system can be mapped on many other problems

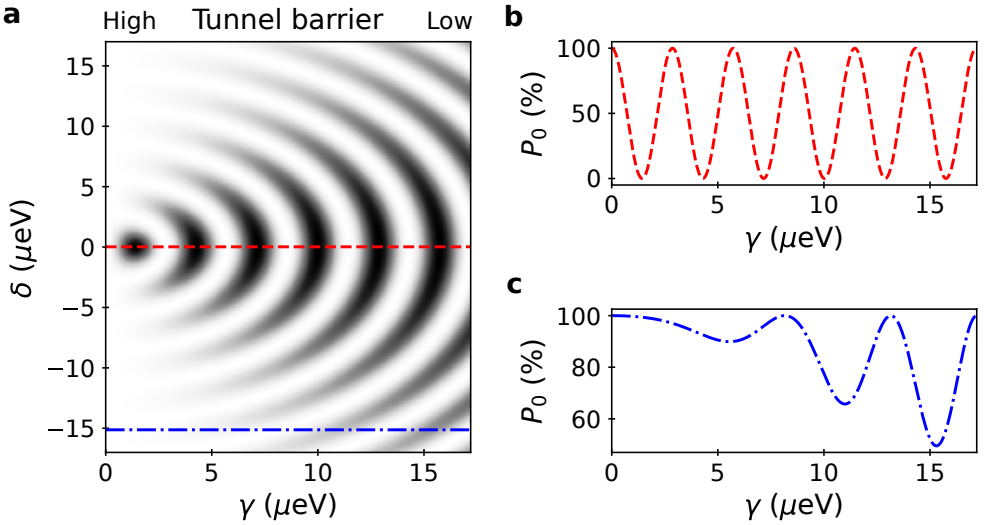

Figure 67: Theoretically expected tunnel oscillations of a flying charge qubit. Shown is the probability, P_0, to end up in the upper side of the double well potential. **(a)** P_0 as function of coupling energy, $\gamma = (E_{\mathrm{AS}} - E_{\mathrm{S}})/2$, and potential detuning, $\delta = (E_0 - E_1)/2$. The data is calculated according to equation I.9 for a SAW-transported electron after propagation along a 2-μm-long tunnel-coupling region. **(b)** Tunnel oscillations for a perfectly symmetric double-well potential, $\delta = 0$ μeV. **(c)** Tunnel oscillations for asymmetric double-well potential with $\delta \approx -15$ μeV.

such as spin qubits or masers [SN18]. Figure 67 shows a plot of equation I.9 assuming propagation of a SAW-transported electron along a 2-μm-long tunnel-coupled region.[27] The plot shows that the tunnel-oscillation amplitude quickly goes down for small values of potential detuning, δ.

J Preliminary measurements on undoped devices

In the following we present data from a first investigation of a nanoelectric device realised in an undoped GaAs/AlGaAs heterostructure. The device was fabricated in the course of a secondment at the Cavendish Laboratory in Cambridge. The measurements were performed at the the Institute Néel in Grenoble. The idea of the implemented sample is to have both accumulation and depletion gates directly deposited on the surface of the GaAs/AlGaAs heterostructure. The ohmic contacts represent a central component in such an undoped architecture. Figure 68a schematically shows the structure of the employed ohmic contacts. Electrical connection to the quantum well is established via an AuGeNi alloy that is deposited in a trench that is etched into the GaAs/AlGaAs heterostructure.[28] This ohmic connection is isolated via a Al_2O_3 layer from a bridging gate that allows accumulation of electrons below a surface gate that brings the charge carriers along the quantum well to the nanostructure. An optical microscopy image of two ohmic contacts from the fabricated prototype sample is shown in Fig. 68b. For details on this type of ohmic contacts we refer to the thesis of Tzu-Kan Hsiao [Hsi18].

Ramping up the voltage of the surface gate with a sufficiently positivly polarised bridging gate (here +1.1 V), charge carriers accumulate in the quantum well below the accumulation gate. Depending of the quality of the isolation layer there is at some point a leakage current occuring between the ohmic connection and the surface gate as exemplarily shown in Fig. 68c. The voltage on the bridging and surface gate has to be chosen in a way such that a proper balance between accumulation and leakage is achieved. To monitor the suppression of leakage current, we present in the following two-terminal measurements where an IV converter is respectively placed on each ohmic contacts. The electric potential on an ohmic connection is determined by the reference voltage, V_R, on the current amplification setup. V_R basically determines the Fermi energy of the ohmic connection, whereas V_S determines the potential of below the surface gate allowing accumulation of charge carriers at the nanostructure. The voltages of the ohmic contact, the bridging gate and the surface gate are typically chosen in a way that: $V_\mathrm{R} + 0.8\ \mathrm{V} < V_\mathrm{S} < V_\mathrm{B} - 0.8\ \mathrm{V}$. When sweeping V_R, it is important to change V_S accordingly in order to keep the electron density constant. The measurements

[27] The propagation time of the flying electron is $t \approx 0.72$ ns.

[28] To accumulate electron holes AuBe can be used instead.

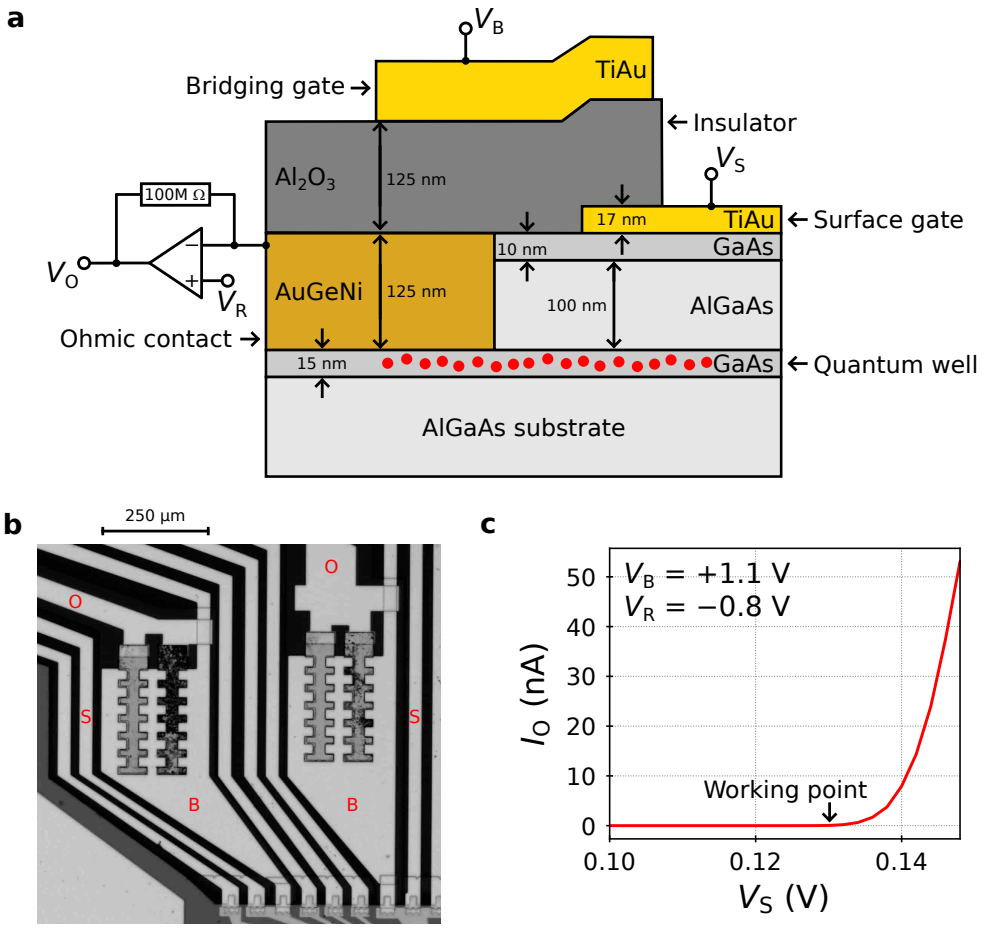

Figure 68: Design and characterisation of ohmic contacts in undoped samples. **(a)** Schematic showing the structure of layers forming the ohmic contact. The ohmic contact (AuGeNi) is deposited in an etched trench of about 120 nm depth. Applying a positive voltage, V_B, on the bridging gate charge carriers (red points) get accumulated in the quantum well. These charge carriers are then brought to the nanostructure by polarising also the surface gate positively (via V_S). V_R indicates the reference voltage on the ohmic contact. **(b)** Optical microscopy image showing the surface gate (S), the bridging gate (B) and the ohmic contact (O) of the fabricated sample. **(c)** Leakage characteristic of an ohmic contact. Increasing the voltage on the surface gate, V_S, there is at some point a leakage current occurring. Sufficient accumulation of charge carriers can be typically achieved below the surface gate (S) when putting the working point just below the leakage region.

showed that it is easier to accumulate charge carriers close to the nanostructure when putting V_S only slightly above ground potential. With the present setup of ohmic contacts it is important to avoid the occurrence of leakage currents in order to guarantee charge stability. When measuring the current between two ohmic contacts, we therefore mount an IV converter at each ohmic connection in order to verify current conservation.

SEM images of the fabricated nanostructure are shown in Fig. 69a and Fig. 69b. Figure 69a shows the QD and QPC region. Accumulation and depletion gates are shaded in blue and red. Figure 69b shows the whole nanostructure. The device consists out of two surface-gate defined QDs that are placed at the end of a 4 μm transport channel. Next to each QD we place a QPC. It turned out that due to electrostatic charge up measurements on the fabricated device were very unstable. This rendered the reproducibility of measurements difficult. With these experimental limitations it was not possible, to stay at a certain working point of a QPC pinch-off characteristic to sense the presence of an electron in a QD. Consequently, we were only able to perform a few measurements that we discuss in the following.

Accumulating electrons below the two reservoir gates of the left QPC, we measured the pinch-off characteristics. In such a measurement it is necessary that the voltage of the pinch-off gate is always more negative or equal to the voltage of the reservoir gates in order to avoid charge up. Figure 69c shows an exemplary pinch-off characteristic with a large bias of 25 mV. The QPC characteristics showed two very flat conductance plateaus, however, at extremely low values of current. The current characteristic was, however, only slightly dependent on the voltage of a side gate what indicates that the QPC constriction is not well defined. To measure larger parts of the QPC pinch-off characteristic, we propose to avoid placing accumulation gates in a row. In order to obtain better control of the presence of charge carriers, it is beneficial to have a depletion gate always placed in between two accumulation gates in first investigations of such undoped nanostructures.

We also tried to send an acousto-electric current through the transport channel. For this purpose, we placed a single-finger IDT as SAW source about 1.2 mm beside the nano-structure. In order to achieve continuous SAW-driven transport of charge carriers, it was necessary to apply an extremely positive voltage on the central transport-channel gate. At a voltage of about +3.3 V it was indeed possible to send a SAW-driven current from one reservoir to the other. The relatively high tension between the nanoelectric surface gates, however, caused an electric breakthrough, which fused the respective surface gates – see SEM image in Fig. 69d. Consequently, it was not possible to perform further measurements on this sample.

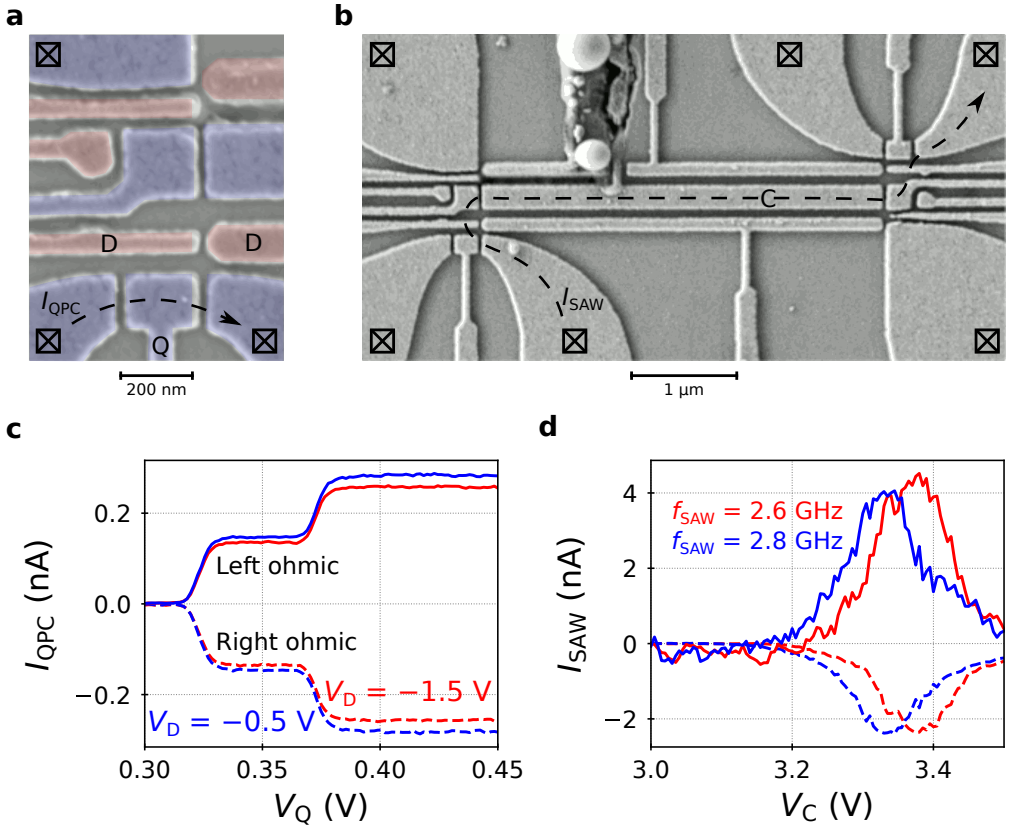

Figure 69: Preliminary measurements in an undoped architecture of quantum dots and quantum point contacts. (a) SEM image of the QD and QPC region. Accumulation and depletion gates are shaded in blue and red. Ohmic contacts are indicated via crossed boxes. The dashed arrow indicates the path of the QPC current measurement presented in (c). **(b)** SEM image of the whole nanostructure. The dashed arrow indicates the path of the SAW current measurement presented in (d). **(c)** Measurement of the pinch-off characteristic. Shown are the currents through the left (positive) and right (negative) QPC for different values of the side gates with voltage V_D. **(d)** Measurement of a continuous SAW current, I_{SAW}, for different voltages, V_C, on the central transport-channel gate. Here the side gates of the transport channel were polarised to -0.8 V. The QD and QPC gates were polarised to about + 1.0 V. Due to leakage currents, the current through the left (positive) and right (negative) ohmic contact do not match.

Résumé de la thèse en français

La mécanique quantique a fortement amélioré notre compréhension de la nature. La description quantique des structures cristallines a conduit à l'émergence de la physique de l'état solide et a permis une compréhension complète des propriétés mécaniques, thermiques et électriques des composés des matériaux [Kit04; AM76]. Ces progrès ont permis l'invention de dispositifs électroniques à semi-conducteurs qui ont déclenché une révolution technologique qui façonne la vie dans notre société moderne [Bar56; Bra56; Sho56]. Le succès de l'industrie des semi-conducteurs s'est accompagné du développement d'un vaste ensemble de nouvelles technologies qui ont considérablement accru les perspectives de la science. Le tournant de la recherche expérimentale moderne sur les dispositifs à semi-conducteurs a certainement été marqué par la découverte de l'effet Hall quantique [KDP80; vKl85]. Cette découverte révolutionnaire a permis d'établir une norme de résistance électrique basée sur le quantum de conductance e^2/h. En outre, il a stimulé la motivation pour de nouvelles études sur les effets de la quantification de la conductance électronique dans les dispositifs à semi-conducteurs.

Les progrès sur l'épitaxie par faisceau moléculaire [Joy88], le dépôt chimique en phase vapeur [HLW91] et la lithographie par faisceau d'électrons [MDD92] ont permis la fabrication de dispositifs électriques dans des transistors à haute mobilité électronique (HEMT) sur une échelle nanométrique. En raison de ses propriétés exceptionnelles d'appariement des réseaux, les hétérostructures GaAs/AlGaAs sont devenues une plateforme particulièrement intéressante pour réaliser des expériences avec des électrons dans ces nanostructures à des températures cryogéniques [Smi96]. Dans ces dispositifs HEMT, des électrons peuvent être accumulés à l'interface GaAs/AlGaAs via des grilles de surface à polarisation positive. Alternativement, il est possible d'introduire un gaz électronique bidimensionnel permanent à l'interface GaAs/AlGaAs via l'introduction d'une couche dopée Si-δ. Dans ce dernier cas, le gaz électronique sous une grille de surface peut être épuisé en polarisant l'électrode avec une tension négative.

De ce progrès technologique sont nés plusieurs dispositifs nanoélectriques importants, qui ont permis la démonstration expérimentale de nouveaux phénomènes de mécanique quantique. La mise en œuvre de contacts à points quantiques (QPC) définis par la grille de surface a permis par exemple l'observation de plateaux

de conductance quantifiés [vWe88; Wha88]. En utilisant des électrodes de surface pour former des structures de points quantiques (QD) dans le paysage du potentiel bidimensionnel, il a en outre été possible de démontrer le régime de blocage de Coulomb dans un transistor à un seul électron [vHo92]. Suite à ces développements, les QPC ont également été utilisés pour détecter la présence d'électrons simples dans un point quantique (QD) à grille de surface définie [Ash92; Fie93]. Les progrès des techniques de nanofabrication ont en outre déclenché le développement de structures d'interféromètres électroniques à grille de surface définie. Avec ces interféromètres électroniques, il a été possible d'observer des oscillations Aharanov–Bohm (AB) montrant que le transport balistique des électrons a une composante cohérente [Yac95]. Ces développements ont illustré le potentiel des HEMTs comme plateforme fructueuse pour la démonstration et l'étude des phénomènes de mécanique quantique avec les électrons.

Le titre de la présente thèse fait référence à l'optique quantique. Ce terme est généralement associé aux photons. Il s'agit d'un domaine de recherche qui étudie les phénomènes de mécanique quantique de la lumière et ses interactions subatomiques avec la matière. Les outils centraux d'investigation exploitent les effets d'interférence et les processus d'absorption des photons. Deux exemples célèbres dans le domaine de l'optique quantique sont le Hanbury-Brown–Twiss (HBT) [HBT54] et l'effet Hong–Ou–Mandel (HOM) [HOM87]. Ces deux effets s'enracinent dans la nature bosonique de la lumière: Le nombre de photons occupant le même état quantique n'est pas limité. Par conséquent, les photons ont tendance à se regrouper dans le même état quantique. Pour démontrer ces effets, on utilise généralement un dispositif séparateur de faisceau avec des détecteurs de photons tels que des photodiodes à avalanche placées aux deux sorties de l'appareil. Quand deux photons indiscernables entrent simultanément dans un tel séparateur de faisceau par la même entrée (effet HBT) ou par deux entrées différentes (effet HOM), ils ont tendance à se regrouper dans le même état et à quitter l'appareil en conséquence à la même sortie. En analysant les statistiques de comptage de ces détecteurs, on trouve donc une anti-corrélation dans les événements subséquents de détection de photons ce qui indique une faible probabilité que deux photons indiscernables arrivent respectivement en même temps aux deux détecteurs.

Le domaine de l'optique quantique est déjà bien avancé. Des installations expérimentales photoniques ont par exemple été utilisées pour démontrer l'intrication d'informations quantiques codées dans la polarisation de la lumière [O'B03], dans les champs de cavité [Del08] ou dans les états de spin des ions atomiques piégés [BW08]. La démonstration d'opérations de logique quantique sur des rayons lumineux cohérents a en outre stimulé l'idée d'un ordinateur quantique photonique [Lan08]. Une application intéressante des expériences d'optique

quantique est la mise en œuvre de puces photoniques quantiques pour résoudre les problèmes de valeur propre des Hamiltoniens chimiques [San18]. Un problème central de l'informatique quantique avec les photons est cependant qu'ils interagissent à peine avec d'autres particules. Il est donc difficile de stocker les photons et de les coupler efficacement. En plus de ces aspects, il est également exigeant de réaliser des sources monophotoniques efficaces qui émettent ces particules dans des intervalles de temps réguliers. Et aussi la détection de photons individuels est jusqu'à présent plutôt basée sur des processus d'absorption stochastique [Had09]. Ces questions font que les portes de la logique quantique photonique ont jusqu'à présent travaillé sur une efficacité relativement faible.

Par analogie avec l'optique quantique, le domaine de recherche de l'optique quantique électronique étudie les phénomènes de mécanique quantique des électrons volants et leur interaction avec la matière et les atomes artificiels tels que les points quantiques. Ce domaine de recherche est plutôt récent.[29] En raison des propriétés d'un électron, il est préférable de mener de telles expériences en optique quantique dans un cadre à l'état solide. Un électron porte la charge élémentaire, $q_e = -e$, qui permet à la particule de se propager dans un champ électrique par interaction de Coulomb. Cette propriété rend les phénomènes d'interférence des électrons accessibles via des phénomènes quantiques tels que l'effet AB. Avec leur spin demi-entier, les électrons sont des fermions et obéissent au principe d'exclusion de Pauli. Cette propriété les limite à occuper le même état quantique. En imaginant l'expérience HBT ou HOM susmentionnée pour les électrons, on s'attend donc à ce que deux particules ne soient pas en faisceau en raison de la répulsion de Pauli et Coulomb. Par conséquent, deux électrons qui interagissent dans un séparateur de faisceau quittent l'appareil toujours à l'opposé, mais jamais par la même sortie.

La question de savoir si le principe d'exclusion de Pauli ou l'interaction de Coulomb est la force motrice de la répulsion des électrons est maintenant une question critique. Le mécanisme dominant dépendra de l'échelle de longueur, du temps d'interaction et des échelles d'énergie impliquées. Pour acquérir une compréhension approfondie des mécanismes sous-jacents, il est nécessaire d'effectuer de telles expériences d'optique quantique électronique d'une manière plus contrôlable au niveau de la particule unique.

Les effets de l'interférence HOM ont déjà été expérimentalement rencontrés dans le passé en utilisant un flux continu d'électrons traversant une structure de séparateur de faisceau qui a été mise en œuvre dans un dispositif à semi-conducteurs [Liu98; Oli99]. Ces barrières étroites permettaient le couplage d'électrons volants avec un dispositif semblable à un séparateur de faisceau dans le

[29] Les premières expériences d'interférence d'électrons ont été réalisées en 1995 [Yac95]. Une interférence fiable des électrons volants sur deux voies a toutefois été établie 17 ans plus tard [Yam12; Tak15].

régime de transport balistique. En polarisant simultanément les canaux d'entrée d'un tel séparateur de faisceau, on a observé une réduction de la puissance de bruit actuelle par rapport à la polarisation individuelle des deux canaux d'entrée, ce qui reflétait l'interférence HOM des électrons volants.[30] Cette découverte de l'anti-bunching d'électrons a illustré le potentiel d'une telle structure de séparateur de faisceau pour d'autres applications dans des expériences d'optique quantique des électrons.

La disponibilité de blocs de construction bien contrôlables tels que les QPC et les QD a inspiré la réalisation du premier interféromètre électronique de type Mach–Zehnder (MZ) à structures de rupture de ligne [Yac95; Sch97]. Les structures de l'interféromètre électronique ont été perfectionnées à l'aide de barrières à effet tunnel définies par des grilles de surface pour la formation de séparateurs de faisceaux électroniques, afin d'assurer l'interférence à deux voies des électrons volants. Ces progrès ont permis la démonstration d'opérations de logique quantique de base pour un flux balistique d'électrons volants [Yam12] et l'étude de questions fondamentales de physique mésoscopique comme l'effet Kondo [Kon64; GG98; Tak14; Tak16]. L'élaboration de critères de fiabilité pour l'interférence à deux voies des électrons [Bau14b; Tak15] a ouvert la voie à l'étude de questions de longue date soulevées par les résultats des premières expériences dans le domaine de l'interférométrie électronique à deux voies.

Utilisant un dispositif d'interféromètre électronique multi-terminal, Schuster *et al.* [Sch97] a réussi à mesurer le déphasage caractéristique de transmission le long d'une résonance de blocus de Coulomb. De façon inattendue, ils ont rencontré un changement de phase abrupt entre deux résonances successives. [31] Par la suite, cette observation a été attribuée à un régime générique où de telles interruptions de phase de transmission se produisent de manière universelle [Hac01]. Des travaux ultérieurs ont fait référence à cette observation comme à un comportement de phase de transmission universelle [AK05]. La question d'un tel comportement universel a suscité beaucoup d'intérêt [OG97; HHW97; AuS98; Pat98; VLM98; Wu98; BG99; Kan99; Lee99; TB99; SI00; LB00; HM18; GG06; BG07; Kar07; Gol09; Mol12; Jal14]. Malgré de nombreux efforts théoriques, une explication claire d'un tel régime universel fait toutefois toujours défaut. En raison de leur difficulté expérimentale, de telles expériences d'optique quantique électronique avec un seul transistor électronique sont rarement réalisées. Seuls quelques groupes ont réussi à effectuer de telles mesures de phase de transmission [Sch97; Sig04; Aik04a; AK05]. Cette situation donne à penser que d'autres études expérimentales seront menées sur ce sujet.

La première partie de cette thèse est donc consacrée à réétudier cette question

[30] Cet anti-bunching des électrons a également été observé dans les conducteurs Hall quantiques [Ned07; Fre15].

[31] Ils mentionnent un balayage de la phase de transmission sur 10 résonances successives.

de longue date sur le comportement en phase de transmission universelle en expérimentation. Pour ce faire, nous utilisons les éléments de base susmentionnés de séparateurs de faisceaux définis par barrière tunnel et de canaux de transport unidimensionnels pour réaliser une expérience d'interférométrie à deux voies avec des électrons volants dans le régime de transport balistique. Dans cette expérience, l'aspect monoparticulaire entre en jeu à partir d'un grand QD, qui est inséré comme milieu déphasant dans une branche de la structure de l'interféromètre. Nos mesures de phase de transmission montrent clairement un comportement de phase non universel et fournissent plusieurs indications pour le comportement de phase de transmission dépendant de la parité théoriquement attendu [Lee99; TB99]. Nos résultats placent les observations susmentionnées d'expériences pionnières sur l'interférométrie électronique à deux voies dans une nouvelle perspective et résolvent le puzzle de longue date sur un comportement de phase de transmission universel dans les grands QDs [Edl17]. Nous prévoyons que les mesures de phase de transmission représentent un outil utile pour révéler la structure interne des points quantiques en expérimentation. Nous nous attendons à ce que nos résultats stimulent d'autres recherches expérimentales sur les mesures de phase de transmission et sur d'autres sujets fondamentaux, tels que les systèmes électroniques corrélés [Tho96; Bau13; Iqb13].

Il est maintenant intéressant d'aller au-delà du régime de transport balistique et d'étudier les phénomènes de mécanique quantique à l'aide d'électrons volants simples dans le cadre d'expériences à tir unique. Cette approche permet essentiellement d'étudier le comportement d'une particule complètement isolée et fournit un contrôle spatial et temporel sur l'électron volant, ce qui permet une étude plus détaillée de l'interaction des électrons volants individuels. Outre l'intérêt scientifique, de telles expériences d'optique quantique électronique à un seul coup promettent de démontrer des opérations de logique quantique pour des qubits à charge unique. Afin de fournir une telle plate-forme pour des expériences de type optique quantique avec des électrons volants uniques, différentes approches de sources d'électrons uniques ont été développées au cours des dernières années. Soulignons ici trois de ces sources qui permettent des taux de répétition dans le régime GHz : condensateurs mésoscopiques [Fèv07; Boc12; Boc13], pompes à barrière accordable [Blu07; Fle12; Gib12; Ubb14; Fri14] et Levitons [Dub13; Jul14]. Avec ce type de sources de particules, quelques expériences de type optique quantique ont déjà été menées avec succès avec des électrons volants simples.

Dans le régime quantique de Hall, des électrons simples peuvent être lancés le long de canaux de bord par un signal de tension oscillant appliqué sur un condensateur mésoscopique [Fèv07]. Cette approche permettait déjà d'observer l'antibrouillage d'électrons individuels dans un HBT [Boc12] ou HOM setup [Boc13]. Une approche conceptuellement plus avancée est la pompe à barrière accordable où une structure à points quantiques (QD) est utilisée pour mélanger un électron d'un

réservoir de charge à l'autre [Blu07]. Cette source d'un seul électron permet d'ajuster l'énergie de la particule émies d'une manière très contrôlable. Avec des champs magnétiques élevés [Fle12; Gib12] ou des émetteurs connectés en série et cadencés [Fri14] ce type de source monoélectronique fournit des plateaux de courant extrêmement stables pour de très petits courants $I = e \cdot f \ll 1$ nA. Par conséquent, ce type de sources à un seul électron présente un fort potentiel pour les futures normes unitaires dans le régime des courants extrêmement faibles où l'incertitude relative des nouveaux générateurs de courant quantique programmable (PQCG) augmente fortement. La pompe à électrons à barrière accordable a également permis de démontrer l'interaction répulsive d'électrons à très haute visibilité dans une installation HBT [Ubb14].

La troisième source considérée est celle qu'on appelle les Levitons. Ce type de quasiparticule est une excitation collective d'un seul électron volant au-dessus de la mer de Fermi. Elle peut être formée par une impulsion de Lorentz appliquée par un contact ohmique au 2DEG. La particularité de cette excitation pulsatoire est sa distribution d'énergie exponentielle qui laisse la mer de Fermi complètement intacte. Grâce au découplage de la mer de Fermi, les Levitons devraient avoir des propriétés de cohérence exceptionnelles. Démontrant la réduction du bruit de tir dans une installation HOM, la présence de Levitons a été démontrée dans des hétérostructures GaAs/AlGaAs par excitation par impulsions de tension de Lorentz [Dub13]. Par la suite, de telles réalisations expérimentales de Levitons ont également été appliquées avec succès pour la tomographie à l'état quantique [Jul14].

Les critères de DiVincenzo pour la réalisation d'un ordinateur quantique ont identifié la transmission d'informations quantiques entre des nœuds stationnaires de calcul comme une exigence centrale pour la réalisation d'un ordinateur quantique [DiV00]. Plusieurs travaux théoriques ont développé davantage cet aspect vers l'idée d'une architecture de calcul quantique à électrons volants [Ber00; IAU01]. Pour mettre en œuvre de telles propositions dans l'expérimentation, il faut fondamentalement trois composantes : une source bien contrôlable d'électrons uniques, un moyen de transport et de manipulation cohérent et un détecteur de qubits d'électrons volants uniques. Toutes les expériences susmentionnées avec des condensateurs mésoscopiques, des pompes électroniques à barrière accordable et des levitons sont réalisées par l'analyse des corrélations dans les mesures de courant. Cette approche de mesure est fondamentalement suffisante pour démontrer et étudier jusqu'à un certain point les expériences d'optique quantique électronique. Pour étudier plus en détail l'interaction des électrons volants individuels, il est cependant nécessaire d'effectuer des expériences à un seul tir. De telles expériences nécessitent un détecteur ou un récepteur d'électrons volants uniques. Pour les approches de transfert à un seul électron susmentionnées,

cet élément constitutif manquait jusqu'à présent.[32] L'absence de cet élément constitutif a rendu d'autres approches plus lentes préférables pour la première démonstration d'approches de calcul quantique avec des électrons volants simples.

Pour piéger et détecter un seul électron dans un dispositif à l'état solide, dans le passé, on utilisait principalement des QD définis par la grille de surface [Fie93]. La transmission réussie d'un qubit d'électrons a été récemment démontrée dans des dispositifs à l'état solide via des réseaux de tels QDs [Fle17; Fuj17; Mor18]. Dans ces recherches, l'accent a été mis sur l'état de rotation des électrons qui se propagent.[33]. Il y a aussi des propositions récentes pour mélanger les électrons à travers un réseau linéaire à contrôle dynamique de points quantiques [Mil19]. À l'intérieur de ce cadre expérimental, les électrons sont transférés d'un point quantique à un autre et détectés par l'intermédiaire de QPCs voisins. Les ondes acoustiques de surface (SAW) constituent une alternative attrayante au brassage contrôlé par la grille de surface des électrons individuels.

Grâce à la modulation du potentiel électrique peu profond sur un substrat piézoélectrique tel que le GaAs, les SAWs permettent le déplacement des porteurs de charge. La modulation piézoélectrique de l'onde sonore forme un train de QDs mobiles en envoyant un seul electron à travers un canal de transport défini par une grille de surface. Ce train SAW permet maintenant de transporter un nombre quantifié d'électrons à travers un tel rail quantique. Utilisant des QD stationnaires comme source et récepteur d'électrons, un train SAW peut envoyer un porteur de charge unique sur plusieurs pistes de plusieurs microns de long avec une efficacité prometteuse [Her11; McN11]. Récemment, on a signalé un transfert d'électrons polarisés par spin individuel commandé par SAW [Ber16a]. Puisque l'électron est fortement confiné dans un tel point quantique en mouvement, ce mécanisme de transport représente un candidat prometteur pour la transmission et la manipulation des qubits d'un seul électron volant.[34]

Les SAWs pourraient être utilisés par exemple pour propager des électrons volants simples à travers un circuit de rails quantiques définis par des grilles de surface. Si la longueur de cohérence d'un électron volant dans un tel circuit à un seul électron piloté par SAW est suffisamment longue, une telle architecture pourrait permettre

[32] Juste récemment, la détection à un seul tir a également été signalée pour les pompes à un seul électron [Fre19]. Ici, une fidélité globale de 99,6 % a été atteinte avec un taux de répétition global de 24 Hz.

[33] Notons à ce stade un aspect intéressant concernant les qubits de rotation volants : Le déplacement d'un électron permet d'améliorer son temps de cohérence de spin [Fle17]. Il y avait aussi des propositions intéressantes pour la suppression de la relaxation des spins par phononon[ZHH16].

[34] Récemment, il y a eu aussi des propositions théoriques d'utiliser des SAWs à contrepropagation pour la formation des ondes stationnaires [Sch17]. Ces ondes sonores stationnaires sont considérées comme des treillis acoustiques permettant le piégeage d'électrons individuels.

la mise en œuvre d'expériences d'optique quantique électronique [Boc13; Dub13; Ubb14; Bäu18] et de calculs de nombres au niveau des particules uniques [BSR00; AS17]. Pour atteindre ces objectifs, il est nécessaire de mettre au point des sources et des détecteurs à un seul électron très efficaces, des déclencheurs pour synchroniser le transport le long de rails quantiques parallèles et une structure de séparateur de faisceau accordable qui ne perturbe pas un transport cohérent. En outre, il est nécessaire de montrer des phénomènes d'interférence cohérents avec des qubits de charge transportés par SAW et de tester la longueur de cohérence avec des structures interférométriques à deux voies de taille croissante successive.

Ces tâches sont au centre de la deuxième partie de cette thèse. Nous avons étudié la faisabilité des blocs de construction des portes quantiques avec des qubits d'électrons volants utilisant des SAWs comme moyen de transport. Au cours de nos recherches, nous avons franchi d'importants jalons pour nous diriger vers le contrôle cohérent des qubits d'électrons volants qui surfent sur une onde sonore. Tout d'abord, nous avons fait la démonstration d'un système de transport d'électrons uniques à commande SAW très efficace le long d'un circuit de rails quantiques couplés en tunnel d'une longueur de 22-μm. Deuxièmement, nous avons démontré avec succès la capacité du dispositif actuel de partitionner un seul électron d'un rail quantique à l'autre, tout en maintenant un transfert très efficace. En effectuant des simulations de mécanique quantique de nos données expérimentales, nous avons en outre montré que la largeur de la transition du coupleur directionnel reflète directement l'énergie d'excitation de l'état de l'électron volant. En effectuant des simulations temporelles de la propagation d'électrons commandée par des scies à ruban, nous avons identifié des transitions abruptes dans le paysage potentiel comme étant la principale source d'excitation de charge. L'ampleur de l'excitation indique que ce processus provoque les transitions observées expérimentalement de la fonction de l'onde électronique dans les minima ultérieurs de la scie circulaire. Nous avons en outre montré que la largeur d'une transition de coupleur directionnel reflète l'étendue de l'excitation de la charge. Cette quantité peut donc servir de critère utile pour évaluer l'occupation des états propres par l'électron volant dans les expériences futures. À l'aide d'un déclencheur tension-impulsion, nous avons également fait la démonstration d'un outil puissant pour synchroniser le processus d'envoi d'électrons simples piloté par SAW à partir des QDs source. Avec cette réalisation, nous répondons à une exigence centrale: coupler une paire d'électrons simples dans une installation à séparateur de faisceau. En utilisant cette technique de pulsation également au niveau du récepteur, nous avons effectué des mesures du temps de vol, qui ont montré que l'excitation susmentionnée de l'électron volant provoque des transitions de la fonction des ondes dans les minima SAW ultérieurs. Cette découverte expérimentale est en accord avec les résultats de la simulation qui montrent que l'énergie attendue due à l'excitation de charge est de l'ordre de l'amplitude SAW. Corroboré par les simulations susmentionnées de transport d'électrons uniques

pilotés par SAW, nos mesures du temps de vol ont montré qu'un électron transporté par SAW est en effet ramené dans les minima SAW ultérieurs lorsque l'onde sonore se propage dans la région à couplage tunnel de l'installation actuelle de diviseur de faisceau. En augmentant le confinement de l'électron volant dans le SAW, nous prévoyons que le couplage d'électrons simples dans une installation de séparateur de faisceau pilotée par SAW est facilement réalisable avec la technique de déclenchement d'envoi démontrée. Pour des configurations asymétriques très spécifiques du potentiel à double puits dans la région couplée en tunnel, nous avons également observé des caractéristiques de type oscillation dans les probabilités de transfert qui pourraient indiquer la présence de processus cohérents de construction de tunnels.

Bibliography

AB59 Aharonov, Y. & Bohm, D. Significance of Electromagnetic Potentials in the Quantum Theory. *Physical Review* **115,** 485–491. https://link.aps.org/doi/10.1103/PhysRev.115.485 (1959).

Aha14 Aharony, A, Takada, S, Entin-Wohlman, O, Yamamoto, M & Tarucha, S. Aharonov-Bohm interferometry with a tunnel-coupled wire. *New Journal of Physics* **16,** 83015. http://dx.doi.org/10.1088/1367-2630/16/8/083015 (2014).

Aik04a Aikawa, H., Kobayashi, K., Sano, A., Katsumoto, S. & Iye, Y. Interference effect in multilevel transport through a quantum dot. *Journal of the Physical Society of Japan* **73,** 3235–3238. https://doi.org/10.1143/JPSJ.73.3235 (2004).

Aik04b Aikawa, H., Kobayashi, K., Sano, A., Katsumoto, S. & Iye, Y. Observation of "Partial Coherence" in an Aharonov-Bohm Interferometer with a Quantum Dot. *Physical Review Letters* **92.** https://doi.org/10.1103/physrevlett.92.176802 (2004).

Ake93 Akera, H. Aharonov-Bohm effect and electron correlation in quantum dots. *Physical Review B* **47,** 6835–6838. https://doi.org/10.1103/physrevb.47.6835 (1993).

Ake99 Akera, H. Correlations and spin flips in tunneling through a quantum dot. *Physical Review B* **59,** 9802–9805. https://doi.org/10.1103/physrevb.59.9802 (1999).

AuS98 Alhassid, Y. & Stone, A. D. Conductance peak distributions in quantum dots at finite temperature: Signatures of the charging energy. *Physical Review B* **58,** R7524–R7527. https://link.aps.org/doi/10.1103/PhysRevB.58.R7524 (1998).

And18 Andersson, G., Suri, B., Guo, L., Aref, T. & Delsing, P. Nonexponential decay of a giant artificial atom. *arXiv:1812.01302* **58,** R7524–R7527. https://arxiv.org/abs/1812.01302 (2018).

Are16 Ares, N., Schupp, F. J., Mavalankar, A., Rogers, G., Griffiths, J., *et al.* Sensitive Radio-Frequency Measurements of a Quantum Dot by Tuning to Perfect Impedance Matching. *Physical Review Applied* **5,** 034011. https://link.aps.org/doi/10.1103/PhysRevApplied.5.034011 (3 2016).

AS17 Arvidsson-Shukur, D. R. M., Lepage, H. V., Owen, E. T., Ferrus, T. & Barnes, C. H. W. Protocol for fermionic positive-operator-valued measures. *Physical Review A* **96,** 052305. https://doi.org/10.1103/PhysRevA.96.052305 (2017).

AM76 Ashcroft, N. W. & Mermin, N. D. *Solid State Physics* R7524–R7527. ISBN: 978-0-03-083993-1. https://www.cengagebrain.co.uk/shop/isbn/9780030839931 (Wiley, 1976).

Ash92 Ashoori, R. C., Stormer, H. L., Weiner, J. S., Pfeiffer, L. N., Pearton, S. J., *et al.* Single-electron capacitance spectroscopy of discrete quantum levels. *Physical Review Letters* **68,** 3088–3091. https://doi.org/10.1103/PhysRevLett.68.3088 (1992).

AC78 Askar, A. & Cakmak, A. S. Explicit integration method for the time-dependent Schrödinger equation for collision problems. *The Journal of Chemical Physics* **68,** 2794–2798. https://aip.scitation.org/doi/abs/10.1063/1.436072 (1978).

AK05 Avinun-Kalish, M, Heiblum, M, Zarchin, O, Mahalu, D & Umansky, V. Crossover from 'mesoscopic' to 'universal' phase for electron transmission in quantum dots. *Nature* **436,** 529–533. http://dx.doi.org/10.1038/nature03899 (2005).

BG99 Baltin, R. & Gefen, Y. An approximate sign sum rule for the transmission amplitude through a quantum dot. *Physical Review Letters* **83,** 5094–5097. https://doi.org/10.1103/PhysRevLett.83.5094 (1999).

Bar56 Bardeen, J. *Semiconductor Research Leading to the Point Contact Transistor* Nobel Lecture. 1956. https://www.nobelprize.org/prizes/physics/1956/bardeen/lecture/.

BSR00 Barnes, C. H. W., Shilton, J. M. & Robinson, A. M. Quantum computation using electrons trapped by surface acoustic waves. *Physical Review B* **62,** 8410–8419. https://link.aps.org/doi/10.1103/PhysRevB.62.8410 (2000).

Bas79 Bass, S. J. Silicon and germanium doping of epitaxial gallium arsenide grown by the trimethylgallium-arsine method. *Journal of Crystal Growth* **47,** 613 –618. ISSN: 0022-0248. http://www.sciencedirect.com/science/article/pii/0022024879900022 (1979).

Bau13 Bauer, F., Heyder, J., Schubert, E., Borowsky, D., Taubert, D., *et al.* Microscopic origin of the '0.7-anomaly' in quantum point contacts. *Nature* **501,** 73. http://dx.doi.org/10.1038/nature12421 (2013).

Bäu18 Bäuerle, C., Glattli, D. C., Meunier, T., Portier, F., Roche, P., *et al.* Coherent control of single electrons: a review of current progress. *Reports on Progress in Physics* **81,** 056503. http://stacks.iop.org/0034-4885/81/i=5/a=056503 (2018).

Bau14a Bautze, T. *Towards quantum optics experiments with single flying electrons in a solid state system* Dissertation (Université de Grenoble, 2014), 170 pages. https://tel.archives-ouvertes.fr/tel-01367013.

Bau14b Bautze, T., Süssmeier, C., Takada, S., Groth, C., Meunier, T., *et al.* Theoretical, numerical, and experimental study of a flying qubit electronic interferometer. *Physical Review B* **89,** 125432. http://dx.doi.org/10.1103/PhysRevB.89.125432 (2014).

Ber77 Berry, M. V. Regular and irregular semiclassical wavefunctions. *Journal of Physics A* **10,** 2083. http://stacks.iop.org/0305-4470/10/i=12/a=016 (1977).

Ber00 Bertoni, A., Bordone, P., Brunetti, R., Jacoboni, C. & Reggiani, S. Quantum Logic Gates based on Coherent Electron Transport in Quantum Wires. *Physical Review Letters* **84,** 5912–5915. http://dx.doi.org/10.1103/PhysRevLett.84.5912 (2000).

BG07 Bertoni, A. & Goldoni, G. Phase lapses in scattering through multi-electron quantum dots: Mean-field and few-particle regimes. *Physical Review B* **75,** 235318. http://dx.doi.org/10.1103/PhysRevB.75.235318 (2007).

Ber16a Bertrand, B., Hermelin, S., Takada, S., Yamamoto, M., Tarucha, S., *et al.* Fast spin information transfer between distant quantum dots using individual electrons. *Nature Nanotechnology* **11,** 672. http://dx.doi.org/10.1038/nnano.2016.82 (2016).

Ber16b Bertrand, B., Hermelin, S., Mortemousque, P.-A., Takada, S., Yamamoto, M., *et al.* Injection of a single electron from static to moving quantum dots. *Nanotechnology* **27,** 214001. http://stacks.iop.org/0957-4484/27/i=21/a=214001 (2016).

Bir07 Birner, S., Zibold, T., Andlauer, T., Kubis, T., Sabathil, M., *et al.* nextnano: General Purpose 3-D Simulations. *IEEE Transactions on Electron Devices* **54,** 2137–2142. https://ieeexplore.ieee.org/document/4294186 (2007).

BW08 Blatt, R. & Wineland, D. Entangled states of trapped atomic ions. *Nature* **453,** 1008. https://doi.org/10.1038/nature07125 (2008).

Blu07 Blumenthal, M. D., Kaestner, B., Li, L., Giblin, S., Janssen, T. J. B. M., *et al.* Gigahertz quantized charge pumping. *Nature Physics* **3,** 343. https://doi.org/10.1038/nphys582 (2007).

Boc12 Bocquillon, E., Parmentier, F. D., Grenier, C., Berroir, J.-M., Degiovanni, P., *et al.* Electron Quantum Optics: Partitioning Electrons One by One. *Physical Review Letters* **108,** 196803. https://doi.org/10.1103/PhysRevLett.108.196803 (2012).

Boc13 Bocquillon, E., Freulon, V., Berroir, J.-M, Degiovanni, P., Plaçais, B., *et al.* Coherence and Indistinguishability of Single Electrons Emitted by Independent Sources. *Science* **339,** 1054–1057. http://science.sciencemag.org/content/339/6123/1054 (2013).

Bra56 Brattain, W. H. *Surface Properties of Semiconductors* Nobel Lecture. 1956. https://www.nobelprize.org/prizes/physics/1956/brattain/lecture/.

HBT54 Brown, R. H. & Twiss, R. A new type of interferometer for use in radio astronomy. *The London, Edinburgh, and Dublin Philosophical Magazine and Journal of Science* **45,** 663–682. https://doi.org/10.1080/14786440708520475 (1954).

Cam89 Campbell, C. *Surface Acoustic Wave Devices and their Signal Processing Applications* R7524–R7527. ISBN: 978-0-12-157345-4. https://doi.org/10.1016/B978-0-12-157345-4.X5001-2 (Elsevier, 1989).

Car12 Carmi, A., Oreg, Y., Berkooz, M. & Goldhaber-Gordon, D. Transmission phase shifts of Kondo impurities. *Physical Review B* **86,** 115129. https://link.aps.org/doi/10.1103/PhysRevB.86.115129 (11 2012).

COK98 Cronenwett, S. M., Oosterkamp, T. H. & Kouwenhoven, L. P. A Tunable Kondo Effect in Quantum Dots. *Science* **281,** 540–544. http://science.sciencemag.org/content/281/5376/540 (1998).

Del08 Deléglise, S., Dotsenko, I., Sayrin, C., Bernu, J., Brune, M., *et al.* Reconstruction of non-classical cavity field states with snapshots of their decoherence. *Nature* **455,** 510. https://doi.org/10.1038/nature07288 (2008).

DiV00 DiVincenzo, D. P. The Physical Implementation of Quantum Computation. *Fortschritte der Physik* **48,** 771–783. https://arxiv.org/abs/quant-ph/0002077 (2000).

Dub13 Dubois, J., Jullien, T., Portier, F., Roche, P., Cavanna, A., *et al.* Minimal-excitation states for electron quantum optics using levitons. *Nature* **502,** 659. https://doi.org/10.1038/nature12713 (2013).

Dum19 Dumur, Satzinger, K. J., Peairs, G. A., Chou, M.-H., Bienfait, A., *et al.* Unidirectional distributed acoustic reflection transducers for quantum applications. *Applied Physics Letters* **114,** 223501. https://doi.org/10.1063/1.5099095 (2019).

Dup19 Duprez, H., Sivre, E., Anthore, A., Aassime, A., Cavanna, A., *et al.* Transferring the quantum state of electrons across a Fermi sea with Coulomb interaction. *arXiv:1902.07569* **58,** R7524–R7527. https://arxiv.org/abs/1902.07569v1 (2019).

Edl17 Edlbauer, H., Takada, S., Roussely, G., Yamamoto, M., Tarucha, S., *et al.* Non-universal transmission phase behaviour of a large quantum dot. *Nature Communications* **8,** 1710. ISSN: 2041-1723. https://doi.org/10.1038/s41467-017-01685-z (2017).

ES49 Ehrenberg, W & Siday, R. E. The Refractive Index in Electron Optics and the Principles of Dynamics. *Proceedings of the Physical Society. Section B* **62,** 8. http://stacks.iop.org/0370-1301/62/i=1/a=303 (1949).

Eks17 Ekström, M. K., Aref, T., Runeson, J., Björck, J., Boström, I., *et al.* Surface acoustic wave unidirectional transducers for quantum applications. *Applied Physics Letters* **110,** 073105. https://doi.org/10.1063/1.4975803 (2017).

Ema19 Emary, C., Clark, L. A., Kataoka, M. & Johnson, N. Energy relaxation in hot electron quantum optics via acoustic and optical phonon emission. *Phys. Rev. B* **99,** 045306. https://link.aps.org/doi/10.1103/PhysRevB.99.045306 (2019).

EPC12 EPCOS AG. *SAW Components B3533* Chapter "Minimising the crosstalk" on page 6. https://product.tdk.com/search-template/en/documents/data_sheet/40/ds/ae/B3533.pdf.

Fan18 Fandan, R, Pedros, J, Schiefele, J, Bosca, A, Martinez, J, *et al.* Acoustically-driven surface and hyperbolic plasmon-phonon polaritons in graphene/h-BN heterostructures on piezoelectric substrates. *Journal of Physics D: Applied Physics* **51,** 204004. http://stacks.iop.org/0022-3727/51/i=20/a=204004 (2018).

Fèv07 Fève, G., Mahé, A., Berroir, J.-M., Kontos, T., Plaçais, B., *et al.* An On-Demand Coherent Single-Electron Source. *Science* **316,** 1169–1172. http://science.sciencemag.org/content/316/5828/1169 (2007).

Fie93 Field, M., Smith, C. G., Pepper, M., Ritchie, D. A., Frost, J. E. F., *et al.* Measurements of Coulomb blockade with a noninvasive voltage probe. *Physical Review Letters* **70,** 1311–1314. https://doi.org/10.1103/PhysRevLett.70.1311 (1993).

FSS11 Filipiak, J, Solarz, L. & Steczko, G. Surface Acoustic Wave Vibration Sensor Electronic System. *Acta Physica Polonica Series a* **120,** 598–603. https://doi.org/10.12693/APhysPolA.120.598 (2011).

Fle17 Flentje, H., Mortemousque, P.-A., Thalineau, R., Ludwig, A., Wieck, A. D., *et al.* Coherent long-distance displacement of individual electron spins. *Nature Communications* **8,** 501. https://doi.org/10.1038/s41467-017-00534-3 (2017).

Fle12 Fletcher, J. D., Kataoka, M., Giblin, S. P., Park, S., Sim, H.-S., *et al.* Stabilization of single-electron pumps by high magnetic fields. *Physical Review B* **86,** 155311. https://doi.org/10.1103/PhysRevB.86.155311 (2012).

Fle19 Fletcher, J., Johnson, N., Locane, E., See, P., Griffiths, J. P., *et al.* Quantum Tomography of Solitary Electrons. *arXiv:1901. 10985* **58,** R7524–R7527. https://arxiv.org/abs/1901.10985 (2019).

Fol96 Folk, J. A., Patel, S. R., Godijn, S. F., Huibers, A. G., Cronenwett, S. M., *et al.* Statistics and parametric correlations of coulomb blockade peak fluctuations in quantum dots. *Physical Review Letters* **76,** 1699–1702. http://dx.doi.org/10.1103/PhysRevLett.76.1699 (1996).

For17 Ford, C. J. B. Transporting and manipulating single electrons in surface-acoustic-wave minima. *Physica Status Solidi B* **254,** 1600658. https://onlinelibrary.wiley.com/doi/abs/10.1002/pssb.201600658 (2017).

Fre19 Freise, L., Gerster, T., Reifert, D., Weimann, T., Pierz, K., *et al.* Full counting statistics of trapped ballistic electrons. *arXiv:1902.11253* **58,** R7524–R7527. https://arxiv.org/abs/1902.11253 (2019).

Fre15 Freulon, V, Marguerite, A, Berroir, J.-M., Plaçais, B, Cavanna, A, *et al.* Hong-Ou-Mandel experiment for temporal investigation of single-electron fractionalization. *Nature communications* **6,** 6854. https://doi.org/10.1038/ncomms7854 (2015).

Fri14 Fricke, L., Wulf, M., Kaestner, B., Hohls, F., Mirovsky, P., *et al.* Self-Referenced Single-Electron Quantized Current Source. *Physical Review Letters* **112,** 226803. https://link.aps.org/doi/10.1103/PhysRevLett.112.226803 (2014).

Fri52 Friedel, J. XIV. The distribution of electrons round impurities in monovalent metals. *The London, Edinburgh, and Dublin Philosophical Magazine and Journal of Science* **43,** 153–189. https://doi.org/10.1080/14786440208561086 (1952).

FHH04 Fujisawa, T., Hayashi, T. & Hirayama, Y. Controlled decoherence of a charge qubit in a double quantum dot. *Journal of Vacuum Science & Technology B: Microelectronics and Nanometer Structures Processing, Measurement, and Phenomena* **22,** 2035–2038. https://avs.scitation.org/doi/abs/10.1116/1.1771679 (2004).

Fuj17 Fujita, T., Baart, T. A., Reichl, C., Wegscheider, W. & Vandersypen, L. M. K. Coherent shuttle of electron-spin states. *npj Quantum Information* **3,** 22. https://doi.org/10.1038/s41534-017-0024-4 (2017).

Ger00 Gerland, U., von Delft, J., Costi, T. A. & Oreg, Y. Transmission Phase Shift of a Quantum Dot with Kondo Correlations. *Physical Review Letters* **84,** 3710–3713. https://doi.org/10.1103/physrevlett.84.3710 (2000).

Gib12 Giblin, S. P., Kataoka, M., Fletcher, J. D., See, P., Janssen, T. J. B. M., *et al.* Towards a quantum representation of the ampere using single electron pumps. *Nature Communications* **3,** 930. https://doi.org/10.1038/ncomms1935 (2012).

GG98 Goldhaber-Gordon, D., Shtrikman, H., Mahalu, D., Abusch-Magder, D., Meirav, U., *et al.* Kondo effect in a single-electron transistor. *Nature* **391,** 156. http://dx.doi.org/10.1038/34373 (1998).

Gol09 Goldstein, M., Berkovits, R., Gefen, Y. & Weidenmüller, H. A. Transmission phase of quantum dots: Testing the role of population switching. *Physical Review B* **79,** 125307. https://doi.org/10.1103/PhysRevB.79.125307 (2009).

GG06 Golosov, D. I. & Gefen, Y. Transmission through quantum dots: Focus on phase lapses. *Physical Review B* **74,** 205316. https://doi.org/10.1103/PhysRevB.74.205316 (2006).

Hac01 Hackenbroich, G. Phase coherent transmission through interacting mesoscopic systems. *Physics Reports* **343,** 463–538. http://dx.doi.org/10.1016/S0370-1573(00)00084-3 (2001).

HHW97 Hackenbroich, G., Heiss, W. D. & Weidenmüller, H. A. Deformation of Quantum Dots in the Coulomb Blockade Regime. *Physical Review Letters* **79,** 127–130. https://link.aps.org/doi/10.1103/PhysRevLett.79.127 (1997).

HM18 Hackenbroich, G. & Mendez, R. A. Bouncing-ball tunneling in quantum dots. *arXiv:cond-mat/0002430* **58,** R7524–R7527. https://arxiv.org/abs/cond-mat/0002430 (2018).

Had09 Hadfield, R. H. Single-photon detectors for optical quantum information applications. *Nature Photonics* **3.** Review Article, 696. https://doi.org/10.1038/nphoton.2009.230 (2009).

Hah50 Hahn, E. L. Spin Echoes. *Physical Review* **80,** 580–594. https://link.aps.org/doi/10.1103/PhysRev.80.580 (4 1950).

Han07 Hanson, R, Kouwenhoven, L. P., Petta, J. R., Tarucha, S. & Vandersypen, L. M. K. Spins in few-electron quantum dots. *Reviews of Modern Physics* **79,** 1217–1265. http://dx.doi.org/10.1103/RevModPhys.79.1217 (2007).

Hay03 Hayashi, T., Fujisawa, T., Cheong, H. D., Jeong, Y. H. & Hirayama, Y. Coherent Manipulation of Electronic States in a Double Quantum Dot. *Physical Review Letters* **91,** 226804. https://link.aps.org/doi/10.1103/PhysRevLett.91.226804 (22 2003).

Hel15 Hellmüller, S, Bischoff, D, Müller, T, Beck, M, Ensslin, K, *et al.* Spin pairs in a weakly coupled many-electron quantum dot. *Physical Review B* **92,** R7524–R7527. http://dx.doi.org/10.1103/PhysRevB.92.115401 (2015).

Hen99 Henny, M., Oberholzer, S., Strunk, C., Heinzel, T., Ensslin, K., *et al.* The Fermionic Hanbury Brown and Twiss Experiment. *Science* **284,** 296–298. https://science.sciencemag.org/content/284/5412/296 (1999).

Her11 Hermelin, S., Takada, S., Yamamoto, M., Tarucha, S., Wieck, A. D., *et al.* Electrons surfing on a sound wave as a platform for quantum optics with flying electrons. *Nature* **477,** 435. http://dx.doi.org/10.1038/nature10416 (2011).

HOM87 Hong, C. K., Ou, Z. Y. & Mandel, L. Measurement of subpicosecond time intervals between two photons by interference. *Physical Review Letters* **59,** 2044–2046. https://link.aps.org/doi/10.1103/PhysRevLett.59.2044 (1987).

Hou18 Hou, H., Chung, Y, Rughoobur, G, Hsiao, T. K., Nasir, A, *et al.* Experimental verification of electrostatic boundary conditions in gate-patterned quantum devices. *Journal of Physics D: Applied Physics* **51,** 244004. http://stacks.iop.org/0022-3727/51/i=24/a=244004 (2018).

Hsi18 Hsiao, T.-K. *A Single-photon Source Based on a Lateral n-i-p Junction Driven by a Surface Acoustic Wave* Dissertation (University of Cambridge, 2018), 181 pages. https://www.repository.cam.ac.uk/bitstream/handle/1810/283189/TKH28_PhD_thesis_for_hardbound.pdf.

Hsi19 Hsiao, T.-K., Rubino, A., Chung, Y., Son Seok-Kyun, H. H., Pedrós, J., *et al.* Single-photon Emission from an Acoustically-driven Lateral Light-emitting Diode. *arXiv:1901.03464* **58,** R7524–R7527. https://arxiv.org/abs/1901.03464 (2019).

HLW91 Hsu, W. C., Lin, W. & Wang, C. A quantum well δ-doped GaAs FET fabricated by low-pressure metal organic chemical vapor deposition. *Solid-State Electronics* **34,** 649–653. ISSN: 0038-1101. https://doi.org/10.1016/0038-1101(91)90139-P (1991).

Ihn07 Ihn, T., Sigrist, M., Ensslin, K., Wegscheider, W. & Reinwald, M. Interference in a quantum dot molecule embedded in a ring interferometer. *New Journal of Physics* **9,** 111. http://dx.doi.org/10.1088/1367-2630/9/5/111 (2007).

IAU01 Ionicioiu, R., Amaratunga, G. & Udrea, F. Quantum Computation with ballistic electrons. *International Journal of Modern Physics B* **15,** 125–133. https://doi.org/10.1142/S0217979201003521 (2001).

Iqb13 Iqbal, M. J., Levy, R., Koop, E. J., Dekker, J. B., de Jong, J. P., *et al.* Odd and even Kondo effects from emergent localization in quantum point contacts. *Nature* **501,** 79. http://dx.doi.org/10.1038/nature12491 (2013).

JSA92 Jalabert, R. A., Stone, A. D. & Alhassid, Y. Statistical theory of Coulomb blockade oscillations: Quantum chaos in quantum dots. *Physical Review Letters* **68,** 3468–3471. https://doi.org/10.1103/PhysRevLett.68.3468 (23 1992).

Jal14 Jalabert, R. A., Weick, G., Weidenmüller, H. A. & Weinmann, D. Transmission phase of a quantum dot and statistical fluctuations of partial-width amplitudes. *Physical Review E* **89,** R7524–R7527. http://dx.doi.org/10.1103/PhysRevE.89.052911 (2014).

Jal17 Jalabert, R. A., Molina, R. A., Weick, G. & Weinmann, D. Correlation between peak-height modulation and phase lapses in transport through quantum dots. *Phys. Rev. E* **96,** 062208. https://link.aps.org/doi/10.1103/PhysRevE.96.062208 (6 2017).

JH00 Janssen, T. & Hartland, A. Accuracy of quantized single-electron current in a one-dimensional channel. *Physica B: Condensed Matter* **284-288,** 1790 –1791. ISSN: 0921-4526. http://www.sciencedirect.com/science/article/pii/S0921452699029786 (2000).

Ji00 Ji, Y., Heiblum, M., Sprinzak, D., Mahalu, D. & Shtrikman, H. Phase Evolution in a Kondo-Correlated System. *Science* **290,** 779–783. ISSN: 0036-8075. https://science.sciencemag.org/content/290/5492/779 (2000).

JHS02 Ji, Y., Heiblum, M. & Shtrikman, H. Transmission Phase of a Quantum Dot with Kondo Correlation near the Unitary Limit. *Physical Review Letters* **88,** 076601. https://link.aps.org/doi/10.1103/PhysRevLett.88.076601 (7 2002).

Ji03 Ji, Y., Chung, Y., Sprinzak, D, Heiblum, M, Mahalu, D, *et al.* An electronic Mach-Zehnder interferometer. *Nature* **422,** 415–418. http://dx.doi.org/10.1038/nature01503 (2003).

Joy88 Joyce, B. Molecular beam epitaxy: Recent trends and future developments. *Journal of Physics and Chemistry of Solids* **49,** 237 –242. https://doi.org/10.1016/0022-3697(88)90073-X (1988).

Jul14 Jullien, T., Roulleau, P., Roche, B., Cavanna, A., Jin, Y., *et al.* Quantum tomography of an electron. *Nature* **514,** 603. https://doi.org/10.1038/nature13821 (2014).

Kan99 Kang, K. Coherent transport through a quantum dot embedded in an Aharonov-Bohm ring. *Physical Review B* **59,** 4608–4611. https://link.aps.org/doi/10.1103/PhysRevB.59.4608 (1999).

Kar07 Karrasch, C., Hecht, T., Weichselbaum, A., Oreg, Y., von Delft, J., *et al.* Mesoscopic to universal crossover of the transmission phase of multilevel quantum dots. *Physical Review Letters* **98,** 186802. https://doi.org/10.1103/PhysRevLett.98.186802 (2007).

Kat09 Kataoka, M., Astley, M. R., Thorn, A. L., Oi, D. K. L., Barnes, C. H. W., *et al.* Coherent Time Evolution of a Single-Electron Wave Function. *Physical Review Letters* **102,** 156801. https://doi.org/10.1103/PhysRevLett.102.156801 (2009).

Kel15 Keller, A. J., Peeters, L., Moca, C. P., Weymann, I., Mahalu, D., *et al.* Universal Fermi liquid crossover and quantum criticality in a mesoscopic system. *Nature* **526,** 237. https://doi.org/10.1038/nature15261 (2015).

KBS14 Khatua, P., Bansal, B. & Shahar, D. Single-Slit Electron Diffraction with Aharonov-Bohm Phase: Feynman's Thought Experiment with Quantum Point Contacts. *Physical Review Letters* **112,** 010403. https://link.aps.org/doi/10.1103/PhysRevLett.112.010403 (2014).

Kit04 Kittel, C. *Introduction to Solid State Physics* R7524–R7527. ISBN: 978-0-471-41526-8. https://www.wiley.com/en-us/Introduction+to+Solid+State+Physics\%2C+8th+Edition-p-9780471415268 (Wiley, 2004).

Kob02 Kobayashi, K., Aikawa, H., Katsumoto, S. & Iye, Y. Tuning of the Fano effect through a quantum dot in an Aharonov-Bohm interferometer. *Physical Review Letters* **88,** R7524–R7527. https://doi.org/10.1103/physrevlett.88.256806 (2002).

Kob04 Kobayashi, K., Aikawa, H., Sano, A., Katsumoto, S. & Iye, Y. Fano resonance in a quantum wire with a side-coupled quantum dot. *Physical Review B* **70,** R7524–R7527. https://doi.org/10.1103/physrevb.70.035319 (2004).

Kon64 Kondo, J. Resistance Minimum in Dilute Magnetic Alloys. *Progress of Theoretical Physics* **32,** 37–49. http://dx.doi.org/10.1143/PTP.32.37 (1964).

KG01 König, J. & Gefen, Y. Coherence and Partial Coherence in Interacting Electron Systems. *Physical Review Letters* **86,** 3855–3858. 10.1103/physrevlett.86.3855 (2001).

KG02 König, J. & Gefen, Y. Aharonov-Bohm interferometry with interacting quantum dots: Spin configurations, asymmetric interference patterns, bias-voltage-induced Aharonov-Bohm oscillations, and symmetries of transport coefficients. *Physical Review B* **65,** R7524–R7527. 10.1103/physrevb.65.045316 (2002).

Kou97 Kouwenhoven, L. P. *Electron Transport in Quantum Dots* https://doi.org/10.1007/978-94-015-8839-3_4 (Springer, 1997).

Kou91 Kouwenhoven, L. P., van der Vaart, N. C., Johnson, A. T., Harmans, C. J. P. M., Williamson, J. G., *et al.* Charging effects in quantum dots. *Festkörperprobleme* **31,** https://doi.org/10.1007/BFb0107875 (1991).

Lac10 Lacoste, R. in *Robert Lacoste's The Darker Side* 3–16 (Newnes, Boston, 2010). ISBN: 978-1-85617-762-7. https://doi.org/10.1016/B978-1-85617-762-7.00001-0.

LA61 Langer, J. S. & Ambegaokar, V. Friedel Sum Rule for a System of Interacting Electrons. *Physical Review* **121,** 1090–1092. https://link.aps.org/doi/10.1103/PhysRev.121.1090 (1961).

Lan08 Lanyon, B. P., Barbieri, M., Almeida, M. P., Jennewein, T., Ralph, T. C., *et al.* Simplifying quantum logic using higher-dimensional Hilbert spaces. *Nature Physics* **5,** 134. https://doi.org/10.1038/nphys1150 (2008).

Lee99 Lee, H.-W. Generic transmission zeros and in-phase resonances in time-reversal symmetric single channel transport. *Physical Review Letters* **82,** 2358–2361. http://dx.doi.org/10.1103/PhysRevLett.82.2358 (1999).

Lev96 Levitov, L. S., Lee, H. & Lesovik, G. B. Electron counting statistics and coherent states of electric current. *Journal of Mathematical Physics* **37,** 4845–4866. https://doi.org/10.1063/1.531672 (1996).

LB95 Levy Yeyati, A. & Büttiker, M. Aharonov-Bohm oscillations in a mesoscopic ring with a quantum dot. *Physical Review B* **52,** R14360–R14363. http://dx.doi.org/10.1103/PhysRevB.52.R14360 (1995).

LB00 Levy Yeyati, A. & Büttiker, M. Scattering phases in quantum dots: An analysis based on lattice models. *Physical Review B* **62,** 7307–7315. ISSN: 01631829. https://doi.org/10.1103/PhysRevB.62.7307 (2000).

Li14 Li, H.-O., Cao, G., Xiao, M., You, J., Wei, D., *et al.* Fabrication and characterization of an undoped GaAs/AlGaAs quantum dot device. *Journal of Applied Physics* **116,** 174504. https://doi.org/10.1063/1.4900915 (2014).

Lin02 Lindemann, S, Ihn, T, Heinzel, T, Zwerger, W, Ensslin, K, *et al.* Stability of spin states in quantum dots. *Physical Review B* **66,** R7524–R7527. http://dx.doi.org/10.1103/PhysRevB.66.195314 (2002).

Lio17 Liou, Y.-T., Hernández-Mínguez, A, Herfort, J, Lopes, J. M. J., Tahraoui, A., *et al.* Acousto-electric transport in MgO/ZnO-covered graphene on SiC. *Journal of Physics D: Applied Physics* **50,** 464008. http://stacks.iop.org/0022-3727/50/i=46/a=464008 (2017).

Lit07 Litvin, L. V., Tranitz, H.-P., Wegscheider, W. & Strunk, C. Decoherence and single electron charging in an electronic Mach-Zehnder interferometer. *Physical Review B* **75,** R7524–R7527. https://doi.org/10.1103/physrevb.75.033315 (2007).

Liu98 Liu, R. C., Odom, B., Yamamoto, Y. & Tarucha, S. Quantum interference in electron collision. *Nature* **391,** 263. https://doi.org/10.1038/34611 (1998).

MLP00 Maestri, J. J., Landau, R. H. & Páez, M. J. Two-particle Schrödinger equation animations of wave packet–wave packet scattering. *American Journal of Physics* **68,** 1113–1119. https://doi.org/10.1119/1.1286310 (2000).

Mal19 Malinowski, F. K., Martins, F., Smith, T. B., Bartlett, S. D., Doherty, A. C., *et al.* Fast spin exchange across a multielectron mediator. *Nature Communications* **10,** 1196. https://doi.org/10.1038/s41467-019-09194-x (2019).

Man17 Manenti, R., Kockum, A. F., Patterson, A., Behrle, T., Rahamim, J., *et al.* Circuit quantum acoustodynamics with surface acoustic waves. *Nature Communications* **8,** 975. ISSN: 2041-1723. https://doi.org/10.1038/s41467-017-01063-9 (2017).

MDD92 Marrian, C. R. K., Dobisz, E. A. & Dagata, J. A. Electron-beam lithography with the scanning tunneling microscope. *Journal of Vacuum Science & Technology B: Microelectronics and Nanometer Structures Processing, Measurement, and Phenomena* **10,** 2877–2881. https://avs.scitation.org/doi/abs/10.1116/1.585978 (1992).

McN11 McNeil, R. P. G., Kataoka, M., Ford, C. J. B., Barnes, C. H. W., Anderson, D., *et al.* On-demand single-electron transfer between distant quantum dots. *Nature* **477,** 439. http://dx.doi.org/10.1038/nature10444 (2011).

Mil19 Mills, A. R., Zajac, D. M., Gullans, M. J., Schupp, F. J., Hazard, T. M., *et al.* Shuttling a single charge across a one-dimensional array of silicon quantum dots. *Nature Communications* **10,** 1063. ISSN: 2041-1723. https://doi.org/10.1038/s41467-019-08970-z (2019).

Mol12 Molina, R. A., Jalabert, R. A., Weinmann, D. & Jacquod, P. Scattering Phase of Quantum Dots: Emergence of Universal Behavior. *Physical Review Letters* **108,** 076803. https://link.aps.org/doi/10.1103/PhysRevLett.108.076803 (2012).

Mor10 Morgan, D. *Surface acoustic wave filters: With applications to electronic communications and signal processing* R7524–R7527. ISBN: 9780123725370. https://www.elsevier.com/books/surface-acoustic-wave-filters/morgan/978-0-12-372537-0 (Academic Press, 2010).

Mor18 Mortemousque, P.-A., Chanrion, E., Jadot, B., Flentje, H., Ludwig, A., *et al.* Coherent control of individual electron spins in a two dimensional array of quantum dots. *arXiv:1808.06180* **58,** R7524–R7527. https://ui.adsabs.harvard.edu/\#abs/2018arXiv180806180M (2018).

Nar01 Narimanov, E. E., Baranger, H. U., Cerruti, N. R. & Tomsovic, S. Semiclassical theory of Coulomb blockade peak heights in chaotic quantum dots. *Physical Review B* **64,** 235329. https://link.aps.org/doi/10.1103/PhysRevB.64.235329 (2001).

Ned07 Neder, I., Ofek, N., Chung, Y., Heiblum, M., Mahalu, D., *et al.* Interference between two indistinguishable electrons from independent sources. *Nature* **448,** 333. https://doi.org/10.1038/nature05955 (2007).

Nys17 Nysten, E. D. S., Huo, Y. H., Yu, H., Song, G. F., Rastelli, A., *et al.* Multi-harmonic quantum dot optomechanics in fused $LiNbO_3$-(Al)GaAs hybrids. *Journal of Physics D: Applied Physics* **50,** 43LT01. http://stacks.iop.org/0022-3727/50/i=43/a=43LT01 (2017).

O'B03 O'Brien, J. L., Pryde, G. J., White, A. G., Ralph, T. C. & Branning, D. Demonstration of an all-optical quantum controlled-NOT gate. *Nature* **426,** 264. https://doi.org/10.1038/nature02054 (2003).

Oli99 Oliver, W. D., Kim, J., Liu, R. C. & Yamamoto, Y. Hanbury Brown and Twiss-Type Experiment with Electrons. *Physical Review B* **284,** 299–301. http://science.sciencemag.org/content/284/5412/299 (1999).

OG97 Oreg, Y. & Gefen, Y. Electron scattering through a quantum dot: A phase lapse mechanism. *Physical Review B* **55,** 13726–13729. https://link.aps.org/doi/10.1103/PhysRevB.55.13726 (1997).

Pat98 Patel, S. R., Stewart, D. R., Marcus, C. M., Alhassid, Y., *et al.* Changing the Electronic Spectrum of a Quantum Dot by Adding Electrons. *Physical Review Letters* **81,** 5900–5903. https://link.aps.org/doi/10.1103/PhysRevLett.81.5900 (1998).

Pek13 Pekola, J. P., Saira, O.-P., Maisi, V. F., Kemppinen, A., Möttönen, M., *et al.* Single-electron current sources: Toward a refined definition of the ampere. *Reviews of Modern Physics* **85,** 1421–1472. https://link.aps.org/doi/10.1103/RevModPhys.85.1421 (4 2013).

Pet10 Petersson, K. D., Petta, J. R., Lu, H. & Gossard, A. C. Quantum Coherence in a One-Electron Semiconductor Charge Qubit. *Physical Review Letters* **105,** 246804. https://link.aps.org/doi/10.1103/PhysRevLett.105.246804 (2010).

Pet04 Petta, J. R., Johnson, A. C., Marcus, C. M., Hanson, M. P. & Gossard, A. C. Manipulation of a Single Charge in a Double Quantum Dot. *Physical Review Letters* **93,** 186802. https://link.aps.org/doi/10.1103/PhysRevLett.93.186802 (2004).

Pot07 Potok, R. M., Rau, I. G., Shtrikman, H., Oreg, Y. & Goldhaber-Gordon, D. Observation of the two-channel Kondo effect. *Nature* **446,** 167. https://doi.org/10.1038/nature05556 (2007).

RuS Rhode & Schwarz SMA100A. Image taken on the 11th May 2019. https://www.testunlimited.com/images/products/RohdeSchwarz_SMA100A.jpg.

Ron10 Rontani, M. Exchange and correlation effects in the transmission phase through a few-electron quantum dot. *Physical Review B* **82,** 045310. https://link.aps.org/doi/10.1103/PhysRevB.82.045310 (2010).

Ron06 Rontani, M., Cavazzoni, C., Bellucci, D. & Goldoni, G. Full configuration interaction approach to the few-electron problem in artificial atoms. *The Journal of Chemical Physics* **124,** 124102. https://doi.org/10.1063/1.2179418 (2006).

Rou08 Roulleau, P., Portier, F., Roche, P., Cavanna, A., Faini, G., *et al.* Direct Measurement of the Coherence Length of Edge States in the Integer Quantum Hall Regime. *Physical Review Letters* **100,** 126802. https://link.aps.org/doi/10.1103/PhysRevLett.100.126802 (12 2008).

Rou18 Roussely, G., Arrighi, E., Georgiou, G., Takada, S., Schalk, M., *et al.* Unveiling the bosonic nature of an ultrashort few-electron pulse. *Nature Communications* **9,** 2811. https://doi.org/10.1038/s41467-018-05203-7 (2018).

SN18 Sakurai, J. J. & Napolitano, J. *Modern Quantum Mechanics* ISBN: 978-1-108-49999-6. https://www.cambridge.org/core/books/modern-quantum-mechanics/AAE1925F1A0963C6124421B03D7801AE (Cambridge University Press, 2018).

San18 Santagati, R., Wang, J., Gentile, A. A., Paesani, S., Wiebe, N., *et al.* Witnessing eigenstates for quantum simulation of Hamiltonian spectra. *Science Advances* **4,** 5900–5903. http://advances.sciencemag.org/content/4/1/eaap9646 (2018).

SAWtr *SAWtrain network*. An innovative training network from the European Union's Horizon 2020 research and innovation programme that is coordinated by Augsburg University. http://www.sawtrain.eu.

Sch06 Schneble, R. J., Kataoka, M., Ford, C. J. B., Barnes, C. H. W., Anderson, D., *et al.* Quantum-dot thermometry of electron heating by surface acoustic waves. *Applied Physics Letters* **89,** 122104. https://doi.org/10.1063/1.2346372 (2006).

Sch17 Schuetz, M. J. A., Knörzer, J., Giedke, G., Vandersypen, L. M. K., Lukin, M. D., *et al.* Acoustic Traps and Lattices for Electrons in Semiconductors. *Physical Review X* **7,** 041019. https://link.aps.org/doi/10.1103/PhysRevX.7.041019 (2017).

Sch15 Schülein, F. J. R., Zallo, E., Atkinson, P., Schmidt, O. G., Trotta, R., *et al.* Fourier synthesis of radiofrequency nanomechanical pulses with different shapes. *Nature Nanotechnology* **10,** 512. https://doi.org/10.1038/nnano.2015.72 (2015).

Sch97 Schuster, R., Buks, E, Heiblum, M, Mahalu, D, Umansky, V, *et al.* Phase measurement in a quantum dot via a double-slit interference experiment. *Nature* **385,** 417–420. http://dx.doi.org/10.1038/385417a0 (1997).

Shi96 Shilton, J. M., Talyanskii, V. I., Pepper, M, Ritchie, D. A., Frost, J. E. F., *et al.* High-frequency single-electron transport in a quasi-one-dimensional GaAs channel induced by surface acoustic waves. *Journal of Physics: Condensed Matter* **8,** L531. http://stacks.iop.org/0953-8984/8/i=38/a=001 (1996).

Sho56 Shockley, W. B. *Transistor Technology Evokes New Physics* Nobel Lecture. 1956. https://www.nobelprize.org/prizes/physics/2000/shockley/lecture/.

Sig04 Sigrist, M., Fuhrer, A, Ihn, T, Ensslin, K, Ulloa, S. E., *et al.* Magnetic-field-dependent transmission phase of a double-dot system in a quantum ring. *Physical Review Letters* **93,** 66802. http://link.aps.org/doi/10.1103/PhysRevLett.93.066802 (2004).

SI00 Silvestrov, P. G. & Imry, Y. Towards an explanation of the mesoscopic double-slit experiment: A new model for charging of a quantum dot. *Physical Review Letters* **85,** 2565–2568. https://doi.org/10.1103/PhysRevLett.85.2565 (2000).

Smi96 Smith, C. G. Low-dimensional quantum devices. *Reports on Progress in Physics* **59,** 235–282. https://doi.org/10.1088\%2F0034-4885\%2F59\%2F2\%2F003 (1996).

Sto17 Stockklauser, A., Scarlino, P., Koski, J. V., Gasparinetti, S., Andersen, C. K., *et al.* Strong Coupling Cavity QED with Gate-Defined Double Quantum Dots Enabled by a High Impedance Resonator. *Physical Review X* **7,** 011030. https://link.aps.org/doi/10.1103/PhysRevX.7.011030 (2017).

Stö79a Störmer, H. L., Dingle, R., Gossard, A. C., Wiegmann, W. & Sturge, M. D. Two-dimensional electron gas at differentially doped GaAs-$Al_xGa_{1-x}As$ heterojunction interface. *Journal of Vacuum Science and Technology* **16,** 1517–1519. https://doi.org/10.1116/1.570238 (1979).

Stö83 Störmer, H. Electron mobilities in modulation-doped GaAs-(AlGa)As heterostructures. *Surface Science* **132,** 519 –526. ISSN: 0039-6028. https://doi.org/10.1016/0039-6028(83)90558-7 (1983).

Stö79b Störmer, H., Dingle, R., Gossard, A., Wiegmann, W. & Sturge, M. Two-dimensional electron gas at a semiconductor-semiconductor interface. *Solid State Communications* **29,** 705 –709. ISSN: 0038-1098. https://doi.org/10.1016/0038-1098(79)91010-X (1979).

Tak14 Takada, S., Bäuerle, C., Yamamoto, M., Watanabe, K., Hermelin, S., *et al.* Transmission phase in the kondo regime revealed in a two-path interferometer. *Physical Review Letters* **113,** 126601. http://link.aps.org/doi/10.1103/PhysRevLett.113.126601 (2014).

Tak15 Takada, S., Yamamoto, M., Bäuerle, C., Watanabe, K., Ludwig, A., *et al.* Measurement of the transmission phase of an electron in a quantum two-path interferometer. *Applied Physics Letters* **107,** 63101. http://dx.doi.org/10.1063/1.4928035 (2015).

Tak16 Takada, S., Yamamoto, M., Bäuerle, C., Alex, A., von Delft, J., *et al.* Low-temperature behavior of transmission phase shift across a Kondo correlated quantum dot. *Physical Review B* **94,** 081303(R). https://link.aps.org/doi/10.1103/PhysRevLett.81.5900 (2016).

Tak17 Takada, S., Yamamoto, M., Bäuerle, C., Ludwig, A., Wieck, A. D., *et al.* Mesoscopic phase behavior in a quantum dot around crossover between single-level and multilevel transport regimes. *Physical Review B* **95,** 241301. https://link.aps.org/doi/10.1103/PhysRevB.95.241301 (2017).

Tak19 Takada, S., Edlbauer, H., Lepage, H. V., Wang, J., Mortemousque, P.-A., *et al.* Sound-driven single-electron transfer in a circuit of coupled quantum rails. *Nature Communications* **10,** 4557. https://doi.org/10.1038/s41467-019-12514-w (2019).

Tal97 Talyanskii, V. I., Shilton, J. M., Pepper, M., Smith, C. G., Ford, C. J. B., *et al.* Single-electron transport in a one-dimensional channel by high-frequency surface acoustic waves. *Physical Review B* **56,** 15180–15184. https://link.aps.org/doi/10.1103/PhysRevB.56.15180 (1997).

TB99 Taniguchi, T. & Büttiker, M. Friedel phases and phases of transmission amplitudes in quantum scattering systems. *Physical Review B* **60,** 13814–13823. https://doi.org/10.1103/physrevb.60.13814 (1999).

AWG Tektronix AWG7122b. Image taken on the 11th May 2019. https://www.used-line.com/handlers/ImageProxy.ashx?itemID=12222497.

Tho96 Thomas, K. J., Nicholls, J. T., Simmons, M. Y., Pepper, M., Mace, D. R., *et al.* Possible Spin Polarization in a One-Dimensional Electron Gas. *Physical Review Letters* **77,** 135–138. https://link.aps.org/doi/10.1103/PhysRevLett.77.135 (1996).

THR14 Tracy, L. A., Hargett, T. W. & Reno, J. L. Few-hole double quantum dot in an undoped GaAs/AlGaAs heterostructure. *Applied Physics Letters* **104,** 123101. https://doi.org/10.1063/1.4868971 (2014).

Ubb14 Ubbelohde, N., Hohls, F., Kashcheyevs, V., Wagner, T., Fricke, L., *et al.* Partitioning of on-demand electron pairs. *Nature Nanotechnology* **10,** 46. https://doi.org/10.1038/nnano.2014.275 (2014).

VLM98 Vallejos, R. O., Lewenkopf, C. H. & Mucciolo, E. R. Coulomb Blockade Peak Spacing Fluctuations in Deformable Quantum Dots: A Further Test of Random Matrix Theory. *Physical Review Letters* **81,** 677–680. https://link.aps.org/doi/10.1103/PhysRevLett.81.677 (1998).

vHo92 Van Houten, H. Coulomb blockade oscillations in semiconductor nanostructures. *Surface Science* **263,** 442 –445. https://doi.org/10.1016/0039-6028(92)90385-J (1992).

vWe88 Van Wees, B. J., van Houten, H., Beenakker, C. W. J., Williamson, J. G., Kouwenhoven, L. P., *et al.* Quantized conductance of point contacts in a two-dimensional electron gas. *Physical Review Letters* **60,** 848–850. https://link.aps.org/doi/10.1103/PhysRevLett.60.848 (1988).

vdW00 Van der Wiel, W. G., Franceschi, S. D., Fujisawa, T., Elzerman, J. M., Tarucha, S., *et al.* The Kondo Effect in the Unitary Limit. *Science* **289,** 2105–2108. http://science.sciencemag.org/content/289/5487/2105 (2000).

Van17 Vandersypen, L. M. K., Bluhm, H., Clarke, J. S., Dzurak, A. S., Ishihara, R., *et al.* Interfacing spin qubits in quantum dots and donors–hot, dense, and coherent. *npj Quantum Information* **3,** 34. https://doi.org/10.1038/s41534-017-0038-y (2017).

Vil17 Villa, B., Bennett, A. J., Ellis, D. J. P., Lee, J. P., Skiba-Szymanska, J., *et al.* Surface acoustic wave modulation of a coherently driven quantum dot in a pillar microcavity. *Applied Physics Letters* **111,** 011103. https://doi.org/10.1063/1.4990966 (2017).

KDP80 Von Klitzing, K., Dorda, G. & Pepper, M. New Method for High-Accuracy Determination of the Fine-Structure Constant Based on Quantized Hall Resistance. *Physical Review Letters* **45,** 494–497. https://link.aps.org/doi/10.1103/PhysRevLett.45.494 (1980).

vKl85 Von Klitzing, K. *The Quantized Hall Effect* Nobel Lecture. 1985. https://www.nobelprize.org/prizes/physics/1985/klitzing/lecture/.

Wan18 Wang, J. *Surface acoustic wave engineering for single-electron transport* Master thesis (2018), 65 pages. http://www.upm.es/.

WW57 Weinreich, G. & White, H. G. Observation of the Acoustoelectric Effect. *Physical Review* **106,** 1104–1106. https://link.aps.org/doi/10.1103/PhysRev.106.1104 (1957).

Wha88 Wharam, D. A., Thornton, T. J., Newbury, R, Pepper, M, Ahmed, H, *et al.* One-dimensional transport and the quantisation of the ballistic resistance. *Journal of Physics C: Solid State Physics* **21,** L209–L214. https://iopscience.iop.org/article/10.1088/0022-3719/21/8/002/pdf (1988).

WKW86 Wixforth, A., Kotthaus, J. P. & Weimann, G. Quantum Oscillations in the Surface-Acoustic-Wave Attenuation Caused by a Two-Dimensional Electron System. *Physical Review Letters* **56,** 2104–2106. https://link.aps.org/doi/10.1103/PhysRevLett.56.2104 (19 1986).

Wu98 Wu, J., Gu, B.-L., Chen, H., Duan, W. & Kawazoe, Y. Resonant Tunneling in an Aharonov-Bohm Ring with a Quantum Dot. *Physical Review Letters* **80,** 1952–1955. https://link.aps.org/doi/10.1103/PhysRevLett.80.1952 (1998).

Yac95 Yacoby, A, Heiblum, M, Mahalu, D & Shtrikman, H. Coherence and phase sensitive measurements in a quantum dot. *Physical Review Letters* **74,** 4047–4050. http://dx.doi.org/10.1103/PhysRevLett.74.4047 (1995).

Yam12 Yamamoto, M., Takada, S., Bäuerle, C., Watanabe, K., Wieck, A. D., *et al.* Electrical control of a solid-state flying qubit. *Nature Nanotechnology* **7,** 247. https://doi.org/10.1038/nnano.2012.28 (2012).

Zaf08 Zaffalon, M., Bid, A., Heiblum, M., Mahalu, D. & Umansky, V. Transmission Phase of a Singly Occupied Quantum Dot in the Kondo Regime. *Physical Review Letters* **100,** 226601. https://link.aps.org/doi/10.1103/PhysRevLett.100.226601 (22 2008).

ZHH16 Zhao, X., Huang, P. & Hu, X. Doppler effect induced spin relaxation boom. *Scientific Reports* **6,** 23169. https://doi.org/10.1038/srep23169 (2016).

Acknowledgements

First, I would like to express my deep gratitude to my supervisor Christopher Bäuerle. The planning of this project was just great! I encountered exciting topics, challenging but realistic goals, a laboratory environment that is well organised and exceptionally good guidance. During my time at the Institute Néel, Chris was basically always available for discussing scientific as well as technical issues. His presence in the laboratory is extraordinary. I profited a lot from his ideas on specific measurement problems, his profound knowledge on cryogenics and his practical laboratory skills. Thank you very much for guiding me through this PhD project!

Furthermore, I would like to express special gratitude to my colleague and mentor Shintaro Takada. Shintaro taught me how to conduct nanoelectric experiments from conception through fabrication to the actual measurements. It was him, who provided the two nanoelectronic devices that led to the central results of this thesis. I also want to say special thanks for hosting me at the AIST in Tsukuba during my scientific visit in Japan. ありがとう!

I would moreover like to acknowledge all of my colleagues of the M building at the Institute Néel in Grenoble! Particularly, I would like to acknowledge very fruitful discussions with Tristan Meunier, Pierre-André Mortemousque, Benoit Bertrand, Vivien Thiney, Giorgos Georgiou, Baptiste Jadot, Junliang Wang, Everton Arrighi, Bernhard Klemt, David Niegemann, Emmanuel Chanrion and Matias Urdampilleta and with our visitors Barkay Guttel and Masahiko Yokoi. I would like to thank Junliang Wang additionally for his investigations on novel routes to enhance SAW generation and for continuing the work on the SAW-driven charge qubit project. I believe that you have the enthusiasm, curiosity and endurance to achieve really nice results! Further, I would like to thank Cameron Spence for the nice discussions during coffee breaks connected with short lessons in Japanese and for the careful reading of this manuscript. I would also like to highlight stimulating talks in Bavarian with Martin Schalk – it is really relaxing to speak mother tongue when being abroad. And I would like to acknowledge support in the laboratory by Damir Pinek, Mathias Solana and Ariel Haziot. I would further like to thank my colleagues for the motivating working atmosphere, the great parties, tabletop-soccer tournaments and skiing trips!

This work was enabled by the technical staff of Institute Néel! Particularly, I would like to thank Pierre Perrier for his support in technical problems. Also I would like to express special thanks to Kévin Herbe, Raphaël Iannone and

Johan Guilhot for their important support to provide liquid Helium. And I thank the people of the nano-fabrication team for their support in the clean-room. Especially, I would like to thank Jean-Francois Motte, Thierry Crozes and Bruno Fernandez for sharing their expertise. Without the support of the people from the cryogenic, electronic and nanofabrication department none of our experiments would be possible in the course of a three/four years PhD project.

During my doctoral studies, I had the possibility to discuss specific scientific questions with scientists having great expertise. I would like to acknowledge fruitful discussions on the transmission phase of quantum dots with Rodolfo Jalabert, Dietmar Weinmann, Michihisa Yamamoto and Xavier Waintal. Additionally, I would like to thank Xuedong Hu for critical reading the first manuscript that was written in the course of my thesis.

I thank Prof. Chris Ford for building up collaborations on quantum mechanical simulations with Hugo Lepage and on investigations of undoped heterostructures with Antonio Rubino. During my secondment at the Cavendish laboratory in Cambridge I learned a lot on these topics! I would also like to acknowledge Paulo Santos for teaching me simulations of SAW propagation during my secondment at the PDI in Berlin and for helpful discussions on SAW-driven charge transport. Let me also acknowledge all of my colleagues from the SAWtrain network for the stimulating discussions and the good time we passed together. The network meetings and ESR retreats were just SAWsome!

Finally, I would like to thank my family – especially my mother, my grandmother on the mother's side (R.I.P.), my father, my sister and my brother – who supported and motivated me for my PhD project and my friends – particularly Aline, Camille, Jakub, Laurenz, Magalie, Melina, Moritz, Nathaneil, Nicolas, Nico, Pablo, Sebastian, Valentin and Yasmin – who backed-up my working morale and with whom I passed a great time during the free time of my PhD project in the amazing mountain scenery of Grenoble and in other beautiful places of Europe.

This project has received funding from European Union's 2020 research and innovation program under the Marie Skłodowska-Curie grant agreement No. 642688.

SAWtrain
network